Gravity Separation of Two-Phase Flow in Steam Drum : Experiments and CFD simulation

By

R. K. Bagul

ENGG01201204021

Bhabha Atomic Research Center, Mumbai

A thesis submitted to the

Board of Studies in Engineering Sciences

In partial fulfillment of requirements

for the Degree of

DOCTOR OF PHILOSOPHY

of

HOMI BHABHA NATIONAL INSTITUTE

February, 2019

Homi Bhabha National Institute[1]

Recommendations of the Viva Voce Committee

As members of the Viva Voce Committee, we certify that we have read the dissertation prepared by Ritesh K. Bagul entitled "Gravity Separation of two-phase flow in steam drum : Experiments and CFD simulation" and recommend that it may be accepted as fulfilling the thesis requirement for the award of Degree of Doctor of Philosophy.

Chairman – Dr. A. K. Nayak **Date:**

Guide / Convener – Prof. J. B. Joshi **Date:**

Co-guide - Dr. P. K. Vijayan **Date:**

Examiner – Dr. A. K. Das **Date:**

Member 1- Dr. Abhijeet Vaidya **Date:**

Member 2- Prof. Ashwin Patwardhan **Date:**

Final approval and acceptance of this thesis is contingent upon the candidate's submission of the final copies of the thesis to HBNI.

I/We hereby certify that I/we have read this thesis prepared under my/our direction and recommend that it may be accepted as fulfilling the thesis requirement.

Date:

Place: **<Signature>** **<Signature>**

Co-guide (if applicable) **Guide**

[1] This page is to be included only for final submission after successful completion of viva voce.

STATEMENT BY AUTHOR

This dissertation has been submitted in partial fulfillment of requirements for an advanced degree at Homi Bhabha National Institute (HBNI) and is deposited in the Library to be made available to borrowers under rules of the HBNI.

Brief quotations from this dissertation are allowable without special permission, provided that accurate acknowledgement of source is made. Requests for permission for extended quotation from or reproduction of this manuscript in whole or in part may be granted by the Competent Authority of HBNI when in his or her judgment the proposed use of the material is in the interests of scholarship. In all other instances, however, permission must be obtained from the author.

Ritesh K. Bagul

DECLARATION

I, hereby declare that the investigation presented in the thesis has been carried out by me. The work is original and has not been submitted earlier as a whole or in part for a degree / diploma at this or any other Institution / University.

Ritesh K. Bagul

List of Publications arising from the thesis

Journal

1. "Entrainment phenomenon in gas–liquid two-phase flow: A review, R. K. Bagul, D. S. Pilkhwal, P. K. Vijayan and J. B. Joshi, *Sadhana,* Vol. 38, Part 6, December 2013, pp. 1173–1217.

2. Steady state flow analysis of two-phase natural circulation in multiple parallel channel loop, V.H. Bhusare, R.K. Bagul, J.B. Joshi, A.K. Nayak, Umasankari Kannan, D.S. Pilkhwal, P.K. Vijayan, Nuclear Engineering and Design 305 (2016) 706–716.

3. Air Water Loop for investigation of flow dynamics in a steam drum: Steady state two-phase natural circulation experiments and validation, R. K. Bagul, D. S. Pilkhwal, S.P. Limaye, P.K. Vijayan and J. B. Joshi, Nuclear Engineering and Design, 328 (2018), 266-282.

4. Air Water Loop for investigation of flow dynamics in a steam drum: carryover experiments and CFD simulation, R. K. Bagul, D. S. Pilkhwal, P. K. Vijayan and J. B. Joshi, , Nuclear Engineering and Design, 333 (2018), 145-160.

5. "Experimental investigations on carryover in a gravity separation based steam drum.", R. K. Bagul, D. S. Pilkhwal, P. K. Vijayan and J. B. Joshi, Journal of Nuclear Engineering and Sciences, **2019**, 5, 011004/1-12

Conferences

1. Experiments on two phase natural circulation using air water mixture and its validation, R.K. Bagul, D.S. Pilkhwal, P.K. Vijayan, Proceedings of the 23rd National Heat and Mass Transfer Conference and 1st International ISHMT-ASTFE Heat and Mass Transfer Conference IHMTC2015, Paper no. ISHMTC-659, 17-20 December, 2015, Thiruvananthapuram, India.

2. Experimental investigations on entrainment phenomenon during two-phase flow separation in steam drum geometry, R.K. Bagul, D.S. Pilkhwal, P.K. Vijayan, Proceedings of the 23rd National Heat and Mass Transfer Conference and 1st International ISHMT-ASTFE Heat and Mass Transfer Conference IHMTC2015, Paper no. ISHMTC-695, 17-20 December, 2015, Thiruvananthapuram, India.

Ritesh K. Bagul

ACKNOWLEDGEMENTS

I hereby first wish to express my sincere gratitude to my Guide Prof. J. B. Joshi for giving constant encouragement and guidance because of which I could successfully complete the work presented here. I am highly indebted to my co-guide Dr. P. K. Vijayan and my senior colleague Shri D. S. Pilkhwal who provided crucial support during design of experimental facility and execution of experiments. I am also extremely thankful to Head, Reactor Engineering Division, Shri S. K. Sinha and all the staff members from Operations group, Instrumentation group and Workshop of Reactor Engineering Division, BARC for their kind support for execution of experiments and analysis work. I also hereby express my thanks to Doctoral Committee and HBNI for their constant guidance and critic enhancing the value of this work. Last but not the least I am greatly thankful to my family members and friends for their unvarying love, affection and support.

CONTENTS

			Page no.
		SYNOPSIS	1
		LIST OF FIGURES	13
		LIST OF TABLES	21
		NOMENCLATURE	23
Chapter 1		**Introduction**	29
1.1		Background	29
1.2		Geometry under consideration	30
1.3		Project work plan	35
Chapter 2		**Literature Survey**	38
2.1		Introduction	38
2.2		Analytical development	41
2.3		Experimental work	47
2.4		Empirical correlations	64
2.5		Two Phase flow – CFD approaches	81
2.6		Summary and conclusions on literature survey	97
Chapter 3		**Air-Water Loop – Experimental facility**	108
3.1		Aim and objectives	108
3.2		Scaling philosophy	108
3.3		Description of Air-Water Loop	109
3.4		Instrumentation	115
Chapter 4		**Steady State Experiments and validation**	116
4.1		Steady state experiments	116
4.2		Uncertainties in measurements	119
4.3		Numerical analysis of steady state data	125
4.4		Results and discussions	137
Chapter 5		**Carryover Experiments and CFD simulations**	149
5.1		Experimental observations	149
5.2		Droplet size distribution measurement	153
5.3		Euler-Lagrangian methodology for carryover prediction	159
5.4		1-D Euler-Lagrangian approach	159
	5.4.1	Formulation of 1-D Euler-Lagrangian equations	159
	5.4.2	Test Cases for 1-D simulation	163
	5.4.3	Entrainment prediction for Air-Water Loop	165
5.5		3-D Euler-Lagrangian approach	170

	5.5.1	OpenFOAM solver – governing equations	170
	5.5.2	Validation test case for OpenFOAM solver	173
	5.5.3	Euler-Lagrangian simulations for AWL	182
5.6		Euler-Lagrangian simulation for AHWR steam drum	198
5.7		Summary and conclusion	204
Chapter 6		**Experiments and analysis of pool void fraction and swell level**	206
6.1		Introduction	206
6.2		Experimental measurements on pool void fraction in AWL	207
6.3		Prediction of pool void fraction using drift flux models	211
6.4		Photographic investigations on bubble size distribution	223
6.5		CFD simulation of void distribution	228
	6.5.1	OpenFOAM solver "*twoPhaseEulerFoam*": Governing equations	228
	6.5.2	Validation test cases for solver "*twoPhaseEulerFoam*"	235
	6.5.2.1	Geometry and Meshing	235
	6.5.2.2	Boundary conditions	237
	6.5.2.3	Salient results of validation test cases	245
6.6		CFD simulations for AWL drum pool	249
	6.6.1	Simulation cases considered for AWL drum	251
	6.6.2	Salient results and discussions	253
6.7		Development of drift flux model using CFD simulations	260
	6.7.1	Drift flux model equations	260
	6.7.2	Calculation of distribution parameters from CFD simulation	263
	6.7.3	Recommendations for drift flux model based on CFD	268
6.8		Experimental measurement of local void fraction and comparison with CFD	270
6.9		Prediction of variation of swell level for AHWR steam drum	283
6.10		Conclusion	287
7		**Summary**	290
8		**References**	294
9		**Appendix-A**	309
10		**Appendix-B**	316

Homi Bhabha National Institute

SYNOPSIS REPORT

Advanced Heavy Water Reactor (AHWR) currently being developed in India is a 900 MWth vertical pressure tube type, light water cooled and heavy water moderated nuclear reactor. Figure 1 shows the Main Heat Transport System (MHTS) of AHWR. In AHWR, the heat from the fuel bundles in core is removed by two-phase natural circulation. The two-phase steam-water mixture generated in core is separated in steam drums (4 Nos). The Steam drum is a horizontal cylindrical vessel of 4-meter diameter and 11-meter length and steam is separated purely based on gravity. The flow from tail pipes forms a bubbling pool inside the steam drum and water droplets are formed at the free separation interface as a result of bubble collapse/rupture. This can leads to carryover, i.e. pneumatic conveyance of water droplets by steam which means reduced separation efficiency. Carryover is thus undesirable and it needs be to minimized by careful design.

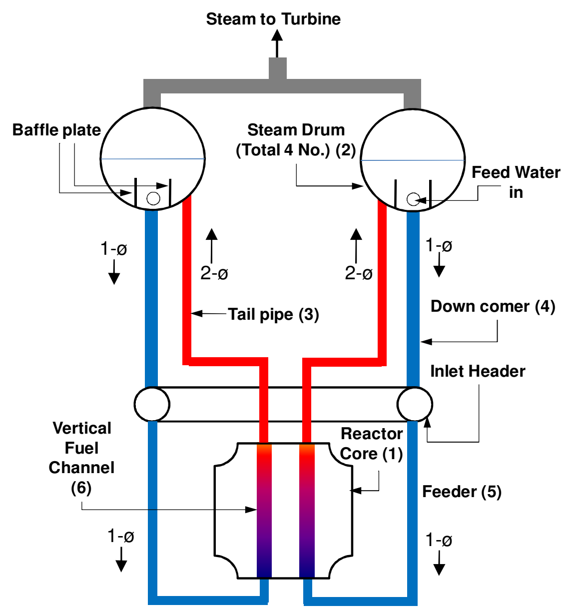

Figure 1: MHTS of AHWR

Aim/Objective of the present research work is to accurately estimate carryover for AHWR steam drum, supported by experimental and numerical study of flow dynamics for horizontal steam drum geometry.

Literature survey points out that reliable experimental data for the geometry relevant to AHWR is unavailable and therefore applicability of the empirical correlations derived from experiments in simpler geometry is also questionable. This forms main impetus for the present work. Table 1 shows the challenges/gap areas identified, objectives/work plan and major results/highlights of the present work.

Table 1: Challenges, Objectives and results of the research work.

Challenges/Gap area	Objectives/Work Plan	Results/Highlights
• No reliable experimental database for entrainment, droplet size distributions, swell level variation as a function of boundary flows in a geometry relevant to AHWR steam drum.	• Design, fabrication, installation, commissioning of a scaled down test facility, perform relevant experiments, numerical analysis/validation exercise.	• Experiments performed using air-water mixture in a scaled down test facility measuring pool void fraction, two-phase natural circulation flow rates, pressure drops, carryover, near surface entrainment, droplet distributions. • Validation exercise identified accurately predicting void fraction correlations for tail pipe and drum pool. • Size distribution functions for droplet obtained by fitting the data with Upper Limit Log Normal (ULLN) curve.
• Prediction of carryover for model and prototype (AHWR steam drum). • Prediction of swell level using numerical techniques and correlations.	• Assessments of existing empirical correlations, Development of CFD methods, use of open Source CFD software Open FOAM.	• Euler-Lagrangian simulations with validated solver predicted the trends which are comparable with correlations and experimental data. • Thresholds of operating steam drum level to minimize carryover obtained. • Standard drift flux models fail to predict pool void fraction. • Identified applicable correlations for pool void fraction and thus swell level. • Two-phase CFD solver validated for pipe geometries. Drift flux parameters can be obtained for pool conditions using CFD simulations.

<u>Issue 1: Generation of experimental database for carryover, pool swell level, droplet size distribution for horizontal steam drum geometry.</u>

Air-Water Loop (AWL), which simulates the scaled down steam drum using air-water mixture, was designed (see Figure 2), constructed and experiments were carried out. The model drum represents 1/8th slice of prototype geometry. Volume of drum is then scaled down by ratio of 1:4 to the prototype. The component sizes are chosen such that the superficial velocity of gaseous phase (j_g)and liquid phase (j_l) in tailpipe and various cross-section of drum are identical to prototype. Local flow losses are also identical to prototype. Steady state experiments were performed in AWL by injecting compressed air at the bottom of tail pipes. The natural

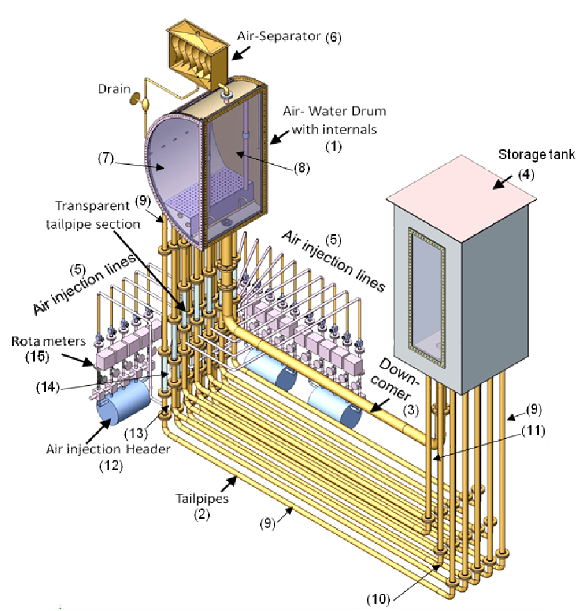

Figure 2: 3-D view of AWL

circulation flow rates and two-phase pressure drop measured during experiments were validated by solving mass conservation and momentum balance in feeder and tail pipe section of loop. 15 different void fraction correlations (which included various drift flux and slip ratio based models were considered in calculations. The best performing correlations include correlation by Thom [2], Zivi [3] Baroczy [4]. Figure 3 & 4 shows the comparison between experiments and predictions. Thom [2] correlation predicts flow rates within ± 30 % and two-phase pressure drop with accuracy of +10 to -15 % of the measured values.

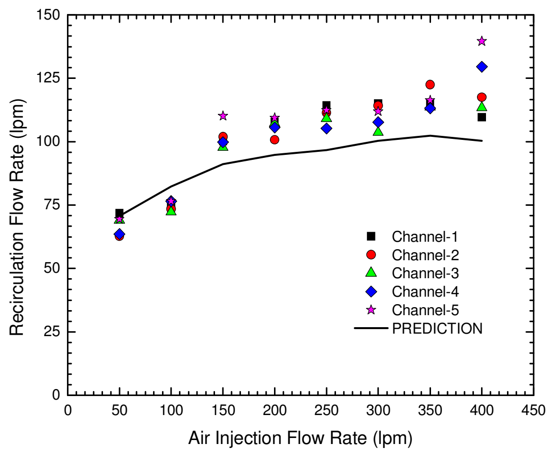

Figure 3: Prediction of recirculation flow rate

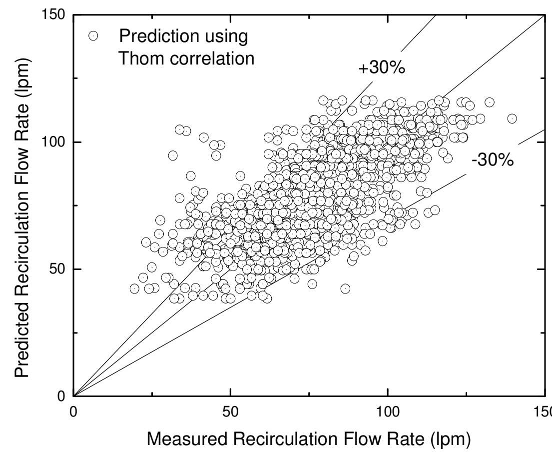

Figure 4: Prediction of water recirculation flow rates

Swell level as a function of water and air flow rate was measured and average pool void fraction is estimated based on the volume of water present in drum and volume corresponding to swell level as follows:

$$Average\ pool\ void\ fraction = 1.0 - \frac{Total\ water\ volume\ in\ drum}{Volume\ corresponding\ to\ swell\ level} \text{ Where} \tag{1}$$
$$Total\ water\ volume\ in\ drum = \ Intial\ water\ volume + Water\ volume\ displaced\ from\ water\ tank\ and\ tailpipes$$

The swell level was predicted using various drift flux correlations. Since the cross-sectional flow area changes along with height of drum, the void fraction is calculated in small volume with height Δh as shown in Figure 5. The void fraction also gives the liquid hold-up which is summed up and calculation is repeated iteratively until liquid hold up matches with experimental value. The corresponding height is the predicted swell level. Drift flux models were found to over predict the void fraction owing to the fact that large recirculation flows are observed in drum which is not accounted in correlations. However, it was found that a correlation by Boesmans et. al. [5] specifically developed for pool conditions predict the swell level accurately within ±5% of measurement (Figure 6).

Measurement of Entrainment: The entrainment was measureable only for swell levels close to drum exit. Figure 7 shows photographs for these conditions, where large liquid fragments are also seen to be entrained in flow, as the air velocity increases sharply near the exit. As per literature, the maximum entrainment for air-water system is about 4 [6]. Entrainment measured during these experiments is of same order (see Figure 8). At operating levels below 1.8 m the carryover was not measureable; however the droplet size distributions were measured using high speed photography with shadowgraph technique aided by image processing (Figure 9). Figure 10 shows the DSD obtained with image processing in which the image is converted to black and white by subtracting the background and then thresholding. The wavy interface is removed from image by morphological operations and image with only droplets is obtained.

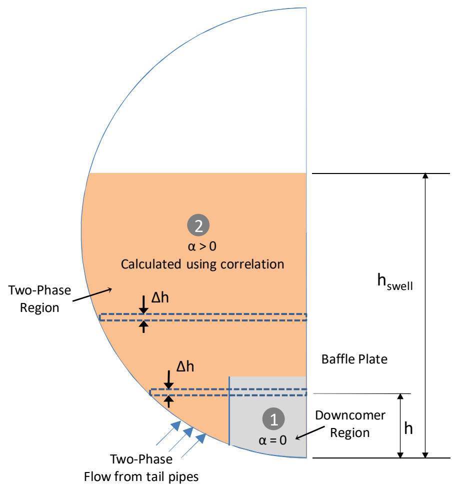

Figure 5: Calculation of void fraction for drum geometry

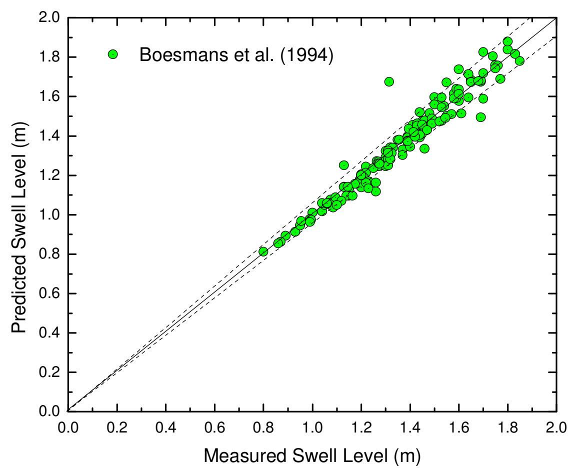

Figure 6: Prediction of swell level by Boesmans et. al. [5]

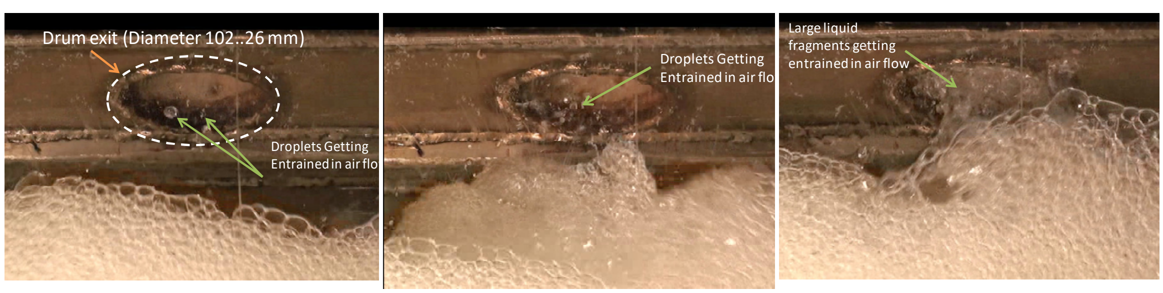

Figure 7: Liquid fragments getting entrained in flow

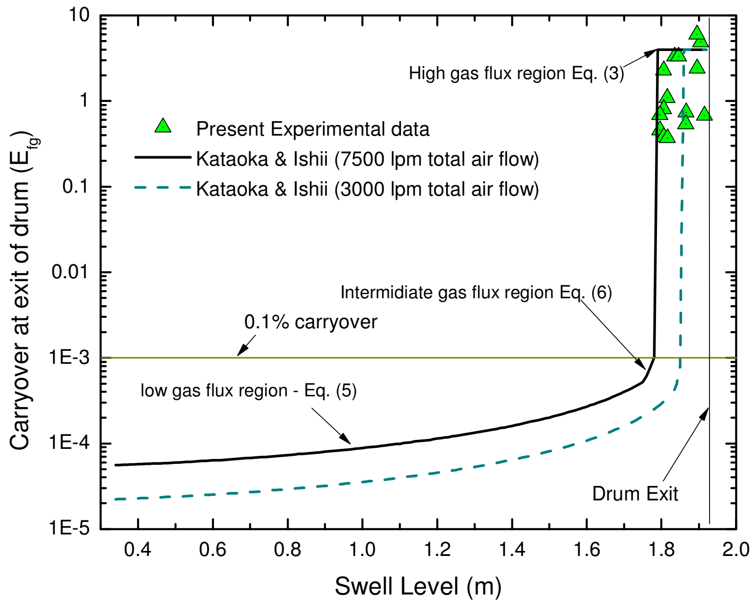

Figure 8: Experimental data on carryover compared with Kataoka and Ishii correlation [6].

The Droplet Size Distribution (DSD) has been found to follow Upper Limit Log Normal (ULLN) distribution curve. The distribution is fitted with curve given by following.

$$f(\eta) = \frac{\delta d_{max}}{\sqrt{\pi} d(d_{max} - d)} e^{-\delta^2 \eta^2} \tag{2}$$

$$\text{Where } \eta = ln\left(\frac{ad}{d_{max} - d}\right)$$

Where d is the droplet diameter, d_{max} is maximum droplet diameter, a and δ are distribution parameters.

The distribution parameters were found out to be $a = 10.0,\ \delta = 0.9$ and $d_{max} = 0.0027\ m$ by curve fitting to the experimental data.

(a) (b) (c)

Figure 9: (a) original image, (b) binary image obtained after subtraction of background and thresholding, (c) Image of only droplets after removal of interface by morphological operations.

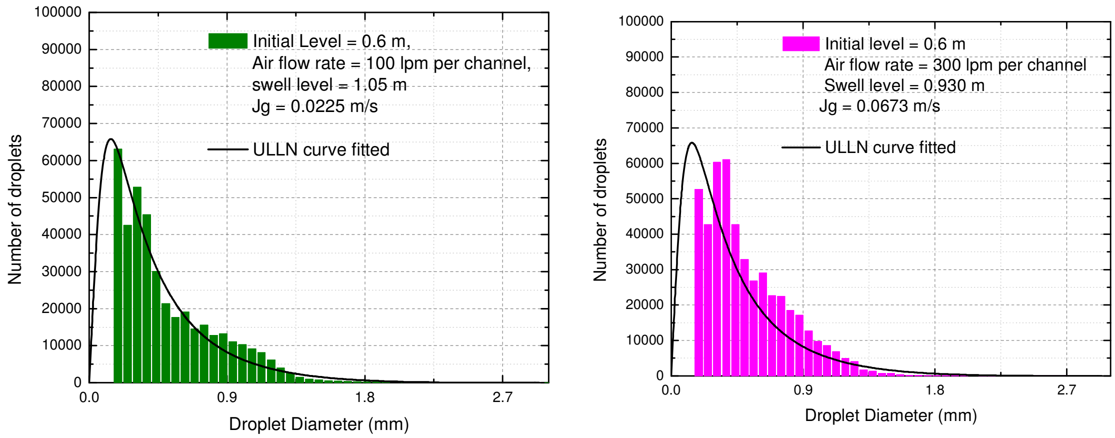

Figure 10: DSD obtained using shadowgraph technique.

Issue 2: Prediction of carryover for model and prototype geometries using numerical techniques.

Solution: Euler-Lagrangian (EL) approach is used for prediction of carryover. In this approach the steam/air is treated as Eulerian phase and droplet trajectories are estimated with Lagrangian approach. 3-D E-L calculations for AWL drum were carried out using open source CFD software OpenFOAM. A solver called "simpleReactingParcelFoam" was used which can solve compressible turbulent flows along with particle dynamics. Computational domain represents the air space above the swell level. CFD cases were constructed for swell levels varying from 0.3 to 1.8 m and air injection flow rate of 7500, 6000 and 3000 lpm covering the range of experiments. Figure 11 to 13 shows the geometry, mesh and salient results for a case with swell level of 0.965 m and air flow rate of 7500 lpm. The mesh used was arrived after performing grid independence study. Figure 12 shows the flow patterns for air capturing the flow acceleration near the exit as the area reduces sharply. DSD obtained in experiments is used for simulation of droplets. The heavier droplets were seen to fall back to interface while small droplets follow the bulk flow pattern (Figure 13).

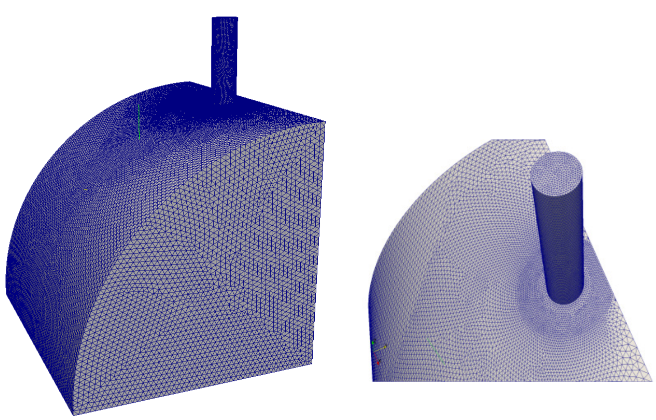

Figure 11: Mesh used for AWL drum simulation (1164 k tetrahedral elements)

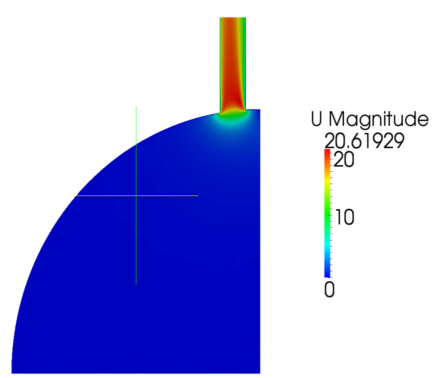

Figure 12: Velocity field for Air obtained using Euler Simulation

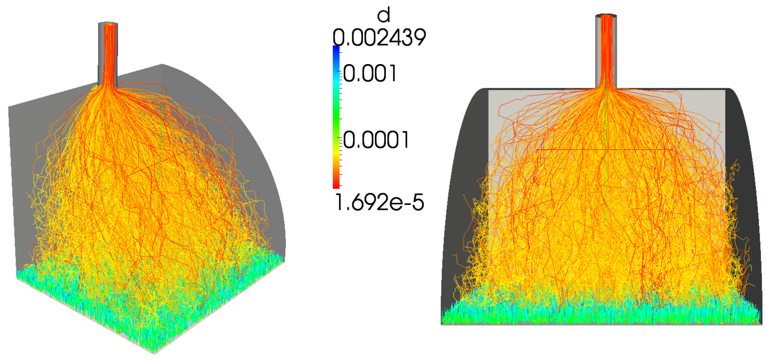

Figure 13 : Droplet trajectories colored with size

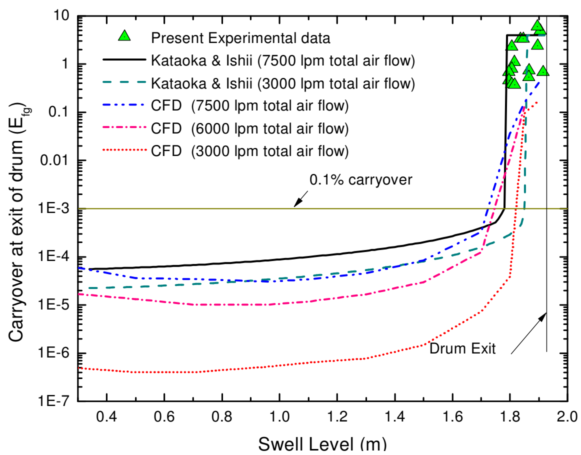

Figure 14: Comparison of carryover predicted by correlation [6] , CFD and experiments

The sum of droplets at exit gives the value of carryover which is compared with the correlation (Figure 14). It was found that in a gravity separation, entrainment increases faster after a certain threshold value of bulk flow superficial velocity. Here for AWL case it can be noted that such transition occurs at level of 1.8 m. E-L CFD calculations under predict the carryover for high swell levels as it cannot account for oscillating levels and formation of non-spherical large liquid fragments and its motion with bulk flow. However, for lower swell levels the trends are similar to correlation.

Carryover simulations for AHWR steam drum: Similar E-L approach is followed for AHWR steam drum. CFD cases are constructed by keeping the steam flow rate constant at 102 kg/s (corresponding to 100 % full power operation of reactor) and varying the swell level, so that a threshold value of level where carryover increases sharply can be found out. Figure 15 shows the 3-D model and mesh used in calculations. The DSD for the prototype conditions (70 bar and 285 ^{O}C) is a critical input for simulations but it is also unknown. However, the DSD measured for Air-Water can be transferred to AHWR conditions with the background knowledge that the droplet formation mechanisms would be identical but the size will be smaller as a result of fluid properties (The surface tension for air-water at 1 atmospheric and 30 ^{O}C is 0.0712 N/m and for steam-water at 70 bar and 285 ^{O}C is 0.0176 N/m, i.e. nearly 4 times smaller than air-water mixture). The droplet formation processes are often characterized with Weber number which is ratio of kinetic energy to surface energy of droplet. Assuming that the maximum Weber number, $We_{max} = \rho U^2 d_{max}/\sigma$ is conserved for model and prototype, the maximum droplet diameter for prototype i.e. AHWR steam drum is found out to be 0.9 mm. Figure 16 shows corresponding DSD. Figure 17 & 18 show the flow patterns obtained and the droplet trajectories for case of swell level of 2.0 m.

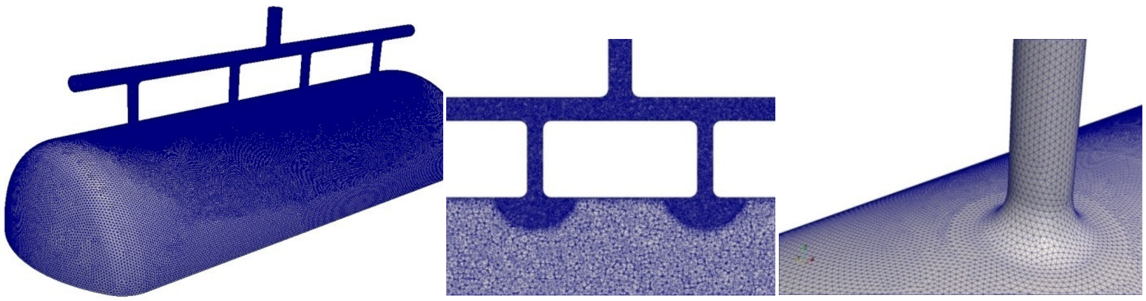

Figure 15: 3-D modeling and Meshing of AHWR steam drum

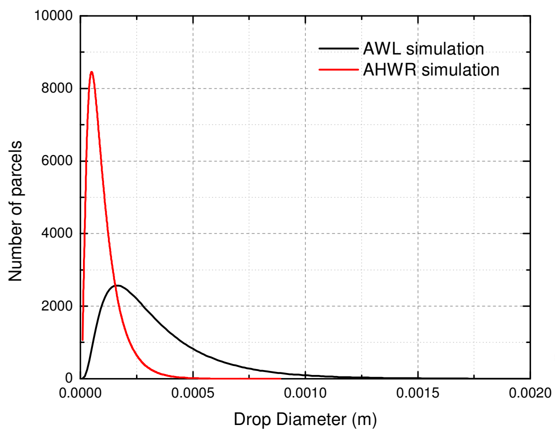

Figure 16: DSD obtained for AHWR simulation

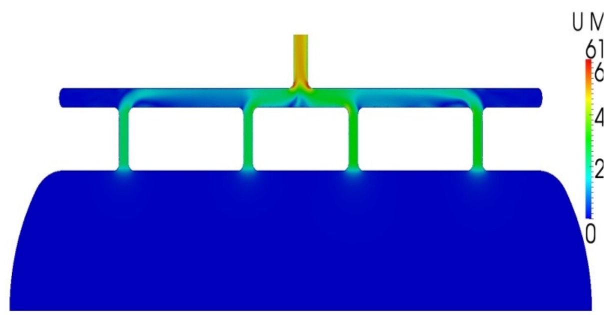

Figure 17: Velocity field for AHWR steam drum (swell level 2.0 m & steam flow rate 102 kg/s)

Figure 19 shows carryover predicted by CFD for various swell levels in AHWR steam drum. It shows that for AHWR at normal full power operation, carryover is within the limits (<0.1%) if swell level is maintained below 3.5 m.

Swell level is function of boundary flows to drum. Figure 20 shows the variation of swell level and average pool void fraction for AHWR steam drum calculated using the correlation [5] and methodology validated for AWL drum. It can be noted that at 100% FP the swell level is estimated to be 2.23 m, and carryover corresponding to it is negligible. The steam quality at drum exit for 100% FP and 2.23 m level is predicted as 99.97% by Kataoka & Ishii correlation [6] and 99.98% by CFD method (Figure 21)

Figure 18: Droplet trajectories calculated by OpenFOAM

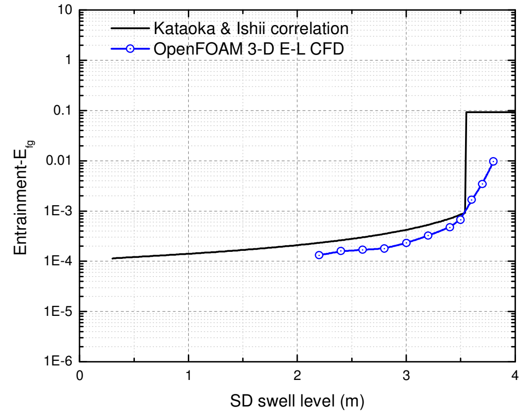

Figure 19: Entrainment at drum exit as a function of swell level for steam flow rate of 102 kg/s.

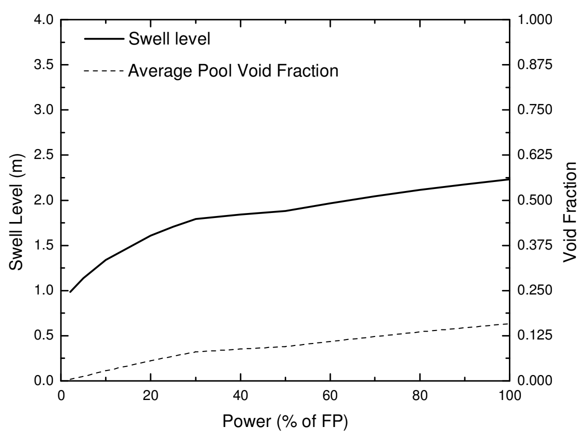

Figure 20: Swell level and pool void fraction in AHWR SD

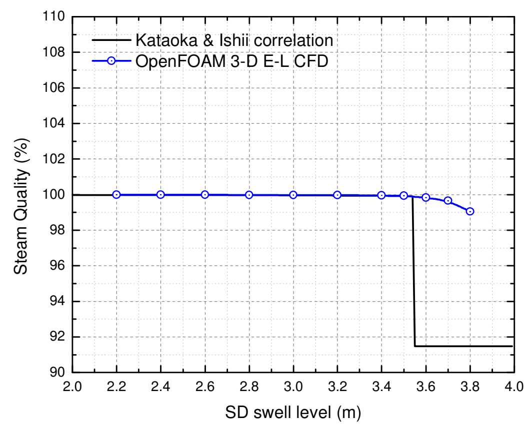

Figure 21: Steam quality as a function of swell level

Issue 3: Simulation of two-phase flow distribution below the separation interface and calculation of gas hold up.

Solution: 3-D CFD simulation of two-phase flow inside the drum using Euler-Euler (E-E) methodology has been carried out. OpenFOAM solver "twoPhaseEulerFoam" was validated for bubble column two-phase flow experiment by Hills [7] (see figures 22 & 23). After validation the 3-D simulations for AWL geometry and experimental conditions are carried out to predict the swell level and pool void fraction. Figure 24 shows a snapshot from transient simulation and Figure 25 shows the comparison of swell level predicted by CFD simulations with the experimental measurements and drift flux model [5] predictions.

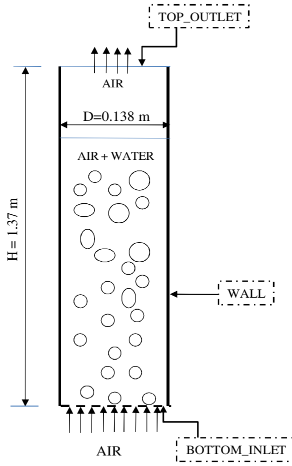

Figure 22 : Geometry of test section by Hills et al. [7]

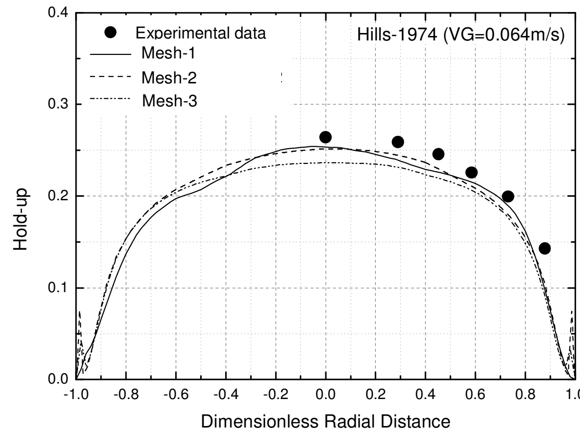

Figure 23: Comparison between CFD and experiments

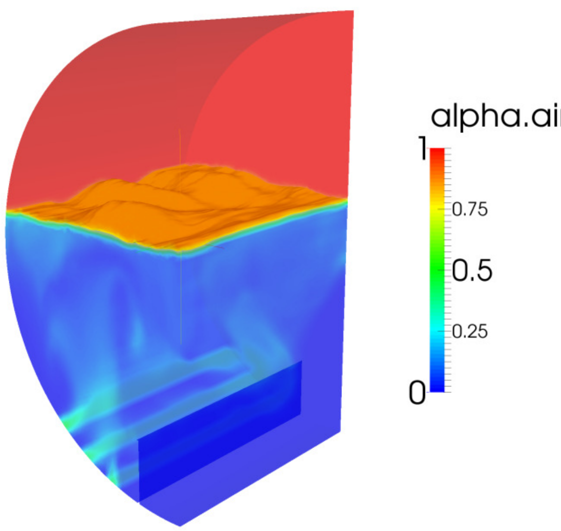

Figure 24: Instantaneous void fraction distribution obtained using CFD for experiement in AWL (initial water level =0.650m, Air flow rate=3000 lpm total).

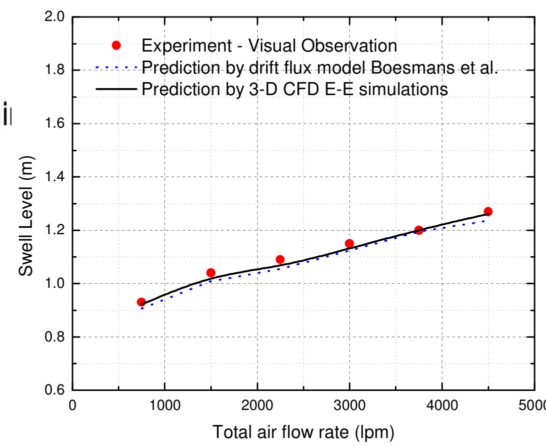

Figure 25: Comparison of swell level predicted by CFD simulations with experimental measurements.

Conclusion:

A scaled down model of AHWR steam drum was designed which has 1/24th symmetry with prototype and it conserves the superficial velocities of phases and local pressure losses. Experiments were carried out with air-water mixture. Measurements were made for two-phase natural circulation flow rate, pressure drop in the various sections, average pool void fraction; swell level, carryover and droplet size distribution. The recirculation flow rates and pressure drop data was validated using numerical technique based on momentum balance in feeder and tail pipe section of the loop. Void fraction correlation by Thom [2] predicts the results accurately. However such drift flux models do not predict pool void fraction satisfactorily because there are large internal recirculation of water flow inside the pool. A dedicated correlation for pool type conditions developed by Boesmans et al [3] was found to be accurately predicting the swell level (within ± 5%).

Near surface entrainment at high swell levels were measured and found to be in the range of 30-600%. At lower swell levels (lower superficial velocities) the carryover was not measurable. Droplet size distribution was measured using high speed photography and their distribution parameters were obtained. The motion of droplets was simulated using E-L method in Open FOAM. The CFD predictions were found to be comparable to correlation [4]. The E-L simulations under predict carryover for the cases with swell level near the exit because it is difficult to incorporate the effects of level fluctuations and violent ejection of water fragments in the current CFD set-up. The E-L methodology was extended for prototype calculations. The predictions show that for AHWR at normal full power operation, carryover is within the limits (<0.1%) if swell level is maintained below 3.5 m. The steam quality predicted by CFD simulations is 99.98 % for the 100%FP operating conditions of AHWR and swell level of 2.23 m. The CFD calculations thus confirm that steam drum design is adequate to minimize the carryover and gravity separation is effectively achieved.

References:

1. R. K. Sinha, A. Kakodkar, 2006, Design and development of the AHWR – The Indian Thorium fueled innovative nuclear reactor, Nucl. Eng. Des. 236, 683–700.

2. Thom J. R. S., 1964, Prediction of Pressure Drop During Forced Circulation Boiling of water, International Journal of Heat and Mass Transfer, 7, 709–724.

3. Zivi S. M., 1964, Estimation of Steady State Steam Void Fraction by Means of the Principle of Minimum Entropy Production, Trans. ASME, Journal of Heat Transfer, 86, 247–252.

4. Barcozy C. J., 1966, A Systematic Correlation for Two Phase Pressure Drop, Chemical Engineering Progress, 62(44), 232–249.

5. B. Boesmans and J. Berghmans, 1994, Level swell in pool boiling with liquid recirculation, Int. J. Heat and Mass transfer, 38(6), 989-998.

6. Kataoka I. and M. Ishii, 1984, Mechanistic modeling of pool entrainment phenomenon, Int. J. Heat and Mass Transfer 27(11), 1999.

7. Hills J. H., 1974, Radial nonuniformity of velocity and voidage in the bubble column, Trans. IChemE(2), 1-9.

LIST OF FIGURES

Sr. No.	Caption	Page No.
1.1	Schematic of Main Heat Transport System of AHWR.	31
1.2	Cross-sectional view of AHWR steam drum.	32
1.3	Ex-service turbine blade showing the water droplet erosion	34
2.1	Structure of floating bubbles at separation interface	42
2.2	Formation of droplets due to rupture of bubble at free surface	42
2.3	Mechanism for jet droplet formation	43
2.4	Height of projection of water drop at different steam velocities and pressures	45
2.5	Schematic representation of entrainment and dispersion in gas-solid fluidization	46
2.6	Size and frequency of film and jet droplets by Newitt et al. [11]	49
2.7	Frequency of droplets of different sizes [taken from Garner et al. [12]]	50
2.8	Entrainment as a function of droplet diameter [taken from Garner et al. [12]]	51
2.9	Relationship between Bubble diameter and droplet size [taken from Garner et al. [12]]	52
2.10	Effect of bubble diameter on frequency of droplet production [taken from Garner et al. [12]]	52
2.11	Entrainment as function of superficial velocity of steam and height of the vapor dome [taken from Sterman [21]]	56
2.12	Mechanisms of Entrainment	56
2.13	Formation of film droplets by shear [taken from Kataoka and Ishii [30]]	70
2.14	Regions of entrainment above the separation interface [taken from Kataoka and Ishii [30]]	73
2.15	Prediction by correlations for experimental data by Garner et al. [12]	77

2.16	Prediction by correlations for experimental data of Sterman [21] at 1.27 atmospheric pressure	77
2.17	Prediction by correlations for experimental data of Sterman [21] and Kolkolostev [22] at 17 atmospheric pressure	78
2.18	Prediction by correlations for experimental data of Sterman [21] and Kolkolostev [22] at 36 atmospheric pressure	78
2.19	Prediction by correlations for experimental data of Sterman [21] and Kolkolostev [22] at 91 atmospheric pressure	79
2.20	Prediction by correlations for experimental data of for Sterman [21] and Kolkolostev [22] at 110 atmospheric pressure.	79
2.21	(a) Euler-Euler simulation of two-phase flows (b) Euler-Lagrangian simulation of two-phase flows	84
2.22	Example of Numerical problems related to sharp jump in the volume fraction function	90
2.23	Geometric reconstruction of interface in 1-D	91
2.24	SLIC configurations with four face cell	92
2.25	Example of 2D flux of $\emptyset$ using SLIC	92
2.26	PLIC configurations with four face cell	93
3.1	Cross-section of AHWR steam drum considered for scaling	101
3.2	Entrainment variation with respect to height of vapor space to diameter ratio	105
3.3	Entrainment variation with respect to j_g^*/h^*.	105
3.4	Air-Water natural circulation loop configuration for design analysis	108
3.5	Scaling between prototype and model (design calculations) (a) tail pipe void fraction as a function of superficial velocity of lighter phase (b) superficial velocity of water (corresponding to natural circulation flow generated) as a function of superficial velocity of lighter phase	109
3.6	Air Water Loop – 3D view	110
3.7	Air water drum and Water tank	112
3.8	Air injection Header and Air injection lines.	112
3.9	Tail pipes and Air injection lines.	112
3.10	Simplified schematic of AWL.	113
3.11	Flow calibration curve	114

4.1	Variation of single phase pressure drop for Type-I channels measured during experiment (Initial Drum Level = 650 mm)	117
4.2	Variation of total phase pressure drop in two-phase region for Type-I channels measured during experiment (Initial Drum Level = 650 mm)	118
4.3	Variation of level in Drum and Water tank measured during experiment (Initial Drum Level = 650 mm)	119
4.4	Flow chart for prediction of steady state parameters	136
4.5	Comparison of predicted recirculation flow rate for water (Thom [69] correlation void fraction and Muller Steinhegan Heck [81] for two-phase pressure drop) against experimental measurements for complete database (Type-I, II and III channels, all experiments).	138
4.6	Comparison of predicted two-phase pressure drop (Thom [69] correlation void fraction and Muller Steinhegan Heck [81] for two-phase pressure drop) against experimental measurements for complete database (Type-I, II and III channels, all experiments).	139
4.7	(a): Prediction of water recirculation flow rate for Type-I channels (Initial Drum Level = 900 mm) (b): Prediction of water recirculation flow rate for Type-II channels (Initial Drum Level = 900 mm) (c): Prediction of water recirculation flow rate for Type-III channels (Initial Drum Level = 900 mm)	141
4.8	(a): Prediction of gradient of total pressure drop in two-phase leg for Type-I channels (Initial Drum Level = 900 mm) (b): Prediction of gradient of total pressure drop in two-phase leg for Type-II channels (Initial Drum Level = 900 mm) (c): Prediction of gradient of total pressure drop in two-phase leg for Type-III channels (Initial Drum Level = 900 mm)	142
4.9	Comparison of superficial velocity of water for AWL and for prototype.	145
4.10	Comparison of tail pipe void fraction for AWL and for prototype.	146
5.1	Photographs showing entrainment phenomenon at operating levels near the exit.	150
5.2	Carryover data compared with Kataoka & Ishii correlation	152
5.3	Shadowgraph technique	153
5.4	Steps in image processing for droplet size measurement: (a) Original Image, (b) Binary image after grayscale conversion and thresholding, (c) Image of only droplets after morphological operations, (d) Superimposition of 500 images of only droplets.	155
5.5	Droplet Size Distributions measured at (a) Swell level 1.05 m i.e h = 0.92, j_g= 0.0225 m/s, (b) Swell level 0.930 i.e h = 1.0, j_g= 0.0673 m/s, (c) Swell level 1.86 m i.e h = 0.07 m, j_g= 0.0750 m/s, (d) Swell level 1.48 m i.e h = 0.45, j_g= 0.0530 m/s,	157
5.6	Formation of droplets due to bursting of the bubble film	158

5.7	Particle positions for test case.	164
5.8	Particle velocity for the test case	165
5.9	Critical droplet diameter for air-water mixture at atmospheric pressure and temperature.	166
5.10	Estimating amount of entrainment at drum exit as a fraction of near surface entrainment.	167
5.11	Prediction of carryover for AWL drum by correlations and 1-D particle tracking code	168
5.12	Schematic of Cyclone separator (Ji et. al. [85])	174
5.13	Particle size distribution measured by Ji. et. al.[85] and Rosin-Rammler Fit [86] to data.	175
5.14	Mesh used for calculation of validation of cyclone separator case (714 $\times 10^3$ tetrahedral cells).	176
5.15	Velocity contours obtained for case with inlet air velocity of 30 m/s (a) Mesh-1(84$\times 10^3$ cells) (b) Mesh-2 (307$\times 10^3$ cells) (c) Mesh-3 (714 $\times 10^3$ cells)	180
5.16	(a) Velocity vectors obtained using Euler-Lagrangian simulation for cyclone separator validation test case at inlet air velocity of 30 m/s, using Mesh-3 (714 $\times 10^3$ cells)	181
	(b) Particle tracks obtained using Euler-Lagrangian simulation for cyclone separator validation test case at inlet air velocity of 30 m/s, using Mesh-3 (714 $\times 10^3$ cells)	
5.17	Separation efficiency predictions by CFD compared with experimental data.	182
5.18	Geometry of AWL drum.	183
5.19	Mesh used for case-4 (swell level 0.965m) 1523 k tetrahedral elements	185
5.20	Velocity field for Air obtained using Euler Simulation	189
5.21	Velocity magnitude predicted along line AB (as shown in Figure 5.20) for different meshes considered	189
5.22	Velocity magnitude predicted along line CD (as shown in Figure 5.20) for different meshes considered	190
5.23	Particle tracks obtained for CFD simulation case-4 (Table-5.3): (a) tracks colored with droplet diameter (b) tracks colored with droplet velocity.	191
5.24	Mesh used for AWL Euler-Lagrangian simulation case no 8. (a) 3-D view, (b) cross-sectional view showing mesh density near exit	192
5.25	Velocity contours obtained for AWL Euler-Lagrangian simulation case no 8.	192

5.26	Particle tracks obtained for AWL Euler-Lagrangian simulation case no 8. (a) tracks colored with droplet diameter (b) tracks colored with droplet velocity	193
5.27	Histogram of droplets from CFD simulation	194
5.28	Droplet distribution at the inlet	195
5.29	Droplet distribution at the outlet	195
5.30	Comparison of prediction of carryover by E-L simulations, correlations and experimental data.	197
5.31	3-D modeling and Meshing of AHWR steam drum	198
5.32	Velocity field calculated for AHWR steam drum (case-1, Table-5.5)	200
5.33	Droplet size distributions considered for AWL and AHWR simulation cases	201
5.34	Particle tracks / droplet trajectories colored with diameter obtained for Case-3, Table-5.5.	203
5.35	Particle tracks / droplet trajectories colored with velocity obtained for Case-3, Table-5.5.	203
5.36	Carryover prediction for AHWR steam drum based on CFD calculations	204
6.1	Calculation of volume of horizontal drum for given operating level (a) when level is below centerline (b) when level is above the centerline of cross-section	209
6.2	Average pool void fraction data from AWL experiments.	211
6.3	Calculation of void fraction for AWL drum with varying cross-sectional area	217
6.4	Comparison between predicted void fraction (by Hibiki and Ishii [89] correlation) with experiment (initial level = 0.650 m)	218
6.5	Comparison between predicted swell level (by Hibiki and Ishii [89] correlation) with experiment (initial level = 0.650 m)	218
6.6	Void fraction predicted by Hibiki and Ishii [89] correlation for several set of experiments in AWL	219
6.7	Distribution of bubbles inside large pool and flow recirculation patterns	221
6.8	Idealized flow pattern for large pool with core occupied by bubbles and liquid recirculation close to walls	221
6.9	Comparison of swell level predicted with correlation by Boesmans et al. [92] with experimental measurements (initial level =0.650 m)	222
6.10	Comparison of pool void fraction predicted with correlation by Boesmans et al. [92] with experimental measurements (initial level =0.650 m).	222

6.11	Comparison of predicted void fraction using correlation by Boesmans et al. [92] with experiments.	223
6.12	Comparison of predicted swell level using correlation by Boesmans et al. [92] with experiments.	223
6.13	Photograph of bubbling pool of AWL drum.	224
6.14	(a): Sample image-1 of bubbles in AWL drum pool, (b) Binary image obtained after processing sample image-1 as shown in Figure 6.14 (a)	225
6.15	(a) Sample image-2 of bubbles in AWL drum pool, (b) Binary image obtained after processing sample image-2 as shown in Figure 6.15 (a)	226
6.16	Histogram / Frequency count of bubbles	227
6.17	Relative Cumulative Frequency of bubbles	227
6.18	PIMPLE algorithm of *twophaseEulerFoam* solver.	234
6.19	Geometry of Bubble Column for validation test case	236
6.20	(a) : Cross-sectional view of Mesh-1, (b): 3-D view of Mesh-1, (c): Cross-sectional view of Mesh-2, (d): Cross-sectional view of Mesh-3	236
6.21	Void fraction (hold-up) for air at z = 0.598 m (validation test case for Hills [96] experiment)	245
6.22	Axial velocity of water at z = 0.598 m (validation test case for Hills [96] experiment)	245
6.23	Axial variation of void for air (validation test case for Hills [96] experiment)	246
6.24	Axial variation of water velocity (validation test case for Hills [96] experiment)	246
6.25	Comparison of void fraction of air predicted by CFD with experimental data by Hills [96].	247
6.26	Comparison of axial velocity of water predicted by CFD with experimental data by Hills [96]	247
6.27	Comparison of void fraction profile predicted by CFD with experimental data (Menzel et al. [97])	248
6.28	Comparison of axial velocity of water predicted by CFD with experimental data (Menzel et al. [97])	248
6.29	Geometry and boundaries considered for AWL drum two phase simulation	250
6.30	Mesh used for AWL drum two-phase simulation (total cells-3.67 lacs)	251
6.31	Instantaneous void fraction distribution obtained using CFD for case-4, Table 6.5 at time (a) t=0, (b) t= 95 s. (c) t= 96 s., (d) t= 97 s.	254

6.32	Time averaged void fraction distribution in drum (t = 100 seconds)	255
6.33	Time averaged water velocity vector plot for case-4, Table-6.5, t = 100 sec.	255
6.34	Void fraction (time averaged) profiles inside the drum at various elevations (Y=0.3 to 1.0 m) for case-4 described in Table 6.5.	256
6.35	Profiles of time averaged local air and water velocity and slip velocity at different elevations inside the AWL drum pool (case-4, Table 6.5).	258
6.36	Comparison of swell level predicted by CFD simulations with experimental measurements (initial level =0.650 m)	259
6.37	Comparison of void fraction predicted by CFD simulations with experimental measurements (initial level =0.650 m)	259
6.38	Cross-sectional view of two-phase flow in a pipe.	261
6.39	Drift flux parameter C_1 estimated from CFD simulations	267
6.40	Drift flux parameter C_0 estimated from CFD simulations.	267
6.41	Variation of $\frac{C_0}{\langle J_g \rangle}$ with respect to local hold up.	268
6.42	Comparison of predicted swell level using proposed drift flux correlation with experimental measurements.	269
6.43	Multi-point conductance probe (working principle)	270
6.44	Locations of Conductance probes installed in AWL drum.	272
6.45	Geometric details of multi-point conductance probes.	272
6.46	(a) Transient signal from conductance probe and (b) time averaged void fraction estimated from transient signal	273
6.47	Comparison of probe data with CFD simulations for air flow rate of 300 lpm per channel (initial drum level 650 mm)	275
6.48	Comparison of probe data with CFD simulations for air flow rate of 250 lpm per channel (initial drum level 650 mm)	277
6.49	Comparison of probe data with CFD simulations for air flow rate of 200 lpm per channel (initial drum level 650 mm)	278
6.50	Comparison of probe data with CFD simulations for air flow rate of 250 lpm per channel (initial drum level 650 mm)	280
6.51	Comparison of probe data with CFD simulations for air flow rate of 250 lpm per channel (initial drum level 650 mm)	281
6.52	Comparison of probe data with CFD simulations for air flow rate of 250 lpm per channel (initial drum level 650 mm)	283

6.53	Schematic of Main Heat Transport System (MHTS) of AHWR	285
6.54	Variation of void fraction in AHWR tail pipe with power.	286
6.55	Variation of steam and water flow rate with power for AHWR	286
6.56	Predicted variation of swell level and average pool void fraction for AHWR	287
A-1	\Simplified schematic of prototype steam drum.	310
B-1	Main code of solver "*simpleReactingParcelFoam*"	316
B-2	Algorithm of "*simpleReactingParcelFoam*"	317
B-3	"UEqn.H" employed in "*simpleReactingParcelFoam*" solver	318
B-4	"YEqn.H" employed in "*simpleReactingParcelFoam*" solver	319
B-5	"EEqn.H" employed in "*simpleReactingParcelFoam*" solver	320
B-6	Implementation of pressure correction equations in "*simpleReactingParcelFoam*"	323

LIST OF TABLES

Sr. No.	Caption	Page No.
1.1	Major challenges/gap areas for the proposed work and work plan	36
2.1	Summary of previous analytical work	58
2.2	Summary of published literature: Experimental work on carryover	62
3.1	Parameters for scaling the AHWR steam drum	103
3.2	Geometrical specifications for channels in AWL (refer Figure 3.10)	111
4.1	Accuracy and uncertainty of Instruments and measurement techniques	124
4.2	Uncertainty calculation for AWL- Natural Circulation Flow rate	124
4.3	Uncertainty calculation for AWL- Two-Phase Pressure Drop (Pa)	124
4.4	Void fraction correlations used in the code	128
4.5	Comparison of various correlations for prediction of experimental data – (Muller Steinhegan Heck model [81]for pressure drop)	147
4.6	Comparison of various correlations for prediction of experimental data – (Homogeneous model [82] for pressure drop)	148
5.1	Experimental parameters and entrainment measured during experiment	152
5.2	Descritization schemes used in OpenFOAM	179
5.3	Simulation cases for AWL & boundary conditions	183
5.4	Descritization schemes used in OpenFOAM simulation of cyclone separator	187
5.5	Simulation cases for AHWR steam drum & boundary conditions	199
6.1	Mesh Properties (validation test case for Hills [96] experiment)	237
6.2	Boundary conditions used for OpenFOAM CFD simulation of bubble column	242
6.3	Discretization schemes used in OpenFOAM CFD simulation of	243

bubble column

6.4 Test conditions considered for two-phase simulation in AWL drum 252

6.5 Boundary condition for inlet boundary for two-phase flow simulation 252

6.6 Values of superficial velocities, void fraction and drift flux parameters calculated by CFD for case-2, Table 6.5. 264

6.7 Values of superficial velocities, void fraction and drift flux parameters calculated by CFD for case-3, Table 6.5. 265

6.8 Values of superficial velocities, void fraction and drift flux parameters calculated by CFD for case-4, Table 6.5. 265

6.9 Values of superficial velocities, void fraction and drift flux parameters calculated by CFD for case-5, Table 6.5. 266

Nomenclature

a	Distribution parameter in Eqn. 5.1 and 5.2.
A	Cross-sectional area (m^2)
A_r	Non dimensional number as per equation 2.30
C_D	Coefficient of drag
C_p	Heat capacity at constant pressure (J/kg K)
C_v	Heat capacity at constant volume (J/kg K)
C_0	Drift flux parameter (Eq. (4.9), (6.14))
C_1	Drift flux parameter (Eq. (6.25), (6.52))
d	Droplet diameter (m)
d_{max}	Maximum droplet diameter (m)
D	Diameter (m)
D_H	Hydraulic diameter of vessel/equipment (m)
D_H^*	Non Dimensional Hydraulic diameter of vessel/equipment, $\left(D_H/\sqrt{\sigma/g(\rho_f-\rho_g)}\right)$
$\mathcal{D}$	Diffusion coefficient (Eq. (5.28))
e	Error
E_{fg}	Entrainment
Eu	Euler number $\Delta P/\rho v^2$
f	Friction factor
f_D	Variable defined as per Eq. 5.13, 5.14 and 5.15
F	Force (N)
Fr	Froude number (Eq. ())
g	Gravitational acceleration constant (m/s^2)

G	Mass flux (kg/m^{2}s)
h	Height above separation interface (m)
h^*	Non dimensional height from the separation interface, $h/\sqrt{\sigma/g(\rho_f-\rho_g)}$
h_{fg}	Latent heat of evaporation (J/kgK)
H	Level (m)
$\mathcal{H}$	Enthalpy (J/kgK)
I	Turbulent Intensity
J	Superficial velocity (m/s)
J_g^*	Non dimensional superficial velocity of gas, $\left(J_g/(\sigma g(\rho_f-\rho_g)/\rho_g^2)^{\frac{1}{4}}\right)$
$\boldsymbol{j}$	Diffusion mass flux (kg/m^{2}s)
K_L	Local loss coefficient
K	Kinetic energy (J)
k	Turbulent kinetic energy (m^2/s^2)
l	size/length of liquid fragment (m)
L	length of pipe section (m)
m	Mass (kg)
$N_{\mu g}$	Gas viscosity number, $\left(\mu_g\Big/\sqrt{\rho_g\sigma\sqrt{\sigma/g(\rho_f-\rho_g)}}\right)$
$N_{\mu f}$	liquid viscosity number, $\left(\mu_f\Big/\sqrt{\rho_g\sigma\sqrt{\sigma/g(\rho_f-\rho_g)}}\right)$
n	number of readings
P	Pressure (N/m^2)
ΔP	Differential Pressure / pressure loss (N/m^2)

q	Heat flux (W/m^2)
Re	Reynolds number
R	Radius (m)
r	Radial co-ordinate
s	Standard Deviation (Eq. (4.1))
S	Source term
t	Time (s)
Δt	Time step (s)
T	Temperature (K)
ΔT	Temperature difference (K)
U	Velocity (m/s)
$\boldsymbol{u}$	Velocity vector
V	Volume (m^3)
v	Velocity (m/s)
We	Weber number ($\frac{\rho U^2 d}{\sigma}$)
W	Weight of droplet (Kg)
w	Dryness fraction of steam
x	X axis coordinate
y	Y axis coordinate
Y	Mass fraction of specie.
z	Z axis coordinate

Greek Symbols:

ρ	Density (kg/m^3)

σ	Surface tension (N/m)
μ	Dynamic viscosity (Ns/m^2)
η	Transformed variable as per Equation 5.1
δ	distribution parameter as per Equation 5.2
α	void fraction
τ	Shear stress (N/m^2)
$\emptyset$	Fluid phase (air or water/ gas or liquid)
χ	Flow quality
ε	Hold up (fraction) of a fluid phase
ϵ	Turbulent kinetic energy dissipation rate (m^2/s^3)
ω	Vorticity (1/s)
ϑ	Kinematic viscosity (m^2/s)
γ	Bulk viscosity (kg/ms)
Γ	Thermal diffusivity ($J/(m^3K)$)
ψ	Slip ratio
$\boldsymbol{\tau}$	Stress tensor

Subscripts

$1-\emptyset$	Single phase (fluid)
$2-\emptyset$	Two phase mixture
B	Buoyancy
b	Bubble
c	Carrier gas phase
d	Droplet

D	Drag
$drag$	Drag force
$drum$	Drum
eff	Effective
ev	Evaporation
f	Fluid
fc	Cell face
fg	Liquid dispersion gas
g	Gas
G	Gravity
H	Hydraulic
he	Heat exchange
i	Initial
j	Jet
l	Liquid
L	Lift
m	Mass
M	Model
max	Maximum
mmt	Measurement
mo	Momentum exchange
O	Outside (of bubble / pipe)
p	Particle
P	Prototype

r	Relative
ref	Reference
rms	Root mean square
s	Saturation
$surf$	Surface
T	Total
t	Turbulent
TD	Turbulent dispersion
V	Vapor space
VM	Virtual mass
x	X axis component
z	Elevation

Acronyms and Abbreviations

AHWR	Advanced Heavy Water Reactor
AWL	Air-Water Loop
1-D	One Dimensional

Chapter -1

Introduction

1.1 Background:

Steam drum is one of the important component of power plants. Design of steam drum is aimed at achieving high efficiency of separation, along with compact, robust and cost effective construction. Mechanical steam separators (Cyclone, Chevron type separators) are often employed to improve the separated steam quality, however such equipments introduce additional pressure drop in the system. In order to simplify the equipment, gravity based steam separation poses an attractive alternative and is being sought in some of the advanced reactor designs. Performance of steam drum system depends on the dynamics of two-phase flow inside the geometry which is complex in nature. The behavior of two-phase flow distribution below vapor-liquid interface, turbulence and separation of phases at the interface and flow dynamics of dispersed liquid phase in bulk of the vapor phase above the vapor-liquid interface needs to be understood thoroughly. Details of such processes can be modeled empirically with series of simplifying assumptions; however, their applicability and accuracy for a given practical geometry under different combinations of parameters remains a question. Thorough experimental validation of the empirical models/methodologies is therefore of utmost important. Therefore experiments are performed on models/prototypes prior to design implementation to develop mathematical models for prediction of equipment performance. Development of computational fluid dynamics (CFD) techniques has added another dimension to the understanding that can be developed altogether. CFD is also being extensively employed to derive information on complex flow characteristics in steam generators and its impact on structures, system response to the change in operating conditions and to apply design modification and optimization. Multi-phase flow CFD is yet an evolving field of research and there is huge potential to develop/validate the models used. CFD models having known the capabilities and limitations can simultaneously be applied to an evolving engineering design. This proposed research derives motivation from the current developments in CFD with an objective to reduce the simplifying assumptions, adding details to the modeling and simulation of steam generator processes.

1.2 Geometry under consideration

Geometry under consideration in the present study is the steam drum of Advanced Heavy Water Reactor (AHWR). Advanced Heavy Water Reactor (AHWR) is a vertical pressure tube type, boiling light water cooled and heavy water moderated nuclear reactor [1]. AHWR employs two-phase natural circulation as a mode of coolant recirculation through the reactor core. Thermal hydraulic design ensures that the natural circulation flow efficiently removes the heat generated in fuel rod bundle in normal as well as accidental operating conditions. In order to enhance the flow, geometry of flow loop is designed such that it minimizes the pressure drop and provides maximum driving buoyancy head. Figure 1.1 shows the schematic of two-phase natural circulation loop in Main Heat Transport System (MHTS) of AHWR. The coolant flow through core is a result of balance between buoyancy and pressure drop in the MHTS loop. The two-phase boiling water from the core (1) of the reactor is transported to steam drum (2) situated 30 meters above the reactor core, via tail pipes (3). The separated water returns to core via down comer (4) and feeders (5). The steam drum is a horizontal pressure vessel with circular cross-section having 4 meters in diameter and 11 meters in length. There are total 452 fuel channels (6), 452 tail pipes and 452 feeders which are connected to 4 number of steam drums. Each steam drum receives flow from 113 tail pipes which are arranged symmetrically and are connected from sides at the bottom portion of drum. Vertical baffles are placed inside the drum to avoid mixing between two-phase flow entering the drum and the separated water in down comer region. As steam leaves the drum and MHTS, equal amount of mass of feed water is introduced in the drum. The steam gets separated by gravity i.e. due to density difference between steam and water. No mechanical separator is used. The horizontal orientation of steam drum provides large area for steam-water separation.

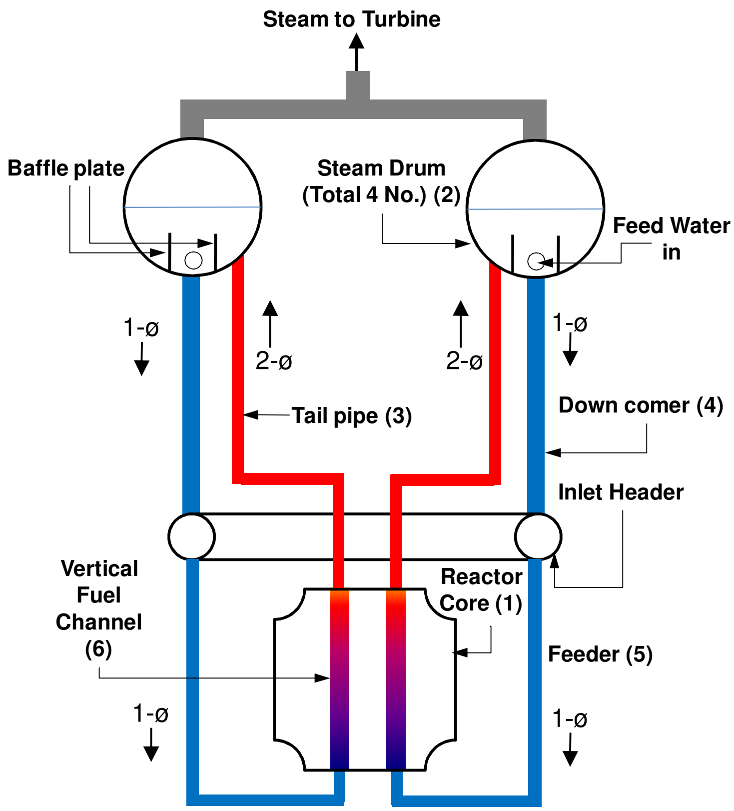

Figure 1.1: Schematic of Main Heat Transport System of AHWR.

Figure 1.2 shows the cross-sectional view of AHWR steam drum. AHWR steam drum is a horizontal pressure vessel with cylindrical cross-sectional closed at the ends with torispherical dish heads. The internal diameter of steam drum is 4.0 m and total length of vessel is 11.0 m. There are 4 down comers (300 NB Sch. 120 pipe) provided at the bottom centre of steam drum. 113 tail pipes enter into steam drum from both sides of the down comer at different angles as shown in cross-sectional view. Longitudinal baffle plates are provided to prevent the two-phase mixture from tail-pipe to enter in down comer region. Lower submerged perforated plate is provided at the top of baffle plate, which breaks down large slug bubbles coming from tailpipe into smaller bubbles. This shall reduce the fluctuations of the separation interface. Upper submerged perforated plate is provided in steam drum pool region just above the centerline. This plate distributes the bubbles in the pool and thus functions to reduce the turbulence of the free surface at separation interface. Overhead perforated plate offers additional resistance to the steam flow and minimizes the droplets entraining in the steam flow. There are four nozzles and piping (200 NB Sch. 120) provided for steam collection into the steam collector header (300 NB Sch. 120). Steam is sent from collection header to the turbine for power production.

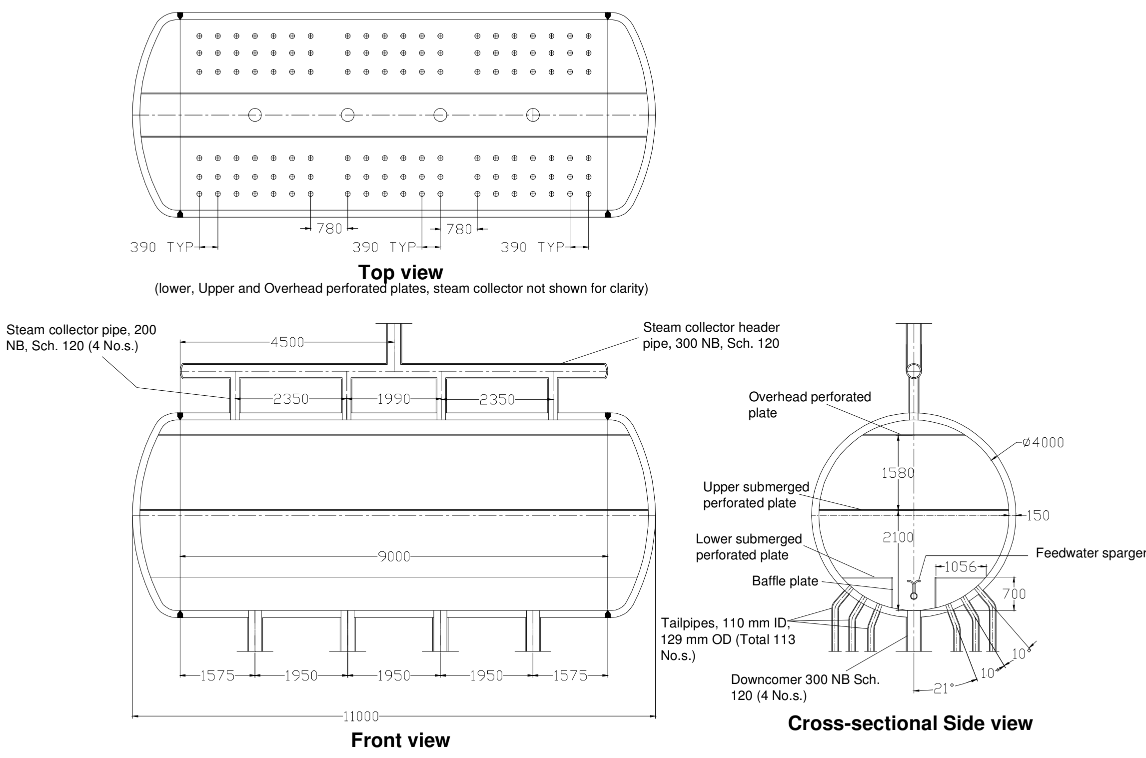

Figure 1.2: Cross-sectional view of AHWR steam drum.

Due to horizontally placed steam drum, large separation interface is available which reduces the superficial velocity of steam at separation interface. This assists for efficient gravity separation. As the steam separates by gravity i.e. due to density difference between steam and water, without aid of any mechanical separators, it simplifies the operation of steam drum. Gravity separation also improves the economy as lesser parts involved in construction and subsequent maintenance requirements are reduced. However, the effectiveness of gravity separation depends on the amount of carryover. Carryover is the entrainment of liquid droplets in the vapor phase. When the steam bubbles arrive at the separation interface, it bursts out and water droplets are formed as result of breakage of water film surrounding the bubble. Some of these small droplets may get carried out of the drum along with steam to the turbine circuit, if the separation of steam-water in the steam drum is not complete. Carryover should be eliminated as much as possible to avoid erosion corrosion of the turbine blades.

The steam at the exit of drum may contain droplets of various sizes ranging from few micros to few millimeters depending on the efficiency of separation in the drum. Even after careful design and use of mechanical separators fine droplets are still entrained in the steam flow. These droplet subsequently impact on the turbine blades rotating at high velocity. For example if turbine blade having height of 2 m rotates at 3000 RPM, the tip speed is of the order of 625 m/s. Water being an incompressible fluid, droplet impact on blade surface generates high pressure on the impact area. The contact stresses at the impact interface cause the material to flow and create depressions and asperities. These surface irregularities enhance the surface roughness and subsequently continuous impact of droplets lead to formation of pits and cracks. These surface defects aggravate the fatigue loading and blade may fail during service. This subject of water droplet erosion has been focus of several researchers till date.

Wang et al [2] and Mazur et al [3] studied failures of steam turbine blades, and concluded that blades mainly fail due to fatigue cracking, which occurs due to surface wear. In a case study of turbine failure at Dresden power plant, Chynoweth et al [4] performed a root cause analysis and showed that surface erosion was one of the reasons for such failure. Failure of turbine has serious economic consequences in any power plant.

The droplet size is one of the important factors that decide severity of surface erosion of turbine blades. Small droplets of size 0.1 to 4 μm deposits on blade surface and may coalesce to form film which after breakage gives large droplets(> 1 mm). These large droplets however get atomized in to smaller droplets (10-400 μm) due to high rotational speed of blades [5]. Förster [6], has claimed that the effective droplet size that causes erosion is between 50–200 μm. He added that droplets smaller than 50 μm in size do not cause damage, and those larger than 200 μm atomize into smaller dropletes.

Figure 1.3 shows a photograph of turbine ex-service blade from LP stage turbine where at the end of expansion significant amount of water droplets are generated. The photograph is taken from study published by Kirlos et al. [7]. The photograph shows the water droplet erosion occurring at the trailing edge of blade and it is severe near the tip of blade.

Figure 1.3: Ex-service turbine blade showing the water droplet erosion.

The systematic study by Kirlos et al. [7] on microstructure of the surface reveal that the rough surface asperities were of the size in the range of 200 μm, which can be related to the effective droplet sizes range impacting the surface, 50–200 μm. The results of above mentioned studies are not only important to erosion in Low Pressure turbines but the conclusions are generic and applicable to water droplet erosion due to carryover. Thus the consequences of carryover / presence of water droplet can be severe.

The carryover depends on the geometrical parameters of the steam drum like diameter, height available for separation along with the operating conditions like pressure and steam velocity. Estimation of carryover thus forms an important aspect of steam drum design for AHWR.

In the normal operating conditions of the reactor the average core exit quality is about 19.1% which corresponds to a void fraction of 82.79%. This causes a swelling in the steam drum (i.e. an increase in the steam drum level). The void fraction correlations for the small diameter pipes (Such as tail pipes) are available which are validated but for the large diameter pipe or pool (such as steam drum) information on validated models is scarce. The swell level inside determines the available vapor space height. The swell level should have sufficient distance from exit location so that carryover is minimized. Therefore, studies are required to know the exact void fraction and swelling in the steam drum.

1.3 Project work plan:

Objectives of the proposed research work are as following

1. To construct model of prototype having sufficient windows for flow visualization.
2. Experimental Measurements – Droplet size and flow distribution inside steam drum model. Attention will be focused on drop size and velocity distribution at the vapor liquid interface. These are useful for setting up the boundary conditions for carryover

simulations. Swell level and vapor hold up below the separation interface will also be measured. This will be required to validate the CFD multi-phase flow models.

3. CFD simulations in model and validation of CFD methodology and flow visualization strategy.
4. Validation / testing of empirical models for carryover and pool void fraction.
5. CFD Simulation of scale steam drum describing the concentration and velocity profile of the droplets (carryover) in the vapor phase and pool swell dynamics.
6. To establish adequacy of steam drum design and margins with respect to design goals.

Table 1.1 gives the summary of the gap areas of the topic under consideration and the work planned.

Table 1.1: Major challenges/gap areas for the proposed work and work plan

Challenges/Gap area	Objectives/Work Plan
• No reliable Experimental database for ❑ Entrainment, ❑ Droplet Size Distributions ❑ swell level variation i.e. location of separation interface as a function of boundary flows of liquid and vapor phase ❑ Bubble size and its distribution in a geometry relevant to AHWR steam drum.	• Design, fabrication, installation, commissioning of a scaled down test facility simulating gravity separation process in AHWR steam drum and carry out relevant experiments. • Generate database on swell levels as a function of two-phase natural circulation flows, carryover, near surface entrainment rates at various operating conditions. • Optical investigations on nature of interface, droplet formation mechanisms, Droplet size distribution, bubble size distribution.

• Prediction of carryover for model and prototype (AHWR steam drum) geometries using numerical techniques. • Prediction of two-phase flow dynamics below the separation interface using numerical techniques.	• Develop CFD techniques and workflow for simulating carryover process in model and prototype geometries using open source CFD software OpenFOAM.

Chapter 2– Literature review

2.1 Introduction

Estimation of carryover in the design of new equipment is still based on the empirical correlations developed upon the experimental data. The chronological development of the subject has occurred in both: experimental and analytical approaches culminating into the empirical correlations. Computational fluid dynamics is relatively new and has not yet been extensively applied to simulate the carryover phenomenon.

First comprehensive approach to estimate the carryover for the case of high pressure industrial boilers has been given by Davis [8]. He used information from photographic studies on bursting of bubbles and droplet formation in order to estimate the droplet sizes that may be formed at the interface inside the boilers. He presented an expression for maximum height that can be attained by droplets and thus the variation of carryover above the separation interface was predicted. Davis [8] could estimate the limiting vapour flow rates for minimizing the carryover. His calculations were very conservative; however a systematic approach was presented by him. This approach was later used by Zenz and Weil [9] for estimation of carryover from fluidized bed reactor. Cheng and Teller [10] also followed similar methodology to analyze carryover in sieve tray column for air-water system. These analytical works also stress on the development of database for droplet size distribution in order to produce accurate and reliable results.

The earlier experimental work on measurement of carryover and droplet size distribution includes studies by Newitt et al. [11] and Garner et al. [12]. Newitt et al. [11] measured droplet sizes for air-water system using magnesium oxide coated plates. Garner et al. [12] studied entrainment in an evaporator geometry (diameter 0.3 m) at pressures ranging from 2.0 to 12.5 bar. Garner et al. [12] found out that 95% of the carryover is composed of droplets smaller than 20 μm. Also they observed that, for a large sized bubbles (diameter greater than

5 mm), droplets are generated from rupture of liquid film of bubble domes. Spiel [13] studied droplets generation by bursting of bubbles up to size of 3 mm in air-water system and noticed that large droplets are formed by rupture of small bubbles. Aiba and Yamada [14] have measured droplet size distribution for fluids such as air-water, air-butanol, air-glycerine mixtures. Experimental geometry used by Aiba and Yamada [14] was a vertical glass cylinder of 0.096 m diameter and air superficial velocity was varied from 0.086 to 0.1037 m/s. Rozen et al. [15] have studied the droplet size distribution in vertical cylindrical geometries (diameter varying from 0.4 to 0.6 m) with steam-water at 1 and 2 atmospheric pressures. Apart from these, there are numerous studies available in literature on the fundamental process of bubble collapse and droplet formation, such as Afeti & Resch [16] , Wu [17] and Gunther et al. [18]. These studies show that two types of droplets are formed after bubble rupture. The larger sized droplets are formed from the liquid jet arising from momentum of liquid surrounding the bubble. As bubble collapses the surrounding liquid rushes in and a central spout is thrown upwards, which further breaks up into droplets. These are called jet droplets which are of the order of few milli meters (Kientzler et al. [19]). Very fine sized droplets are also found to be generated from the disintegration of thin liquid film of bubble dome. These are called film droplets. Afeti & Resch [16], Wu. [17], Blanchard et al. [20] have reported formation of film droplets as small as 20 μm. Gunther et al. [18] have also presented a summary of various previous experimental studies on the droplet formation. Most of such experiments show that for larger bubble diameters (greater than 4 mm), jet droplets are not observed and formation of film droplet is the only dominant mechanism.

Sterman [21] and Kolkolostev [22] have investigated carryover for steam-water mixture operating at high pressure and temperature. Sterman [21] has provided experimental database for in a vertical cylindrical geometry of diameter 0.24 m with steam-water mixture operating at 17.22, 36.47, 92.20, 111.47 & 187.45 bar pressure. Kolkolostev [22] measured entrainment fraction in a cylindrical vessel of diameter 0.3 m for steam-water mixture at pressures 17.22, 36.47, 92.20, 111.47 & 187.45 bar.

Very few geometry specific carryover experiments are available in literature. Mochizuki and Hirao [23] have experimentally studied the carryover in steam separator geometry using air-water mixture. Cosandy et al. [24, 25] studied the entrainment from a bubbling pool that is formed in reactor containment during accidental conditions scenario in a scaled down model. Recently Sun et al. [26-27] have experimentally studied the entrainment from upper plenum of AP-1000 during the blow-down and depressurization conditions. The carryover was found to be primarily dependent on the operating level in PWR vessel, where the entrainment increases significantly when levels are close to side exit of vessel. These experiments were carried out in a scaled down facility [26] with steam-water conditions. Subsequently the phenomenon has been also studied in air-water system with test section (0.380 m diameter and 2.2 m height) having side and top exit [28].

Empirical correlations existing in literature are based on dimensional analysis and fit to the experimental database, for example, Sterman [21], Kruzihilin [29] etc. Kataoka and Ishii [30] proposed a set of correlations based on a mechanistic model incorporating information from all the experimental data available at that time. The approach and correlations provided by Kataoka and Ishii [30] have been used to predict the entrainment fractions by Nayak et al. [31] and Koch et al. [32] in their respective geometries under consideration.Subsequent studies have found & pointed out some deviations from Kataoka and Ishii [30] model in their own measurements, for example Iyer et al. [33], Cosandy et al. [24], Zhang et al. [28]. However, it remains the most well known correlation.

Previous experimental studies which are relevant to AHWR steam drum have been done by Iyer et al. [33] and Basu et al. [34]. Iyer et al. [33] have conducted experiments in vertical cylindrical geometry (0.3 meter diameter, 1.2 meter long and 0.437 meter diameter, 1.45

meter long) using air-water mixture. Experiments were carried out for superficial velocities of the phases similar to that of AHWR steam drum. Iyer et al. [33] found some deviations from Kataoka and Ishii [30] model and proposed an extension of correlation to fit their experimental data. Basu et al. [34] conducted experiments in transparent horizontal drum of diameter 0.8 m and length 1.2 m using air-water mixture. Basu et al. [34] showed that the amount of carryover increased with an increase in the superficial velocity of air for a given initial level of water.

From the foregoing discussion, it is clear that, a good number of papers have been published to address the issue of entrainment. It was thought desirable to classify the published papers into four categories: (a) mathematical description of the phenomenon using analytical models (b) experimental studies (c) development of empirical correlations and (d) recent studies on numerical models. All available literature has been analysed and critically reviewed in the following sections.

2.2 Analytical Development

Davis [8] addressed the issues related to the production of steam at high pressures in industrial boilers and the problems of mechanical failure of components due to salts deposited by the entrainment carried by the steam. He studied the bubble generation at the heater tubes, their movement in the pool towards the separation surface and the behaviour of steam bubbles at the free level. When a bubble arrives at the free level, it forms a nearly complete hemispherical dome shaped lamina of liquid and remains floated with stability for certain time duration before rupture.

Figure 2.1 shows the various structures of the surface bubbles as visualized by Davis [8].

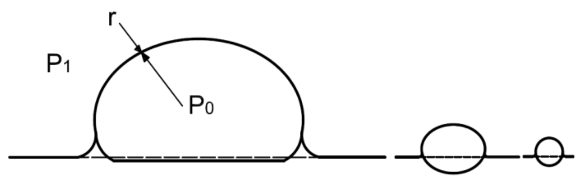

Figure2.1: Structure of floating bubbles at separation interface

The hemispherical shape is due to the formation of a thin water film which is a result of balance between the excess pressure inside the bubble and the surface tension.

Size of bubble dome is given by:

$$P_1 - P_0 = \frac{8\sigma}{D_b} \tag{2.1}$$

However the bubble at the free interface is unstable and rupture of thin liquid film at the dome takes place. The rupture of the film of bubble dome gives rise to formation of number of small droplets termed as film rupture droplets (see Figure 2.2). Film droplets are very small of the order of few microns. Afeti & Resch [16], Wu. [17], Blanchard et al.[20] have measured film droplets as small as 20 µm.

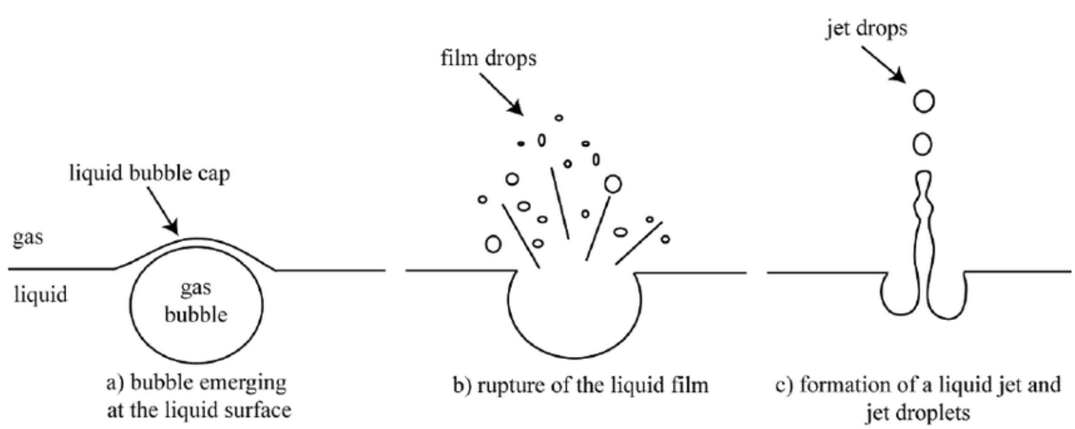

Figure 2.2: Formation of droplets due to rupture of bubble at free surface.

Following the rupture of film, the surface tension rapidly pulls the rim where they intersect outward and downward. Eventually, a ring of fluid at the base of what was the bubble contracts to a point, throwing a plume of fluid upward in the form of a high-speed jet. The jet will often break up into a number of drops. These large droplets are call jet droplets (see Figure 2.2). These jet droplets are comparatively larger than the film droplets and are of the order of few mm (Kientzler et al. [19]).

Davis [8] has proposed the following stepwise mechanism for the "jet droplet" generation:

(a) when the bubble dome ruptures the rim of the bubble sinks

(b) which leads to rise of the depressed portion at the bubble centre due to momentum of inflowing liquid

(c) it throws a spout upwards

(d) the tip of which necks of under the action of surface tension into separate drops.

Based on the above mechanism (see Figure 2.3), it can be understood that only small bubbles can eject droplets, as large bubbles do not depress the liquid sufficiently in proportion to their size to cause rise of centre of depression.

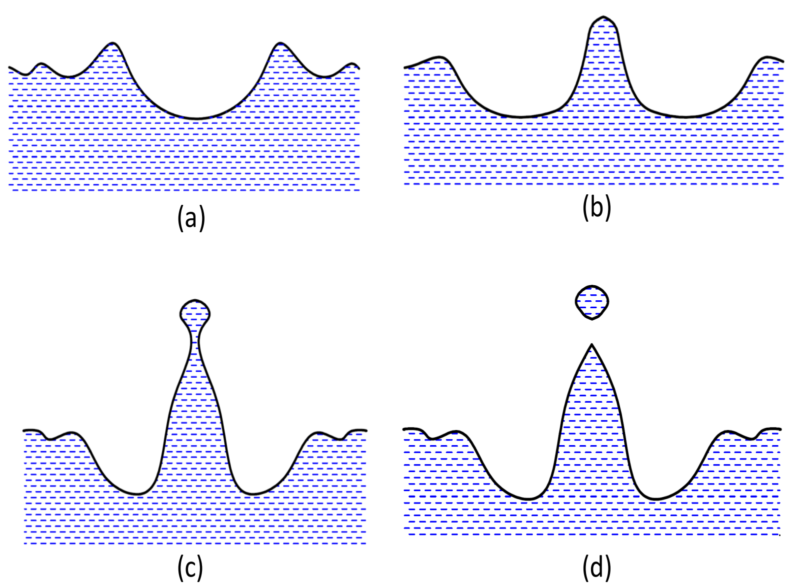

Figure 2.3: Mechanism for jet droplet formation *(a) Bubble rim sinks following the rupture of bubble dome (b) the central depressed portion rises up due to momentum of liquid (c) A spout is thrown upwards (d) the tip of the sprout necks under action of surface tension and a droplet is formed* [taken from Davis [8]]

Davis [8] pointed that the height up to which the droplet can rise depends on the droplet velocity after formation and resistance of the vapour while rising. He developed equation based on the force balance for the droplet to predict the maximum height gained by a droplet ($\boldsymbol{h_{max}}$) in vapour space.

Considering force balance on the droplet, during upward flight of droplet we can write

$$\frac{W}{g}\frac{dv_r}{dt} = -K_{drag}v_r^2 - W \tag{2.2}$$

And during downward motion of droplet

$$\frac{W}{g}\frac{dv_r}{dt} = K_{drag}v_r^2 - W \tag{2.3}$$

At height y from free surface at time t, it can be written as

$$v_r = \frac{dy}{dt}\ hence \frac{dv_r}{dt} = v_r\frac{dv_r}{dy} \tag{2.4}$$

Using above equation and integrating it can be found that

$$h_{max} = \frac{(v_{terminal})^2}{2g}\left[ln\left\{1 + \frac{\left(v_i - v_g\right)^2}{q^2}\right\} - ln\left\{1 - \frac{v_g^2}{q^2}\right\}\right] + \frac{v_g v_{terminal}}{2g}\left[tan^{-1}\left(\frac{v_i - v_g}{q}\right) + ln\left(\frac{v_{terminal} + v_g}{v_{terminal} - v_g}\right)\right] \tag{2.5}$$

Where $v_{terminal}$ is terminal velocity of droplet and is given as

$$(v_{terminal})^2 = \frac{W}{K_{drag}} \tag{2.6}$$

It can be seen from equation (2.5) that the droplet having terminal velocity equal or very close to vapour velocity gets carried all the way in the vapour flow, which happens to be the minimum amount of carry over that will always be present in the flow. The above expression requires the knowledge of velocity of projection and diameter of droplet and the terminal velocity of droplet i.e. drag coefficient during the various stages of motion. Davis [8] pointed out the importance of the experimental evidence for validation. Davis [8] made several simplifications and based on the observations of earlier experiments deduced that the average velocity of projection of droplets can be taken as 1.4 m/s. Based on the knowledge of bubble size at the heater tubes and their growth while reaching the free surface he could deduce the bubble diameter and the corresponding droplet dimension. Using equation (2.5) he predicted the quantity of carry-over for different steam flow rates. Davis [8] also calculated the permissible velocities or steam rates at various pressures (see Figure 2.4).

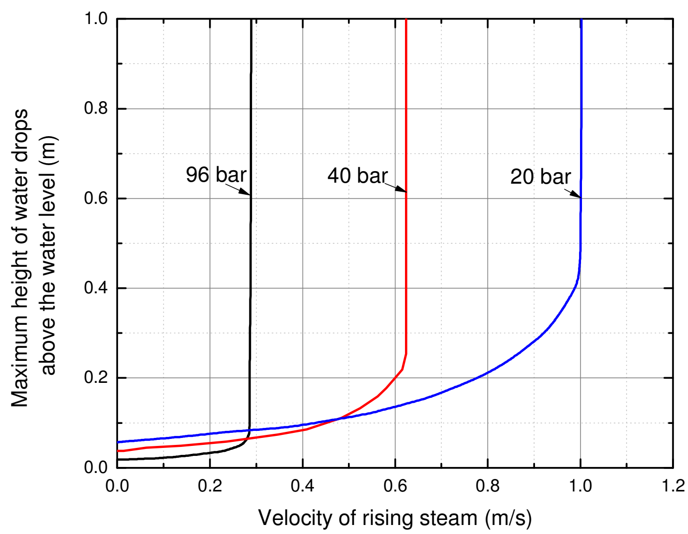

Figure 2.4: Height of projection of water drop at different steam velocities and pressures

Davis [8] estimated that the calculations had a factor of safety of 4 when compared with the actual entrainment at the exit of boiler. It may be noted that Davis [8] attempted to obtain the entrainment rates based on the force balance for the droplets. However, the size and velocity distribution of droplets and their generation rates at the free surface was not completely understood at that point of time. Davis [8] has further pointed out that the entrainment depends on the bubble dynamics in the pool below. He has also brought out the importance of the design of internals in the phenomena of carry-over. Thus it may be pointed out that Davis [8] has made pioneering contribution to the subject of entrainment.

Cheng and Teller [10] followed the approach developed by Davis [8] to analyze behavior of entrained particles in the zone between trays in a sieve tray column for the air-water system. The droplet size distribution was experimentally obtained and was found to have log-normal distribution. In the absence of velocity data, the velocities of drops were assumed/ deduced from the experiments of Aiba and Yamada [14]. The carryover estimation was found to agree within 28% when compared with the experimental measurements.

Zenz and Weil [9] addressed the problem of particle entrainment in fluidized bed. Figure 2.5 shows schematic representation of the phenomenon. An equation of motion for the solid particles was formulated for instantaneous velocity of particle, terminal velocity of particle and maximum height attained by a particle using similar approach developed by Davis [8]. However, to obtain the complete entrainment gradient pattern, the entrainment rate for various size particles must be known at the free surface. The entrainment rate at free surface was empirically modeled by authors.

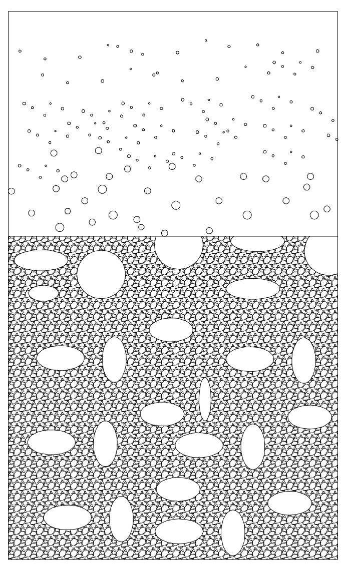

Figure. 2.5: Schematic representation of entrainment and dispersion in gas solid fluidization

Nayak et al. [31] analytically studied the carryover of water droplets by the steam in a 3.5 m diameter, horizontal steam drum. The steam-water separation by gravity was modeled. The droplet size and velocity distribution at the separation interface was assumed and trajectory of the droplets was computed. The droplet size distribution suggested by Kocamustafagullari et al. [35] was used in the calculation. The maximum droplet size and ejection velocity distribution was estimated based on the mechanistic model given by Kataoka and Ishii [30]. Droplet dynamics considered the equation of motion of drop as a perfect sphere under the action of drag and buoyancy forces in a constant velocity field. Parametric study was carried out to predict the critical droplet diameter and carryover for the various steam flow rates. Nayak et al. [31] concluded that carryover is less than 0.1% when steam velocity at separation interface is less than 0.7 m/s. The analysis however did not consider the effect of change of flow cross-section and acceleration of steam flow towards the exit. The various analytical studies conducted on carryover and the various assumptions made are summarized in Table 2.1. From above analytical work carried by various researchers, it can be noted that the subject of droplet size distribution, velocity distribution and number of parameters affecting it including the geometries is complex. However to obtain initial estimations, simplified approach as given by Davis [8] can be followed with knowing the fact that empirical models involved can lead to conservative designs.

2.3 Experimental work

Newitt et al. [11] carried out experimental studies on bubble bursting at the air-water free surface. They studied the bubble behavior with photography techniques. They measured the droplet size distribution using microscope slides coated with magnesium oxide and measuring the impression made by the droplets after impact on the coating (measurement accuracy 20μm). The entrainment was obtained at different heights above the pool surface. The authors proposed the following stepwise mechanisms:

(a) Disintegration of liquid film of stable bubble at the free surface (film drops).

(b) Fragmentation of jet ejected due to rushing liquid as bubble rim sinks and center of depression rises (Jet drops).

Figure 2.6 shows the experimental observations by Newitt et al. [11] which indicate existence of film droplets of small diameters with high frequency of generation and large sized jet droplets with lower frequency of generation.

Newitt et al. [11] further compared the jet droplet size observed experimentally with the theoretical analysis. The jet formed after bubble collapse was assumed to have hyperbolic shape (in x-y plane). They have shown the height of the rising jet to be:

$$h_j = \sqrt{\frac{2}{\left(\frac{g\rho_f}{\sigma}\right) - \left(\frac{1}{xy}\right)}} \tag{2.7}$$

They have further estimated the velocity of the rising jet and is given by:

$$v_j = \frac{3}{2}\frac{\left(P_o + \frac{4\gamma}{D_j}\right)}{D_j\rho_f}t \tag{2.8}$$

Newitt et al. [11] assumed t to be of the order of 0.00003 seconds and found that the observed velocity of jet droplets agrees well with that given by equation (2.8). They considered the criterion of break-up of cylindrical liquid column into drops when its length becomes greater than the circumference. Further, they employed the recommendation of Weber upon the favorable wave length at which such breakup occurs. As a result, they have shown that the jet droplet diameter is related with the jet diameter by the following equation:

$$d = 1.89D_j \tag{2.9}$$

Experimental observations by Newitt et al. [11] for jet droplet diameter were close to those given by the above equations. Authors also developed equations of drop ballistics based on the force balance for droplets. The maximum height attained by the droplets was found to be predicted accurately by the proposed theoretical procedure.

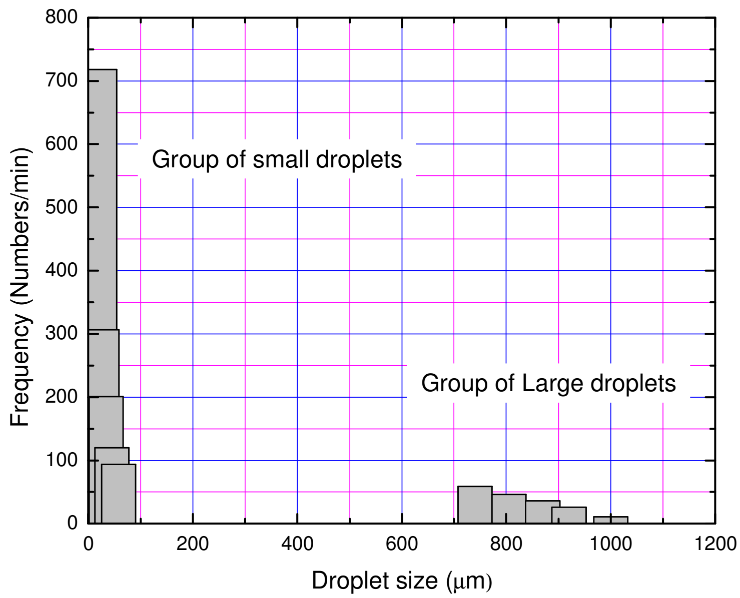

Figure. 2.6: Size and frequency of film and jet droplets by Newitt et al. [11]

Garner et al. [12] measured the droplet size distribution (using MgO coated slides) inside an evaporator apparatus for different steam rates. They measured the entrainment carried at the exit of equipment by chemical analysis of salt (potassium nitrate) premixed in water. They also investigated the effect of bubble size on the production of various sizes of droplets. For this purpose, they used air-water system.

Figure 2.7 shows the experimental observations of Garner et al. [12] for the frequency of generation of various sized droplets. The results appear to be consistent with the findings of Newitt et al. [11] thus underlining the fact of existence of very high number of small droplets above the separation surface. More than 95% of droplets were below 20μm size. Figure 2.8 shows the entrainment as a function of droplet diameter. It is interesting to see that, in spite of a decrease in number with an increase in size, the mass fraction of entrainment was found to increase with increase in the droplet diameter as the liquid volume is proportional toD^3. The larger droplets were obviously present closer to separation interface and thus entrainment was found to be high near the surface. Away from the surface up to exit, as expected the entrainment was found to decrease as the mean droplet size decreases. Garner et al. [12] found that 95% of the droplets entrained in the vapor space were having size less than 20μm. However as the size of droplets is small, the total entrainment caused by these droplets is small. Garner et al. [12] found that droplets above 100μm would be the major contributor to entrainment.

Lowering the liquid level inside the evaporator was found to reduce the entrainment. Experimental results point out that the entrainment rises quite fast beyond a certain steam rate. At high vapor rate the liquid droplet flux at the separation interface rises due to agitation of boiling water. This results in to high entrainment rates. Author also noted that in the presence of foaming agent, a foam blanket is formed at the separation interface which acts as a viscous layer eliminating the droplets formed by splashing and thus reducing entrainment.

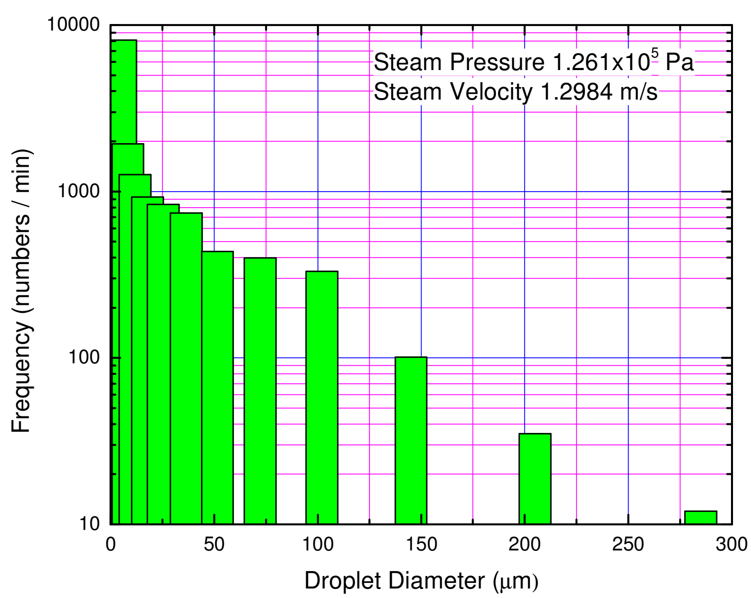

Figure 2.7: Frequency of droplets of different sizes [taken from Garner et al. [12]]

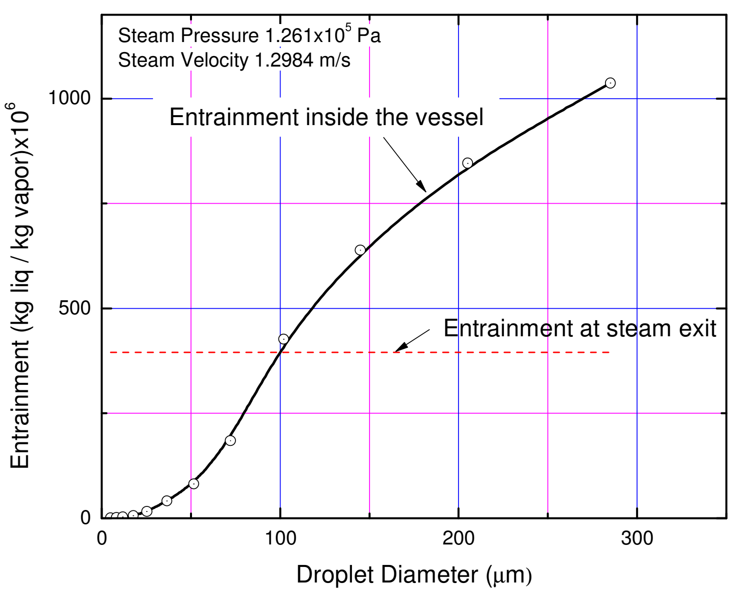

Figure 2.8: Entrainment as a function of droplet diameter [taken from Garner et al. [12]]

Garner et al. [12] investigated factors that influence size of droplets formed in the air-water system. They measured mean bubble diameter and the droplet size distribution at a distance of 10mm above the free surface. The important experimental observations are shown Figure 2.9 and Figure 2.10.

The mean droplet diameter increased initially but after bubble size of 5 mm the mechanism of formation of jet droplet was found to be ineffective to produce droplets. For larger bubbles the mean droplet diameter dropped drastically (below 25µm) and it was observed to be formed by the fragmentation of the liquid film. Thus Garner et al. [12] systematically provided insights into the droplet production mechanisms, their size distribution and influencing factors such as bubble diameter. Further, they have indicated the necessity of extensive experimentation to study the entrainment particularly at high pressures and establish factors affecting the droplet sizes, their projection velocities, resistance offered in the steam space, etc.

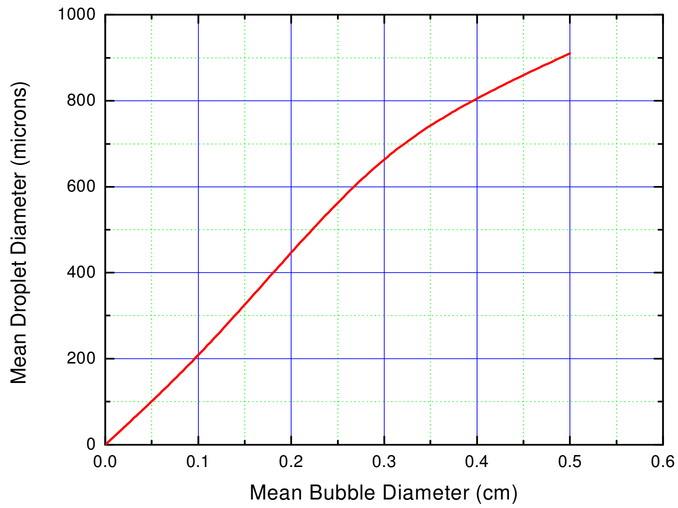

Figure 2.9: Relationship between Bubble diameter and droplet size [taken from Garner et al. [12]]

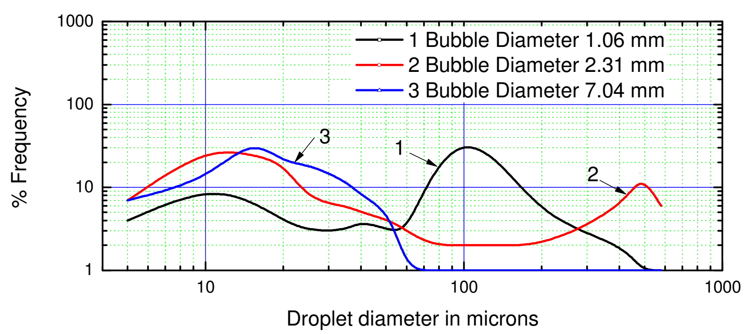

Figure 2.10: Effect of bubble diameter on frequency of droplet production [taken from Garner et al. [12]]

Spiel [13] studied the size distribution of jet drops produced by the bursting of bubbles of dimensions ranging from 350 to 1500 μm at sea as well as fresh water surfaces. He found no difference between the two results. He showed that numbers of drops are produced by single bubble collapse and probability of formation of first drop is highest. The probability of formation decreases for second, third and subsequent droplets. Spiel [13] studied the jet droplets produced by the bubble collapse for different bubble diameters. The size distribution for the drops other than the first top drop was found to be bimodal. The top drop radius was found to be dependent on bubble radius by:

$$R_d = 0.03677 R_b^{1.208} \tag{2.10}$$

Gunther et al. [18] carried out experiments on the droplet production rate at a water surface with the presence of single and multiple air bubbles of same dimensions (3 mm diameter). Effect on the droplet size distribution because of the presence of multiple bubbles was found to be important as the erstwhile correlations were pointed out to be based on the data from collapse of a single bubble. The measurements were carried out using Phase Doppler Analyzer (PDA). It was found that the number of droplets produced by the disintegration of fluid film upon the collapse of bubble is one magnitude higher than the droplets produced by the momentum leading to rise of jet at the centre and its necking. Jet drops from single bubble had higher diameter than in case of multiple bubbles. Coalescence of small bubbles creates larger bubbles of dimensions 4 mm in diameter and the droplets produced by the film disintegration was found to be dominant. Due to insufficient gas velocities all these were found to be re-entrained in the pool.

There are numerous studies on film droplet production based on bursting of single bubble, for example Wu [17], Afeti & Resch [16] etc. Gunther et al. [18] summarised various experimental studies and measurement techniques on the droplet formation by bursting of single bubble in air-water & air-seawater environment. Their experiments showed that for bubble diameters greater than 4 mm, no jet droplets are observed and film droplet formation is the only mechanism. Gunther et al. [18] also concluded that effect of bubble swarm, bubble coalescence on droplet formation should be also carefully studied.

Aiba and Yamada [14] studied the entrainment phenomena experimentally with air-water mixture. Experiments were carried out in a vertical cylinder filled with water and air injection at the bottom with a sparger pipe. Measurement of droplet sizes was carried out at different elevations using glass plates and cascade impactor. From cumulative volume fraction measured at various heights the mean droplet diameters were found out at the corresponding height. Using the equation of motion from force balance for the mean droplet size, projection velocity at separation interface was back calculated. This can be considered to be the most important result of the experiments. Garner et al. [12] and Newitt et al. [11] did not obtain the droplet ejection velocities. Aiba and Yamada [14] made estimation on droplet ejection velocities for the first time. The mean velocity of ejection was shown to decrease with increasing mean droplet size. However, reliable information on the droplet ejection velocity is still needed for case of high pressure systems involving steam-water mixture. Rozen et al. [15] analyzed the carryover in a conventional bubble type evaporators and bubble columns. Experimental measurements included the droplet collection on the plate coated with carbon layer at different elevations in the equipment. The droplet size distribution was found to be normal and distribution parameter was found to be independent of height. Only the mean droplet diameter was observed to change with respect to height. The total carryover out of the equipment was estimated from the samples and measuring the content of soluble salt (sodium chloride). The carryover was described as a function of separator height using the following power-law equation:

$$E_{fg} = c\left(J_g^n\right) \tag{2.11}$$

On the basis of available experimental data Rozen et al. [15] found two regions. In the first region of relatively low vapor velocity the carryover was found to depend weakly on the vapor velocity. The value of power is unity in this region. In the second region of high velocities, the value of power n=4.5 to 5.5. They attributed that the exponent is a result of atomization laws, dispersion and distribution of drop dimensions. First region indicates different mechanism of droplet formation i.e. bubble breakdown.

Figure 2.11 shows the entrainment measured at 185 atmosphere pressure by Sterman [21]. Different regions can be seen depending on the value of J_g/h. Experimental data can be approximated by power law, $E_{fg} = c(J_g/h)^n$ where c and n have different values for different regions. The three different regions can be explained with various scenarios shown in Figure 2.11. Consider a vessel with initial liquid height H_L, and the gas/vapor flux in gradually increased. The two-phase mixture expands and separation interface height increases. At low gas flux values, the exit entrainment consists of small droplets which are carried along the vapor flow. Larger droplets fall back into the liquid. Hence resulting entrainment is small quantitatively. This is regarded as region-I, where exponent of J_g/h is close to unity. As the gas flux increases the mixture height also increases reducing the vapor space above the separation interface. The large sized droplets are also reaching up to the exit and are carried out of the equipment. This shows increase in entrainment and change of slope of the curve. This is regarded as region-II, where exponent of J_g/h is about 3.0 to 4.0. At very high gas flux the height of vapor space further reduces and the separation interface reaches very close to the exit. In this case the entrainment rises sharply. The separation interface is highly agitated at high gas flux and the large liquid fragments and droplets are carried out of equipment along the gas. This is regarded as region-III, where exponent of J_g/h is about 7.0 to 20.0.

Mochizuki and Hirao [23] performed experiments on the pilot model of the steam separator for the Advanced Thermal Reactor (ATR) which is a boiling light water nuclear reactor. The experiments were performed with air-water mixture at atmospheric conditions and the entrainment was measured using tracer salt and with iso-kinetic probe which is generally used in aerosol measurements. Based on the basic data separation efficiency was found to be acceptable for reactor geometry.

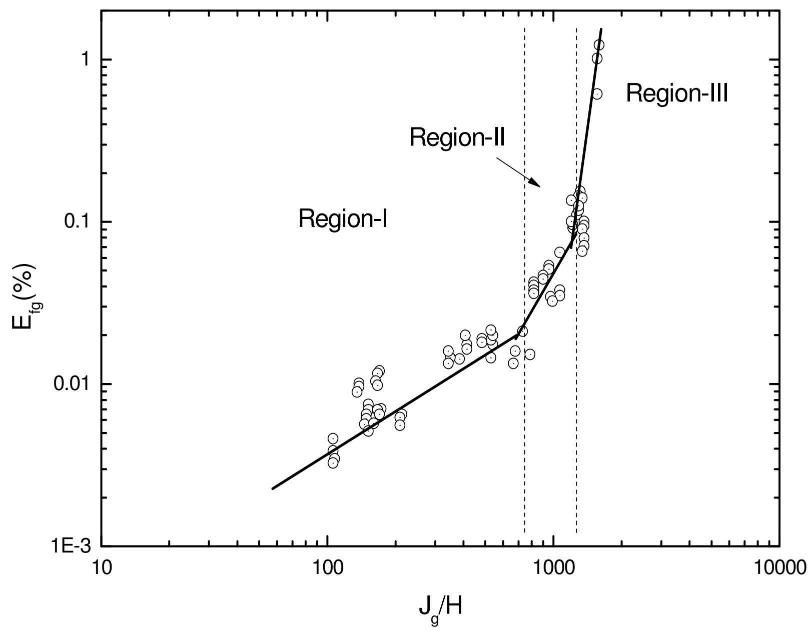

Figure 2.11: Entrainment as function of superficial velocity of steam and height of the vapor dome [taken from Sterman [21]]

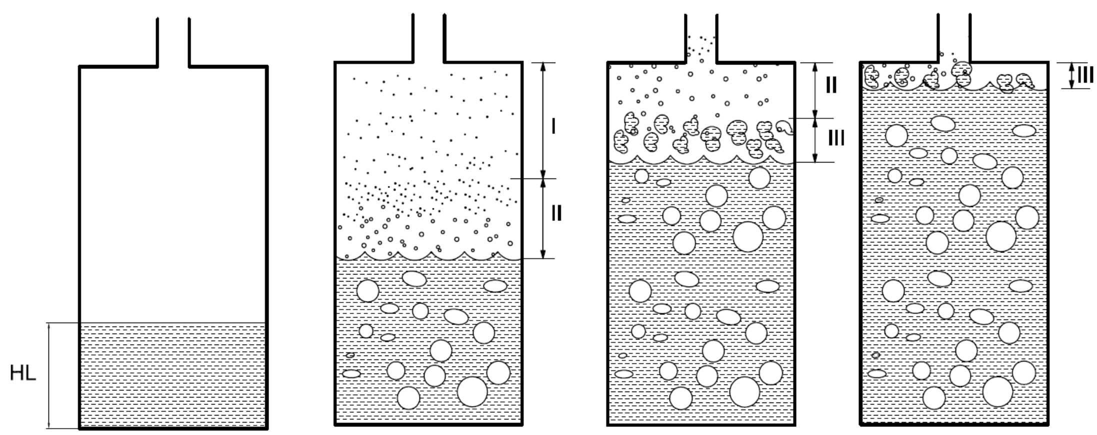

Figure 2.12: Mechanisms of Entrainment

Cosandy et al. [24] analyzed the problem of radio-nuclide entrainment in the reactor containment in case of severe accident where the core melt is covered with the pool of water. Bubbling at the surface of water would transport radionuclides by carryover phenomenon. They performed measurements of carryover at different elevations in the containment model by sampling and measuring the soluble salt concentration (KI, NaI and CsI) and also of solid tracer (alumina).

Koch et al. [32] studied the carryover of radionuclides from bubbling pool of water in case of severe accident. Koch et al. [32] modeled droplet formation at bubbling surface using empirical correlations. The droplet formation at bubbling surface depends on the various mechanisms of formation. The droplets generated from the rising jet disintegration are called as jet droplets. Droplets formed due to disintegration of bubble liquid film are called as film droplets. When the steam flow rates are high, steam jets out at bubbling surface and shearing the liquid into droplets. This are called as churn flow droplets. Authors used correlations for the film droplets and churn flow droplets. The jet droplets were modeled using numerical method, solving the Navier-Stokes equation on eulerian grid. The computer module RECOM (Voβnacke et al. [36]) based on above models was validated against experimental data from KAREX facility (Minges et al. [37]). Good agreement was found by authors between theoretical and experimental results.

Iyer et al. [33] studied the effect of superficial gas velocity and the diameter ratio (of vessel to inlet pipe) on the carryover. The experiments were performed carried out at atmospheric conditions with air and water mixture. The carryover was measured with the help of tissue papers suspended above the separation interface and the collected amount of entrainment was weighed. Authors proposed a new correlation based on experimental data. The proposed correlation satisfies their experimental data within ±375%. The various experimental studies conducted on carryover are summarized in Table 2.2.

Basu et al. [34] performed preliminary studies on carryover for AHWR geometry in a scaled down experimental facility using air-water mixture at atmospheric operating conditions. They scaled down the natural circulation heat transport system loop of AHWR using non-dimensional analysis. They measured entrainment/carryover in a scaled drum of size 0.8 m diameter and 1.2 m length, with two inlets for two-phase flow (tailpipes) and one outlet for separated air at the top (drum exit), and one outlet (down comer) for separated water at bottom. During experiments they could measure the carryover for high swell levels inside the drum. They observed that carryover increases with air flow rate due to highly agitated interface inside the drum. They introduced perforated plates near the drum exit and close to water levels inside the drum and found that it reduced the carryover as droplets with high momentum were effectively separated due to impact on the plates. The study produced overall qualitative observations on carryover process for a horizontal steam drum geometry; however more studies on specifics of phenomenon are required for further understanding.

Sun et al. studied the carryover/entrainment in the upper plenum of pressure vessel of AP-1000 PWR, during the depressurization transient under accidental scenario. During such transient the scenario inside the vessel is similar to pool entrainment. The entrainment through side branch / hot leg was studied in a scaled down facility ADETEL [26] using steam-water as working medium. The pressure vessel diameter used for the studies was 0.6 m. They observed that entrainment reduces significantly with reduction of operating level, i.e. reduction of vapor space height (distance between the exit and two-phase interface). They also observed that increase in steam velocity leads to dramatic increase in entrainment rates. Zang et al. conducted entrainment studies relevant to AP1000 scenario as described above, in a transparent vessel of diameter 0.380 m and length of 2.2 m, using air-water mixture [28]. The experimental measurements covered larger range of superficial velocities and vapor/gas space heights. Based on experimental data they proposed a correlation for entrainment suitable for high gas flux conditions.

Kim and No [38] studied liquid entrainment in the case of a vessel of the depressurization system of Advanced Power Reactor (APR-1400). The liquid off take from the swelled two-phase mixture surface in vessel was studied with experiments on the model with air-water mixture. Entrainment was measured by directly noting the water collected at the end of discharge pipe. Isokinetic probes were also utilized to measure the entrainment fractions. They described the entrainment as a function of the distance between the break location and swell level of two-phase mixture pool. As shown in Figure 2.12 when the break is close to the level of mixture, the vapor accelerates through break due to sudden area change (Bernoulli Effect) and can carry large amount of liquid sheets splashing at the interface. While at lower mixture levels the droplets either may get carried away with flow or fall back into the vessel. Authors developed a new correlation for the liquid entrainment and the experimental data were found to be proportional to the seventh power of $J_g^* h^{*-1}$ and had higher values than other existing correlations.

Table 2.1: Summary of previous analytical work

Srn	Author	Assumptions	Geometrical parameters					System	Pressure (Pa)	Temperature (^{O}C)	Physical Properties					Range of J_g (m/s)
			D_H (m)	D_I (m)	D_O (m)	H (m)	H_{mm} (m)				ρ_f (kg/m^3)	ρ_g (kg/m^3)	μ_f (kg/m.s)	μ_g (kg/m.s)	σ (N/m)	
1	Davis [8]	1, 2, 5, 6, 7, 8, 9, 10, 11, 12, 13, 14						Steam-Water	20×10^5 to 90×10^5	212 to 303	849.8 to 705.0	10.03 to 13.60	1.25×10^{-4} to 8.35×10^{-5}	1.608×10^{-5} to 2.22×10^{-5}	34.98×10^{-3} to 12.60×10^{-3}	0 to 0.9
2	Kataoka and Ishii [30]	1, 2, 3,4, 5, 6, 7, 8, 9, 10, 11, 12, 13	0.2 to 0.305			2.55		Applicable to Steam-Water and Air-water	1.01325×10^5 to 185×10^5	20.0 to 360.2	115.5 to 996.6	0.98 to 145.04	2.39×10^{-4} to 8.54×10^{-4}	1.82×10^{-5} to 6.13×10^{-5}	0.00262 to 0.0717	0 to 1.7
3	Nayak et al. [31]	1, 2, 5, 6, 7, 8, 9, 10, 11, 12, 13, 14	3.75	0.125	0.3	3.75		Steam-Water	70 bar	285.6	740.0	36.53	9.42×10^{-5}	1.90×10^{-5}	0.0177	0.2 to 1.0 m/s
4	Koch et al. [32]	1, 2, 5, 6, 7, 8, 9, 10, 11, 12, 13, 14						Steam-Water	1.01325×10^5	100.0	958.4	0.59	2.82×10^{-4}	1.20×10^{-4}	0.0588	1.0×10^{-4} to 10.0

List of assumptions

1. Droplets are considered of having perfect spherical shape.
2. When the bubble at the free surface bursts and the due to the momentum of falling rim of the bubble, the center of depression rises and forms a jet, disintegration of which due to necking at the tip generates a droplet.
3. When the bubble bursts at the free surface the disintegration of bubble dome generates the droplets.

4. The vapor rushing through the liquid free surface performs the work which is converted into required surface energy for the droplets and initial momentum for droplets formed.
5. The droplets generated at the free surface have different sizes and thus a size distribution.
6. The velocity distribution of the droplets can be simplified by assuming that the droplets of the same diameter are ejected with a representative average velocity.
7. The equation of motion of the droplet can be written by applying Newton's second law and performing force balance.
8. Among the forces upon a droplet, forces considered include drag due to relative motion between droplet and bulk motion of vapor and gravity force.
9. The drag coefficient for droplet can be given as that for a spherical rigid body.
10. Spin and rotation of droplet is neglected.
11. The number of droplets generated at the free surface travel certain trajectory in the vapor space and during their flight in the vapor space the effect of their collision and coalescence is neglected.
12. Effect of droplet evaporation is neglected.
13. The bulk flow of vapor is co-current.
14. The effect of droplets interaction with the solid walls by deposition is neglected.

Table 2.2: Summary of published literature: Experimental work on carryover

Srn	Author	Geometrical parameters					System	Pressure (Pa)	Temperature (^{O}C)	Physical Properties					Range of J_g (m/s)
		D_H (m)	D_I (m)	D_O (m)	H (m)	H_{mm} (m)				ρ_f (kg/m^3)	ρ_g (kg/m^3)	μ_f (kg/m.s)	μ_g (kg/m.s)	σ (N/m)	
1	Newitt et al. [11]					0.0064, 0.0191, 0.0317, 0.0444, 0.0571	Air - Water	1.01325×10^5	Atm.	996.63	1.205	8.54 ×10^{-4}	1.82 ×10^{-5}	0.0717	0
2	Garner et al. [12]	0.305		0.075	2.55	0.203 and 0.4318	Steam-Water	2.254×10^5	124.1	947.89	0.934	2.43 ×10^{-4}	1.26 ×10^{-5}	0.0561	0.459 to 1.161
3	Sterman [21]	0.24				0.5 to 0.9	Steam-Water	1.72×10^5 to 187.0×10^5	115.52 to 360.181	946.65 to 527.60	0.9803 to 145.045	2.39 ×10^{-4} to 8.54 ×10^{-4}	1.82 ×10^{-5} to 6.13 ×10^{-5}	0.05574 to 0.00262	0.01 to 1.3
4	Kolkolostev [22]	0.3				0.5, 0.6	Steam-Water	1.29×10^5 to 110.0×10^5	106.9 to 318.06	953.25 to 671.73	0.749 to 62.606	2.6 ×10^{-4} to 7.9 ×10^{-4}	1.23 ×10^{-5} to 2.0 ×10^{-5}	0.0574 to 0.01027	1.0 to 1.7
5	Aiba and Yamada [14]	0.096			0.47	0.006, 0.025,0.019, 0.044, 0.065, 0.072, 0.1, 0.155, 0.215	Air - Water	1.01325×10^5	Atm.	996.63	1.205	8.54 ×10^{-4}	1.82 ×10^{-5}	0.0717	0
6	Rozen et al. [15]	0.2				0.0 to 3.5	Air – Water	1.01325×10^5	Atm	996.63	1.205	8.54 ×10^{-4}	1.82 ×10^{-5}	0.0717	0.6 to 3.0
7	Spiel [13]						Air – Water	1.01325×10^5	Atm	996.63	1.205	8.54 ×10^{-4}	1.82 ×10^{-5}	0.0717	0
8	Mochizuki and Hirao [23]	0.28			0.95	At exit	Steam-Water	70×10^5	285.6	740.01	36.53	9.42 ×10^{-5}	1.90 ×10^{-5}	0.0177	0.36 to 1.5753
9	Cosandy et al. [24]	1.5			3.5	At 2 m and at exit	Air - Steam - Water	2×10^5 to 6×10^5	120.2 to 158.8	908.2 to 942.8	1.122 to 3.1708	1.709 × 10^{-4} to 2.317 × 10^{-4}	1.28 ×10^{-5} to 1.48 ×10^{-5}	0.04676 To 0.05483	0.005 to 0.027
10	Kim and No [38]	0.3	hole diameter 0.005 m	0.05	2	At exit	Air - Water	1.01325×10^5	Atm	996.63	1.205	8.54 ×10^{-4}	1.82 ×10^{-5}	0.0717	0.09 to 0.35

11	Iyer et al. [33]	0.3 and 0.437	0.05 to 0.08		1.2 and 1.45	0.4 and 0.6 (above the water level)	Air - Water	1.01325×10^5	Atm	996.63	1.205	8.54×10^{-4}	1.82×10^{-5}	0.0717	0.048 to 0.2

2.4 Empirical correlations

Kruzhilin [29] developed a correlation for the entrainment assuming that the droplets generated from the disintegration of a bubble dome contribute little to the entrainment. Further, he opinioned that the entrainment is mainly due to the droplets formed by the action of kinetic energy of vapor. The effect of drop disintegration/coalescence can also be neglected. Kruzhilin [29] listed the parameters that affect the entrainment. These are $\rho_g J_g^2, \rho_f, \sigma, \mu$

Following dimensionless groups were defined:

$$\Pi_1 = \frac{G_f \sigma g}{\left(\rho_g J_g^2\right)^2 J_g}\sqrt{\frac{\rho_f}{\rho_g}} \tag{2.12}$$

$$\Pi_2 = \frac{\mu_f^2 \, \rho_g J_g^2}{\sigma^2 \rho_f} \tag{2.13}$$

$$\Pi_3 = \frac{\rho_g J_g^2}{g \rho_f H_V} \rightarrow Froude\ Number \tag{2.14}$$

$$\Pi_4 = \frac{\sigma}{g \rho_f H_V^2} \rightarrow Weber\ Number \tag{2.15}$$

From the definition of entrainment

$$E_{fg} = \frac{Flux\ of\ liquid\ phase}{Flux\ of\ vapor\ phase} = \frac{\rho_f J_f}{\rho_g J_g} \tag{2.16}$$

Neglecting the effect of droplet coalescence/disintegration, the Weber number was neglected from the dimensionless groups and thus the entrainment was related by the following correlation:

$$E_{fg}=\left[\frac{\rho_g J_g^4}{\sigma g}\sqrt{\frac{\rho_g}{\rho_f}}\right] f\left(\frac{\mu_f^2\,\rho_g J_g^2}{\sigma^2\rho_f},\frac{\rho_g J_g^2}{g\rho_f H_V}\right) \tag{2.17}$$

The function $f\left(\frac{\mu_f^2\,\rho_g J_g^2}{\sigma^2\rho_f},\frac{\rho_g J_g^2}{g\rho_f H_V}\right)$ was assumed to be constant and thus

$$E_{fg}=c_1\left[\frac{\rho_g J_g^4}{\sigma g}\sqrt{\frac{\rho_g}{\rho_f}}\right] \tag{2.18}$$

It must be noted that height of vapor dome H_V has not been included in the above expression; hence it cannot predict entrainment for any general height of vapor dome.

Panasenko [39] attempted to obtain the correlation for the data at the transition point from region II to region III (i.e. region where droplets from bubble disintegration are dominant as compared with the region where highly agitated liquid splashes cause the major entrainment (see Figure 2.12). Authors extended the important results of Kruzhilin [29] and described the entrainment as:

$$E_{fg}=c_2\left[\frac{\rho_g J_g^4}{\sigma g}\sqrt{\frac{\rho_g}{\rho_f}}\right]\Pi_2^m\Pi_3^n\Pi_4^l \tag{2.19}$$

Where Π_2 , Π_3 and Π_4 are given by equation (2.13), (2.14) and (2.15), respectively. The constant was obtained by fitting the experimental data by Sterman [21] and given by the following equation:

$$E_{fg}=1.96\times10^7\,\frac{\left(\rho_g g\right)^{0.48}\mu_f^{1.8}J_g^{1.96}}{g^{0.08}\left(\rho_g g\right)^{1.03}\sigma^{1.25}H_V^{1.18}} \tag{2.20}$$

Note that the above expression shows dependence on H_V i.e. height of vapor space which can be given as

$$H_V = H - H_L\left(\frac{\alpha}{1-\alpha}\right) \tag{2.21}$$

Where the pool void fraction α, is given as:

$$\alpha = 0.67\left(\frac{J_g^2}{g\sqrt{\frac{\sigma}{g(\rho_f - \rho_g)}}}\right)^{1/3}\left(\frac{\rho_f - \rho_g}{\rho_f}\right)^{-1/3}\left(\frac{J_f}{J_g}\right)^{2/9}\left(\frac{D_H}{\sqrt{\frac{\sigma}{g(\rho_f - \rho_g)}}}\right)^{-1/6} \tag{2.22}$$

Sterman [21] attempted to provide groups of dimensionless numbers based on the conservation equations that governs the droplet formation and its transport in vapor space. He neglected the droplets formed due to disintegration of bubble dome and only considered the mechanism where droplets are formed due to kinetic energy of vapor at the free surface. The kinetic energy of vapor rushing out at free surface works against surface tension and friction with liquid film. He described the process using energy balance during drop formation. The rate of change of Kinetic Energy balances the rate of change of Surface energy combined with heat and potential energy of fluid. He also considered force balance on a droplet during flight and heat transfer during evaporation droplet. Based on these governing equations he developed a similarity criteria in as shown below:

$$E_{fg} = f\left\{w, Re_g, Eu, \frac{\rho_g J_g^2 D}{g\sigma}, \frac{J_g^2}{gH_V}, \frac{\Delta P}{\sigma/D}, \left(\frac{A\Delta P}{h_{fg}\rho_g}\frac{T_s}{\Delta T}\right), \alpha, \frac{H_V}{D}, \frac{v_d}{J_g}, \frac{\rho_g}{\rho_f}\right\} \tag{2.24}$$

After neglecting the terms related to droplet evaporation, the similarity criteria was written as:

$$E_{fg} = f\left\{\frac{g\left(\sqrt{\sigma/\rho_g}\right)^3}{v_g^2}, \frac{J_g^2}{gH_V}, \frac{A\sqrt{\sigma/\rho_g}}{h_{fg}}, \alpha, \frac{H_V}{\sqrt{\sigma/\rho_g}}, \frac{\rho_g}{\rho_f}\right\} \tag{2.25}$$

In the above criterion $\frac{H_V}{\sqrt{\sigma/\rho_g}}$ was found to have no significant effect when H_V is small hence it was neglected. Also the self-evaporation of droplet was neglected. Thus the term $\frac{A\sqrt{\sigma/\rho_g}}{h_{fg}}$ was neglected.

Finally, the entrainment was expressed in terms of dryness fraction of steam which is defined as:

$$E_{fg} = 1 - w = f\left\{\frac{g\left(\sqrt{\sigma/\rho_g}\right)^3}{v_g^2}, \frac{J_g^2}{gH_V}, \alpha, \frac{\rho_g}{\rho_f}\right\} \tag{2.26}$$

Sterman [21] analyzed the experimental data of Kolkolostev [22] and Sterman [21]. He proposed following correlation:

$$E_{fg} = 2.75 \times 10^8 \frac{\left(\frac{J_g^2}{\alpha g H_V}\right)^{2.3}}{\left(\frac{g\left(\sigma/g\left(\rho_f - \rho_g\right)\right)^{1.5}}{v_g^2}\right)^{1.1} \left(\rho_g/\left(\rho_f - \rho_g\right)\right)^{0.25}} \tag{2.27}$$

In the above correlation the knowledge of void fraction (α) and height of vapor dome (H_V) is needed. The correlations have been proposed for (α) and (H_V).

$$\alpha = 0.26\left(\frac{J_g^2}{g\sqrt{\sigma/\left(\rho_f - \rho_g\right)}}\right)^{0.4} \left(\rho_g/\left(\rho_f - \rho_g\right)\right)^{0.12} \tag{2.28}$$

$$H_V = H - H_L\left(\frac{\alpha}{1 - \alpha}\right) \tag{2.29}$$

Combining equation (2.27) & (2.28), the final correlation was proposed as follows:

$$E_{fg} = 6.1 \times 10^9 \frac{\left(\frac{J_g^2}{gH_V}\right)^{1.38}}{Ar^{1.1}} \left(\sqrt{\sigma/(\rho_f - \rho_g)}\right)$$

$$where\ Ar = \frac{g\left(\sqrt{\sigma/(\rho_f - \rho_g)}\right)^3}{v_g^2} \frac{\rho_f - \rho_g}{\rho_g} \tag{2.30}$$

The above correlation indicates that the entrainment also depends on hydrodynamics of two-phase flow below the separation interface.

Kataoka and Ishii [30] developed a mechanistic model by combining the physics of phenomenon (droplet formation, size and velocity distribution, droplet motion, etc.) known from the observations and various experimental data (entrainment data with air-water and steam-water) reported by Kolkolostev (1952), Garner et al. [12], Sterman [21] and Rozen et al. [15]. The authors thought that the phenomenon of droplet generation can be treated statistically by introducing the distribution functions for size and velocity. The following relations were found to hold for size distribution function $f(d,J_g)$ and velocity distribution function $f(v_i\,,d,J_g)$:

$$\int_0^\infty f(d,J_g)dd = 1 \tag{2.31}$$

$$\int_0^\infty f(v_i\,,d,J_g)dd = 1 \tag{2.32}$$

Let v_h be the initial velocity required for droplet to attain height h, then the entrainment can be given as,

$$E_{fg}(h,J_g) = \frac{\dot{\epsilon}}{\rho_g J_g} \int_{d=0}^{d=\infty} \int_{v=v_h}^{v=\infty} f(v_i\,,d,J_g)\, f(d,J_g) dv_i dd \tag{2.33}$$

Where $\frac{\dot{\epsilon}}{\rho_g J_g}$ is the entrainment rate at the interface.

The droplets can be categorized into two groups, i.e.

1. $d < d_c$, where $D_c$is critical diameter of droplet for which the terminal velocity is equal to vapor velocity. These droplets are always carried in the flow.
2. $d \geq d_c$, these rise to certain height and then fall back.

Introducing a term representing the entrainment at the surface as:

$$E_0\left(d,J_g\right) = \frac{\dot{\epsilon}}{\rho_g J_g}\int_0^d f\left(d,J_g\right)dd \tag{2.34}$$

Garner et al. [12] measured this quantity, which can be expressed as

$$E_0\left(d,J_g\right) \propto \left(J_g d\right)^{1.5} \tag{2.35}$$

After fitting experimental data, the following correlation was obtained:

$$E_0\left(d,J_g\right) = 0.3975\left(J_g^* d^*\right)^{1.5} \tag{2.36}$$

$$where\ J_g^* = \frac{J_g}{\left(\frac{\sigma g\left(\rho_f - \rho_g\right)}{\rho_g^2}\right)^{0.25}}\ and\ d^* = \frac{d}{\sqrt{\frac{\sigma}{g\left(\rho_f - \rho_g\right)}}} \tag{2.37}$$

Incorporating the effect of pressure in equation (2.38), we get:

$$E_0\left(d,J_g\right) = \frac{\dot{\epsilon}}{\rho_g J_g}\int_0^d f\left(d,J_g\right)dd = 2.48 \times 10^{-4}\left(\frac{\rho_g}{\rho_f - \rho_g}\right)^{-1.0}\left(J_g^* d^*\right)^{1.5} \tag{2.38}$$

Differentiating above equation with respect to d,

$$\sqrt{\frac{\sigma}{g\left(\rho_f - \rho_g\right)}}\frac{\dot{\epsilon}}{\rho_g J_g} f\left(d,J_g\right) = 3.72 \times 10^{-4}\left(\frac{\rho_g}{\rho_f - \rho_g}\right)^{-1.0}\left(J_g^* d^*\right)^{1.5} \tag{2.39}$$

This equation gives the relationship between the entrainment at the interface and the droplet size distribution in terms of steam superficial velocity and the droplet diameter.

It has been known that the droplet formation mechanism depends on the pool hydrodynamics. The gas velocities required for bubbly flow in the pool is given by the drift flux model as follows:

$$J_g^* = 0.325\sqrt{\frac{\rho_g}{\rho_f}} \tag{2.40}$$

For bubbly flow the value of J_g required is very small. Therefore, Kataoka and Ishii [30] stated that, in equipments of practical interest, seldom bubbly flow would exist. Authors envisaged that the churn turbulent flow may be the most dominant flow regime in bubbling pool. Thus the mechanism of droplet generation due to bubble burst (film droplets and jet droplets) was not considered in the formulation. The authors alternatively proposed a mechanism as schematically shown in Figure 2.13.

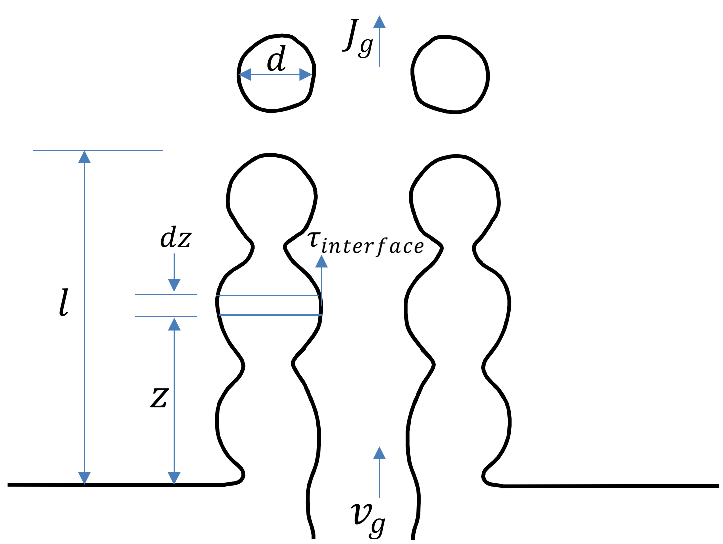

Figure 2.13: Formation of film droplets by shear [taken from Kataoka and Ishii [30]]

The force balance for a liquid film being sheared by the gas is written as:

$$\rho_f D \frac{dv_f}{dt} = \tau_{interface} - (\rho_f - \rho_g) g D \tag{2.41}$$

$$where\ \tau_{interface} = f_{interface} \frac{1}{2} \rho_g v_g^2 \tag{2.42}$$

Neglecting the gravity term, it was obtained that:

$$\frac{dv_f}{\frac{1}{2}\frac{\rho_g}{\rho_f}\frac{1}{D} f_{interfce} v_g^2} = dt = \frac{dz}{v_f} \tag{2.43}$$

Integrating the above equation and putting $(v_f)_{z=l} = v_i$, we get:

$$\frac{1}{2} \rho_f v_i^2 D = \frac{1}{2} f_{interface} \rho_g v_g^2 l \tag{2.44}$$

Above equation shows that the kinetic energy of droplet is equal to the work exerted on the element by the gas flow. In addition, Authors made assumptions that $f_{interface} \approx C_D \approx Re_D^{-0.5}$ and $l \approx D$, and obtained the following relationship:

$$v_i^* \sim (J_g^*)^{3/4} (\alpha)^{-3/4} (N_{\mu g})^{1/4} (d^*)^{-1/4} \left(\frac{\rho_g}{\rho_f}\right)^{1/2} \tag{2.45}$$

The gas velocity is related to the pool void fraction by:

$$v_g = \frac{J_g}{\alpha} \tag{2.46}$$

$$v_i^* \sim (v_g^*)^{3/4} (N_{\mu g})^{1/4} (d^*)^{-1/4} \left(\frac{\rho_g}{\rho_f}\right)^{1/2} \tag{2.47}$$

Where

$$N_{\mu g} = \frac{\mu_g}{\sqrt{\rho_g \sigma \sqrt{\frac{\sigma}{g(\rho_f - \rho_g)}}}} \tag{2.48}$$

$$v_i^* = \frac{v_i}{\left(\frac{\sigma g(\rho_f - \rho_g)}{\rho_g^2}\right)^{0.25}} \quad (2.49)$$

$$v_g^* = \frac{v_g}{\left(\frac{\sigma g(\rho_f - \rho_g)}{\rho_g^2}\right)^{0.25}} \quad (2.50)$$

Kataoka and Ishii [30] proposed the following correlation for the void fraction as:

$$\alpha \sim (J_g^*)^{2/3} (D_H^*)^{-0.28} \left(\frac{\rho_g}{\rho_f - \rho_g}\right)^{-0.153} \quad (2.51)$$

Therefore,

$$v_i^* = C(J_g^*)^{1/4} (N_{\mu g})^{1/4} (D^*)^{-1/4} \left(\frac{\rho_g}{\rho_f}\right)^{1/2} (D_H^*)^{-0.28} \left(\frac{\rho_g}{\rho_f - \rho_g}\right)^{-0.153} \quad (2.52)$$

The velocity distribution for a given size of droplet is neglected and instead it is considered to have average velocity for the given drop diameter. Therefore, it can be expressed with delta function as:

$$f(v_i, d, J_g) dv_i = \delta(v_i^* - \overline{v_i^*}) dv_i^* \quad (2.53)$$

Kataoka and Ishii [30] also proposed a procedure for determining maximum height attained by the droplet. The force balance for the droplet can be written as:

$$\frac{dv}{dt} = \frac{-(\rho_f - \rho_g)}{\rho_f} - \frac{3}{4} C_D \frac{1}{d} \frac{\rho_g}{\rho_f} (v - v_g)|v - v_g| \quad (2.54)$$

Above equation was solved for various drop diameters and the following approximate solution was obtained for the velocity required by a droplet to reach height 'h',

$$v_h = 0 \; for \; d < d_c \quad (2.55)$$

$$v_h = \sqrt{2gh\left(\frac{\rho_g}{\rho_f}\right)} \quad for\ d \geq dD_c \tag{2.56}$$

The entrainment now can be expressed as follows:

$$\begin{aligned} E_{fg}(h, J_g) = \int_{d=0}^{d=\infty} \int_{v_i=v_h}^{v_i=\infty} \delta(v_i^* - \overline{v_i^*}) \times 3.72 \times 10^{-4} \\ \times \left(\frac{\rho_g}{\rho_f - \rho_g}\right)^{-1} (J_g^*)^{1.5} (d^*)^{0.5} dv_i^*\, dD^* \end{aligned} \tag{2.57}$$

Three distinct regions for entrainment as a function of h can be identified as shown in Figure 2.14.

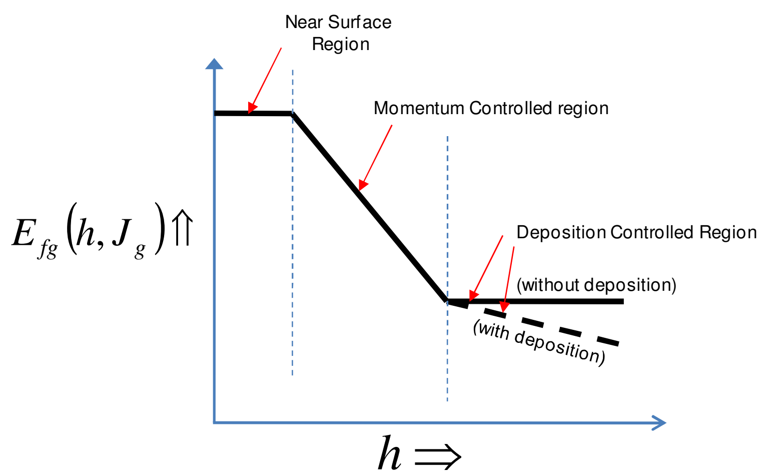

Figure 2.14: Regions of entrainment above the separation interface [taken from Kataoka and Ishii [30]]

The entrainment is maximum at heights very close to separation interface as droplets are formed here as a result of disintegration of gas bubbles and breakage of liquid film surrounding it. This is called near surface region (see Figure 2.14). The near surface region is small and is within few centimeters (4-6 cm) above the interface. The droplets which are ejected with initial momentum at the time of formation reach to certain height and then fall back to liquid due to gravity.

Therefore the entrainment starts reducing as we traverse in vapor space. This region is called momentum controlled region, because droplet momentum (i.e. diameter and velocity) governs the entrainment. After a certain distance from interface most of the droplet attain maximum height and then fall back to liquid, but some droplets which achieve equilibrium with gas flow travel beyond the momentum controlled region and are permanently entrained in flow. Thus entrainment remains practically constant beyond the momentum controlled region. However some of these droplets get deposited on walls of equipment and entrainment may reduce marginally. This is called deposition controlled region as shown in Figure 2.14.

Kataoka and Ishii [30] integrated equation (2.57) and obtained correlations after fitting the experimental data available which covered different fluids and operating parameters. Kataoka and Ishii [30] proposed correlations for all three regions, also showed that in momentum controlled region entrainment has dependence of gas flux. Therefore they proposed three regions within momentum controlled region i.e. high gas flux, intermediate gas flux and low gas flux region, along with their transition criteria. The final set of correlations is as follows:

- **Near Surface Region**

$$E_{fg}(h,J_g) = 4.84 \times 10^{-3}\left(\frac{\rho_g}{\rho_l - \rho_g}\right)^{-1.0} \tag{2.58}$$

- **Deposition controlled region**

$$E_{fg}(h,J_g) = 7.13 \times 10^{-4} J_g^{*3} {N_{\mu g}}^{0.5}\left(\frac{\rho_g}{\rho_l - \rho_g}\right)^{-1.0} e^{\left(\frac{-0.205h}{D_H}\right)} \tag{2.59}$$

- **The momentum controlled region**

For momentum controlled region the correlation for entrainment is given for three gas flux regimes, high, intermediate and low gas flux.

- **Low gas flux regime**

$$E_{fg}(h,J_g) = 2.21{D_H^*}^{1.25}{N_{\mu g}}^{1.5}\left(\frac{\rho_g}{\rho_l-\rho_g}\right)^{-0.31} J_g^*\, h^{*-1} \tag{2.60}$$

- **Intermediate gas flux regime**

$$E_{fg}(h,J_g) = 5.42\times10^6 {J_g^*}^3\, h^{*-3}{D_H^*}^{1.25}{N_{\mu g}}^{1.5}\left(\frac{\rho_g}{\rho_l-\rho_g}\right)^{-0.31} \tag{2.61}$$

- **High gas flux regime**

Equation (2.58) holds good for the high flux regime.

The transition from near surface region to momentum controlled region occurs at condition:

$$h^* > 1.038\times10^3 J_g^*\, {N_{\mu g}}^{0.5}{D_H^*}^{0.42}\left(\frac{\rho_g}{\rho_l-\rho_g}\right)^{0.23} \tag{2.62}$$

The transition from low flux momentum controlled regime to intermediate gas flux momentum controlled regime occurs at

$$J_g^*\, h^{*-1} = 6.39\times10^{-4} \tag{2.63}$$

The transition from intermediate gas flux momentum controlled regime to high flux momentum controlled regime is given by

$$\left(\frac{J_g^*}{h^*}\right) = 5.7\times10^{-4}{D_H^*}^{-0.42}{N_{\mu g}}^{-0.5}\left(\frac{\rho_g}{\rho_l-\rho_g}\right)^{0.10} \tag{2.64}$$

The transition from momentum controlled region to deposition controlled region occurs at a condition given by following equation:

$$h^* e^{\left(-0.068\frac{h^*}{D_H^*}\right)} = 1.97\times10^3{D_H^*}^{0.42}{N_{\mu g}}^{0.33}\left(\frac{\rho_g}{\rho_l-\rho_g}\right)^{0.23} \tag{2.65}$$

Kataoka and Ishii [30] claim that above correlations are the best among the available and fit most of the experimental data available till date. To verify we carried out inter-comparison among these correlations with the experimental data available from literature. Figure 2.15 shows prediction for experimental measurements by Garner et al. [12] for air-water system at atmospheric pressure. The correlations given by Sterman [21], Kruzhilin [29] were developed based on the experiment in steam-water system while Kataoka and Ishii [30] considers experimental data from air-water system also. Thus it was seen that for the case of Garner et al. [12], Kataoka and Ishii [30] gives better prediction compared to others, but still the error is noticeably high (400-1000%). Figure 2.16 to Figure 2.20 show the comparison for experimental data on entrainment by Sterman [21] and Kolkolostev [22] for steam-water system at operating pressures of 1.27, 17.0, 36.0, 91.0 and 110.0 bar respectively. The correlation by Kataoka and Ishii [30] predicts three different regions depending on the gas flux and height at which the entrainment is measured. However, the correlations by Kruzhilin [29] and Sterman [21] do not have such distinction for these three regions. The correlation by Kataoka and Ishii [30] has been found to be most accurate after comparison. Hence, it is recommended to be used for assessment of carryover in steam-water systems. It can be noted that it is valid for equipments having constant cross-sectional flow area. This correlation was also used in subsequent experimental work by Cosandy et al. [24] and Iyer et al. [33]. But these authors have found disagreements between correlation and experimental observations.

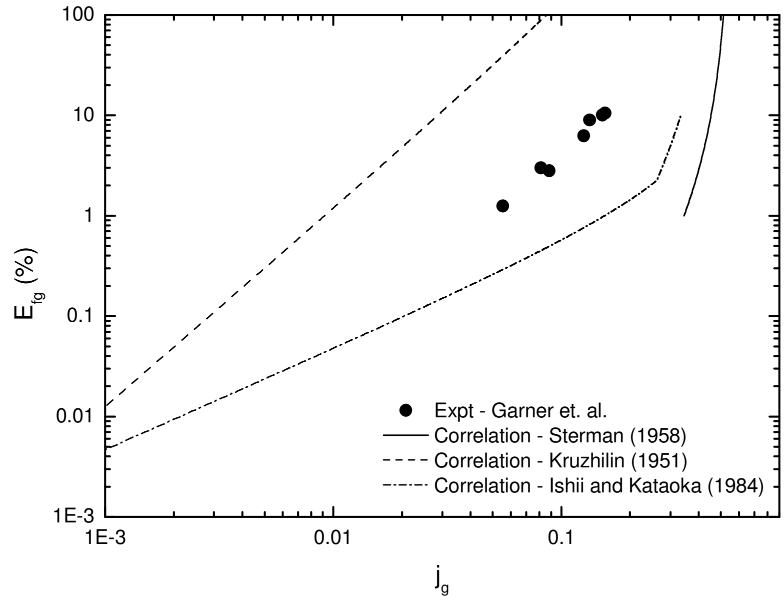

Figure 2.15: Prediction by correlations for experimental data by Garner et al. [12]

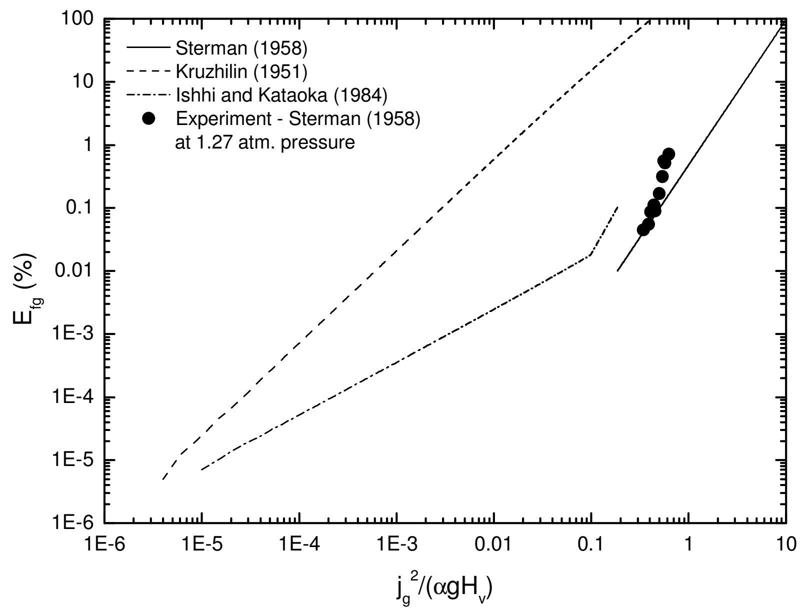

Figure 2.16: Prediction by correlations for experimental data of Sterman [21] at 1.27 atmospheric pressure

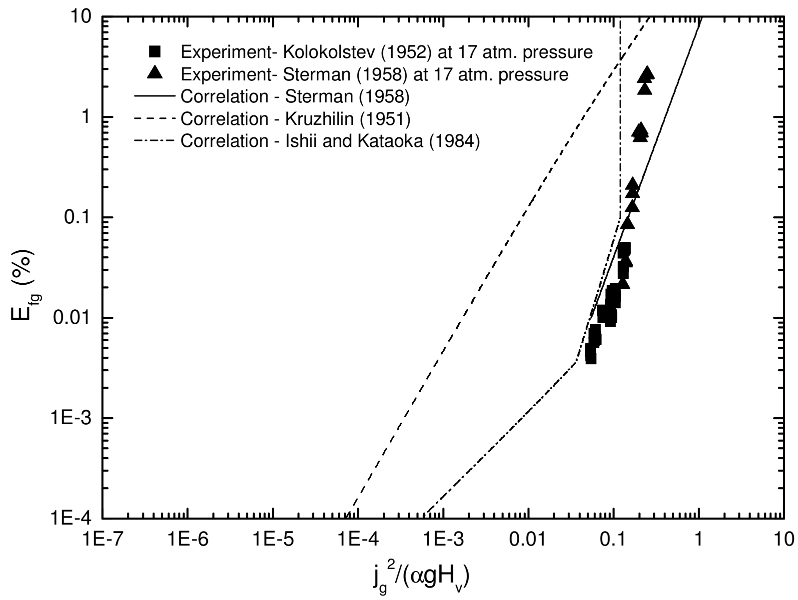

Figure 2.17: Prediction by correlations for experimental data of Sterman [21] and Kolkolostev [22] at 17 atmospheric pressure

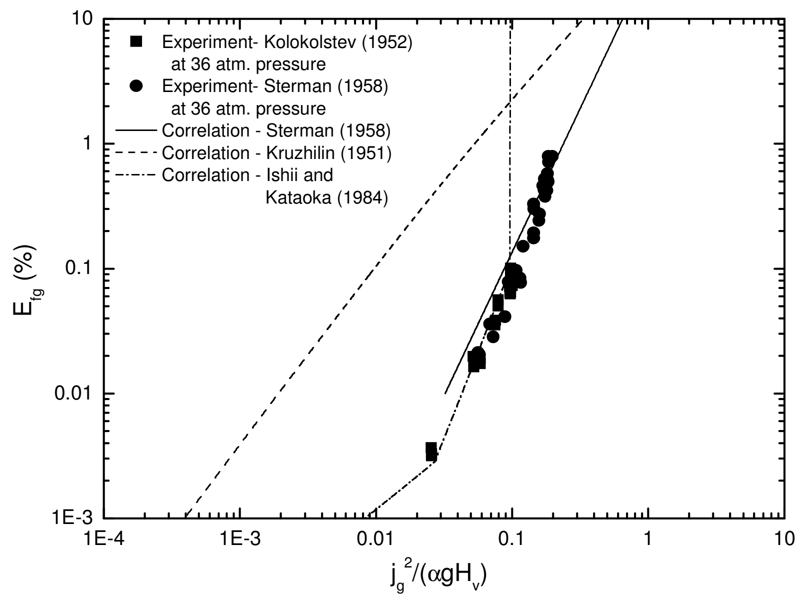

Figure 2.18: Prediction by correlations for experimental data of Sterman [21] and Kolkolostev [22] at 36 atmospheric pressure

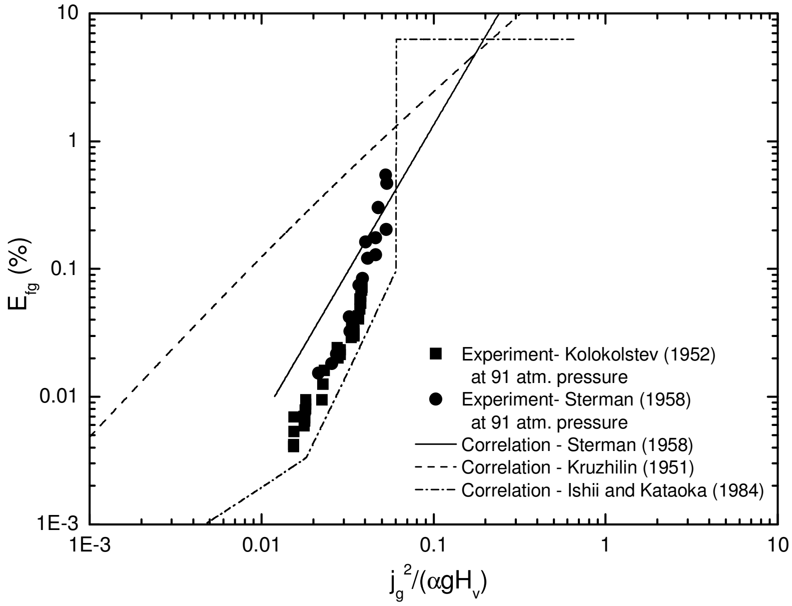

Figure 2.19: Prediction by correlations for experimental data of Sterman [21] and Kolkolostev [22] at 91 atmospheric pressure

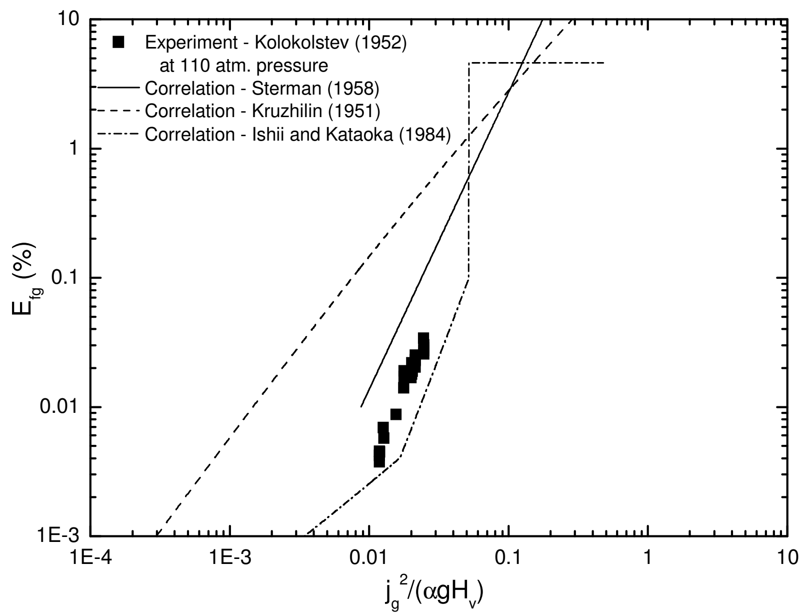

Figure 2.20: Prediction by correlations for experimental data of for Sterman [21] and Kolkolostev [22] at 110 atmospheric pressure.

Cosandy et al. [24] analyzed the problem of radio-nuclide entrainment in the reactor containment in case of severe accident where the core melt is covered with the pool of water. Bubbling at the surface of water would transport radionuclides by carryover phenomenon. Authors predicted the measured carryover fractions using the correlation provided by Kataoka and Ishii [30]. The entrainment factors predicted in upper momentum controlled region agreed well with the correlation but overall trend in the momentum controlled region and entrainment in deposition controlled region was measured to be as high as 5 times the prediction by Kataoka and Ishii [30] correlation. This difference was attributed to the following possible reasons.

a) The fit of Kataoka and Ishii [30] correlation is based on the data with higher superficial velocities (>0.5 m/s) whereas the superficial velocities in the experiment were between 5 to 27 mm/s.

b) Concentration of solid tracer particles in and above the pool can affect the entrainment. This has not been accounted for in the Kataoka and Ishii [30] correlation. Therefore it can be inappropriate to compare the experimental results with the correlation by Kataoka and Ishii [30].

It was also stated that the Kataoka and Ishii [30] correlation was good for the prediction of solid fission products in air-steam atmosphere above the pool, but was erroneous for pure steam atmosphere as the effect of pressure is not properly described.

Iyer et al. [33] studied the effect of superficial gas velocity and the diameter ratio (of vessel to inlet pipe) on the carryover. The experiments were performed at atmospheric conditions with air and water mixture. The carryover was measured with the help of tissue papers suspended above the separation interface and the collected amount of entrainment was weighed. The entrainment was measured with vessel to inlet diameter ratio = 1, where the bubbles were generated through gird plate with hole diameter 5 mm. It was found to agree very well with the Kataoka and Ishii [30] correlation. With diameter ratio more than unity it was observed to be higher than the prediction by correlation and this was attributed to the jetting effect of two-phase mixture that issues from the riser. Thus in the first case with grid plates it appears that the bubbles at the interface had uniform distribution while without grid plate the separation interface is turbulent and there is splashing of liquid. Author concluded that thus the mechanism of droplet generation and associated size and velocity distribution considered by Kataoka and Ishii [30] may not hold good for the experimental case.

2.5 Two-phase flows – CFD approaches:

Numerical models for fluid-particle flows are based either on one-way or two-way coupling. In a model based on one-way coupling it is assumed that the presence of the particulate phase has a negligible effect on the properties of the carrier phase. The assumption of one-way coupling is typically valid for small particle-fluid mass concentration ratios and/or high Stokes numbers. Two-way coupled models include the effect of the particles on the carrier phase. For example, a two-phase turbulent flow model that includes the effect of the particles on the turbulent velocity fluctuations would be two-way coupled. The ideal numerical model for a fluid-particle flow would provide the properties of each particle in the field and the detailed properties of the carrier phase at any point in the fluid. Thus the motion of each particle, as well as the particle temperature and mass, would be obtained by integrating the particle equations using the local velocity, temperature, and density of the carrier flow and accounting for all particle-particle collisions. The model for the carrier phase would require the direct solution of the Navier-Stokes equations including the boundary conditions imposed by all the particles in the field. Such an exact model is well beyond current computational capability so approximate models are required to carry out the numerical analyses Numerical models for the particle field in turbulent fluid-particle flows have developed along two parallel paths according to the manner in which the dispersed phase is treated. In the Lagrangian model Crowe et a1. [40] the particle field is represented by particle trajectories obtained from integrating the particle motion equation. Simultaneously, the particle mass, velocity, and temperature are calculated along the trajectories. A mixture of 100-micron particles in air at standard conditions with a particle mass concentration ratio of unity would require tracking 10^9 particles per cubic meter of mixture, well beyond current computer capability. Current Lagrangian models identify a packet of particles as a single computational particle with the same properties as the physical particles. The other approach is the two-fluid model. Volume-averaged properties of the particulate phase are used. Conservation equations are developed for the mass, momentum, and energy of the particle cloud and these are integrated to predict the volume averaged particle properties throughout the field.

The modeling equations are composed keeping in mind the Eulerian and Lagrangian framework; we model the continuous phase by Eulerian method and depending upon the complexity of the flow we consider if the dispersed/ secondary phase can be modeled by either Eulerian or Lagrangian framework. Multiphase flow can be modeled mainly by three different approaches listed below.

- Eulerian – Lagrangian Approach: Eulerian framework for the continuous phase and Lagrangian framework for dispersed phases

- Eulerian – Eulerian Approach: Eulerian framework for both the phases

- Volume of Fluid Approach: Eulerian framework for both the phases with specialized interface treatment.

2.5.1 Eulerian-Eulerian approach:

In Euler-Euler model each phase is treated as a continuum, each inter-penetrating each other, and is represented by averaged conservation equations. The averaging process introduces the phase fraction, α into the equation set, which is defined as the probability that a certain phase is present at a certain point in space and time. Figure 2.21 (a) shows a sketch of the two-fluid model. The velocity of each phase is represented by one set of velocity vectors, which are shown in red and blue for fluid 1 and 2, respectively. The phase fraction of the dispersed phase is shown by small numbers in the lower right corners of the cells. Due to the loss of information associated with the averaging process, additional terms appear in the averaged momentum equation for each phase, which require closure. In addition to the Reynolds stresses, which enter into the averaged single-phase flow equations, an extra term that accounts for the transfer of momentum between the phases appears. This term is known as the averaged inter-phase momentum transfer term and accounts for the average effect of the forces acting at the interface between continuous phase and the dispersed phase/ particles. The Euler-Euler methodology is applicable to all flow regimes, including separated, dispersed or intermediate regimes, since the topology of the flow is not prescribed. However, the formulation of the inter-phase momentum transfer term and the two-phase turbulence model is the crux of the Euler-Euler methodology because it depends on the exact nature of the flow. Consequently, the resulting predictive capabilities rely heavily on them. The main components of inter-phase momentum term are due to the drag, lift and virtual mass forces acting at the interface between the two phases.

The dispersed phase or particle characteristics can also be discretised using the multi-group approach, where the number density becomes a vector such that each group is identified by a particular characteristic range, e.g. groups based on separate particle diameter ranges to simulate a polydisperse flow field. In this case, transport equations are need for each Eulerian group. The Euler-Euler approach is valid for denser (>10%) volume fractions of dispersed phase. e.g. fluidized bed reactors, bubble column reactors, multiphase stirred reactors, etc.

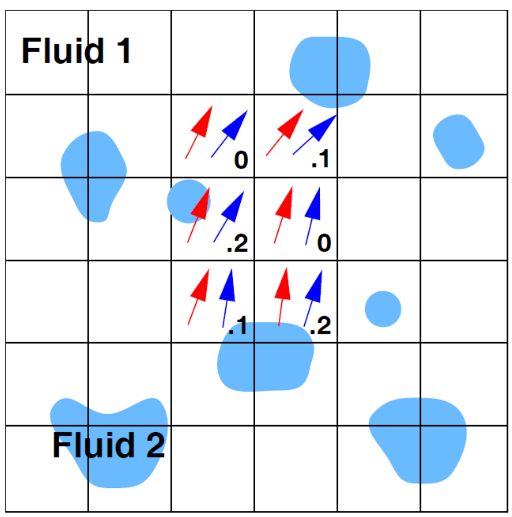

Figure 2.21 (a):Euler-Euler simulation of two-phase flows

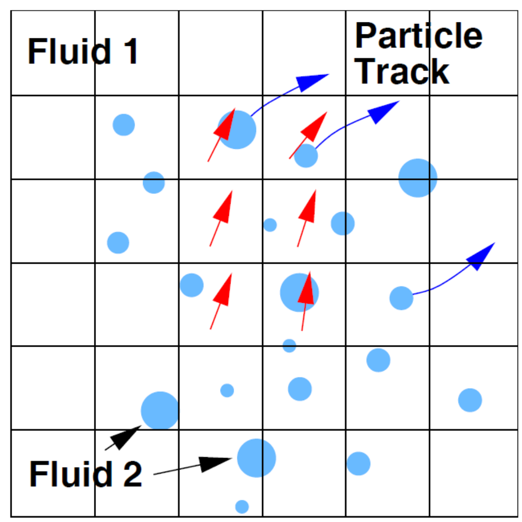

Figure 2.21 (b): Euler-Lagrangian simulation of two-phase flows

2.5.2 DNS of two-phase flows

Direct Numerical Simulation (DNS) is the branch of CFD in which the Navier-Stokes equations are numerically solved without any turbulence model. DNS differs from conventional CFD in that the turbulence is explicitly resolved, rather than modeled by a Reynolds-averaged Navier-Stokes (RANS) closure. It differs from large-eddy simulation (LES) in that all scales, including the very smallest ones, are captured, removing the need for a subgrid-scale model. DNS can thus be viewed as a numerical experiment producing a series of non-empirical solutions, from first principles. Its great strength is the ability to provide complete knowledge, unaffected by approximations, at all points within the flow, at all times within the simulation period. DNS is therefore ideal for addressing basic research questions regarding turbulence physics and modeling. This ability, however, comes at a high price, which prevents DNS from being used as a general-purpose design tool. The defining characteristics of DNS stem from the distinctive characteristics of turbulence. Because turbulence is inherently unsteady and three-dimensional, DNS requires time dependent calculations within a three-dimensional domain. These two features are shared with LES (and therefore LES/RANS hybrid strategies such as detached eddy simulation (DES)). The unique feature of DNS is associated with the manner in which turbulence is affected by viscosity. This is responsible for the two chief drawbacks of DNS – its extreme computational cost ($\sim Re^3$), and severe limitation on the maximum Reynolds number that can be considered.

From a mathematical point of view multiphase flow problems are notoriously difficult and much of what we know has been obtained by experimentation and scaling analysis. Not only are the equations, governing the fluid flow in both phases, highly nonlinear, but the position of the phase boundary must generally be found as a part of the solution. In order to solve the Navier-stokes equations for two-phase systems, one fluid formation is considered where the both fluid share the same velocity, the fluid properties are defined as function of phase fraction or with proper interface jump condition. The one fluid formation allows the simplification with a methodology for interface tracking. Variety of numerical methods have been devised and are broadly categorized in surface tracking methods (Marker And Cell, Level Set Methods), Moving mesh methods and Volume tracking methods (Volume of Fluid). Each of these have their own limitations and advantages. Most popular method for simulation include Volume Of Fluid (VOF) methods which conserves the fluid mass accurately. Advanced methods combining VOF and Level Set (LS), Ghost Fluid Method, LES/VOF methods have been also evolved to include advantages from each individual method. True DNS of multi-phase flow is still not yet possible, so far the LES/VOF has been the state of art.

2.5.2.1 MAC methods

The MAC method first appeared in 1965. It was developed by Harlow and Welch [41, 42] specifically for free surface flows. Based on an Eulerian staggered grid system, the MAC method is a finite difference solution technique for investigating the dynamics of an incompressible viscous fluid. It employs the primitive variables of pressure and velocity. One of the key features is the use of Lagrangian virtual particles, whose coordinates are stored, and which move from a cell to the next according to the latest computed velocity field. If a cell contains a particle it is deemed to contain fluid, thus providing flow visualization of the free surface.

2.5.2.2 Level Set (LS) Method

Motion of both the fluids is assumed to be governed by the incompressible Navier-Stokes equation. The interface between the fluids Γ is the zero level set of ψ

$$\Gamma = \{x | \psi(x,t) = 0\} \tag{2.66}$$

Also

$$\psi(x,t) = \begin{cases} > 0 \; in\ the\ liquid \\ = 0 \; at\ interface \\ < 0 \; in\ the\ gas \end{cases} \tag{2.67}$$

Thus the domain which is discontinuous at interface is now can be expressed as continuous function of level set$\psi(x,t)$. Velocity is also continuous by defining as follows:

$$u = \begin{cases} u_l, \psi > 0 \\ u_g, \psi \leq 0 \end{cases} \tag{2.68}$$

The evolution of surface is then be given by

$$\frac{\partial \psi}{\partial t} + u.\nabla\psi = 0 \tag{2.69}$$

To determine the gas-liquid interface evolution, above equation is first parameterized with co-ordinates(x, y). The resulting equation is then non-dimensionlized. The fluid properties like density and viscosity are also expressed as continuous function using Heaviside function. The velocity terms are represented by stream functions in the final equation of motion valid over entire domain. The detailed formulation and solution procedure can be found in the references.

The advantage of Level Set method is that the level set function is continuous throughout the domain which numerically very convenient method to represent the interface. It's is easy to directly locate the interface on a fixed grid and calculate accurate surface normal and curvature and related surface tension terms. But LS methods have been found to incur significant error in amount of liquid mass as the calculations advance in time domain [43] and special procedures are required to alleviate this problem [45, 46]. These limitations of LS method gave rise to formulation of volume of fluid method where interface is reconstructed/tracked based on the volume fraction function.

2.5.2.3 Volume Of Fluid (VOF) method

VOF belongs to the class of Eulerian methods which are characterized by a mesh that is either stationary or is moving in a certain prescribed manner to accommodate the evolving shape of the interface. As such, VOF is an advection scheme—a numerical recipe that allows the programmer to track the shape and position of the interface, but it is not a standalone flow solving algorithm. The Navier–Stokes equations describing the motion of the flow have to be solved separately. The same applies for all other advection algorithms.

2.5.2.3.1 Formulation of VOF

In VOF one-fluid formulation for a multiphase flow is used. According to this model, dynamics of viscous, incompressible and immiscible fluids is governed by single Navier-Stokes equations (2.24) and continuity equation (2.25) as follows:

$$\frac{\partial(\rho u_i)}{\partial t} + \frac{\partial(\rho u_j u_i)}{\partial x_j} = -\frac{\partial p}{\partial x_i} + \frac{\partial}{\partial x_j}\left[\mu\left(\frac{\partial u_i}{\partial x_j} + \frac{\partial u_j}{\partial x_i}\right)\right] + \rho g_i + \sigma k n_i \tag{2.70}$$

$$\frac{\partial u_i}{\partial x_i} = 0 \tag{2.71}$$

where u_i is the i-th velocity component, ρ denotes density, μ is the dynamic viscosity, p is the pressure, g_i is the i-th component of the gravitational acceleration. The additional term that appears in Navier-Stokes equation (2.24) is inherited from one-fluid formulation. This term represents surface tension acting locally at the interface between fluids. In the case of constant surface tension coefficient σ the force resulting from surface tension acts in the direction normal to the interface given by:

$$n = \frac{\nabla \emptyset}{|\nabla \emptyset|} \tag{2.72}$$

Where $\emptyset$ denotes the volume fraction of the background fluid.

$$\emptyset = 1, \qquad for\ a\ point\ inside\ the\ fluid$$

$$0 < \emptyset < 1, \qquad for\ a\ point\ in\ transition\ region$$

$$\emptyset = 0, \qquad for\ a\ point\ inside\ the\ fluid$$

One needs to notice that $\nabla \emptyset$ has a non-zero value only at the interface, indicating a local character of the surface tension term. From the definitions of the indicator function/volume fraction, the effective local density and viscosity in a computational cell can be estimated as

$$\rho = (1 - \emptyset)\rho_1 + \emptyset \rho_2 \ \ and \ \ \mu = (1 - \emptyset)\mu_1 + \emptyset \mu_2 \tag{2.73}$$

where ρ_j , μ_j represent, respectively, the density and dynamic viscosity of the j-th fluid. Substituting constitutive relation (2.70) to the conservative form of the continuity equation and taking into account the assumption about incompressibility of the fluids, one can derive equation for transport of the volume fraction

$$\frac{\partial \emptyset}{\partial t} + u_j \frac{\partial \emptyset}{\partial x_j} = 0 \tag{2.74}$$

To model a multiphase flow and capture the interface position, one needs to solve equations. (2.70)-(2.73). It should be noticed that both fluids are treated as single continuous since they share the same velocity in each control-volume This simplification allows for relatively easy numerical solution of the problem also when more than two fluids are considered. On the other hand, sharing the same velocity is a disadvantage of this formulation, because one is not able to model the slip phenomenon

The major difficulties to achieve accurate interpretation of interface solving equation (2.74) are the numerical diffusion which may arise due to descritization of second term. We can try to solve the transport equation for the volume fraction, with a normal finite volume descritization scheme. It will do something like this close to the interface:

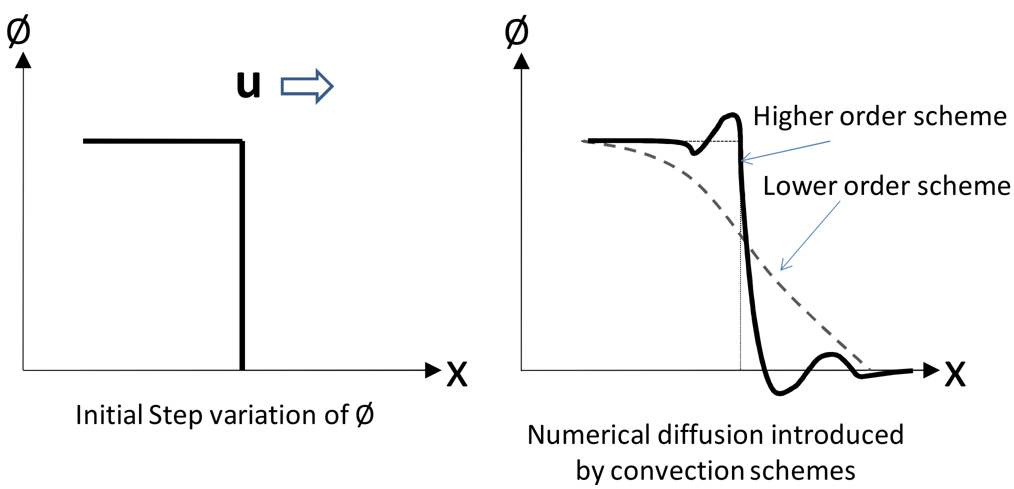

Figure 2.22: Example of Numerical problems related to sharp jump in the volume fraction function

Here the low order schemes cause the surface to become overly diffusive while the higher order schemes causes the volume fraction function to take on unphysical values. Overall mass conservation can be kept, but some cells may get negative amounts of water or more water that the cell volume allows.

Tracking the interface location in Eulerian grids can be performed using interface tracking or interface capturing methods. While the interface tracking methods, such as SLIC [46], PLIC [48] and their variations, demand detailed reconstruction of interfaces using geometric formulations, the interface capturing methods (CICSAM [48] and HRIC [49]) employ algebraic methods to identify the interface locations.

2.5.2.3.2 Geometrical reconstruction

We may use pure geometrical means to flux the surface. As an example, consider the fact that a cell in 1D must fully fill up before the next cell can get any fluid:

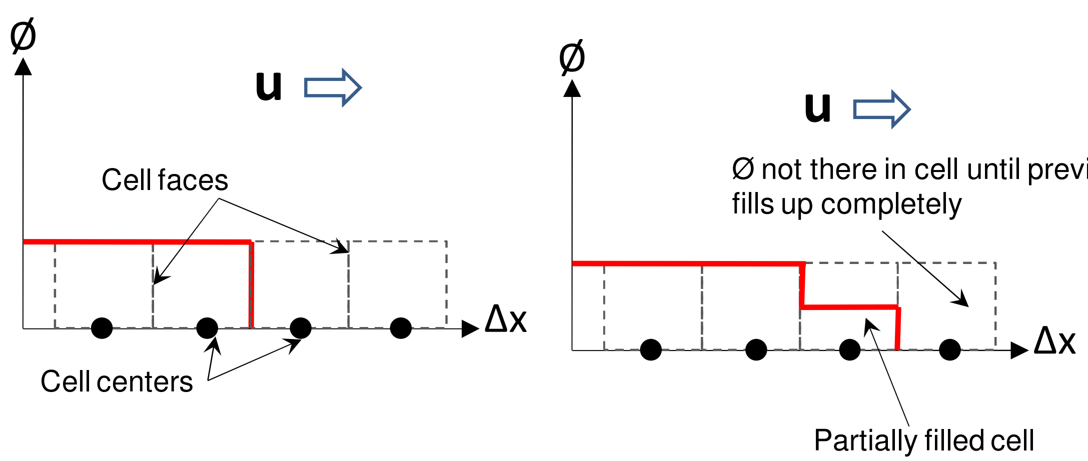

Figure 2.23: Geometric reconstruction of interface in 1D

In 2D and 3D there are two popular choices:

- SLIC: Simple Line Interface Calculation
- PLIC: Piecewise Linear Interface Construction

In the SLIC method the direction of the surface normal is established first, typically based on the value of the volume fraction function Ø in the neighboring cells. There are 4 options for the configuration in 2D if we round the normal direction to the closest 90 degrees on a rectangle cell (see Figure 2.24).

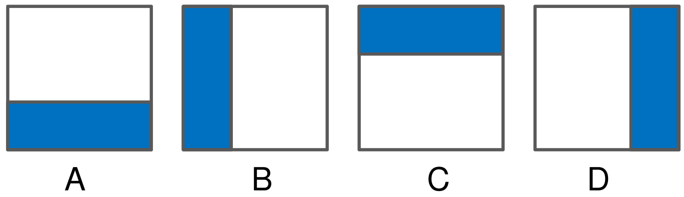

Figure 2.24: SLIC configurations with four face cell

If we take the normal direction into account when we advect the volume fraction function field Ø then we can avoid numerical diffusion in many cases, since we can avoid fluxing through faces that are not wetted.

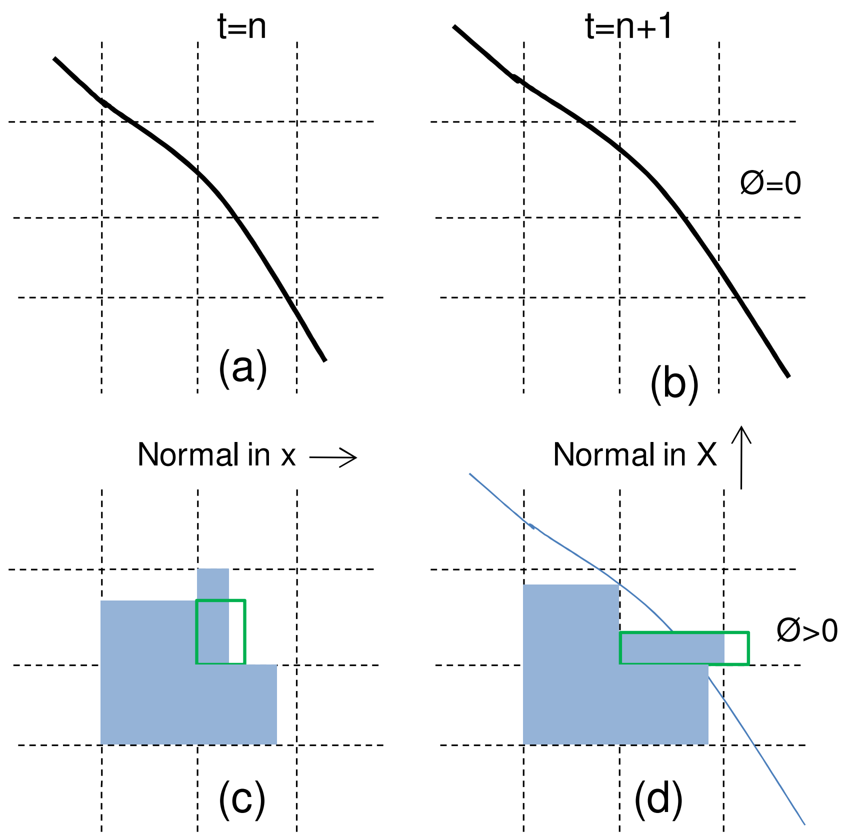

Figure 2.25: Example of 2D flux of Ø using SLIC.

Figure 2.25(a) and 2.25 (b) shows the real position of the interface in two subsequent time steps. The gray fields in 2.25 (c) and 2.25 (d) are two possible descritization of the Figure 2.25 (a) The green fields in Figure 2.25 (c) and (d) are the volume fraction that will be fluxed right between two time steps. Scheme as per Figure 2.25 (d) will cause a numerical diffusion a “drop” will break away from surface.

In the SLIC method the free surface will be staircase shaped, this is the price we pay for simplicity. The more advanced PLIC method identifies the most wetted corner. For a quadrilateral element we can identify four cases for each corner, exemplified for the lower right corner as shown in Figure 2.26.

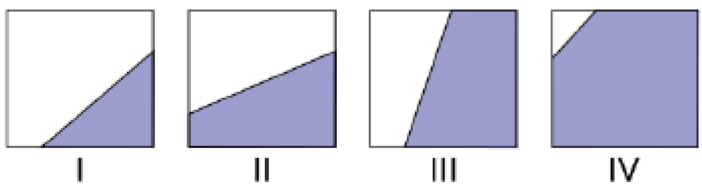

Figure 2.26: PLIC configurations with four face cell

We can then use flux based on the surface angle and a bit of trigonometry which can get further tricky in 3D with irregular meshes.

The geometrical reconstruction methods are not perfect. First of all the surface is not really staircase or piecewise linear. It is also a problem to advect in multiple directions at once. With a regular grid this can be solved by advecting and reconstructing twice, one time in each coordinate direction, the so called direction split scheme. With unstructured meshes this is harder. Typical problems are lack of mass conservation, numerical diffusion and drops that tear free from the surface.

Geometrical reconstruction becomes difficult on unstructured meshes and especially in 3D. Ensuring mass conservation and obtaining a smooth interface may be hard. The geometrical schemes must also be explicit which causes small time steps and slow simulations.

2.5.2.3.3 Higher order schemes for advection of volume fraction

If instead we can solve an equation for the $\emptyset$ field just like for the velocity and pressure then it becomes much easier to implement, but we need a special compressive scheme to make sure the interface stays sharp. The following schemes are most used:

- HRIC: High Resolution Interface Capturing
- CICSAM: Compressive Interface Capturing Scheme for Arbitrary Meshes
- MULES: MUlti-dimensionsal Limiter for Explicit Solution

The MULES algorithm is badly documented in literature and will not be described here. It is only used in OpenFOAM. CICSAM and HRIC are similar algorithms and better documentation of these can be found in literature. Both CICSAM and HRIC uses a combination of the first order upwind differencing scheme (UDS) and the first order downwind differencing scheme (DDS). UDS is diffusive and smears the interface, but is unconditionally stable. DDS is compressive, but unstable. It may be interesting to know what the most common CFD programs use in practice for interface capturing. The major commercial codes support a wealth of specialized models (like special particles for thin films on walls), but they also support VOF and many of the schemes mentioned above. Some example programs are:

- OpenFOAM: uses MULES by default, but both CICSAM and HRIC have been implemented by various people, but not in the main source code repository. The OpenFOAM extend project has a CICSAM implementation.

- Fluent: implements CICSAM in an explicit scheme and a modified HRIC in an implict scheme. Also implements geometrical reconstruction.

- Ansys CFX: implements CICSAM in an explicit scheme and a modified HRIC in both implicit and explicit schemes. Also implements geometrical reconstruction.
- Star CCM+: uses HRIC

2.5.2.4 Advanced Methods:

2.5.2.4.1 Combined Level Set and Volume Of Fluid (CLSVOF)

As discussed earlier the Level Set and VOF has their own limitations and strengths, Sussman and pukett [50] developed a coupled approach in which the interface is defined with Level-Set function as well as VOF volume fraction function. They developed methodology for tracking the interface by solving advection equations using higher order operator split scheme. This was termed as CLSVOF.

In level set method the interface is represented by a Level Set Function with value of zero, value of level set function away from interface is represented by a signed distance from interface. The advantage of such formulation is calculation of interface curvature is simplified. But the LS method lacks in conservation of mass during time stepping calculations. VOF conserves the mass but the interface is not maintained as sharp as by LS method. In CLSVOF the volume fraction function is related to LS function as:

$$\emptyset(\Gamma, \mathrm{t}) = \frac{1}{|\Gamma|}\int_{\Gamma} H(\psi(x,t))\,dx \tag{2.75}$$

Where H is the Heaviside function,

$$H = \begin{cases} 1 & if\ \psi > 0 \\ 0 & otherwise \end{cases} \tag{2.76}$$

An advantage of representing the free surface as volume fractions is the fact that one can write accurate algorithms for advecting the volume fraction function so that mass is conserved while still maintaining a sharp representation of the interface.

In the CLSVOF method, the curvature is obtained via finite differences of the level set function which in turn is derived from the level set function and volume-of-fluid function at the previous time step.

Sussmann et. al. [50] showed that in CLSVOF comparable mass conservation properties as with other second order volume-of-fluid advection methods is maintained and it can also accurately compute surface tension driven flows by coupling. Details of CLSVOF advection algorithm can be found in [50].

2.5.2.4.2 Ghost Fluid Method (GFM)

Fedkiw et. al. [51] developed a new technique called Ghost Fluid Method (GFM) in order to address the issue of large oscillations in pressure and velocity near interface for compressible flows using level set methods. One of the central issues with two-phase flow simulations lies in the numerical descritization of the pressure gradient term. Indeed, this term contains the density, which exhibits a jump at the interface, and the pressure itself is discontinuous at the interface because of both the surface tension force and the viscous jump. An efficient descritization of this term requires a specific treatment. The ghost fluid method accounts for the pressure jump caused by surface tension, while the jump caused by the discontinuous viscous stress is handled by the continuum surface force technique. GFM relies on the assumption that all the jump conditions for a given variable and its spatial derivatives are known at the interface. Then, the GFM is based on the extension by continuity of fluid in the gas and of gas in the liquid. This extension allows defining the jump of variable, not only at the interface, but also in the neighborhood of the interface. Details of GFM can be found in [51].

2.6 Summary and conclusion on literature survey:

In gravity separation of two-phase flows, the droplets are generated at the interface as a result of bubble disintegration. Various mechanisms exist such as formation of film droplet from rupture of bubble film, formation of jet droplets from the rising jets after collapse of bubbles. Droplets are also formed at high gas flow rates due to shearing of liquid surface. These droplets have various sizes and have certain initial momentum at the time of formation. Droplets travel in gas space after and either fall back into liquid or are carried along with the flow permanently. The entrained droplets constitute the carryover out of equipment. Carryover can have adverse effects such as corrosion of piping and equipment due to presence of soluble salts. In case of power plants the carryover from steam generator can cause severe damage to steam turbine blades. In case of evaporators, the carryover reduces the equipment efficiency and product yield. It can be noted that complete elimination of carryover is not possible but it can be reduced by proper design. Separators can reduce the carryover further. It is thus important to pay careful attention to the design of equipment to minimize the carryover by controlling the parameters that govern the carryover process.

A review of the prediction procedures for the entrainment/carryover has been carried out. All the procedures consist of the following two steps:

(a) Estimation of liquid fragments, droplets present just above the separation interface.

(b) Prediction of the motion of such liquid droplets above separation interface in the bulk of the gas phase.

Above methodology is applicable where the separation of phases takes place purely by gravity and no mechanical equipments/internals are employed to alter droplet momentum in favorable direction.

Following are the important conclusions derived from the review of available literature and contributions of several researchers to the subject of entrainment/carryover in gas-liquid flows:

1. Experimental investigations on the basic input parameters to the process i.e. the entrainment flux at the interface in terms of droplet size and velocity distribution and droplet production rate has been limited. The following parameters govern the process:
    a) Nature of turbulence at interface
    b) Bubble dynamics below and at the interface
    c) Governing mechanism of droplet formation.

    The bubble dynamics and turbulence at the interface depend on the flow rates of the two phases, geometry of equipment and the fluid properties which in turn depend on operating parameters such as pressure and temperature. Owing to such multi-dimensional array of affecting parameters very few experiments are performed to study the role of these parameters. Also practical difficulties of instrumentation for visualization and measurement at high pressures have limited the scope of experiments. Therefore except few, the reliable data on these basic parameters do not exist.
2. A number of simplifying assumptions have been made regarding the droplet size, velocity distribution by researchers investigating the subject analytically. Such assumptions are either very conservative or sometimes irrelevant. In practice, the geometry and operating parameters for equipment under consideration differs from the geometry used in experiments. As far as the estimation of the liquid droplet dynamics in

gas space is concerned the assumptions on the forces considered (drag, buoyancy and gravity) and their estimation appears to be conservative. All analytical studies have neglected the effect of flow pattern of bulk gas phase on the droplet trajectories. This could present major limitation as the drag forces exhibit different behavior when bulk is flow accelerated or decelerated.

3. Due to complexity of the subject, it is mostly dealt with empirical approach and hence none of the attempts can be regarded as universally applicable. Though such correlations can provide quick estimates but needs validation through the experiments in model closely simulating the equipment under consideration. Such validation would provide better confidence in design. Literature review indicated that applicability of the empirical correlations can be seriously doubted as some experiments show unacceptable deviation from correlations.
4. Computational methods are promising in the view of availability of fast computing tools. CFD tools have great potential to model the basic two-phase processes taking place at the interface with techniques such Level Set methods, VOF, Volume tracking and front tracking methods etc. The dispersed liquid phase in the gas space and gas bubbles in liquid can be efficiently modeled using Euler-Lagrangian methods. Although the CFD offers great potential to address the number issues in detail, a major challenge still remains that is validation of these CFD methodologies with relevant, reliable experimental data.

Chapter 3

Air Water Loop – experimental facility

3.1 Aim and Objectives:

An experimental facility known as Air-Water Loop (AWL) has been set up with an objective to investigate the carry-over phenomena in steam drum of AHWR. The Air-Water Loop has been designed with basic goals as follows:

1. To have a drum geometry similar to AHWR steam drum, i.e. horizontal cylinder with identical configuration of inlet tail pipes, down comer, outlet and internals
2. The set-up should provide scope for visual observations on fundamental aspects of carryover in gravity based separation i.e. droplet generation mechanisms, size distribution etc.

3.2 Scaling philosophy:

Figure 3.1 shows the cross-section of AHWR steam drum and different interfaces/regions considered. In order to simulate the key parameters affecting phenomenon in interest, an attempt has been made to maintain practically same values of the superficial velocities of both phases at different regions inside the drum.

The dimensions of model drum are arrived upon such that the local pressure drop at different junctions is also similar to that of prototype. From the description of the prototype steam drum it appears that if torispherical heads are not considered, the locations of tail pipes and down comers have a $1/4^{th}$ symmetry. Therefore for full scale simulation it is only required to simulate $1/4^{th}$ of steam drum with a single down comer and 28 tail pipes. Semi-circular cross-section has been selected due to symmetry and thus model simulates the $1/8^{th}$ of a steam drum. Further volume scaling ratio of 1:10 was selected. This scaling leads to reduction in drum size i.e. space required for installation and as cross-sectional area reduces the air flow rate and water flow rate requirement is also reduced. The parameters which are conserved in prototype and model are shown in **Table-3.1**.

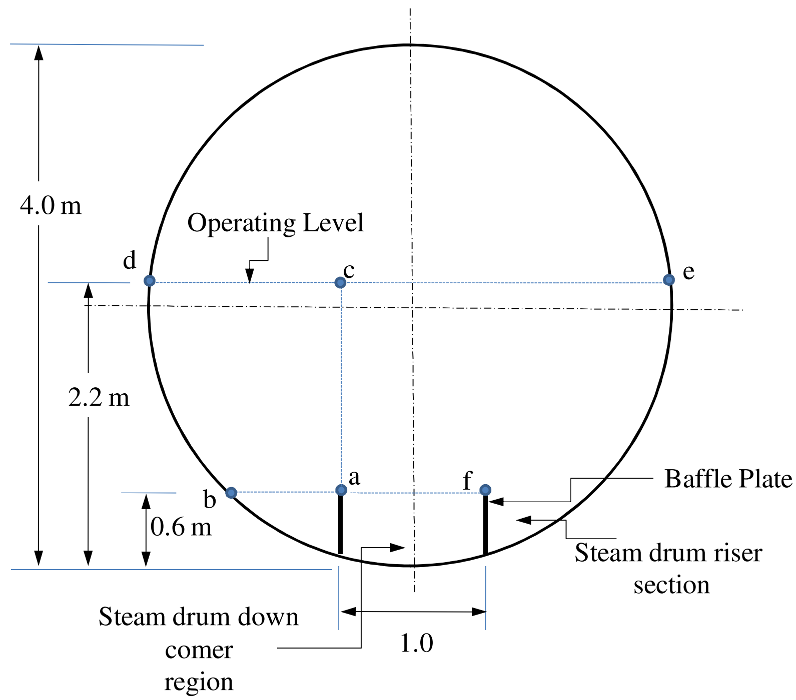

Figure 3.1: Cross-section of AHWR steam drum considered for scaling

Calculations were performed to arrive at suitable size of model drum so that it will preserve these scaling parameters. A drum diameter of 1.93 m with length of 1.154 m and semi circular cross-section was found to be suitable for experiments after design calculations. Table-3.1 also gives the comparison of scaling parameters obtained for the model and the prototype for these dimensions.

In case of AHWR steam drum, the tail pipes enter to steam drum symmetrically on the sides of bottom portion. Baffles are also symmetrically placed. Due to this symmetrical arrangement it was envisaged that for ideal conditions (identical flow rates of phases from both sides of steam drum) the flow patterns would emerge symmetric. Only half portion of steam drum was considered in model. During experiments it is observed that the bubble plume from tail pipes is guided upwards by baffle plate and in upper portion of pool the bubbles spread out uniformly. In our model drum the center plane is a wall instead of symmetric boundary. This has definitely distorted flow pattern near the center plane, however the distortion would be limited to small region near wall (boundary layer portion). Due to presence of wall bubbles are not allowed to cross the center plane. If we imagine full drum then similar conditions would exist in both the half portions and bubbles from one side would try to cross the center plane and such movement would be restricted by bubbles on other side. Thus in our opinion having solid wall would not alter the bubble distribution significantly. The semi-circular cross-section in model has served two purposes in our case (1) it allowed to put a transparent wall at center and we were able to observe, visualize and measure the bubble size distribution across the length of drum and (2) since there was limitation on available flow of compressed air, it would have been difficult to simulate 28 tail pipes with large sized drum.

As discussed in previous section, the previous studies and development of empirical correlations has indicated that superficial velocity and height above separation interface are the key parameters governing amount of carryover.

After the sizing calculations for scaled drum, carryover analysis is performed. This analysis is based on the empirical correlation by Kataoka and Ishii [30] which is best fit to the experimental data from literature. For analysis of model drum, air-water mixture at atmospheric conditions is considered. For prototype geometry, operating conditions of high pressure and temperature (70 bar, 285^{O}C) with steam-water is considered.

Table 3.1: Parameters for scaling the AHWR steam drum

Sr. No.	Parameters for scaling	Location in Steam Drum (refer Figure 3.1)	Model	Prototype
1.	$\left(J_{g-tailpipe}\right)_P = \left(J_{g-tailpipe}\right)_M$	Superficial velocity of gas in the tail pipe	2.1020	2.607
2.	$\left(J_{l-tailpipe}\right)_P = \left(J_{l-tailpipe}\right)_M$	Superficial velocity of liquid in the tail pipe	0.4840	0.5454
3.	$\left(\frac{Tail\ pipe\ pitch}{Tail\ pipe\ diameter}\right)_P = \left(\frac{Tail\ pipe\ pitch}{Tail\ pipe\ diameter}\right)_M$	Ratio of tail pipe pitch and diameter	3.2376	3.5454
4.	$(Entry\ losses)_P = (Entry\ losses)_M$	In to the steam drum	0.8203	0.8584
5.	$\left(J_{g-ab}\right)_P = \left(J_{g-ab}\right)_M$	In the riser at baffle top level	0.1980	0.1922
6.	$(J_{l-ab})_P = (J_{l-ab})_M$	In the riser at baffle top level	0.0456	0.0400
7.	$\left(J_{g-de}\right)_P = \left(J_{g-de}\right)_M$	At interface in the steam drum	0.0823	0.0896
8.	$(J_{l-ac})_P = (J_{l-ac})_M$	Horizontal cross flow over the baffle plate	0.0456	0.0446
9.	$\left(J_{l-af}\right)_P = \left(J_{l-af}\right)_M$	In steam drum down comer region between the longitudinal baffles	0.0858	0.0918
10.	$(local\ losses\ downcomer\ )_P = (local\ losses\ downcomer)_M$	From steam drum to down comer	0.4890	0.4886
11.	$(local\ losses\ at\ steam\ exit\ )_P = (local\ losses\ at\ steam\ exit)_M$	From interface to steam drum exit piping	0.4994	0.4996
12	$\left(\frac{Steam\ drum\ length}{Steam\ drum\ diameter}\right)_P = \left(\frac{Steam\ drum\ length}{Steam\ drum\ diameter}\right)_M$	Ratio of steam drum length and diameter	0.5979	0.4875
13.	$\left(\frac{Baffle\ height}{Steam\ drum\ diameter}\right)_P = \left(\frac{Baffle\ height}{Steam\ drum\ diameter}\right)_M$	Ratio of baffle height and Steam drum diameter	0.1196	0.1335

Figure 3.2 shows the carryover at drum exit for model and prototype with respect to ratio of height available above the separation interface and drum diameter. Since the model and prototype diameter are different the ratio of h/d is taken as x-axis. For h/D closer to 1, the operating level is near the exit. At such conditions due to reduced flow cross-section the superficial velocity of gas is high and the carryover is highest. For air-water and steam-water the correlation gives different values of E_{fg-max} i.e. near surface entrainment. For lower operating levels the entrainment is governed by intermediate and low gas flux momentum region. Here in steam-water the intermediate flux region is negligible and is not visible. For air-water case the region is very small but distinguishable. In low gas flux momentum controlled region we can see the variation/trend is similar in both the cases. This is the region of interest. The operating levels should fall in this region. The transition where the carryover rises suddenly would decide the limiting operating level.

Figure 3.3 shows the carryover analysis for model and prototype with respect to non-dimensional parameter $jg*/h*$. Here also we can notice similar observations that the slope of curve for low gas flux momentum controlled region is same for both the cases. For a given value of $jg*/h*$ the entrainment for steam-water case is almost twice as that of air-water case. This is due to the fact that for steam-water case the droplet sizes produced will be finer as an effect of fluid properties and thus more number of fine droplets will be present at exit, leading to higher entrainment rate.

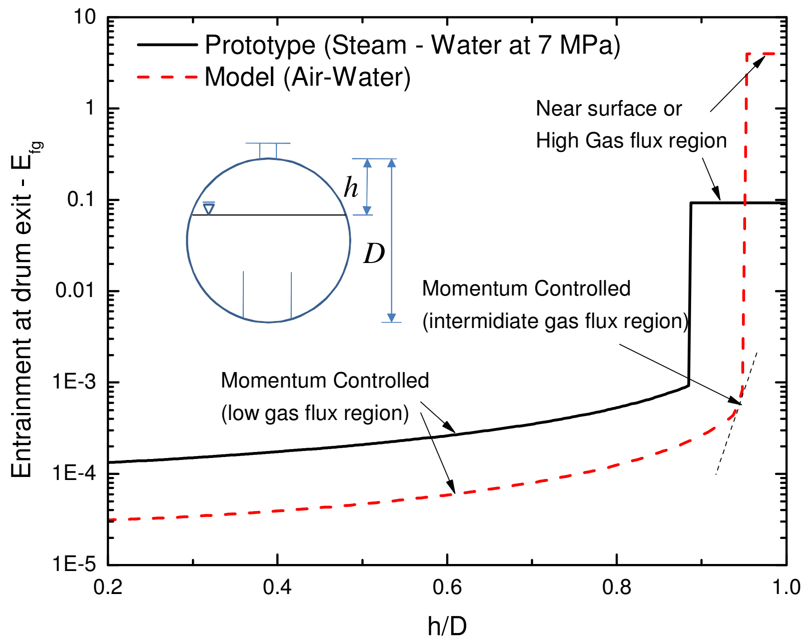

Figure 3.2 : Entrainment variation with respect to height of vapor space to diameter ratio

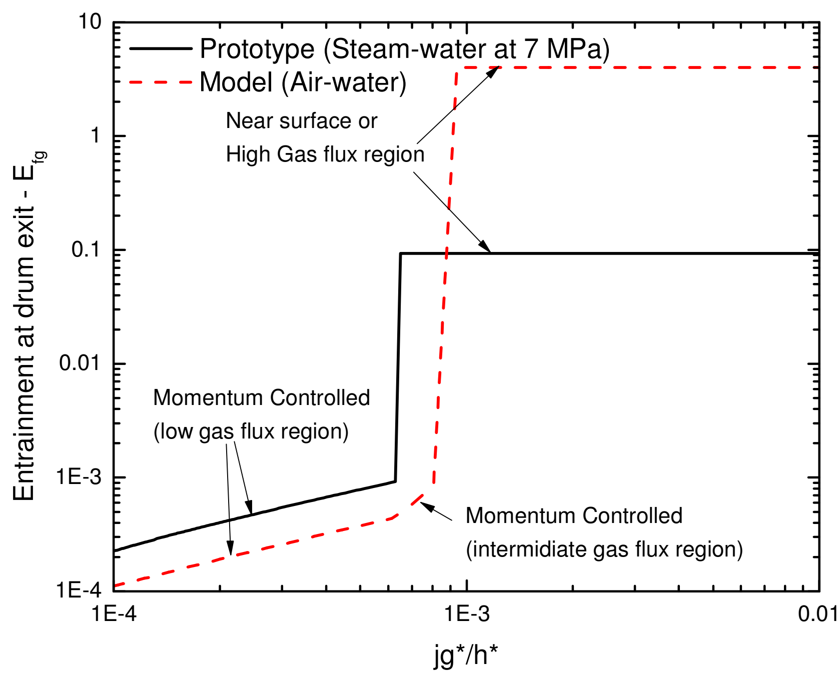

Figure 3.3: Entrainment variation with respect to j_g^*/h^*.

Thus from carryover analysis it is seen that the behavior of carryover cannot be mapped one to one with steam-water conditions except the low flux momentum controlled region. Even with these dissimilarities the air-water is the choice of fluid for most of the two-phase flow experiments. It is impractical to carry out visual observations for steam drum vessel operating at high pressure, high temperature conditions of prototype, while with air-water mixture optically transparent model can be constructed. Air-water is often used to investigate the fundamental two-phase flow phenomenon including entrainment studies. For example Welter et al. [52] studied entrainment in horizontal pipes with vertical up branch (T-junctions, geometry relevant to ADS-4 of AP-1000) in Air Water Test Loop for Advanced thermal hydraulics Studies (ATLAS). They tested various correlations and also developed new models for entrainment. Recently Meng et al. [53] compared the entrainment studies performed in air-water and steam-water experiments for T-junction geometries. They concluded that experimental data of steam-water and air-water have similar trends and correlation developed with air-water can agree well with steam-water experimental data. Meng et al. [53] concluded that the effect of working medium on liquid entrainment is negligible.

In the present research work though we started our analysis with empirical correlation of Kataoka and Ishii [30], a sincere attempt has been made to explore the CFD / numerical simulations to predict the carryover. The CFD methodology needs validation as well as crucial inputs that govern the solution accuracy and the air-water experiments have immensely helped to fill up the missing information required for CFD methods.

In order to simulate the liquid superficial velocities in model the total water circulation flow rate required was estimated to be 1350 lpm, i.e. 90 lpm per channel (total 15 channels).

Instead of using centrifugal pumps (forced circulation) for generating the required water flow rate, relatively simple and economic way of employing natural circulation was chosen. For obtaining required natural circulation flow rate, a configuration shown in Figure 3.4 was envisaged. In this configuration, the air is injected at the bottom of vertical tail pipes to generate two-phase flow. The air gets separated in drum. Drum is connected to storage tank via down comer pipe. The water inventory separated in drum is transported to storage tank and again back to drum through vertical feeders and tail pipes. The density difference between single phase (water) in vertical feeders and two-phase (air-water) in tail pipe is the driving force for the establishment of the flow. The resistive forces include pressure drop across components, skin friction losses and two-phase friction losses. A steady flow is obtained when the total driving force is balanced by the total resistive force in the loop.

Steady state design calculations were carried out. For these calculations, the loop is simulated as a simple closed loop as shown in Figure 3.4. All the tail pipes and feeder pipes have been lumped in to a single pipe. The following steady state equation has been solved iteratively for the estimation of the flow rate through the loop.

$$\Delta P_{1\emptyset} + \Delta P_{2\emptyset} = -g \oint \rho dz \tag{3.1}$$

Where,

$$\Delta P_{1\emptyset} = \sum_{i=1}^{3} \left(\frac{fL_i}{D_i A_i^2} + \frac{K_{L-i}}{A_i^2} \right) \frac{\dot{m}_l^2}{2\rho_l} + \sum_{i=7}^{11} \left(\frac{fL_i}{D_i A_i^2} + \frac{K_{L-i}}{A_i^2} \right) \frac{\dot{m}_l^2}{2\rho_l} \tag{3.2}$$

$$\Delta P_{2\emptyset} = \sum_{i=4}^{6} \left(\frac{fL_i}{D_i A_i^2} + \frac{K_{L-i}}{A_i^2} \right) \frac{\dot{m}_T^2}{2\rho_{2\emptyset}} \tag{3.3}$$

f is calculated based on the Reynolds number estimated assuming the total flow to be water, K_{Li} is the local loss coefficient based on the area changes and the $\rho_{2\emptyset}$ is estimated as follows:

$$\rho_{2\phi} = \alpha\rho_g + (1-\alpha)\rho_l \tag{3.4}$$

Initially, the required flow rate of air and water for the model was given as input. The pressure drops in single-phase and two-phase regions were calculated. The steady state water flow rate is first assumed and pressure drops in various sections of the loop are calculated. For calculation of two phase density and two phase pressure drop, void fraction correlation is required. The void fraction in tail pipe is determined by the correlation of Chexal-Lellouche [54]. The void fraction in the steam drum pool is calculated from Kataoka and Ishii model [55]. Figure 3.5 (a) and (b) shows the comparison of estimated variation of tailpipe void fraction and flow rate in the loop for model and prototype. It indicates the scaling is acceptable and model can closely simulate the flow dynamics expected in prototype.

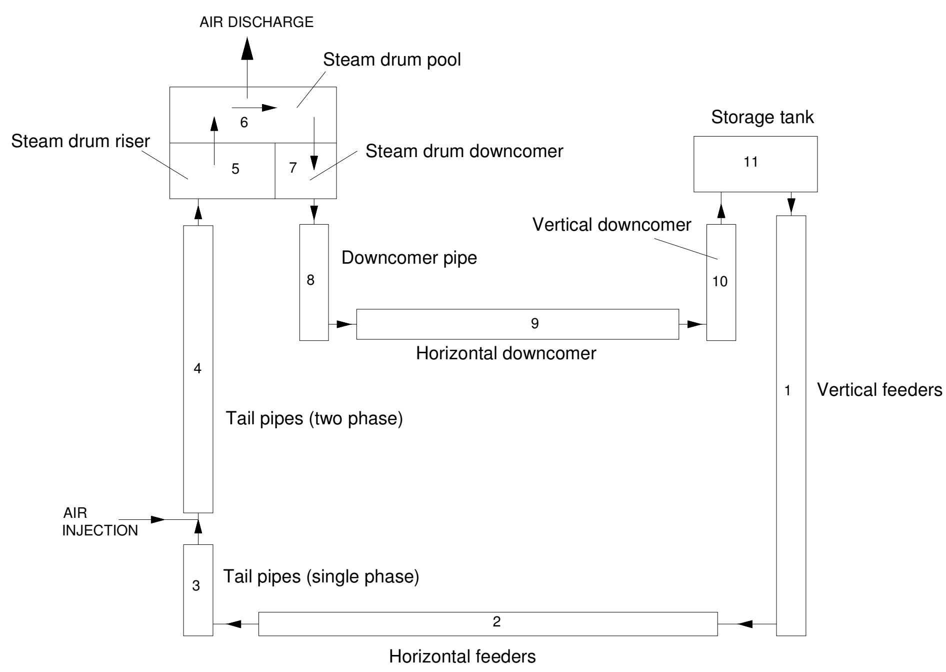

Figure 3.4: Air-Water natural circulation loop configuration for design analysis

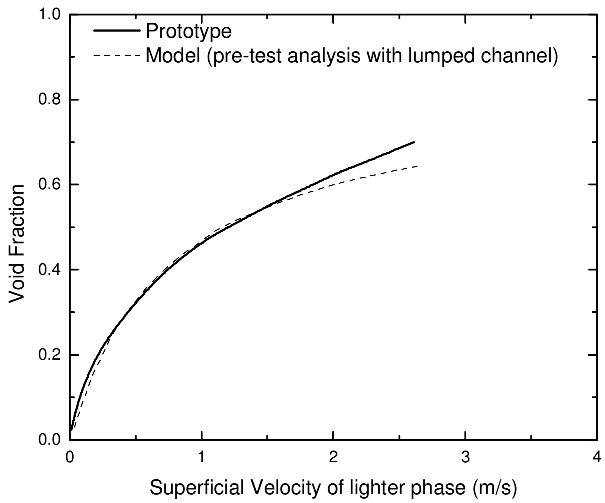

(a)

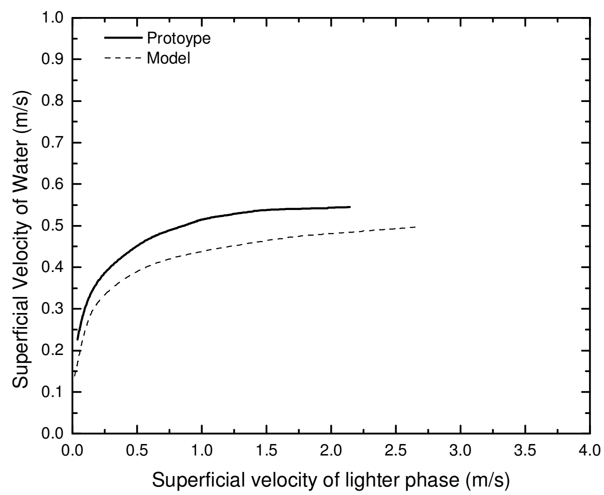

(b)

Figure 3.5: Scaling between prototype and model (design calculations) (a) tail pipe void fraction as a function of superficial velocity of lighter phase (b) superficial velocity of water (corresponding to natural circulation flow generated) as a function of superficial velocity of lighter phase

3.3 Description of Air Water Loop

Figure 3.6 shows the 3-D view of the Air Water Loop. Components of Air Water Loop include air-water drum (1), tail pipes (15 nos.) (2), down comer (3), storage tank (4), air injection lines (5) and air separation line (6) as shown in Figure 3.6. Figure 3.7 to 3.9 show the photographs of various components of Air Water Loop. The air-water drum simulates 1/8th symmetry of the prototype, with 15 tail pipes (62.7 mm ID) and one down comer (97.15 mm ID). Ends of these tail pipes and down comer are connected to the air-water drum and storage tank. The air-water drum has three plane surfaces and once curved surface. The curved surface is constructed with stainless steel plate. The two planes of adjoining sides are made up of transparent Acrylic sheet (7) and the third plane side is made of stainless steel plate (8). The 15 tail pipes are arranged in three different rows: Type-I (outermost row having maximum pipeline length) (9), II (intermediate row) (10) and III (innermost row) (11). Each row has 5 tail pipes & feeders. This arrangement forms three parallel natural circulation loops as shown in Figure 3.10. Specification of each type of channels is given in **Table-3.2**.

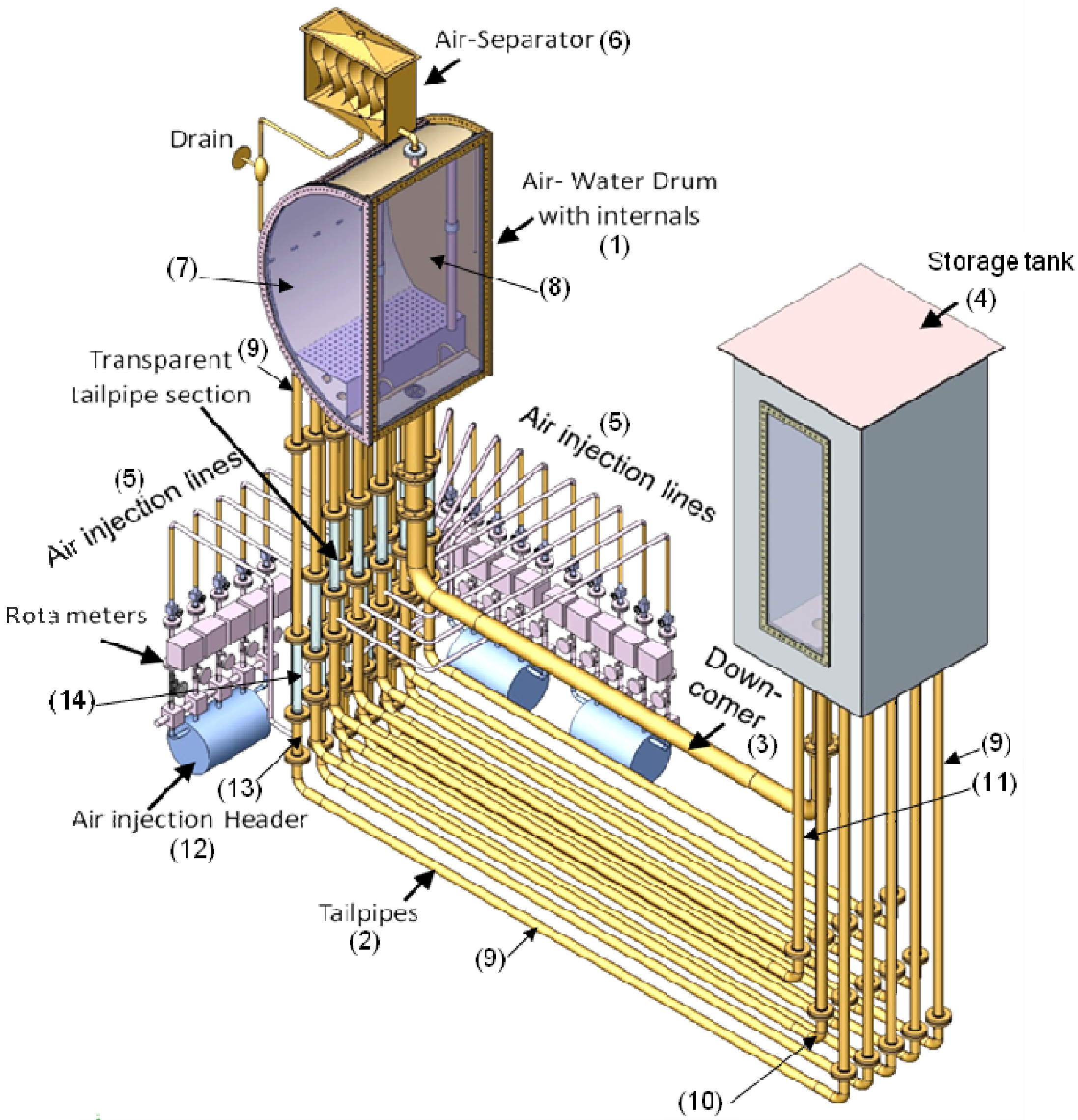

Figure 3.6: Air Water Loop – 3D view

Three separate compressed air headers (12) are used for air injection in Type-I, II and III channel rows respectively. Air is injected at the bottom end of the vertical tail pipe (13) using a sparger. The sparger is made up of 25 mm NB vertical pipe with number of holes of 2 mm diameter on the periphery of pipe surface. Transparent section (15) above the sparger is provided in all tailpipes for visualization of flow. The two-phase flow of air-water mixture then enters the vertical test section and passes through the steam drum riser and finally to the separator drum. Traces of water in the air are separated through a separator, which is open to the atmosphere as shown in the schematic diagram. Loop flow is generated by natural circulation i.e. due to density difference between single-phase water in vertical feeder (section AA', refer to Figure 3.10) and two-phase air-water mixture in tail pipe (section DE, refer Figure 3.10). The water tank is kept open to atmosphere.

Table 3.2: Geometrical specifications for channels in AWL (refer Figure 3.10)

Channel Type	Channel Number	Pipe ID (mm)	Section AB (m)	Section BC (m)	Section DE (m)	Section B'C' (m)	Section D'E' (m)
I	1,2,3,4,5	62.7	4.41	5.0	3.7	3.2	1.805
II	6,7,8,9,10	62.7	4.07	4.52	3.15	2.4	1.43
III	11,12,13,14,15	62.7	3.70	4.07	2.255	2.0	1.0

Compressed air is injected in individual channels at same pressure using spring loaded Pressure Regulative Valve (PRV) in air injection line. Each PRV (total 15 Nos.) is set at 2 bar. The air flow rate is measured using conventional float type rotameters calibrated in instrumentation laboratory. The loop is provided with differential pressure transmitters in horizontal portion of all 15 channels, down comer and tail pipes after the air injection point (refer to Figure 3.10). The level in air-water drum and water tank is measured with level transmitters. Level transmitters measure the differential pressure between atmosphere and pressure at the tapping where they are connected and convert this pressure difference in terms of height of a water column. Thus it gives the collapsed level which is different from actual swell level in the equipment.

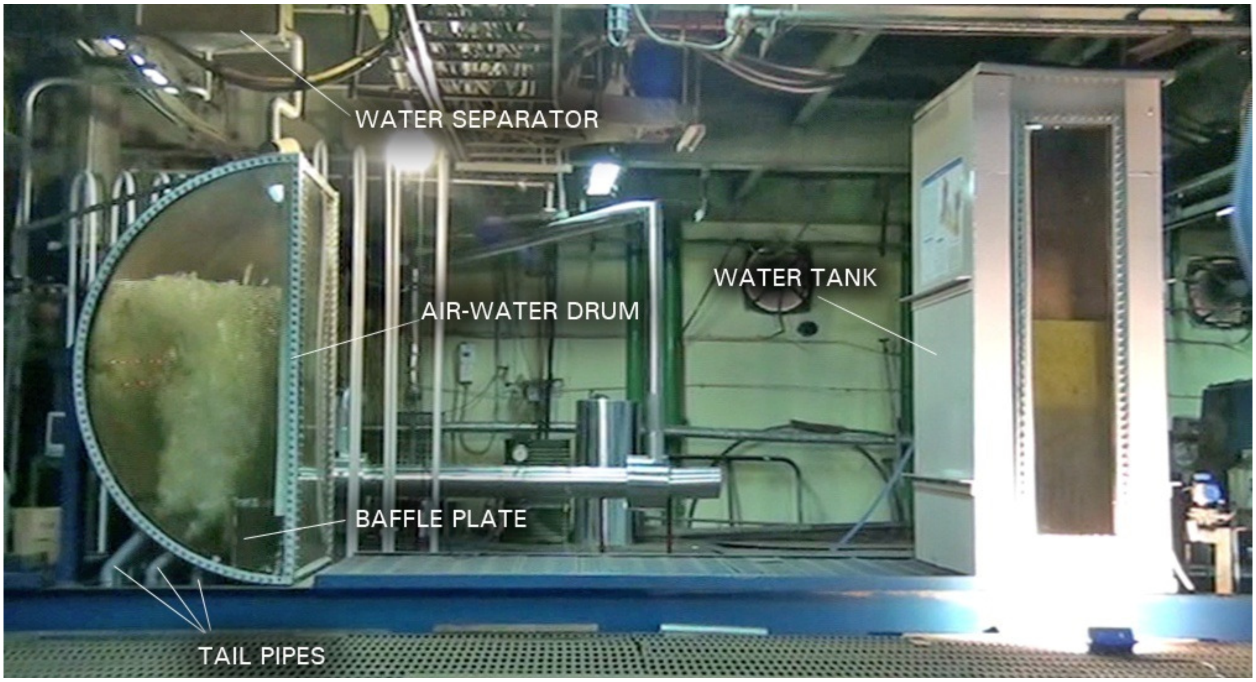

Figure 3.7: Air water drum and Water tank

Figure 3.8: Air injection Header and Air injection lines.

Figure 3.9: Tail pipes and Air injection lines.

The actual position of separation interface i.e. swell level is recorded by visual observation from transparent section of drum using a scale. The natural circulation flow rate in the individual channel is estimated from single-phase pressure drop measured in horizontal portion (across B'C', refer Figure 3.10) of each channel. The pressure drop versus flow characteristics i.e. flow calibration curve for each channel was experimentally established before starting the actual loop experimentation. The flow calibration was carried out using an ultrasonic flow meter. Figure 3.11 gives the calibration curve fitted to experimental data.

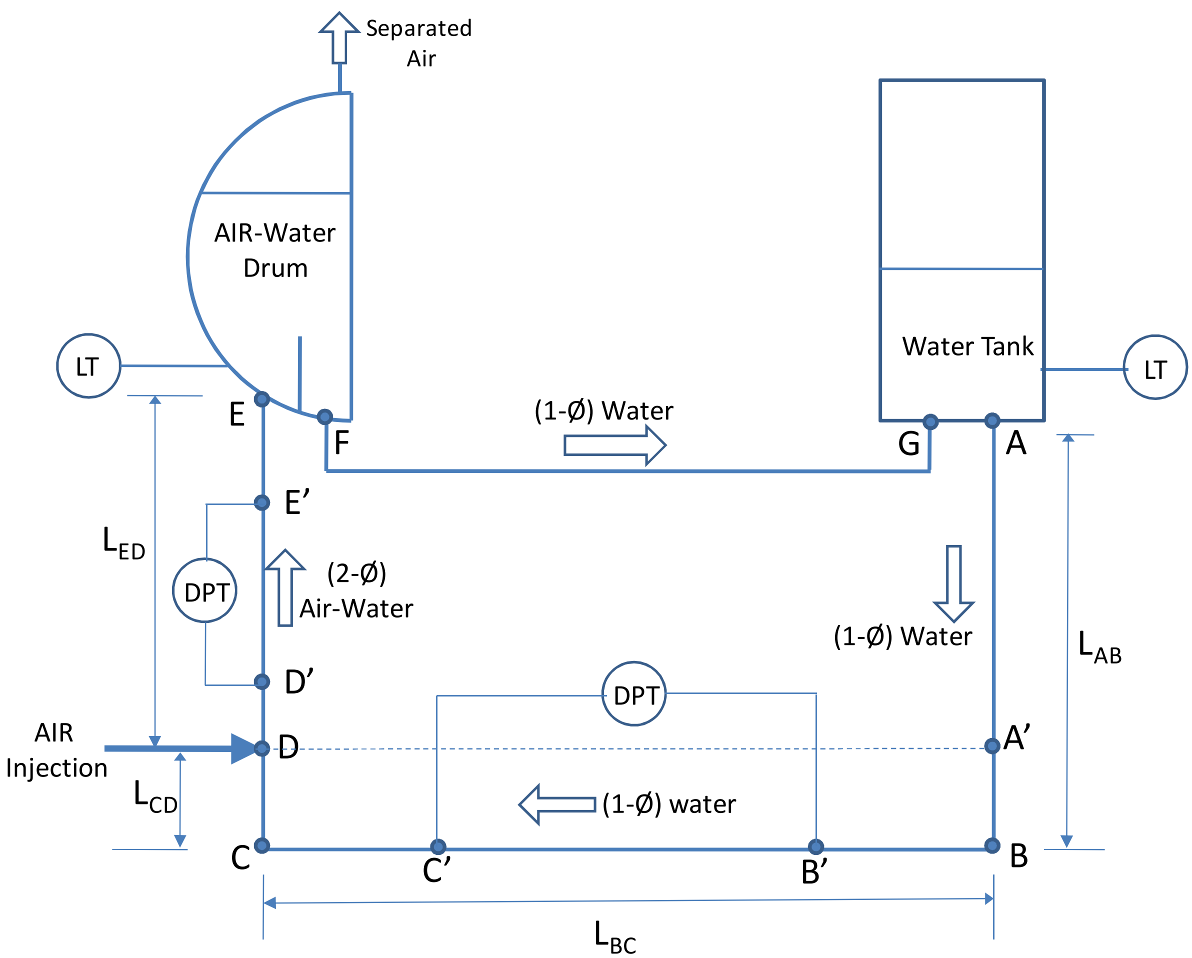

Figure 3.10: Simplified schematic of AWL.

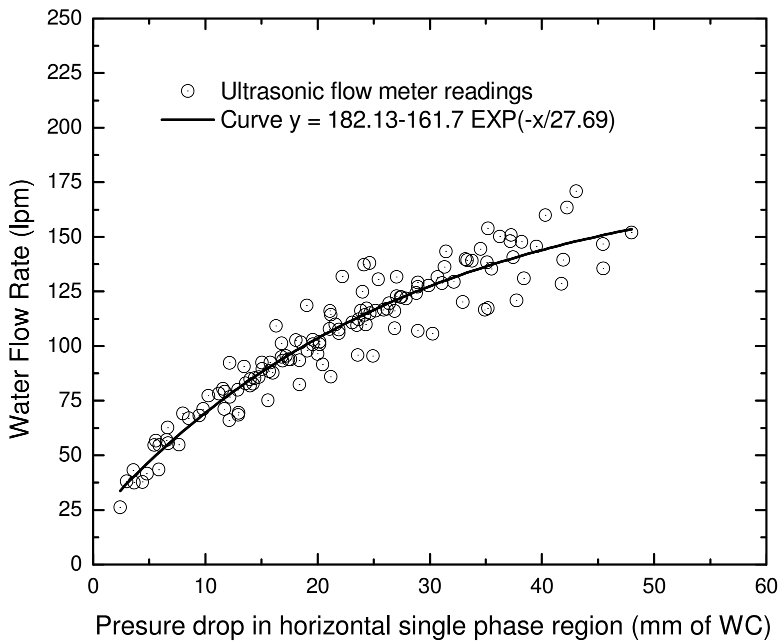

Figure 3.11: Flow calibration curve

3.4 Instrumentation

The different parameters to be measured are as follows

- **Air-Water Drum:** Pressure, swell level, pool void fraction and exit entrainment
- **Tail pipes:** Flow rate and pressure drop
- **Down comer:** Flow rate and pressure drop
- **Entrainment:** Bubble and droplet size

The measurements carried out are as follows:

- **Swell** in the air-water drum is measured by change in measured levels with and without air injection.
- **Flow** measurement in the single-phase horizontal pipe is carried out by calibrated pipe taps (pipe flow meter).
- **Pressure drop and level measurement** is done with differential pressure transducers or transmitters.

- **Pressure measurement** in the steam drum is carried out using pressure transducer.

- **Entrainment (carryover)** is obtained by measuring separated water and High Speed photography.

Chapter 4

Steady State Experiments and its validation

4.1 Steady state experiments

Steady state experiments have been carried out in AWL at atmospheric pressure (top of separator and water tank are kept open to atmosphere) with different initial inventory in Air-Water drum. The loop is filled with water up to the required height in air-water drum. Compressed air is then injected in the tail pipes. The air pressure is set to 2 bar for all channels. For the steady state behavior experiments air injection flow is kept constant in all channels. Experiments are carried out at 50 lpm, 100 lpm, 150 lpm, 200 lpm, 250 lpm, 300 lpm, 350 lpm and 400 lpm air injection flow rate which corresponds to superficial air velocity of 0.27 m/s, 0.54 m/s, 0.81 m/s, 1.08 m/s, 1.35 m/s, 1.62 m/s, 1.89 m/s, 2.16 m/s in each tailpipe respectively. After adjusting the air injection flow rate in each channel, the loop is operated for at least 15 minutes to collect the steady state trends of the measured parameters. Experiments were carried out with initial water level in drum ranging from 500 mm to 1000 mm.

Figure 4.1 shows the transient variation for single-phase pressure drop in horizontal portion of channels 1 to 5 (Type-I) during an experiment with initial drum level 650 mm and air injection flow rate varying from 50 to 400 lpm. With each step rise in air injection flow rate the buoyancy and driving force increase leading to rise in recirculation flow rate. The single phase pressure drop measured across the horizontal leg of each flow channel thus increases with an increase in the air injection flow rate. It can be noted that between the 5 channels in the same group some difference prevails in the single phase pressure drop measured at the same air injection flow rate. This could be due to slight difference in orientation of channels, pipe roughness and also due to pressure fluctuations at ends of channels (which are connected to drum and tank).

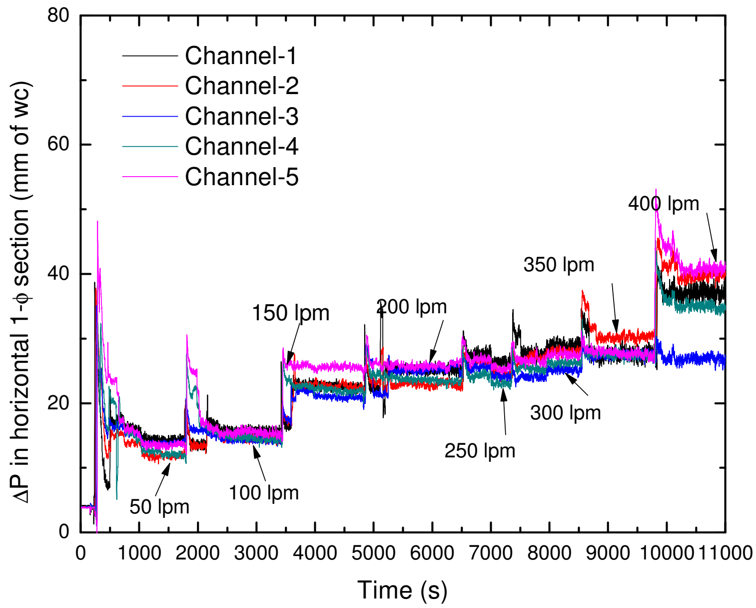

Figure 4.1: Variation of single phase pressure drop for Type-I channels measured during experiment (Initial Drum Level = 650 mm)

Figure 4.2 shows the total pressure drop (gravity and frictional) in two-phase portion of channel 1 to 5 (Type-I) during steady state experiments with initial drum level 650 mm and air injection flow rate from 50 to 400 lpm. The total pressure drop in two-phase portion decreases with an increase in the air injection flow rate, because the hydrostatic head loss decreases as air injection leads to increase in void fraction and two-phase mixture density and hence reduction in total pressure drop.

Figure 4.3 shows the variation of level in air-water drum and water tank. As the air injection flow rate is increased in steps, the level in drum increases and level in tank decreases. The level in drum increases as the two-phase mixture is less dense and occupies more volume. The water inventory is also transported from water tank to drum due to two-phase natural circulation. Law of conservation of mass implies that the water flow rate in down comer shall always be equal to the total water flow rate in channels at steady state. In order to maintain the momentum balance in down comer line (section FG, refer Figure 3.10) the tank level decreases as the total recirculation flow rate increases with an increase in the air injection flow rate. Fluctuations were observed in water tank level and drum which is recorded by level transmitter and also could be visually observed. These perturbations in the level cause perturbation in the pressure drop across the channels and it is also reflected in signal recorded as shown in Figure 4.1 and 4.2. Such high frequency low amplitude flow fluctuations are always present in natural circulation loops. However if these fluctuations do not grow in amplitude with respect to time, the flow is considered to be stable.

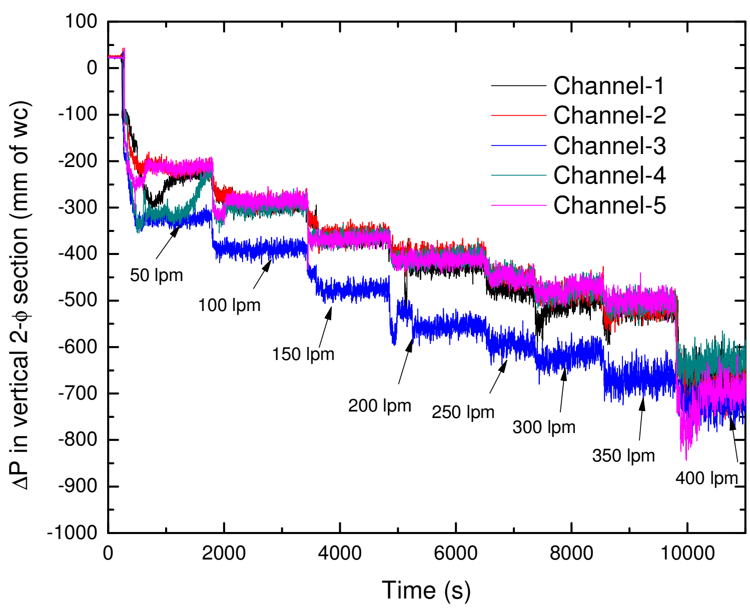

Figure 4.2: Variation of total phase pressure drop in two-phase region for Type-I channels measured during experiment (Initial Drum Level = 650 mm)

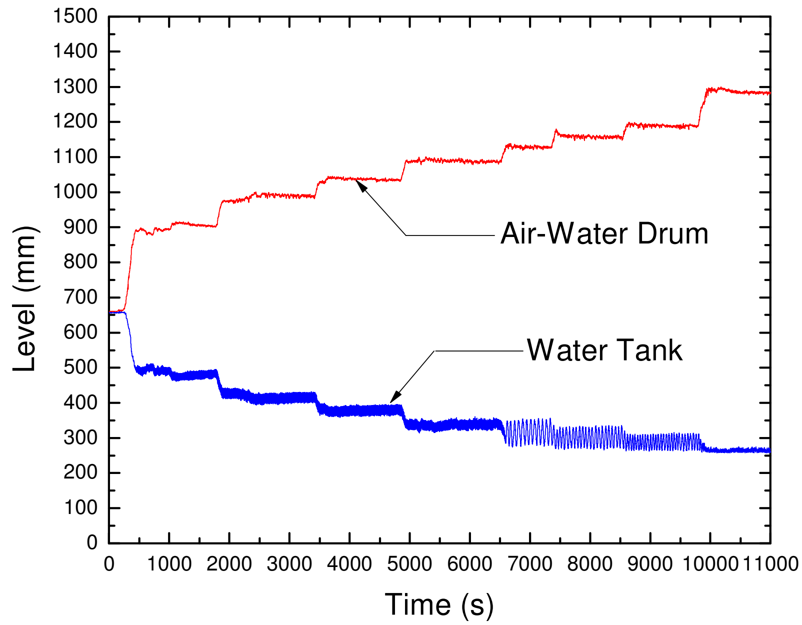

Figure 4.3: Variation of level in Drum and Water tank measured during experiment (Initial Drum Level = 650 mm)

4.2 Uncertainties in measurements:

The experimental measurements are subjected to uncertainties. Uncertainty expresses the doubt about the measurement result. It is different from error where error is the difference between the measurement and true value of parameter. The uncertainty can arise from instrument, the item/parameter being measured, environment, operator and other unknown factors. There are established rules for estimation of uncertainty. The uncertainty can be estimated from statistical analysis of measurements.

4.2.1 Sources of Errors and Uncertainty:

Flaws in the measurement may be visible or invisible. Because real measurements are never made under perfect conditions, errors and uncertainties can come from:

- **The measuring instrument** - instruments can suffer from errors including bias, changes due to ageing, wear, or other kinds of drift, poor readability, noise (for electrical instruments) and many other problems.
- **The item being measured** - which may not be stable? (Imagine trying to measure the size of an ice cube in a warm room.)
- **The measurement process** - the measurement itself may be difficult to make. For example measuring the weight of small but lively animals presents particular difficulties in getting the subjects to co-operate.
- **'Imported' uncertainties** - calibration of your instrument has an uncertainty which is then built into the uncertainty of the measurements you make. (But remember that the uncertainty due to not calibrating would be much worse.)
- **Operator skill** - some measurements depend on the skill and judgment of the operator. One person may be better than another at the delicate work of setting up a measurement, or at reading fine detail by eye. The use of an instrument such as a stopwatch depends on the reaction time of the operator. (But gross mistakes are a different matter and are not to be accounted for as uncertainties.)
- **Sampling issues** - the measurements you make must be properly representative of the process you are trying to assess. If you want to know the temperature at the work-bench, don't measure it with a thermometer placed on the wall near an air conditioning outlet. If you are choosing samples from a production line for measurement, don't always take the first ten made on a Monday morning.
- **The environment** - temperature, air pressure, humidity and many other conditions can affect the measuring instrument or the item being measured.

4.2.2 Estimation of uncertainty:

The uncertainty can be estimated based on statistical parameters such as variance or standard deviation. In most of cases number of repeated measurements of a given quantity under identical conditions is possible from which the standard deviation and standard uncertainty is estimated. This method is called ‘Type A’ or standard calculation. In some cases if such measurements are not possible, the standard deviation can be estimated based on other information. This could be information from past experience of the measurements, from calibration certificates, manufacturer’s specifications, from calculations, from published information, and from common sense. The uncertainty calculated based on this is called ‘Type B’ calculation.

Standard uncertainty-Type ‘A’ calculation

When a set of several repeated readings has been taken (for a Type A estimate), the uncertainty can be expressed in terms of standard deviation as follows:

$$uncertainty = \frac{s}{\sqrt{n}} \tag{4.1}$$

Where Standard Deviation is defined as :

$$s = \sqrt{\frac{\sum_{i=1}^{n}\left(x_i - x_{avg}\right)^2}{n-1}} \tag{4.2}$$

And Arithmetic mean of measurement is defined as:

$$x_{avg} = \frac{\sum_{i=1}^{n} x_i}{n} \tag{4.3}$$

Standard uncertainty-Type 'B' calculation

Sometimes the standard deviation or variance is provided by manufacturer/calibration of handbooks for a given instrument or measurement process. This information can be used to estimate the uncertainty in similar way to type 'A' calculation (equation (4.1)). However many times the accuracy in terms of % of measurement range specified / available for an instrument under consideration. In that case we can expect that a measurement will vary between $x \pm e$. The instrument error band is thus $2e$. The uncertainty then can be calculated as:

$$uncertainty = \frac{(instrument\ error\ bound)/2}{\sqrt{3}} = \frac{e}{\sqrt{3}} \tag{4.4}$$

The purpose of the "Type A" and "Type B" classification is to indicate the two different ways of evaluating uncertainty components and is for convenience of discussion only; the classification is not meant to indicate that there is any difference in the nature of the components resulting from the two types of evaluation. Both types of evaluation are based on probability distributions, and the uncertainty components resulting from either type are quantified by variances or standard deviations.

"Type A" standard uncertainty is obtained from a probability density function derived from an observed frequency distribution, while a Type B standard uncertainty is obtained from an assumed probability density function based on the degree of belief that an event will occur (often called subjective probability). Both approaches employ recognized interpretations of probability.

The accuracy and uncertainty for standard instruments of measurements such as level transmitter, rotameters can be estimated with “Type-B” calculation. The swell level and water recirculation flow rate measurement uncertainty can be estimated using “Type-A” calculation. The results of uncertainty calculation for measuring techniques/ instruments are indicated in Table-4.1. and Table 4.2, and Table 4.3

The swell level by visual observation is difficult due to the reason that the interface is always oscillating due to free surface turbulence. Operator however observes the minima and maxima of such oscillations and records the mean value. However, over the repeated readings there is uncertainty due to human factor. The water recirculation flow rate is estimated from single phase pressure drop and a calibration curve obtained in laboratory. The steady state experiments in AWL were repeated for same initial conditions of water level in AWL drum and same air injection flow rates. The measurements of water flow rate and pressure drop in two-phase portion are then analyzed to obtain standards deviation and uncertainty is calculated as per eq. (4.1). The values estimated are shown in Table 4.2 and 4.3.

As seen from table 4.2 uncertainty at lower air injection rate as high as 5 lpm otherwise it is smaller than 2 lpm. The flow rates measured during experiments are in the range of 30 to 100 lpm. The uncertainty thus in some instances is about 10% of measured value. The single phase pressure drop was having range of 2 mm to 25 mm of water column i.e. 20 to 250 pa. Such low pressure drops was difficult to measure accurately with available instruments. Thus instrument accuracy might have played a role in these large values of uncertainty.

For two phase pressure drop measurements the maximum uncertainty is about 100 pa while during experiments the measurements vary from 5000 to 9000 pa. Compared to range of measured values the uncertainties are small and acceptable to be a reasonably accurate measurement.

Table 4.1: Accuracy and uncertainty of Instruments and measurement techniques

Measurement	Instrument	Range of measurement	Accuracy	Uncertainty
Air flow rate	Rotameter	0-400 lpm	±6 lpm	3.46 lpm (Type-B)
Drum and tank level	Level Transmitter	0-2 m	± 5 mm	2.88 mm (Type-B)
Swell level	Visual observation	0-2 m	± 30 mm	20 mm (Type-A)

Table 4.2: Uncertainty calculation for AWL- Natural Circulation Flow rate

	50 lpm	100 lpm	150 lpm	200 lpm	250 lpm	300 lpm
1	4.34	2.33	1.94	0.87	0.85	0.82
2	1.75	1.22	0.62	0.77	0.35	0.73
3	2.20	1.81	2.22	1.56	1.70	1.81
4	5.55	2.04	0.65	1.76	1.56	1.48
5	4.02	1.18	1.30	0.71	1.41	1.08
6	1.43	1.22	1.25	1.07	1.15	1.11
7	2.31	1.31	1.38	0.92	1.50	1.95
8	3.49	1.35	0.60	1.09	1.21	1.31
9	0.91	0.89	0.75	0.93	0.50	0.80
10	0.72	0.82	1.15	0.54	0.51	1.07
11	1.56	1.91	2.09	2.54	2.10	2.66
12	3.44	2.32	1.77	2.77	2.12	2.28
13	2.26	2.48	1.46	1.23	1.58	2.07
14	2.47	1.69	2.03	1.75	2.01	1.59
15	2.86	2.17	1.68	1.71	2.51	2.32

Table 4.3: Uncertainty calculation for AWL- Two-Phase Pressure Drop (Pa)

	50 lpm	100 lpm	150 lpm	200 lpm	250 lpm	300 lpm
1	99.34	77.50	86.34	70.40	71.58	38.17
2	58.67	77.14	55.83	67.32	68.66	72.19
3	42.41	32.69	11.15	39.92	55.46	11.59
4	62.76	46.06	28.45	32.05	23.50	41.13

5	62.38	49.51	48.51	50.10	41.06	42.50
6	41.36	27.69	55.91	32.60	39.67	82.31
7	42.76	25.32	80.88	98.99	37.25	52.13
8	66.43	38.56	81.23	46.34	41.59	53.99
9	43.31	25.71	36.46	43.26	48.23	80.01
10	40.18	39.52	29.65	27.06	57.48	90.89
11	63.20	34.27	14.75	12.70	23.75	19.16
12	52.91	27.53	10.36	39.28	11.31	24.63
13	35.42	29.70	9.18	17.61	21.78	33.63
14	22.51	11.27	17.45	14.01	18.73	16.04
15	54.67	58.94	48.37	55.76	54.95	61.49

4.3 Numerical analysis of steady state data

Figure 3.10 shows the simplified flow diagram of AWL with one tailpipe. Air-water drum and water tank are connected to each other via tailpipe (point A to E) and a down comer (point F to G). There are 15 tailpipe connections from water tank to air-water drum, arranged in 3 groups of 5 identical tailpipes. A single down comer connection is provided from air-water drum to water tank. For explaining the code formulation single tailpipe is shown in the schematic representation.

Consider momentum balance from point 'A' to 'E'. We can write as follows:

$$P_E - P_A = \rho_l g L_{AB} - \rho_l g L_{CD} - \rho_{2\phi} g L_{DE} - \int_A^D \Delta P_{1\emptyset} - \int_D^E \Delta P_{2\emptyset} - \sum_A^D K_L \frac{\rho_l v_l^2}{2} - \sum_D^E K \frac{\rho_l v_l^2}{2} \varphi \tag{4.5}$$

Upon rearranging,

$$P_E - P_A = (\rho_l - \rho_{2\phi}) g L_{DE} - \int_A^D \Delta P_{1\emptyset} - \int_D^E \Delta P_{2\emptyset} - \sum_A^D K_L \frac{\rho_l v_L^2}{2} - \sum_D^E K_L \frac{\rho_l v_l^2}{2} \varphi \tag{4.6}$$

The two phase density can be written as:

$$\rho_{2\phi} = \varepsilon_g \rho_g + (1 - \varepsilon_g) \rho_l \tag{4.7}$$

The void fraction ε_g is very significant parameter in the description of two-phase flows. Various correlations exist for the estimation of void fraction in two-phase flows. Simplest model is based on homogeneous flow assumption. However, in practical case the velocities of individual phases are not equal due to action of gravity and friction at the interface of the phases. In vertical/upward two-phase flows the lighter phase moves with higher velocity than the heavier phase, and there is slip between the two phases. If such slip between the two phases is accounted then the void fraction is given as:

$$\alpha = \frac{1}{1 + \psi \frac{(1-\chi)}{\chi} \frac{\rho_g}{\rho_l}} \tag{4.8}$$

The parameter slip ratio S contains effects of geometries, orientation etc. and is not deterministic. The slip ratio is therefore empirically found out by undertaking a large number of experiments. The non-homogenous nature of two-phase flow is treated in Drift flux model approach by considering the superficial velocities, distribution parameter and drift velocity. The void fraction based on drift flux model is given as:

$$\varepsilon_g = \frac{J_g}{C_0(J_g + J_l) + U_{gl}} \tag{4.9}$$

The distribution parameter C_0 and drift velocity U_{gl} are found empirically from a large number of experimental observations. In the view of availability of different approaches and number of correlations existing for describing void fraction, choice of suitable correlation is crucial. Several studies on assessment of void fraction correlations against available experimental data are available in literature which include Vijayan et. al. [56, 57], Coddington et. al. [58], Woldesemayat et. al. [59] and Ghajar et. al. [60]. Vijayan et. al [56, 57] carried out assessment of 34 void fraction correlations against experimental database from literature and showed that Chexal-Lellouche [54] and Chexal [61] produced consistently relatively accurate predictions for natural circulation flows even with different orientation of pipe. Coddington et al. [58] reviewed 13 different correlation and recommended use of Chexal [61] correlation. Coddington et al. [57] also suggested the use of correlations by Bestion [62] and Dix [63] which performed very well without using iterative procedure like Chexal [61]. Woldesemayat et al. [59] have reviewed 68 void fraction correlations against 2845 experimental data from literature and produced best performing correlation with modification in correlation by Dix [63]. Recently Ghajar et. al. [60] reviewed 11 correlations based on slip ratio based and drift flux model and recommended correlations by Bhagwat and Ghajar [64] for low values of void fraction (bubbly flow regimes).

In the present study, some of the void fraction correlations as suggested in earlier work [56-60], are used for predicting the experimental results. Table 4.4 summarizes the void fraction correlations used in the present study.

Table 4.4: Void fraction correlations used in the code

Model/ Author	Correlation
Homogene-ous flow model	$\varepsilon_g = \dfrac{1}{1 + \dfrac{(1-\chi)}{\chi}\dfrac{\rho_g}{\rho_l}}$
Lockhart and Martinelli [65]	$\varepsilon_g = \dfrac{1}{1 + 0.28\left(\dfrac{1-\chi}{\chi}\right)^{0.64}\left(\dfrac{\rho_g}{\rho_l}\right)^{0.36}\left(\dfrac{\mu_l}{\mu_g}\right)}$
Chishlom [66]	$\varepsilon_g = \dfrac{1}{1 + \left[\sqrt{1-\chi\left(1-\dfrac{\rho_l}{\rho_g}\right)}\right]\dfrac{(1-\chi)}{\chi}\dfrac{\rho_g}{\rho_l}}$
Spedding and Chen [67]	$\varepsilon_g = \dfrac{1}{1 + 2.22\left(\dfrac{1-\chi}{\chi}\right)^{0.65}\left(\dfrac{\rho_g}{\rho_l}\right)^{0.65}}$
Smith [68]	$\varepsilon_g = \dfrac{1}{1 + \left[0.4 + 0.6\sqrt{\dfrac{\dfrac{\rho_l}{\rho_g} + 0.4\left(\dfrac{(1-\chi)}{\chi}\right)}{1 + 0.4\left(\dfrac{(1-\chi)}{\chi}\right)}}\right]\dfrac{(1-\chi)}{\chi}\dfrac{\rho_g}{\rho_l}}$
Thom [69]	$\varepsilon_g = \dfrac{1}{1 + \left(\dfrac{1-\chi}{\chi}\right)\left(\dfrac{\rho_g}{\rho_l}\right)^{0.89}\left(\dfrac{\mu_l}{\mu_g}\right)^{0.18}}$

Zivi [70]	$\varepsilon_g = \dfrac{1}{1+\left(\dfrac{1-\chi}{\chi}\right)\left(\dfrac{\rho_g}{\rho_l}\right)^{0.67}}$
Baroczy [71]	$\varepsilon_g = \dfrac{1}{1+\left(\dfrac{1-\chi}{\chi}\right)^{0.74}\left(\dfrac{\rho_g}{\rho_l}\right)^{0.65}\left(\dfrac{\mu_l}{\mu_g}\right)^{0.1}}$
Awad and Muzychka [72]	$\varepsilon_g = C_1 + C_2$ $C_1 = \dfrac{1}{2}\left\{\dfrac{1}{1+\left[\left(\dfrac{1-\chi}{\chi}\right)^{0.875}\left(\dfrac{\rho_g}{\rho_l}\right)^{0.65}\left(\dfrac{\mu_l}{\mu_g}\right)^{0.13}\right]^{16/19}}\right\}$ $C_{2=}\dfrac{1}{2}\left\{\dfrac{1}{1+0.28\left[\left(\dfrac{1-\chi}{\chi}\right)^{0.875}\left(\dfrac{\rho_g}{\rho_l}\right)^{0.5}\left(\dfrac{\mu_l}{\mu_g}\right)^{0.125}\right]^{0.71}}\right\}$
Zuber and Findlay [73]	$\varepsilon_g = \dfrac{J_g}{C_0(J_g+J_l)+U_{gl}}, C_0 = 1.13, U_{gl} = 1.41\left(\dfrac{\sigma g\left(\rho_l-\rho_g\right)}{\rho_l^2}\right)^{1/4}$
Rouhani and Axelsson [74]	$\varepsilon_g = \dfrac{J_g}{C_0(J_g+J_l)+U_{gl}}, C_0 = 1.+0.2(1-\chi)\left(\dfrac{gD\rho_l^2}{G^2}\right)$

	$U_{gl} = 1.18\left(\frac{\sigma g(\rho_l - \rho_g)}{\rho_l^2}\right)^{1/4}$
Gomez et. al. [75]	$\varepsilon_g = \frac{J_g}{C_0(J_g + J_l) + U_{gl}}, C_0 = 1.15,$ $U_{GL} = 1.53\left(\frac{\sigma g(\rho_l - \rho_g)}{\rho_l^2}\right)^{1/4}(1 - \varepsilon_g)$
Hibiki and Ishii [76]	$\varepsilon_g = \frac{J_g}{C_0(J_g + J_l) + U_{gl}}, C_0 = 1.2 - 0.2\sqrt{\frac{\rho_g}{\rho_l}}$ $U_{gl} = 1.41\left(\frac{\sigma g(\rho_l - \rho_g)}{\rho_l^2}\right)^{1/4}(1 - \varepsilon_g)^{1.75}$
Chexal-Lellouche [54]	$\varepsilon_g = \frac{J_g}{C_0(J_g + J_l) + U_{gl}}, \quad C_0 = \frac{L}{K_0 + (1 - K_0)\varepsilon_g{}^r}$ $U_{gl} = 1.41\left(\frac{\sigma g(\rho_l - \rho_g)}{\rho_l^2}\right)^{1/4} c_2 c_3 c_4 c_9$ $L = \frac{1 - e^{-c_1\varepsilon_g}}{1 - e^{-c_1}}, c_1 = \frac{4P_{crit}^2}{P(P_{crit} - P)}, K_0 = B_1 + (1 - B_1)\left(\frac{\rho_g}{\rho_l}\right)^{\frac{1}{4}}$ $B_1 = min\left[0.8, \frac{1}{1+e^{(-Re/60000)}}\right], Re = max[Re_l, Re_g],\ r = \frac{1+1.57\frac{\rho_g}{\rho_l}}{1-B_1}$ $c_2 = 0.4757\left[ln\left(\frac{\rho_l}{\rho_g}\right)\right]^{0.7} if\ \frac{\rho_l}{\rho_g} \leq 18.0,$ $c_2 = 1.0 \quad if\ \frac{\rho_l}{\rho_g} > 18.0\ \&\ c_5 \geq 1$

	$$c_2 = \left(1 - e^{\left(\frac{-c_5}{1-c_5}\right)}\right)^{-1} \; if \, \frac{\rho_l}{\rho_g} > 18.0 \;\&\; c_5 < 1$$ $$c_3 = max\left[0.5, 2e^{\left(-Re_l/_{60000}\right)}\right], c_4 = 1.0 \; if \; c_7 \geq 1,$$ $$c_4 = \left(1 - e^{\left(\frac{-c_7}{1-c_7}\right)}\right)^{-1} if \, c_7 < 1 \;, c_5 = \sqrt{150\left(\frac{\rho_g}{\rho_l}\right)} \;, c_7 = \left(\frac{0.09144}{D}\right)^{0.6}$$ $$c_9 = \left(1 - \varepsilon_g\right)^{B_1}$$
Dix [63]	$$\varepsilon_g = \frac{J_g}{C_0(J_g + J_l) + U_{gl}}\,, \qquad C_0 = \left(\frac{J_g}{J_g + J_l}\right)\left[1 + \left(\frac{J_g + J_l}{J_g} - 1\right)\right]^{\left(\frac{\rho_l}{\rho_g}\right)^{0.1}}$$ $$U_{gl} = 2.9\left(\frac{\sigma g\left(\rho_l - \rho_g\right)}{\rho_l^2}\right)^{1/4}$$

The single phase frictional pressure drop can be calculated as follows:

$$\Delta P_{1\emptyset} = \frac{fL\rho_l v_l^2}{2D} \tag{4.10}$$

Blasius [77] has given a correlation for the estimation of friction factor in smooth pipes for laminar and turbulent flows. However, Blasius [77] does not provide friction factor in a transition flow region (i.e. between laminar and turbulent flow). Another limitation of this correlation is that it does not take into account the roughness of internal surface of pipe. Colebrook [78] has provided correlation to calculate the friction factor in rough pipes as:

$$\frac{1}{\sqrt{f}} = -2log_{10}\left(\frac{\epsilon}{3.7D} + \frac{2.51}{Re\sqrt{f}}\right) \tag{4.11}$$

For $Re \geq 4000$

Colebrook [78] does not provide the friction factor for laminar and transition flow regions. Also the correlation for friction factor is implicit which requires iterative procedure which not so convenient. Hence, in the present work, correlation developed by Churchill [79] is used which provides smooth transition between laminar and turbulent flow regime and also accounts for the pipe roughness. The friction factor by Churchill [79] is gives as:

$$f = 8\left[\left(\frac{8}{Re}\right)^{12} + \frac{1}{(A+B)^{1.5}}\right]^{\left(\frac{1}{12}\right)} \tag{4.12}$$

$$A = \left\{2.457ln\left[\frac{1}{\left(\frac{7}{Re}\right)^{0.9} + \left(\frac{0.27\epsilon}{D}\right)}\right]\right\}^{16} \tag{4.13}$$

$$B = \left(\frac{37530}{Re}\right)^{16} \tag{4.14}$$

There are number of correlations proposed for the estimation of two-phase frictional pressure drop. Fang et al. [80] have reviewed 29 different correlations and compared with 3480 experimental data points from the open literature, with the experimental range of hydraulic diameters from 0.0695 to 14 mm, and mass flux from 8 to 6000 kg/m^2. They concluded that Muller-Steinhagen and Heck [81] based on separated flow model and homogeneous model by McAdams [82] performed best over the entire experimental database and recommended them for pressure drop calculations in two-phase flow. In present study frictional pressure drop is estimated from Muller-Steinhagen and Heck [81] and also with homogeneous model by MaAdams [82].

In Homogeneous model the two-phase friction pressure drop is calculated using the same procedure as that of single-phase frictional pressure drop, by replacing the single-phase flow properties by averaged properties of both phases.

$$\Delta P_{2\emptyset} = \frac{f_{2\emptyset} G_{2\emptyset}^2 L}{2D\rho_{2\emptyset}} \tag{4.15}$$

The two phase friction factor is calculated from Churchill [79], replacing the single phase Reynolds number by mixture Reynolds number $Re_{mixture}$ and it is given as:

$$Re_{mixture} = \frac{G_{2\emptyset} D}{\mu_{2\emptyset}} \tag{4.16}$$

Where the void fraction and two phase viscosity is estimated as below:

$$\varepsilon_g = \frac{\chi}{\rho_g} + \frac{(1-\chi)}{\rho_l} \tag{4.17}$$

$$\frac{1}{\mu_{2\phi}} = \frac{\chi}{\mu_g} + \frac{(1-\chi)}{\mu_l} \tag{4.18}$$

The local loss coefficient due to sudden expansion and contraction can be estimated as follows:

$$(K_L)_{expansion} = \left(1 - \frac{A_1}{A_2}\right)^2 \tag{4.19}$$

$$(K_L)_{contraction} = 0.5\left(1 - \frac{A_1}{A_2}\right)^{3/4} \tag{4.20}$$

Two phase local loss coefficient is calculated same as that for single phase loss coefficient, in addition a multiplier is added in the term to account for inter-phase friction as given as:

$$\psi = 1 + \chi\left(\frac{\rho_l}{\rho_g} - 1\right) \tag{4.21}$$

Two-phase pressure drop based on Muller-Steinhagen and Heck [81] is calculated in terms of frictional pressure drop of individual phases and flow quality as follows:

$$\left(\frac{dP}{dL}\right)_{2\emptyset} = \frac{\Delta P_{2\emptyset}}{L} = \left(G^{'}(1-\chi)^{\frac{1}{3}}\right) + (B^{'}\chi^3) \tag{4.22}$$

Where

$$G' = A' + 2(B' - A')\,\chi \tag{4.23}$$

$$A' = \left(\frac{dP}{dL}\right)_l = \frac{f_l \rho_l v_l^2}{2D} \tag{4.24}$$

$$B' = \left(\frac{dP}{dL}\right)_g = \frac{f_g \rho_g v_g^2}{2D} \tag{4.25}$$

And

$$f_l = \frac{64}{Re_l} \quad if\ Re_l \leq 1187 \tag{4.26}$$

$$f_g = \frac{64}{Re_g} \quad if\ Re_g \leq 1187 \tag{4.27}$$

$$f_l = \frac{0.3164}{(Re_l)^{1/4}} \quad if\ Re_l > 1187 \tag{4.28}$$

$$f_g = \frac{0.3164}{\left(Re_g\right)^{1/4}} \quad if\ Re_g > 1187 \tag{4.29}$$

A computer code has been developed in C++ programming language to solve Eqn. (4.5) using Eqn. (4.6) to (4.29) iteratively for all the tailpipe channels. Subroutines were written for the various void fraction correlations used. Figure 4.4 shows the algorithm used for the analysis of steady state experimental data. For estimation of steady state parameters, geometry for each channel in Type-I, II and III and air injection flow rate is read initially. Water recirculation is assumed for iteration. With assumed water velocity single phase frictional drop in feeder portion, void fraction in tail pipe and two-phase pressure drop is estimated. The driving force due to buoyancy is calculated. Iterations are continued till the driving force matches with resistive force of pressure drop, which gives the estimated steady state flow and other parameters such as pressure drop and void fraction in tail pipe.

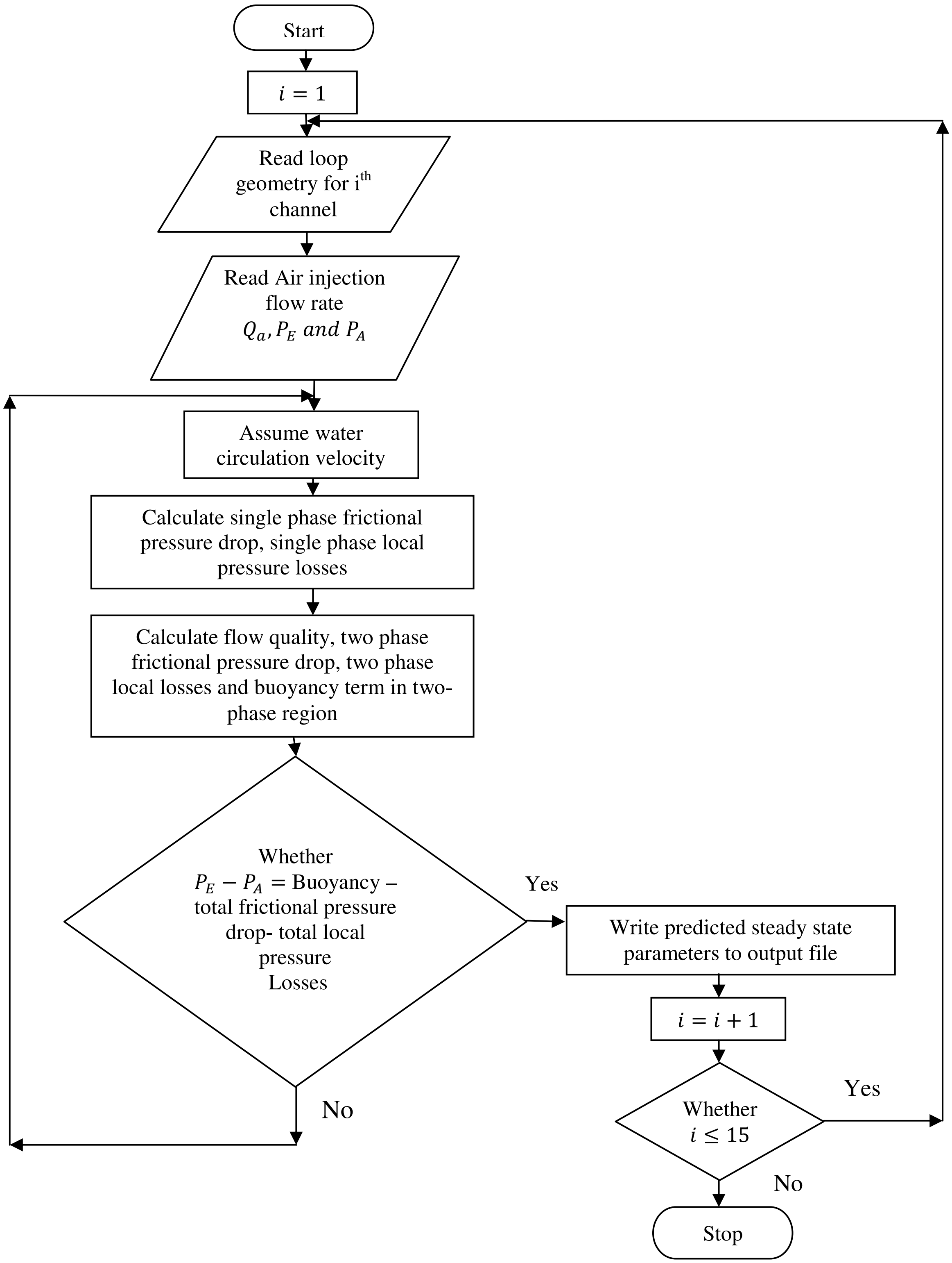

Figure 4.4: Flow chart for prediction of steady state parameters

4.4 Results and discussion on numerical analysis

Steady state water recirculation flow rate in each channel is calculated using the in-house code developed on the methodology explained in previous section. Combination of different void fraction correlations and pressure drop correlations were used. The flow rate and the pressure drop predictions then were analyzed using statistical parameters i.e. error e_i, mean error e_m, absolute mean error e_{ma} , RMS error e_{rms} and standard deviation σ. It was found that use of Muller Steinhagen and Heck correlation [81] for pressure drop calculation over the homogeneous model by McAdams [82] did not produce significant improvement in calculated steady state flow rate. However, the choice of void fraction model affects the predictions significantly, which is more obvious as the void fraction governs the driving buoyancy force. The comparison is shown in Tables 4.5 and 4.6 for two pressure drop models and 15 void fraction correlations described in Table 4.4. From the statistical analysis it is the Thom [69] correlation performs better than the other correlations. The next lowest statistical parameters predicted are by the Baroczy [71] and followed by Zivi [70]. These top three correlations are slip ratio based models. The drift flux based models have not performed well in the present study. The mean error in the predictions of flow rate is less than 30%. The mean error in pressure drop prediction is also low (< 10%).

Figure 4.5 and 4.6 shows the comparison of predicted circulation flow rates and the pressure drop (in two-phase region) with all the experimental results using Thom [69] correlation for the void fraction and Muller Steinhagen Heck [81] for two-phase pressure drop. It has been estimated that for prediction of recirculation flow rate, about 85% predictions are within 30 % of the experimental measurements. In case of the two-phase pressure drop the predictions are within +10 to -15 % of the measured values. The two-phase pressure drop has two components i.e. gravity head loss, which has strong dependence on void fraction, and frictional pressure drop (which includes inter-phase and wall friction). It was found during calculations that the skin friction pressure drop component in total two-phase pressure drop is significantly smaller compared to gravity head loss term. Hence a proper choice of void fraction correlation will also lead to correct prediction of two-phase pressure drop.

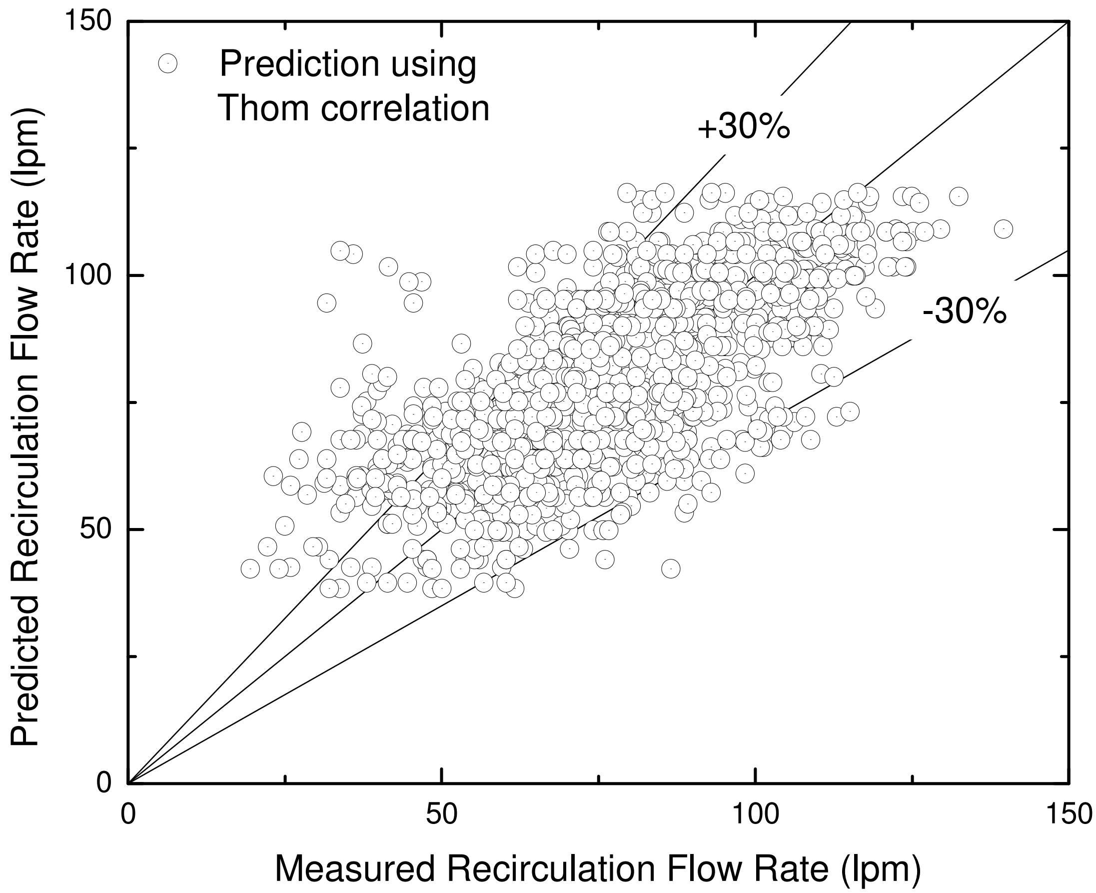

Figure 4.5: Comparison of predicted recirculation flow rate for water (Thom [69] correlation void fraction and Muller Steinhegan Heck [81] for two-phase pressure drop) against experimental measurements for complete database (Type-I, II and III channels, all experiments).

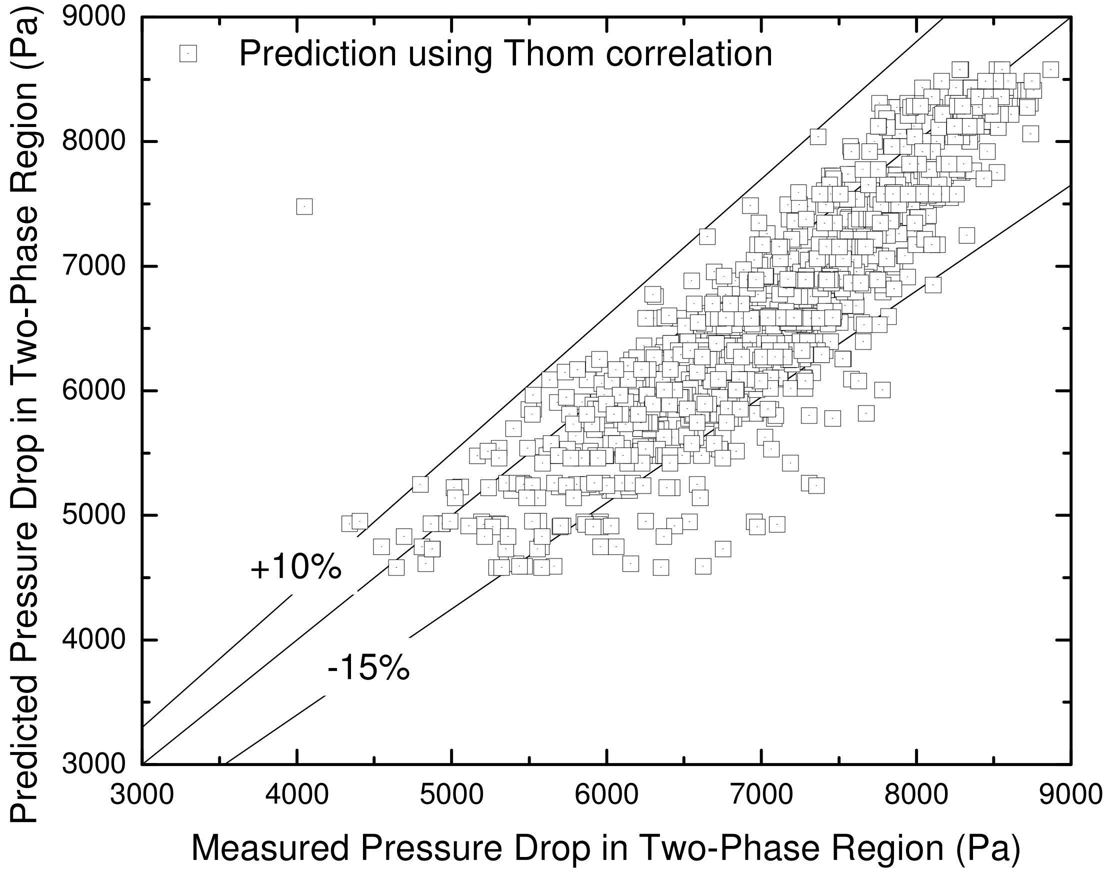

Figure 4.6: Comparison of predicted two-phase pressure drop (Thom [69] correlation void fraction and Muller Steinhegan Heck [81] for two-phase pressure drop) against experimental measurements for complete database (Type-I, II and III channels, all experiments).

Figure 4.7 (a), 4.7 (b) and 4.7 (c) show the comparison between the predicted and the measured water recirculation flow rates for channels in Type-I, II and III, respectively. Figure 4.8 (a), 4.8 (b) and 4.8 (c) show comparison between predicted and total two-phase pressure drop (gravitational head combined with friction pressure drop) measured across section D'E' (refer Figure 3.10) respectively for Type-I, II and III channels. Void fraction correlation by Baroczy [71] and homogeneous model [82] for pressure drop is used for predicted variation shown in these Figures. The predictions follow the similar trend as measured in experiments. The predictions for Type-I are slightly lower than measurements but this is for the particular experiment while Type-II and III predictions follow measurements nicely, however there is spread of experimental data around the prediction. Several experiments were performed with different initial levels in drum. The prediction trends were sometimes following the data nicely and sometimes over predicting or under predicting. There is no definite pattern followed by predictions.

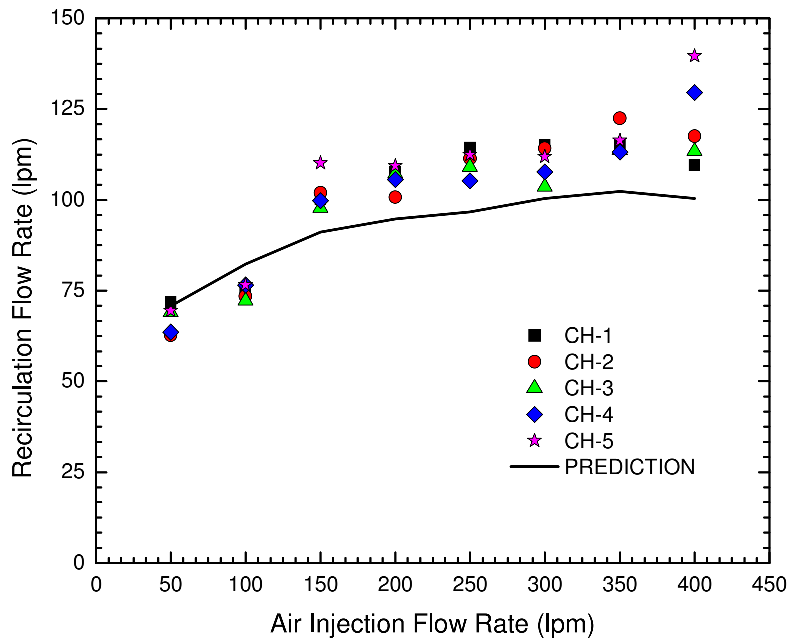

Figure 4.7 (a): Prediction of water recirculation flow rate for Type-I channels (Initial Drum Level = 900 mm)

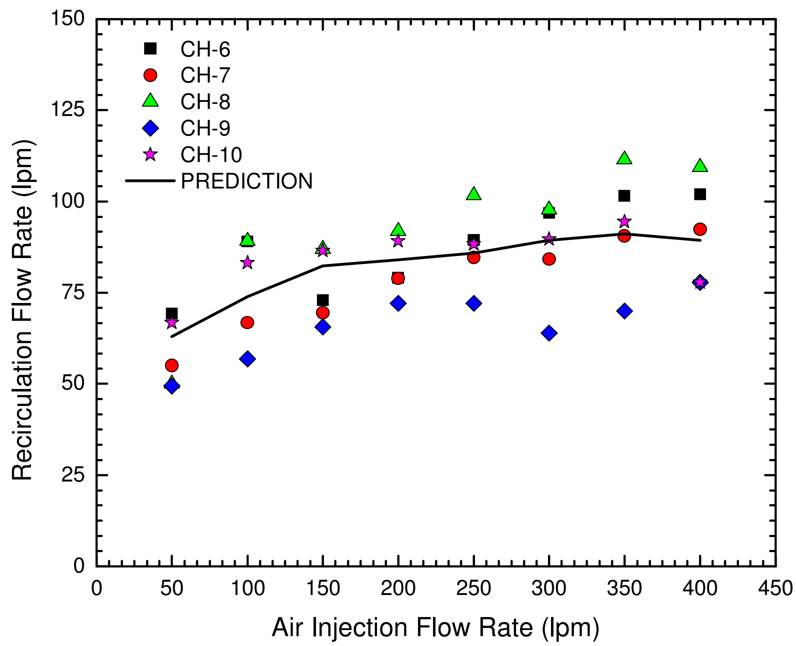

Figure 4.7 (b): Prediction of water recirculation flow rate for Type-II channels (Initial Drum Level = 900 mm)

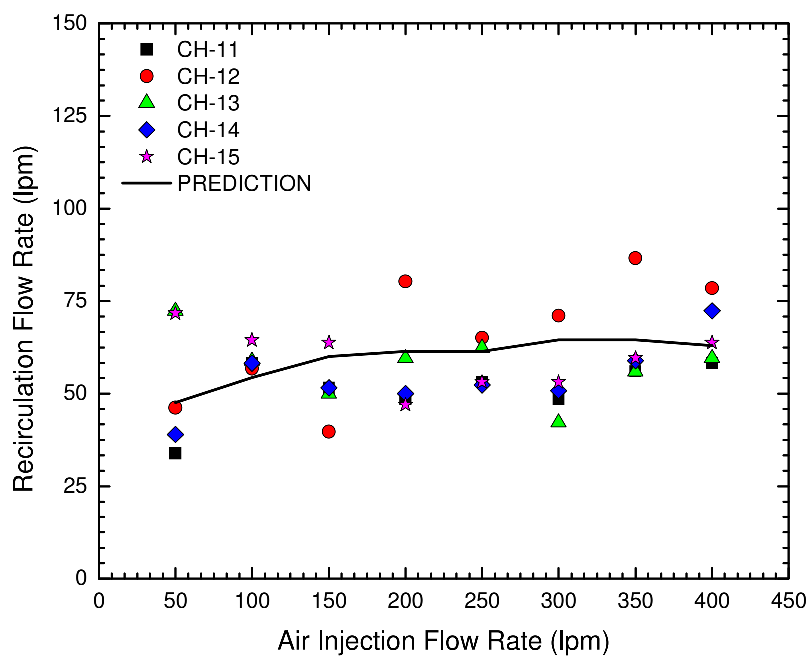

Figure 4.7 (c): Prediction of water recirculation flow rate for Type-III channels (Initial Drum Level = 900 mm)

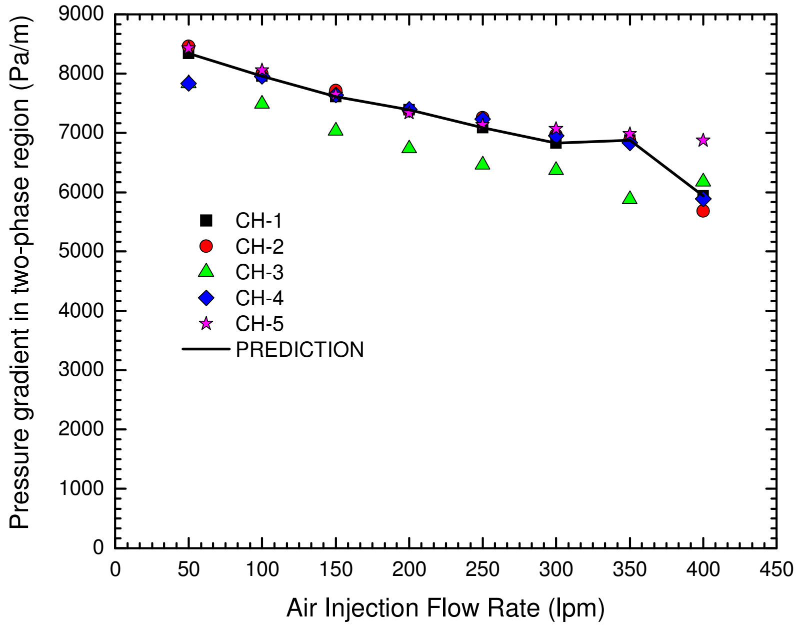

Figure 4.8 (a): Prediction of gradient of total pressure drop in two-phase leg for Type-I channels

(Initial Drum Level = 900 mm)

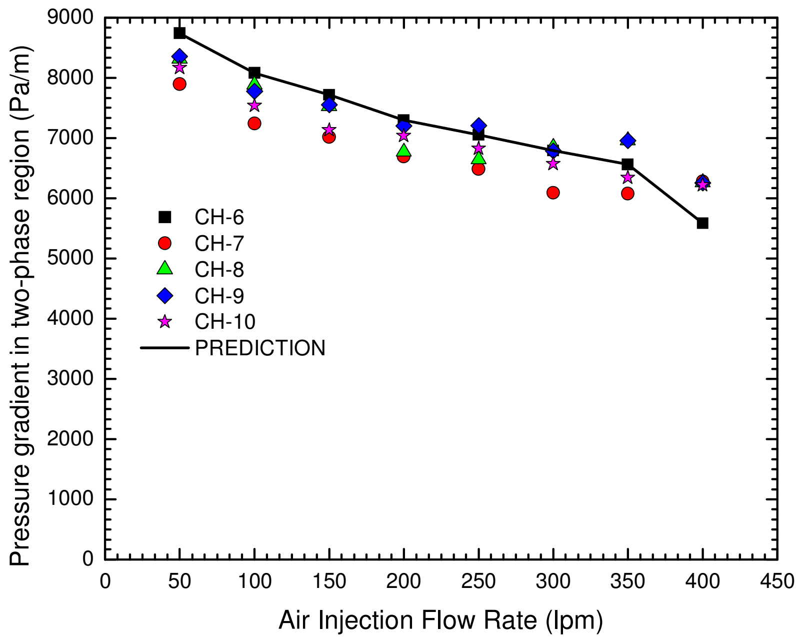

Figure 4.8 (b): Prediction of gradient of total pressure drop in two-phase leg for Type-II channels

(Initial Drum Level = 900 mm)

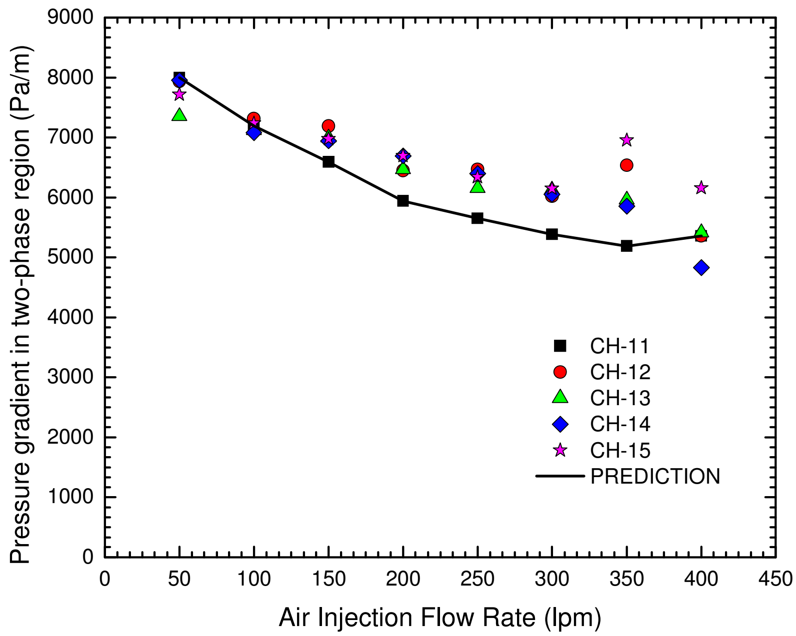

Figure 4.8 (c): Prediction of gradient of total pressure drop in two-phase leg for Type-III channels (Initial Drum Level = 900 mm)

It can be also seen from the 4.7 (a), (b) & (c) that the model predictions for the channels (shown by the solid line) are the same in a given category. This is because in the mathematical model, all the geometrical parameters and the end conditions for the pressure drop across channel are the same. However the experimentally measured values for individual channels differ from each other. The experimental data was carefully scrutinized in order to identify any pattern in measured values which indicate systematic error in measurements for individual channels. It was found that the measured values for the channels show random variation. The measurement of experimental data on recirculation flow rate was affected by some known factors and some unknown factors. While calibrating pressure drop measurement to estimate flow rate, we are aware that the calibration instrument (ultrasonic flow meter) itself has ±3% error. Also all pipe used for construction may not necessarily have same surface roughness and also their deviation from being perfectly horizontal plays role in error/spread of data. Instrument accuracies are known. Pressure drop transmitters have accuracy of ±0.1% of full scale (-100 to +100 mm of water column). The air flow rotameters were calibrated by manufacturer and have accuracy of ±1% of full scale (0-500 lpm). While carrying out the experiment, operator has to set the air flow rate in each channel by visually observing the position of float of rotameters. This can also introduce some amount of human error in spite of utmost care taken by trained operator personnel. When the data is compared with prediction the spread/deviation from prediction indicates the uncertainty of measurement which is accumulated effect all above errors.

Figure 4.9 shows the variation of superficial velocity of water with respect to superficial velocity of air/vapor phase for prototype and experimental measurements in model. As discussed earlier (and evident from Figure 4.7(a) to (c)) the three types of channel produce different flow rates, however the average water & air flow rate into the drum needs to satisfy the criteria of maintaining similar trends of superficial velocities between model and prototype. Figure 4.9 shows that this criterion is very well satisfied. The average flows are as expected from pre-test lumped channel analysis. The deviation between model and prototype is the distortion which is accepted.

Figure 4.10 shows the variation of void fraction in tail pipes with respect to air/vapor superficial velocities for prototype and model. The void fraction is not measured in model, but predicted with correlation given by Thom [69], which was found best suitable correlation from assessment on two-phase natural circulation flow rates and two-phase pressure drop data measured experimentally. Void fraction predicted for all 15 channels is shown in the Figure 4.10. It can be concluded that void fraction simulated in model is close to the prototype. These comparisons (Figure 4.9 & Figure 4.10) have confirmed the adequacy of scaling for two-phase natural circulation for AWL satisfying the design objective.

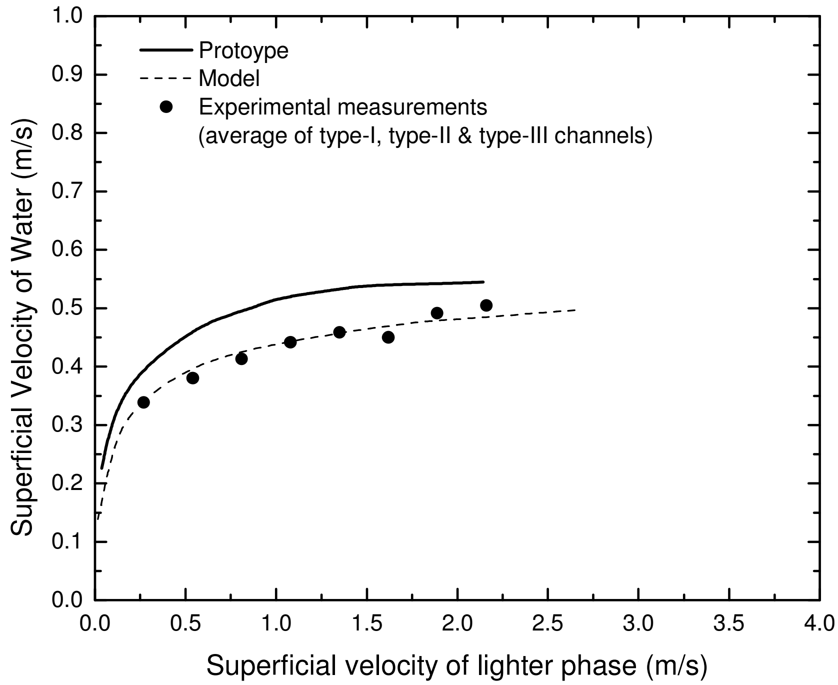

Figure 4.9: Comparison of superficial velocity of water for AWL and for prototype.

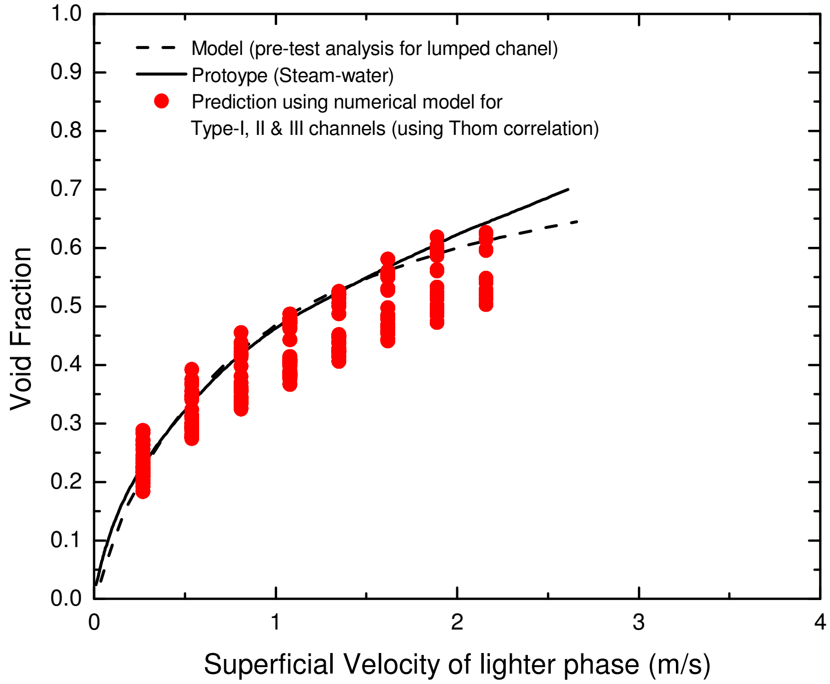

Figure 4.10: Comparison of tail pipe void fraction for AWL and for prototype.

Table 4.5: Comparison of various correlations for prediction of experimental data – (Muller Steinhegan Heck model [81]for pressure drop)

Correlation	Flow Rate				Pressure Drop			
	e_{ma}	e_{mean}	e_{rms}	s	e_{ma}	e_{mean}	e_{rms}	s
Thom [69]	19.87	8.4	29.28	8.32	7.2	-6.3	9.31	6.24
Baroczy [71]	25.09	17.97	37.73	17.8	8.05	-7.45	9.78	7.38
Zivi [70]	33.84	-31.79	36.4	31.49	3.93	0.19	5.55	0.197
LockHart Martinelli [65]	34.63	30.82	49.56	30.53	10.05	-9.71	11.48	9.61
Spedding and Chen [67]	39.56	37.06	54.78	36.71	11.26	-11.01	12.61	10.9
Rouhani and Alexssan [74]	45.3	-25.75	48.58	25.52	5.59	-0.38	8.61	0.38
Chexal Lellouche [54]	52.07	50.91	64.88	50.42	15.37	-15.21	17.08	15.06
Dix [63]	53.32	51.79	67.28	51.3	15.13	-14.96	16.53	14.82
Awad and Muzychka [72]	58.65	-58.24	60.01	57.7	4.51	3.22	6.62	3.19
Zuber and Findley [73]	64.32	64.04	77.43	63.42	18.45	-18.32	19.99	18.15
Gomez et. al. [75]	65.17	64.95	78.25	64.32	18.69	-18.57	20.25	18.39
Smith [68]	66.7	66.47	81.54	65.83	18.21	-18.11	19.28	17.94
Hibiki and Ishii [76]	67.72	67.59	81.02	66.91	19.21	-19.09	20.66	18.91
Chislom [66]	71.89	71.76	86.7	71.07	19.58	-19.48	20.62	19.29
Homogeneous model	98.81	98.81	112.33	97.86	28.07	-27.99	29.54	27.73

Table 4.6: Comparison of various correlations for prediction of experimental data – (Homogeneous model [82] for pressure drop)

Correlation	Flow Rate				Pressure Drop			
	e_{ma}	e_{mean}	e_{rms}	s	e_{ma}	e_{mean}	e_{rms}	s
Thom [69]	21.02	10.9	31.11	10.8	7.65	-6.81	9.8	6.74
Baroczy [71]	26.01	20.54	38.79	20.35	8.57	-8.09	10.36	8.01
Zivi [70]	31.69	-29.35	34.8	29.07	4.29	-0.22	7.06	0.23
LockHart Martinelli [65]	35.32	32.37	49.87	32.06	10.45	-10.17	11.96	10.07
Spedding and Chen [67]	39.98	38.02	54.72	37.66	11.58	-11.37	13.01	11.26
Rouhani and Alexssan [74]	45.28	-7.87	50.17	7.81	8.48	-4.79	11.8	4.74
Chexal Lellouche [54]	50.7	49.64	63.45	49.16	15.11	-14.95	16.87	14.8
Dix [63]	51.85	50.49	65.39	50.01	14.91	-14.75	16.38	14.6
Awad and Muzychka [72]	54.3	-53.68	55.7	53.19	4.47	3.32	6.48	3.29
Zuber and Findley [73]	61.38	61.09	74.53	60.5	17.68	-17.55	19.26	17.38
Gomez et. al. [75]	62.06	61.83	75.21	61.23	17.89	-17.76	19.49	17.59
Smith [68]	63.92	63.71	78.53	63.1	17.61	-17.5	18.77	17.33
Hibiki and Ishii [76]	64.44	64.31	77.83	63.7	18.34	-18.22	19.83	18.05
Chislom [66]	68.22	68.1	82.87	67.45	18.71	-18.61	19.83	18.43
Homogeneous model	88.74	88.74	102.84	87.89	24.76	-24.68	26.05	24.44

Chapter 5

Carryover experiments and CFD simulations

5.1 Experimental observations

With an increase in the air injection flow rate, the pool void fraction and swell level in the air-water drum increases. The operating swell levels during experiment were varied using combination of initial level and air injection flow rate. It was observed that when the operating levels were well below the exit pipe of the drum, the carryover was very low and not even measurable. The loop was allowed to run for long duration but separator did not show collection of any measurable quantity of water. At lower swell levels, the phenomenon of bubble bursting and the formation of droplets were observed and the large droplets were seen falling back to the liquid. During experiments it was observed that when the swell level reaches closer to exit pipe, significant amount of carryover is collected in the separator. Visual observations through transparent acrylic sheet revealed that large chunk of water segments were carried out of the drum by flowing air. As the area drastically reduces near the drum exit, air velocity increases sharply and all droplets reaching close to exit are immediately entrained in the flow. Figure 5.1 shows some snapshots taken during experiments at high swell level which show large droplets as well as liquid filaments can be seen getting entrained in flow. The bubble density below the interface was very high and they were seen coalescing to form larger bubbles at the top. Foamy froth mixture of air-water is observed to form at the top as seen in photographs in Figure 5.1.

The entrainment measured during instances shown in Figure 5.1 corresponds to region-III or near surface entrainment phenomenon. The entrained water in the experiment was collected in separator and measured with measuring flasks. The time duration of collection of water was noted down. Based on total air flow rate, total water collected for the given time span of measurement, average entrainment rates were obtained.

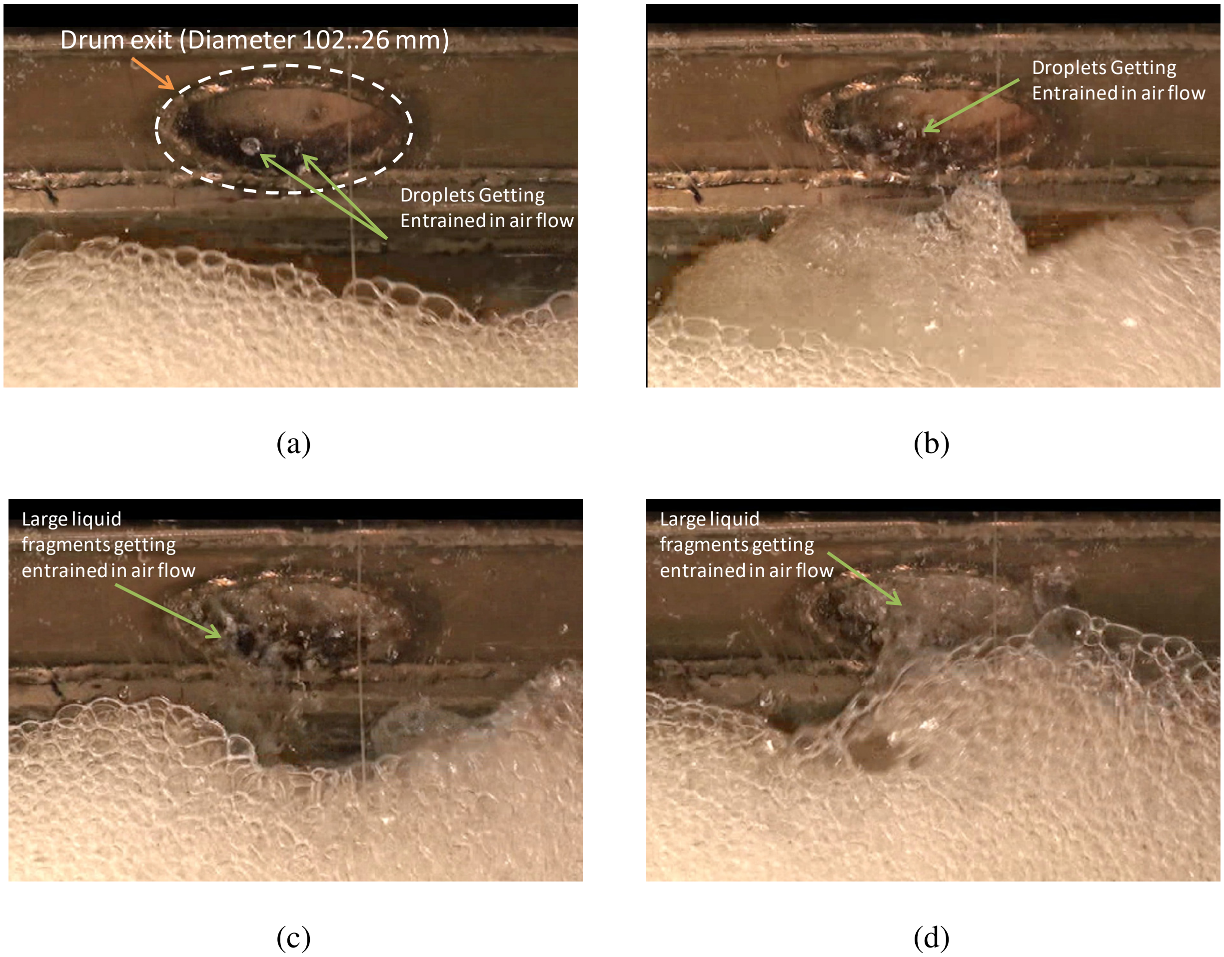

Figure 5.1: Photographs showing entrainment phenomenon at operating levels near the exit.

The operating swell levels were close to exit of the drum. The entrainment varied from 30 to 600 % at these different operating levels closer to exit with total air flow rate varying in the range of 3000 to 7500 lpm per channel. The measured data is shown in Table-5.1. These measurements were compared with correlation given by Kataoka and Ishii [30] as shown in Figure 5.2. The correlation is plotted for total air flow rate of 3000 & 7500 lpm. The correlation predicts entrainment as a function of superficial velocity of gas at the interface and the elevation above the interface. Correlation considers constant velocity of gas above the interface. It can be therefore noted that the effect of curvature of drum on superficial velocity of gas is not considered in correlation. Since the flow cross-section area keeps on reducing as we traverse from interface towards exit, the velocity of gas/air varies accordingly. The comparison shows that correlation by Kataoka and Ishii [30] agrees with the present experimental data from AWL. Kataoka and Ishii [30] stated that for air-water system the maximum near surface entrainment was close to 400%. i.e. $E_{fg} \equiv 4.0$. The maximum entrainment measured during these experiments was also of the similar order. Our experimental data are limited to high gas flux / near surface region and hence entrainment is very high. However, in prototype the operating levels will be well below this condition and carryover will be smaller. As per technical guidance document on steam purity for turbine operation by The International Association for the Properties of Water and Steam (IAPWS), the amount of carryover in saturated steam from BWRs is to be limited to less than 0.1% [83]. The line corresponding to 0.1% carryover is also plotted in Figure 5.2. The operating levels shall be such that the entrainment is sufficiently smaller than the prescribed limit by IAPWS. It is therefore important that method used for predicting the level for limiting carryover should be accurate and reliable. In our experiment carryover at lower operating levels was too small to collect and accurately measure. For example at 7500 lpm total air flow, which corresponds to 0.152 kg/s air flow, if carryover is 0.1%, the amount of water corresponds to 1.52×10^{-4} kg/s in the form of fine droplets. We could measure the droplet size distribution near interface at various operating levels and therefore have attempted to predict carryover for varying swell levels using CFD techniques.

Table 5.1 – Experimental parameters and entrainment measured during experiment

Total Air Flow Rate (lpm)	Swell Level (m)	h (m)	J_g (m/s)	J_g^*	h^*	J_g^*/h^*	E_{fg}
6000	1.866	0.064	0.251	0.435	23.705	0.018	0.740
4500	1.896	0.034	0.256	0.444	12.602	0.035	2.412
5250	1.815	0.115	0.166	0.288	42.561	0.007	1.093
1500	1.905	0.025	0.099	0.172	9.252	0.019	4.900
3250	1.915	0.015	0.277	0.481	5.551	0.087	0.677
3000	1.895	0.035	0.168	0.292	12.953	0.023	6.014
3250	1.865	0.065	0.135	0.234	24.056	0.010	0.541
3750	1.806	0.124	0.114	0.199	45.910	0.004	2.286
4000	1.836	0.094	0.139	0.242	34.807	0.007	3.328
4500	1.806	0.124	0.137	0.239	45.910	0.005	0.806
4750	1.846	0.084	0.174	0.303	31.106	0.010	3.326
5250	1.796	0.134	0.155	0.268	49.611	0.005	0.686
5500	1.796	0.134	0.162	0.281	49.611	0.006	0.459
7000	1.806	0.124	0.214	0.371	45.910	0.008	0.381
7250	1.816	0.114	0.230	0.400	42.209	0.009	0.371

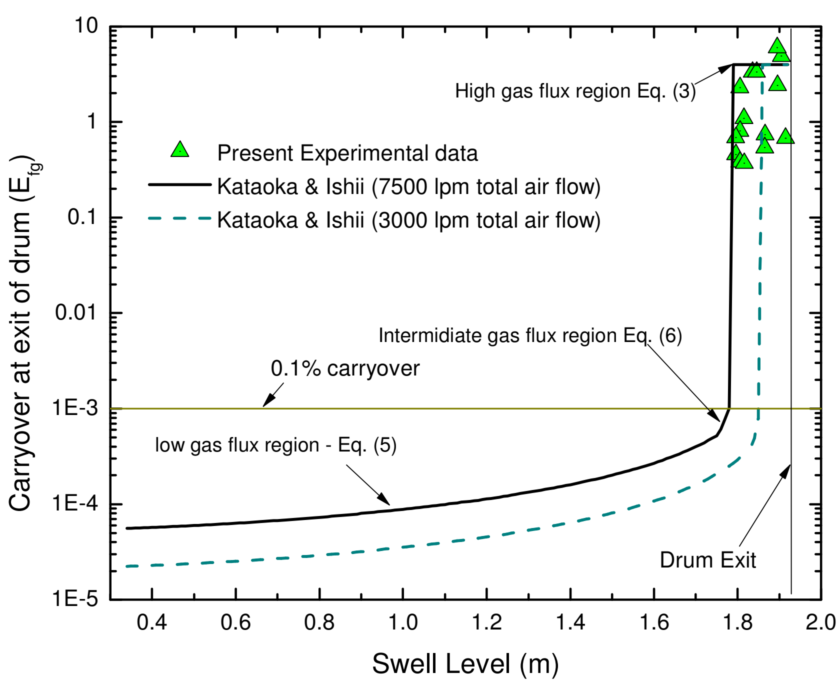

Figure 5.2: Carryover data compared with Kataoka & Ishii correlation

5.2 Droplet size distribution measurements

Droplet size distribution (DSD) was measured at various operating levels using high speed photography and shadowgraph technique. In this technique the camera is placed directly in the path of illumination and droplet images were captured (see Figure 5.3 for schematic of photography set-up).

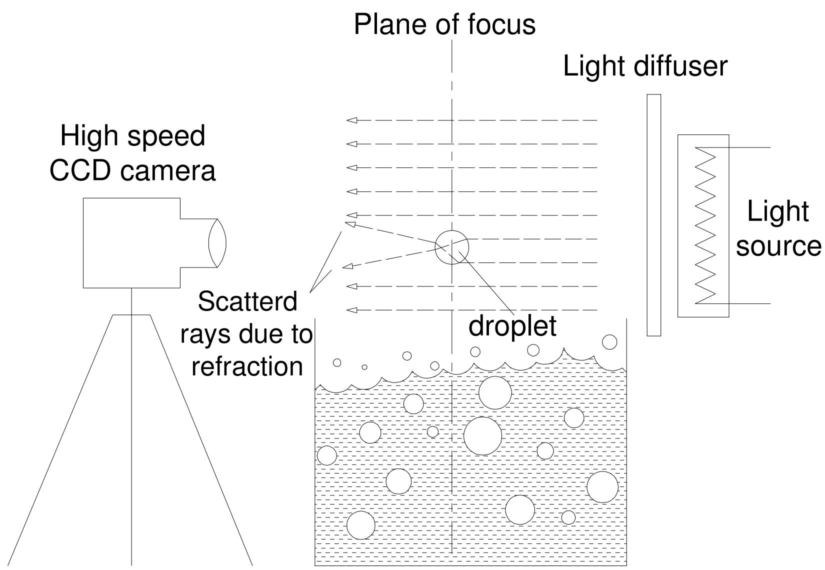

Figure 5.3: Shadowgraph technique

As explained in Figure 5.3, the light entering the droplet gets scattered due to refraction and thus droplet appears dark on bright background. The refraction occurs due to difference in refractive index of air (n=1.0) and water (n=1.3). High speed camera FASTCAM-1280 PCI capable of capturing 1000 frames per second was used with Nikon 50 mm fixed focal length lens. The focal plane was set to be inside the drum. 100 W CFL bulbs were used to illuminate the droplet background. Approximately 18000 images were taken for a given operating swell level, with camera set at frame rate of 60 frames per second. Two sets of such measurements were carried out for each swell level. The images recorded were then processed with an image processing algorithm to obtain images containing only droplets. The various stages of image processing are shown in Figure 5.4(a) to 5.4 (d). Images collected were first converted to Grayscale. An image of background only was then subtracted from the images. This eliminated any background elements present in image. These images were then converted to pure black and white by setting a threshold value (Figure 5.4(b)). The wavy structure of separation interface was also captured in these images which were removed by morphological operations. The wavy structure of interface contains holes of background pixels (pure black) which are removed by hole-filling algorithm. A new image is stored in which droplets were removed first by morphological operation of image erosion, thus containing only the wavy structures of interface. This new image was modified to smoothen and dilate the edges of interface structures. This new image was then subtracted from original image to get final image of only droplets (Figure 5.4(c)). Figure 5.4(d) shows superimposition of 500 such images of only droplets above interface. The data of droplets such as average diameter, centroid and position is stored sequentially in a data structure as all captured images are processed in iteration. Histogram of droplet size and numbers is obtained from the data structure file.

In order to estimate the droplet size in milimeters, the images were calibrated using an image taken with a tube placed at focal plane having outside dimater of 10 mm. The lens and camera set up was used to take images of a tube without disturbing the focus settings of the lens. From this image pixel to millimeter conversion factor was obtained. In most of readings, 1 pixel correpsonded to 126-130 microns. The measurement accuracy with this technique was estimated to be ± 0.200 mm with uncertainity of 0.075 mm. Figure 5.5 shows droplet distributions obtained from image processing.

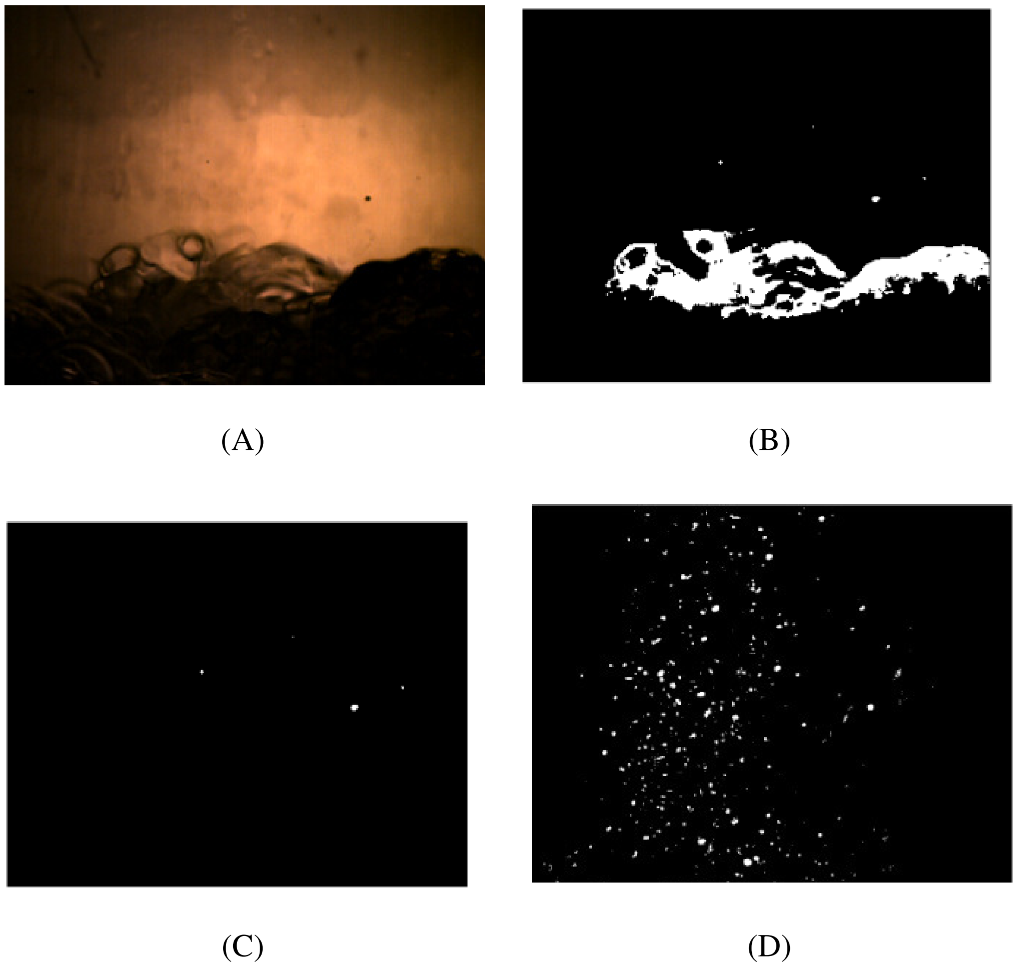

Figure 5.4: Steps in image processing for droplet size measurement: (a) Original Image, (b) Binary image after grayscale conversion and thresholding, (c) Image of only droplets after morphological operations, (d) Superimposition of 500 images of only droplets.

It was found that DSD followed similar trends at different levels. It can be seen that it follows the Upper Limit Log Normal (ULLN) distribution. The ULLN can be described by following set of equations:

$$f(\eta) = \frac{\delta d_{max}}{\sqrt{\pi} d(d_{max} - d)} e^{-\delta^2 \eta^2} \tag{5.1}$$

$$\text{Where } \eta = ln\left(\frac{ad}{d_{max} - d}\right) \tag{5.2}$$

The distribution parameters in the equation (5.1) & (5.2) were found out to be $a = 10.0$, $\delta = 0.9$ and $d_{max} = 0.0027\ m$ by curve fitting to the experimental data as shown in Figure 5.5. It was further observed during experiments that the bubble density near the interface was very high and the coalescence of bubbles occurred. The size of bubble at interface was observed to be of size 30-50 mm for all cases. The high speed photography at 1000 frames per second has revealed that the droplets are generated due to disintegration of bubble dome at interface. Figure 5.6 shows the sequence of the events following the formation of bubble dome and its breakage into number of small droplets. The bubble arrived at surface forms a thin film which is unstable and it continues to thin down due to upward flux of gas/air. The film gets punctured near top and it propagates across the dome creating liquid filaments, which finally are broken up into number of small droplets due to surface tension effects. Image processing showed that the frequency of droplets having size greater than 1.8 mm is very low. Maximum droplet of size up to 2.7 mm was observed as per the photographic measurements.

Shadowgraph and image processing is the simplest and most economic measurement technique available to assess the size distribution of droplet inside the drum. The photograph captures droplet shadow which crosses the plane in focus. During experiments it was observed that bubble density at the interface is quite high and bubbles are uniformly distributed. The process of bubble rupture and droplet ejection was observed to happen uniformly all over the interface. Thus information of droplet sizes at selected 2-D plane of focus would be accurate representation. The error is minimized by taking large number of pictures (about 36,000 photographs were taken for one operating condition).

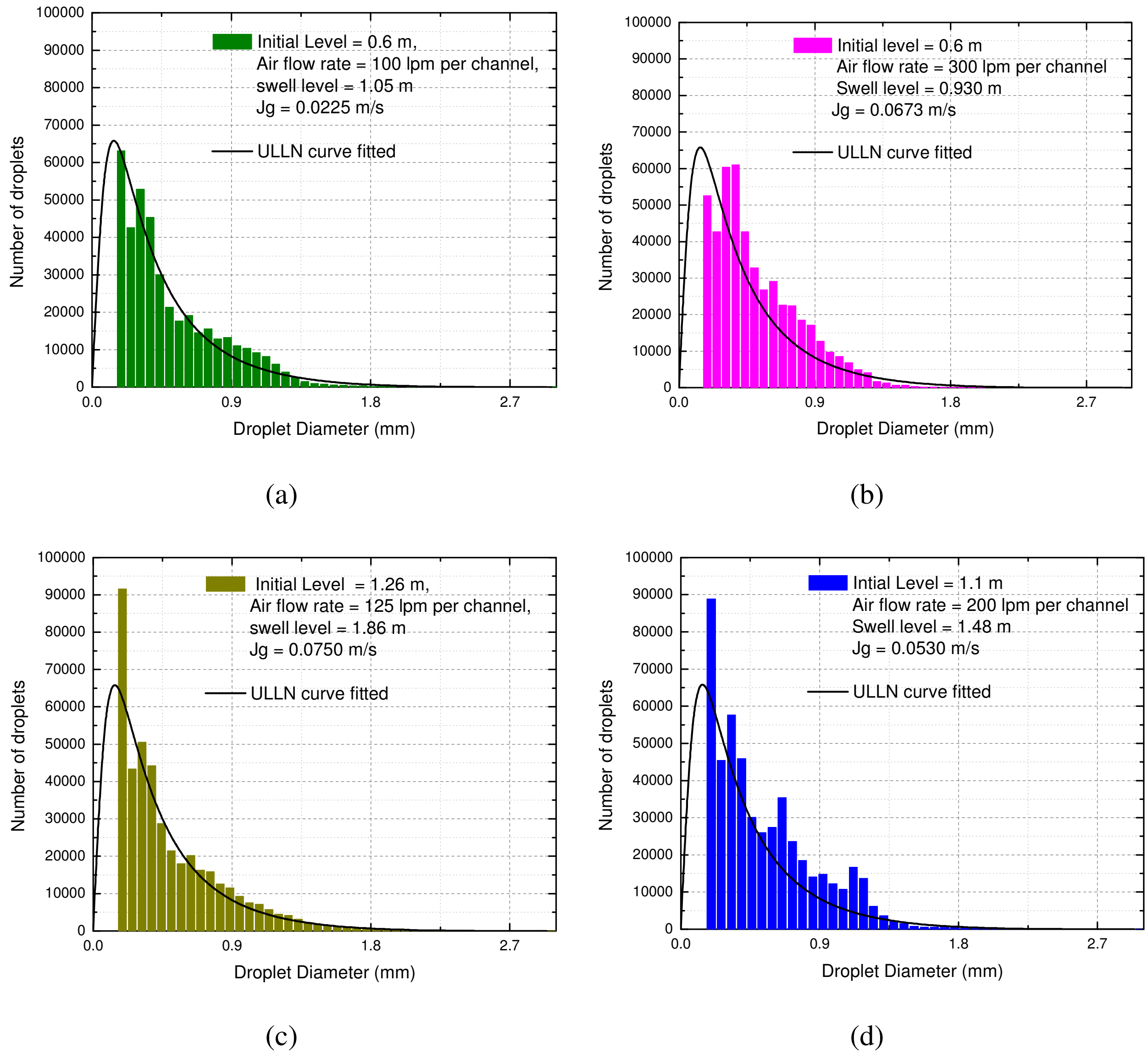

Figure 5.5: Droplet Size Distributions measured at (a) Swell level 1.05 m i.e h = 0.92, j_g= 0.0225 m/s, (b) Swell level 0.930 i.e h = 1.0, j_g= 0.0673 m/s, (c) Swell level 1.86 m i.e h = 0.07 m, j_g= 0.0750 m/s, (d) Swell level 1.48 m i.e h = 0.45, j_g= 0.0530 m/s,


(a)

(b)

(c)
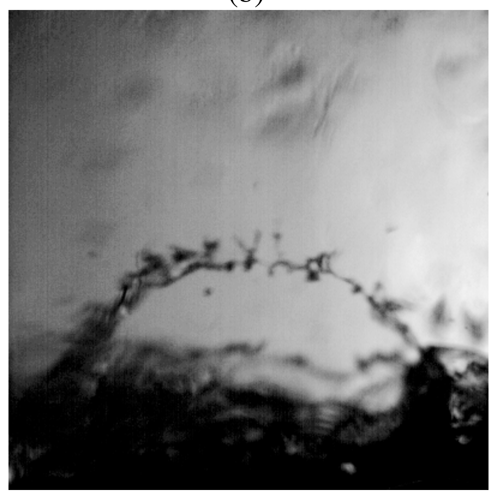
(d)
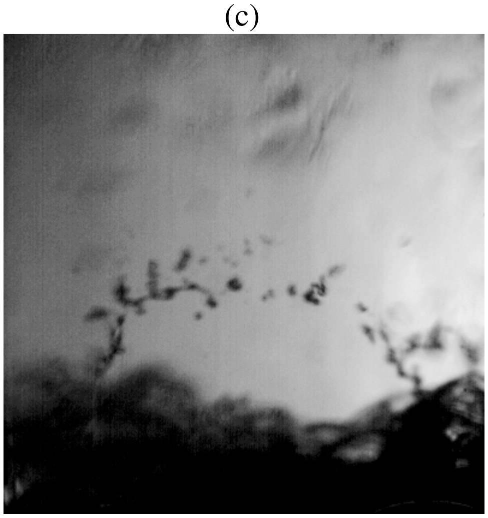
(e)
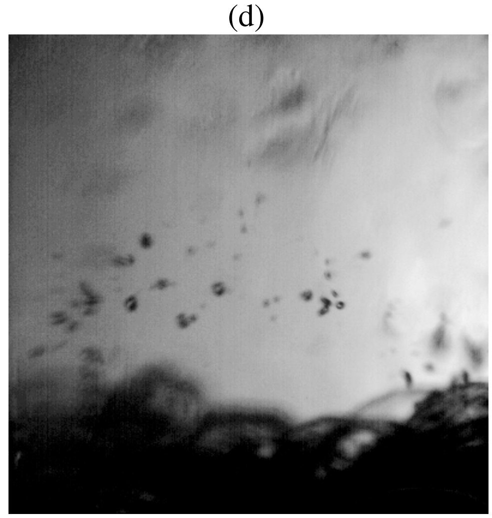
(f)

Figure 5.6: Formation of droplets due to bursting of the bubble film

5.3 Euler-Lagrangian methodology for carryover prediction

It can be noted that the empirical correlations for entrainment are based on the previous experiments in geometries having constant cross-section flow area. While the prototype geometry which is horizontal cylinder with exit at top surface, has varying cross-section as area near the exit reduces gradually. Therefore investigations are necessary to develop a methodology to account for this effect. Generally the carryover prediction methods found in the literature start with assumption of Droplet Size Distribution (DSD) and then their motion in the vapor space is predicted. Same methodology with CFD technique is employed in the present study. With the aid of CFD simulations we are able to obtain 3-D flow patterns above the interface using Eulerian approach and then the droplet movement in vapor/gas space is traced using Lagrangian approach.

5.4 1-D Euler-Lagrangian approach

5.4.1 Formulation of 1-D Euler-Lagrangian equations

The equation of motion of droplet particle can be written and solved with certain simplifying assumptions. The droplet/particle can be considered to be of spherical shape and thus its mass can be given as

$$m_p = \frac{\pi}{6} d_p^3 \rho_p \tag{5.3}$$

The cross-sectional area/projected area of the droplet can be given as,

$$A_p = \frac{\pi}{4} d_p^2 \tag{5.4}$$

Let $U_p$the velocity of droplet. The force balance on the droplet of diameter $d_p$travelling in the bulk of vapour having constant velocity $U_c$can be described as

Inertia Force = Drag Force + Gravity Force – Buoyancy Force

$$m_p \frac{dU_p}{dt} = F_D + F_G - F_B \tag{5.5}$$

Where

$$F_D = Drag\ force\ on\ particle = \ C_D \frac{\rho_c}{2} \left| U_c - U_p \right| \left(U_c - U_p \right) A_p \tag{5.6}$$

$$F_G = Gravity\ force\ on\ particle = \ m_p g \tag{5.7}$$

$$F_B = Buoyancy\ force\ on\ particle = \ \rho_c g V_p \tag{5.8}$$

where ρ_c is density of bulk fluid and $V_p$is volume of the particle

The drag coefficient is given in terms of particle Reynolds Number Re_pdefined as

$$Re_p = \frac{\rho_c d_p \left| U_c - U_p \right|}{\mu_c} \tag{5.9}$$

For the spherical particle the drag coefficient for small Reynolds number (Re_p<0.5) is expressed as:

$$C_D = \frac{24}{Re_p} \tag{5.10}$$

The regime where Re_p<0.5 is often referred as Stokes Flow.

For transition region (0.5 <Re_p<1000) various correlations are available, but the most suitable correlation frequently used is by Schiller and Naumann [84] given as following:

$$C_D = \frac{24}{Re_p} \left(1 + 0.15 Re_p^{0.687} \right) \tag{5.11}$$

In the regime Re_p> 1000 the drag coefficient remains practically constant and is given as

$$C_D \approx 0.44 = \frac{24}{54.54} \tag{5.12}$$

The regime where Re_p> 1000 is referred as Newton-regime.

Now, the equation of motion of particle can be written as:

$$m_p \frac{dU_p}{dt} = \frac{24}{Re_p} f_D \frac{\rho_c}{2} |U_c - U_p| (U_c - U_p) A_p + m_p g - \rho_c g V_p \tag{5.13}$$

Where

$$f_D = 1.0 \quad for\ Stokes\ Flow\ Regime\ (Re_p < 0.5) \tag{5.14}$$

$$f_D = 1 + 0.15 Re_p^{0.687} \quad for\ Transition\ Flow\ Regime\ (0.5 < Re_p < 1000) \tag{5.15}$$

$$f_D = \frac{Re_p}{54.54} \tag{5.16}$$

The equation (5.5) can be written as

$$\frac{dU_p}{dt} = \frac{24}{m_p Re_p} f_D \frac{\rho_c}{2} |U_c - U_p| (U_c - U_p) A_p + g - \rho_c g \frac{V_p}{m_p} \tag{5.17}$$

$$\frac{dU_p}{dt} = \frac{24 \vartheta_c}{\frac{\pi}{6} d_p^3 \rho_p d_p |U_c - U_p|} f_D \frac{\rho_c}{2} |U_c - U_p| (U_c - U_p) \frac{\pi}{4} d_p^2 + g - \rho_c g \frac{V_p}{\rho_p V_p} \tag{5.18}$$

After re-arranging we get,

$$\frac{dU_p}{dt} = \left(\frac{24 \vartheta_c}{d_p} f_D \frac{3}{4} \frac{\rho_c}{\rho_p d_p} \right) (U_c - U_p) + g \left(1 - \frac{\rho_c}{\rho_p} \right) \tag{5.19}$$

The above equation gives the instantaneous velocity of the particle, by integrating during time step between t to $t + \Delta t$, and we get,

$$U_p \big|_{t+\Delta t} = \frac{U_p \big|_t + \left[\left(\frac{24 \vartheta_c}{d_p} f_D \frac{3}{4} \frac{\rho_c}{\rho_p d_p} \right) U_c + g \left(1 - \frac{\rho_c}{\rho_p} \right) \right] \Delta t}{1 + \left(\frac{24 \vartheta_c}{d_p} f_D \frac{3}{4} \frac{\rho_c}{\rho_p d_p} \right) \Delta t} \tag{5.20}$$

Solving above equation, in each time step gives variation of velocity with respect to the time. The instantaneous position of particle can be estimated based on the average velocity during the time step. It can be noted that in Equation (5.20), the term f_D is function of Re_pwhich depends on the velocity of particle during the interval. The Re_p is estimated using only known velocity $U_p\big|_t$ which is not exactly the average velocity during time step. Therefore numerical solution of motion of particle will contain some error, which can be minimized using smaller time steps. A computer code was developed to solve the Equation (5.20). The code enables to obtain the critical droplet diameter, i.e. size of a droplet below which all droplets will be entrained in the vapor flow. All droplets above this critical droplet diameter will travel some finite distance above vapor space and fall back to liquid.

The simplifying assumptions made during above formulation are summarized as below:

1. The droplet is treated as perfect rigid sphere.
2. Droplet is ejected in vertically upward direction. i.e. velocity has no horizontal components.
3. Droplet coalescence and evaporation is not considered.
4. Virtual mass force and Basset's history force on droplet are not considered.
5. The vapor flow is having uniform constant velocity.

The first assumption simplifies the treatment of forces on droplet as well established drag correlations are developed for spheres. Second assumption leads to further simplification as angle of ejection is fixed i.e. perpendicular to surface and upwards. In practice, there is distribution of angle of ejection for droplets. Droplet coalescence will increase droplet diameter and it may get fall back to liquid pool, thus entrainment will be reduced. On the other hand evaporation will lead to reduction in size of droplet and entrainment will increase as smaller droplet tend to attain higher elevations and if the size falls below critical droplet diameter it will get entrained in the flow. The fourth assumption gives conservative estimate as all these are retarding forces for droplet motion. Fifth assumption simplifies the treatment of drag forces as the nature of drag is different in accelerating or decelerating flows. Although these simplifying assumptions introduce uncertainty in prediction, we can have a tool to study basic droplet dynamics and the assumptions can be slowly removed to obtain realistic simulations. The calculation of critical droplet diameter is illustrated in a test case described as follows:

5.4.2 Test cases for 1-D simulation

A test case has been considered for a droplet laden air flow in a domain $x=0$ to $x=1m$.

Following are the inputs for calculation:

Velocity of air	:	U_c	=	5m/s
Droplet diameter	:	d_p	=	1 μm to 2500 μm
Droplet initial velocity	:	$U_p\|_{t=0}$	=	1.0 m/s
Density of air	:	ρ_c	=	1.24 kg/m^3
Viscosity of air	:	μ_c	=	1.82×10^{-5}Pa.s
Density of water droplet	:	ρ_p	=	993.26 kg/m^3

Water droplets of various diameters were considered to be ejected vertically upward (along only x-axis) with initial velocity of 1 m/s, in the bulk of air flow having velocity of 5 m/s. The droplets initial position is at $x = 0.2\ m$. The droplet trajectories are solved in time domain with time step $\Delta t = 0.001\ s$. Calculation is stopped when the droplet hits the domain bottom i.e. $x = 0.0\ m$. Or top of the domain i.e. $x = 1.0\ m$.

Figure 5.7 shows the variation of position of droplet of various sizes with respect to time. It can be seen that very tiny droplets of size 10 μm are transported out of domain along with air in short duration of time. Larger droplets are sluggish as the net force i.e. Drag-gravity is smaller. Droplet of size 1015 μm is seen to attain a steady position inside the vessel and it is perfectly balanced by the forces and floats at that position throughout calculation. Larger droplets find their path towards back to liquid at the bottom of domain due to larger gravity force.

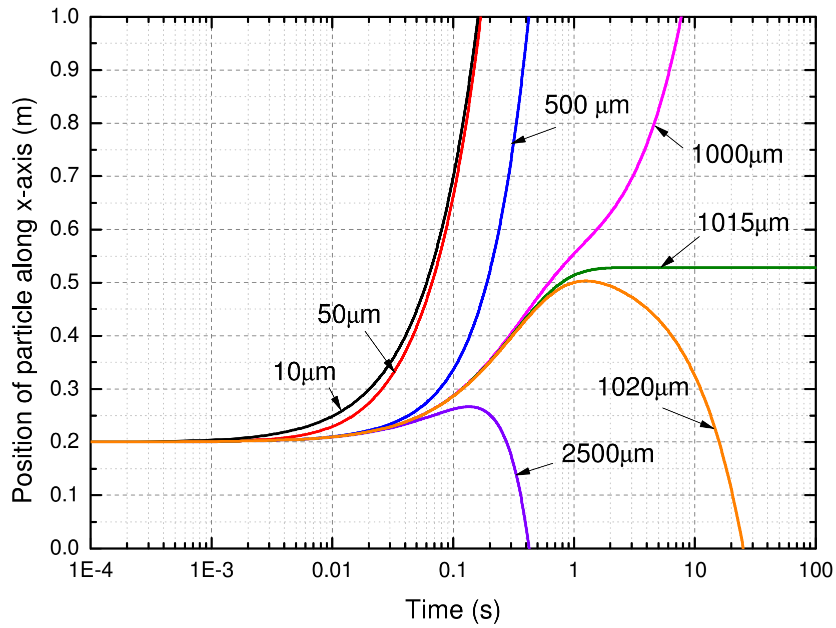

Figure 5.7: Particle positions for test case.

Figure 5.8 shows the velocity variation of particles. It can be seen that small particles attain velocity close to velocity of the bulk flow. When particle steady state velocity is greater than zero it gets entrained in flow. It can be observed that for the case under consideration the critical droplet diameter is 1015 μm.

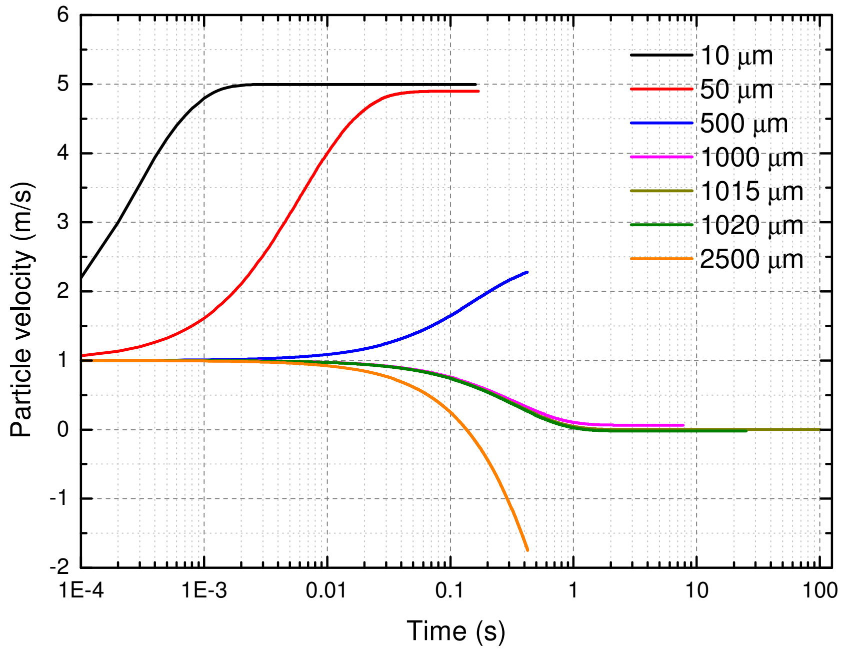

Figure 5.8: Particle velocity for the test case

5.4.3 Entrainment prediction for Air-Water Loop

Further studies are carried out using the Lagrangian particle tracking code for water droplets of various sizes ejected in air medium with varying bulk flow velocity. Please note that analysis is only one dimensional. In this study the critical droplet diameter is found out by simulations for the combinations of bulk gas phase velocity and droplet ejection velocity. Figure 5.9 shows the variation of critical droplet diameter for different gas phase velocities and different ejection velocities.

Figure 5.9 shows the results up to $U_c = 1.0\ m/s$. From Figure 5.9, the critical droplet diameter can be assumed to be independent of initial ejection velocity when $U_c < 1.0\ m/s$. The maximum bulk air velocity for various operating levels in AWL drum is smaller than 1 m/s. Hence we can neglect the effect of initial droplet ejection velocity.

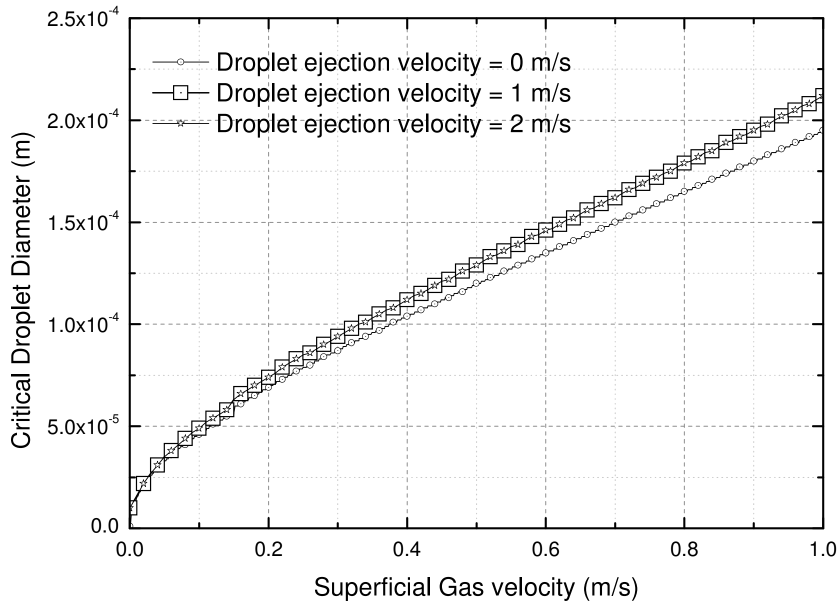

Figure 5.9: Critical droplet diameter for air-water mixture at atmospheric pressure and temperature.

Thus with available experimental measurements on droplet size distribution and particle tracking algorithm we can attempt to predict the carryover for various operating levels of AWL drum. Carryover out of the AWL drum shall consist of group of droplets having diameter smaller than the critical diameter, as well as the droplets which travelled to exit due to their momentum after ejection from surface (See Figure 5.10).

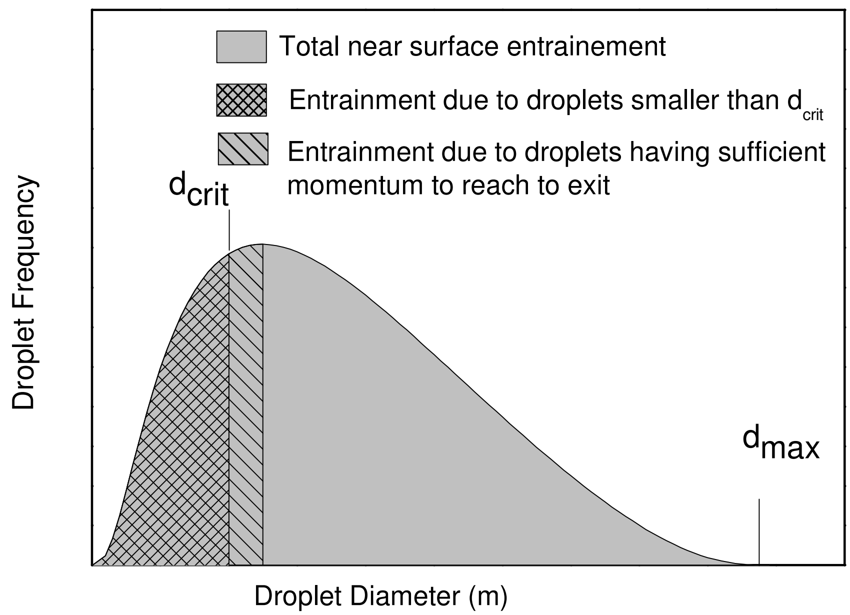

Figure 5.10: Estimating amount of entrainment at drum exit as a fraction of near surface entrainment.

Droplet size distribution parameters obtained experimentally (as described in Section 4.3) is considered for the analysis. From air flow rate, the air superficial velocity above the operating level in the gas space is calculated. The effect of the drum curvature is neglected although the velocity will increase towards the exit due to reduction in flow cross-section. The droplet size distribution in divided in number of groups and their cumulative volume is calculated. This cumulative volume represents the entrainment at the interface. Now the sum of volumes for droplets having diameter less that d_{crit} is calculated. There are some droplets which will reach to exit of drum due to initial momentum. Cumulative volume of all these droplets thus represents the carryover at the drum exit. Figure 5.11 shows carryover predicted at drum exit for various operating levels using correlations and particle tracking method described above.

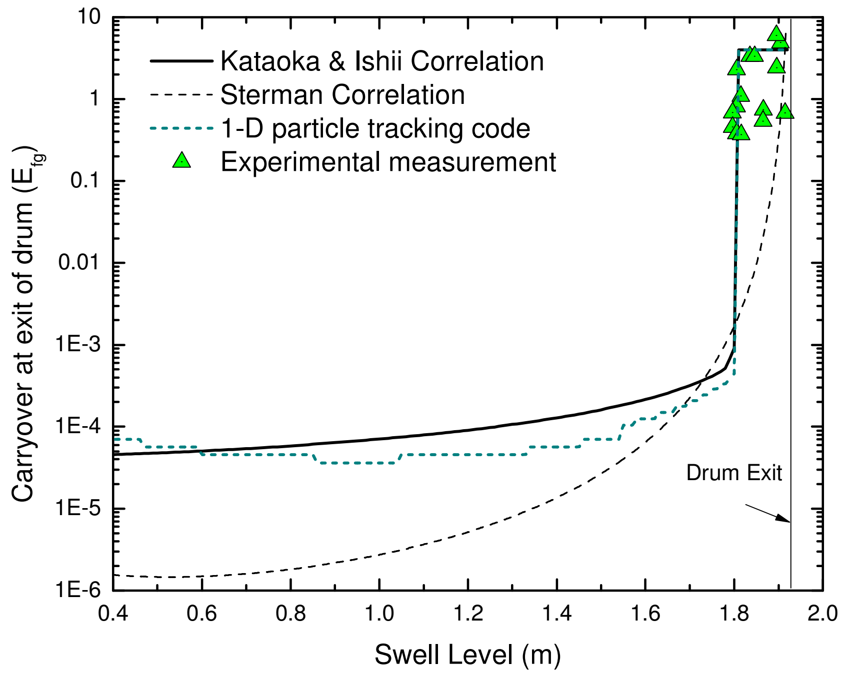

Figure 5.11: Prediction of carryover for AWL drum by correlations and 1-D particle tracking code

It can be seen that the entrainment prediction is closely matching with experiment and Kataoka and Ishii correlation and experiments for operating levels near to drum exit. The carryover increases sharply above swell level 1.8 m, this is due to fact that all droplets with initial ejection velocity have sufficient momentum to reach to exit level. For lower operating levels upto 1.6 m, it can be seen that entrainment remains more or less constant and is comparable to prediction with correlation. The value of entrainment is very low of the order of 10^{-4}. As per technical guidance document on steam purity for turbine operation by The International Association for the Properties of Water and Steam (IAPWS), the amount of carryover in saturated steam from BWRs is to be limited to less than 0.1% i.e. $E_{fg} < 10^{-3}$ [83]. There are differences in values predicted by Kataoka & Ishii correlation and 1-D particle tracking analysis at levels lower than 1.6 m, however those are very small values of entrainment and can be neglected. The entrainment starts rising after level 1.6 m and sharply increases at 1.8

m. The entrainment predicted in this region (level from 0.3 m to 1.8m) is described by equations for deposition controlled region and momentum controlled region with low and intermediate flux. The 1-D analysis predicts similar trends as that of correlation. The difference between predicts starts reducing and threshold of momentum controlled regime from intermediate flux to high flux is predicted to similar by correlation as well as 1-D analysis.

For the available resolution of camera used in the experiments we could only detect droplets as small as 120 μm and therefore the droplet size distribution function was extrapolated for droplets of diameters smaller than 120 μm (see Figure 5.5). For this distribution the cumulative volume is small (< 0.1%) for droplets diameter up to 120 μm. Numerical calculations have shown that for low operating levels (swell level < 1.8 m) and low gas flux values, entrainment at the drum exit mainly consists of small diameter droplets. Therefore the accuracy of prediction is dependent on the extrapolated size distribution for small diameter values. As the carryover value for these conditions is so low that there could not be any reliable measurement of actual carryover in experiments. In the absence of data for the low gas flux values, the prediction is compared with correlation and was found to agree reasonably well with it. Therefore the assumed/extrapolated distribution is acceptable for numerical calculation.

There are various conservative assumptions made for particle tracking for example only one dimensional movement of particles is considered (only upward direction). In practice the droplets travel parabolic path inside the vessel with varying angle of ejection. Also droplets have velocity distribution at the time of ejection from surface, while in this analysis velocity of ejection was considered to be 1.0 m/s for all groups of particles. However, the calculations prove that we can thus conservatively estimate carryover based on the experimental droplet size distribution and equation of motion of droplet.

5.5 3-D Euler-Lagrangian approach

5.5.1 OpenFOAM Solver - Governing equations

The Euler-Lagrangian simulation of droplet transport in Air-Water drum of AWL is performed using opensource CFD software OpenFOAM v2.3.1. The present work is based on the standard solver for steady state calculation of compressible, turbulent flows with a reacting multiphase particle cloud, known as *"simpleReactingParcelFoam"*. Air flow was treated as a continuum (Eulerian) while the droplets were treated as discrete phase (Lagrangian) with two-way coupling i.e. exchange of momentum, energy between the two phases. The solver solves the continuous phase flow using equations for balance of mass, momentum and energy. These governing equations establish a closed system of variables, density (ρ), velocity ($\boldsymbol{u}$), pressure (p) and internal energy (e) or enthalpy (H).

The mass balance:

$$\frac{\partial \rho}{\partial t} + \nabla.(\rho \boldsymbol{u}) = S_{ev} \tag{5.21}$$

Above equation describes the variation of mass due to change in density and convection in a given control volume. The right side term is mass source term appearing due to phase change.

The conservation of momentum:

$$\frac{\partial (\rho \boldsymbol{u})}{\partial t} + \nabla.(\rho \boldsymbol{u}\boldsymbol{u}) = -\nabla P + \nabla.\boldsymbol{\tau} + \rho \boldsymbol{g} + S_{i,mo} \tag{5.22}$$

Where $\boldsymbol{\tau}$ is stress tensor which can be expressed in terms of bulk viscosity (γ), dynamic viscosity (μ), velocity gradient and identity tensor ($\boldsymbol{I}$) as follows:

$$\boldsymbol{\tau} = \left(\gamma + \frac{2}{3}\mu\right)(\nabla.\boldsymbol{u})\boldsymbol{I} + \mu(\nabla \boldsymbol{u} + (\nabla \boldsymbol{u}^T)) - \frac{2}{3}\mu(\nabla.\boldsymbol{u})\boldsymbol{I} \tag{5.23}$$

$S_{i,mo}$is source term due to interaction/momentum exchange with particles.

The energy equation in terms of enthalpy is as follows:

$$\frac{\partial(\rho\mathcal{H})}{\partial t} + \nabla.(\rho h\boldsymbol{u}) + \frac{\partial(\rho K)}{\partial t} + \nabla.(\rho K\boldsymbol{u}) - \frac{\partial P}{\partial t} = -\nabla.q + \nabla.(\boldsymbol{\tau}.\boldsymbol{u}) + \rho\boldsymbol{g}.\boldsymbol{u} + S_{he} \tag{5.24}$$

Where S_{he} is source term due to heat transfer from discrete phase. $K \equiv |\boldsymbol{u}|^2/2$ is kinetic energy, $-\nabla.q$ is heat flux and $q = \lambda\nabla T$, with λ as thermal conductivity. S_{he} is source term arising from exchange between continuous phase and particle phase.

The energy equation expressed in terms of internal energy e takes following form;

$$\frac{\partial(\rho e)}{\partial t} + \nabla.(\rho e\boldsymbol{u}) + \frac{\partial(\rho K)}{\partial t} + \nabla.(\rho K\boldsymbol{u}) - \nabla.(\boldsymbol{u}P) = -\nabla.q + \nabla.(\boldsymbol{\tau}.\boldsymbol{u}) + \rho\boldsymbol{g}.\boldsymbol{u} + S_{he} \tag{5.25}$$

Enthalpy is sum of internal energy and kinematic pressure i.e. $\mathcal{H} \equiv e + p = e + \frac{P}{\rho}$. Also the term $\nabla.(\boldsymbol{\tau}.\boldsymbol{u}) + \rho\boldsymbol{g}.\boldsymbol{u}$ in Equation (5.25) represents source from mechanical energy which can be neglected in the absence of any external mechanical energy source, thus the equation (5.25) takes the following form:

$$\frac{\partial(\rho\mathcal{H})}{\partial t} + \nabla.(\rho\mathcal{H}\boldsymbol{u}) + \frac{\partial(\rho K)}{\partial t} + \nabla.(\rho K\boldsymbol{u}) - \frac{\partial p}{\partial t} = -\nabla.q + S_{he} \tag{5.26}$$

The vapor formed due to evaporation from droplet phase is treated as species i and conservation equation of mass fraction of species Y_i is as below:

$$\frac{\partial(\rho Y_i)}{\partial t} + \nabla.(\rho\boldsymbol{u}Y_i) = -\nabla.\dot{\boldsymbol{J}} + R_i + S_i \tag{5.27}$$

Where $\dot{\boldsymbol{J}}$ is diffusion flux of species which arises due to gradient of concentration, temperature. R_i is source net rate of production of species i by chemical reactions (combustion etc.), S_i is rate of creation by addition from dispersed phase.

Using Fick's Law,

$$\dot{\boldsymbol{J}} = -\rho\mathcal{D}_{i,m}\nabla Y_i \tag{5.28}$$

The thermal diffusion is neglected in above equation. The diffusion of species in turbulent flow is mainly due to mixing action of chaotic turbulent velocity fluctuations. The turbulent diffusion coefficient is calculated from turbulent viscosity μ_t as follows:

$$\mathcal{D}_t = \frac{\mu_t}{\rho Sc_t} \tag{5.29}$$

Where Sc_t is turbulent Schmidt number, which is a model constant and is taken as 0.7 in case of $k - \epsilon$ turbulent models and as 1.0 when Reynolds stress model (RSM) is used.

It can be noted that equation (5.21), (5.22), (5.26 and 5.27) are set of general equations applicable to transient flows, for steady state calculations the transient terms can be neglected and final set of governing equations are as follows:

Conservation of mass:

$$\frac{\partial \rho}{\partial t} + \nabla.(\rho \boldsymbol{u}) = S_{ev} \tag{5.30}$$

Conservation of momentum:

$$\nabla.(\rho \boldsymbol{u}\boldsymbol{u}) = -\nabla p + \nabla.\boldsymbol{\tau} + \rho \boldsymbol{g} + S_{i,mo} \tag{5.31}$$

Conservation of energy:

$$\nabla.(\rho \mathcal{H} \boldsymbol{u}) + \nabla.(\rho K \boldsymbol{u}) = -\nabla.q + S_{he} \tag{5.32}$$

Solution of continuity and momentum equation is not straightforward because explicit equation for pressure is not available. The most common approach is taking divergence of momentum equation and substituting it into continuity equation to obtain a pressure equation. These final set of equations for flow are solved using SIMPLE (Semi-Implicit Method for Pressure Linked Equations) algorithm.

The equation of motion of droplet particle can be written and solved with certain simplifying assumptions. Let U_p the velocity of droplet. The force balance on the droplet of diameter d_p travelling in the bulk of vapour having constant velocity U_c can be described as

Inertia = Drag Force + Gravity Force – Buoyancy Force

$$m_p \frac{dU_p}{dt} = F_{drag} + F_{gravity} - F_{buoyancy} \tag{5.33}$$

Where

$$F_{drag} = Drag\ force\ on\ particle = \ C_D \frac{\rho_c}{2} \left| U_c - U_p \right| \left(U_c - U_p \right) A_p \tag{5.34}$$

$$F_{gravity} = Gravity\ force\ on\ particle = \ m_p g \tag{5.35}$$

$$F_{buoyancy} = Buoyancy\ force\ on\ particle = \ \rho_c g V_p \tag{5.36}$$

where ρ_c is the density of bulk fluid and V_p is volume of the particle. The drag coefficient is given in terms of particle Reynolds Number Re_p defined as

$$Re_p = \frac{\rho_c d_p \left| U_c - U_p \right|}{\mu_c} \tag{5.37}$$

The particle forces that can be considered in the solver are lift, drag, virtual mass etc. The forces can be selected during CFD calculations during case set up, which will be discussed later.

5.5.2 Validation test case (Cyclone separator) for OpenFOAM solver

CFD simulations of cyclone separator were carried out to validate the chosen Euler-Lagrangian solver of OpenFOAM i.e “simpleReactingParcelFoam”.

The cyclone separator is often used in chemical industries and similar construction is used in steam separators of Boiling Water Reactors and separator units of Pressurized Heavy Water

Reactors steam generator. The cyclone separator is ideal case for equipments having accelerating and swirling flow patterns. Strong vortex formation occurs in cyclone separator and it is very challenging problem to simulate the particle trajectories in the complex flow patterns of cyclone. Though there is no vortex formation in drum, we encounter strong flow acceleration near the exit. Therefore cyclone case has been selected as validation test case where all the CFD parameters (such as turbulence models, convection schemes etc.) can be tested and validated with reliable experimental data.

Ji et. al.[85] carried out experimental investigations on separation performance of cyclone separator with particle concentrations of 5-2000 mg/m^3 and inlet velocities of 6-30 m/s at ambient temperature and pressure. Geometry of the cyclone separator used in experiments by Ji et. al. [85] is shown in Figure 5.12 . Solid particles of calcium carbonate, with density of 2700 kg/m^3 and size distribution from 0.6 to 40 μm were used.

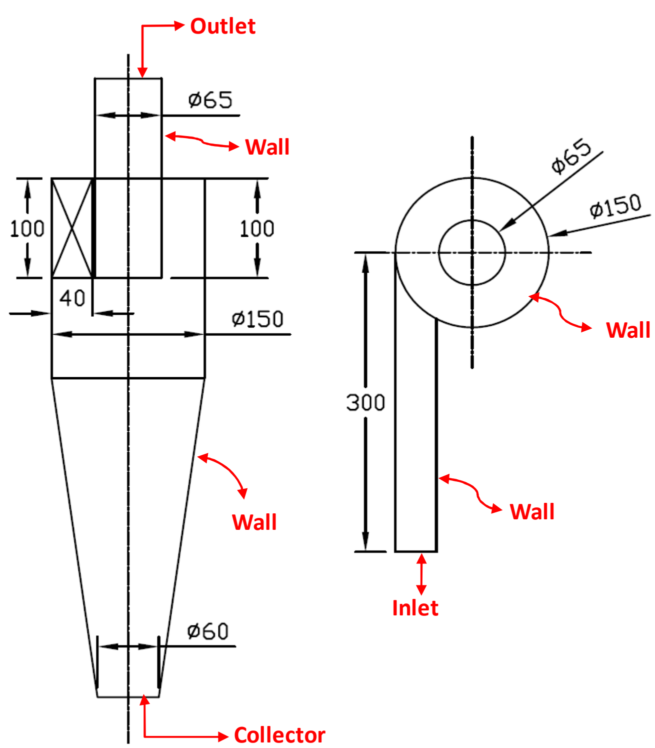

Figure 5.12: Schematic of Cyclone separator (Ji et. al. [85])

Ji et. al. [85] used a particle dispersion generator to feed the solid particles in to the flow and particle size distribution and particle concentration were measured using aerosol spectrometer and isokinetic probes. Figure 5.13 shows the particle size distribution experimentally and a Rosin-Rammler fit [86] to the data. The Rosin-Rammler fit is used as input required for specifying the size distribution of particles during CFD simulations. CFD simulations are carried out to simulate cases with inlet particle concentration on 40 mg/m^3 at air inlet velocities of 6, 8, 10, 12, 15, 18, 20, 22, 25 and 30 m/s.

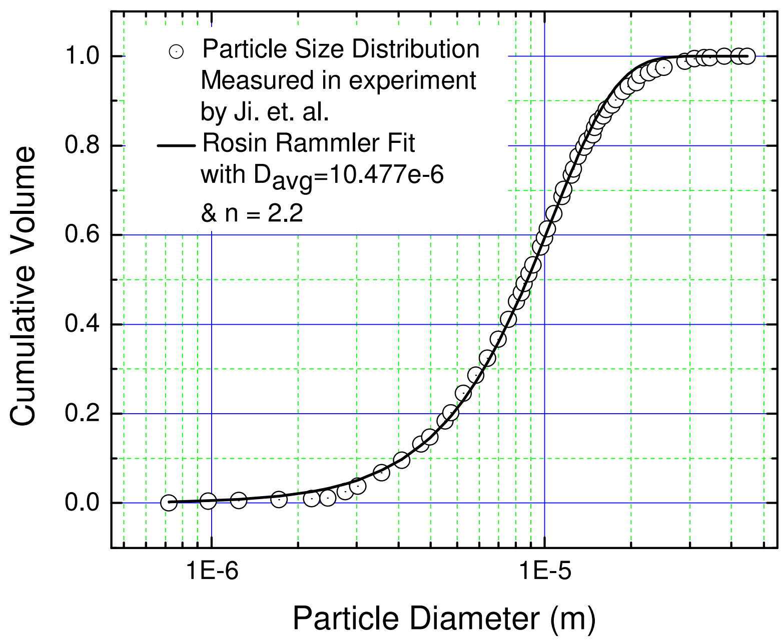

Figure 5.13: Particle size distribution measured by Ji. et. al.[85] and Rosin-Rammler Fit [86] to data.

The geometry has been descritized using tetrahedral elements as shown in Figure 5.14. Various meshes are used to study the effect on the CFD results. The computational domain is closed by four boundaries named Inlet, Outlet, Collector and Wall as shown in Figure 5.12.

The calculations are performed in three steps. First the flow is solved using "*potentialFoam*" solver, a solver for velocity potential to calculate the flux-field from which velocity field is obtained. The velocity field obtained is then used as initial condition for "*simpleReactingParcelFoam*" solver, which solves conservation equations for mass, momentum and energy as described in earlier section. In this step, no particles are injected and a converged solution for flow, pressure and energy field is obtained. In third step, particles are injected in to the flow (converged solution from earlier step) and iterations are performed till the steady state results with particle flow are obtained.

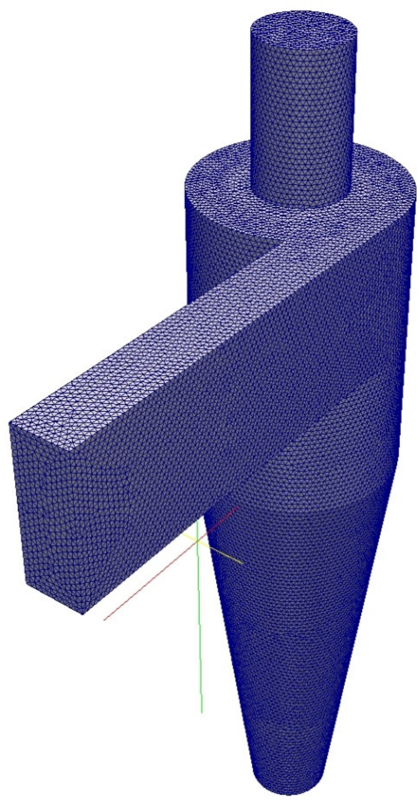

Figure 5.14: Mesh used for calculation of validation of cyclone separator case (714×10^3 tetrahedral cells).

The fluid considered for simulation is air at ambient pressure and temperature. The OpenFOAM solver considers the polynomial based thermodynamic model for properties of fluid under consideration. The properties of air are modeled as follows:

$$\rho_{air} = 4.0097 + (-0.016954) \times T + (3.3057 \times 10^{-5}) \times T^2 + (-3.0042 \times 10^{-8}) \times T^3 + (1.0286 \times 10^{-11}) \times T^4 \quad (5.38)$$

$$C_{p-air} = 948.76 + (0.39171) \times T + (-9.5999 \times 10^{-4}) \times T^2 + (1.393 \times 10^{-6}) \times T^3 + (-6.2029 \times 10^{-10}) \times T^4 \quad (5.39)$$

$$\mu_{air} = 1.5061 \times 10^{-6} + (6.16 \times 10^{-8}) \times T + (-1.819 \times 10^{-11}) \times T^2 \quad (5.40)$$

$$\lambda_{air} = 0.0025219 + (8.506 \times 10^{-5}) \times T + (-1.312 \times 10^{-8}) \times T^2 \quad (5.41)$$

The air temperature T is taken as 300 K. The dispersed phase is represented by solid spherical particles of diameter varying as per Rossin-Rammler fit given by;

$$Y_d = e^{-\left(\frac{d}{d_{avg}}\right)^n} \quad (5.42)$$

Where Y_d is mass fraction of droplets of sizes greater than d. The constant d_{avg} is the value of diameter d for which $Y_d = e^{-1} \approx 0.368$. From the experimental data given by Ji et.al. [85] the constants were found out to be $d_{avg} = 10.477 \times 10^{-6}$ and $n = 2.2$. The minimum and maximum diameter of particle for simulation is taken as 0.6 and 40 μm respectively.

For simulations the spherical drag and gravity forces are considered for particles. No heat transfer, combustion, chemical reaction, radiation and evaporation models are applied for particle phase. The density of particles is taken as 2700 kg/m^3. Temperature of particles is also taken as 300 K. The turbulent dispersion of particles is considered with Discrete Random Walk (DRW) model given by Gosman and Loannids [87]. Interaction of particles with solid wall is considered to be inelastic with coefficient of restitution as 0.9. The particles interaction with inlet and outlet is modeled as escape condition. The particles are injected at the inlet uniformly with velocity equal to velocity of air at inlet.

Initial & Boundary Conditions: The initial conditions for velocity in the computational domain are obtained by using "potentialFoam" solver. Velocity at the wall is taken as zero (No slip condition). For turbulence, $k - \omega - SST$ model by Menter[88] has been used. The values of k and ω are calculated as follows:

$$k = \frac{3}{2}\left(U_{ref} I\right)^2 \tag{5.43}$$

$$\omega = \frac{\varepsilon}{C_\mu k} \tag{5.44}$$

Where

$$\epsilon = C_\mu^{3/4} \frac{k^{3/2}}{0.07L} \tag{5.45}$$

Wall functions are used for k and ω at the solid walls. Pressure is fixed at the outlet and zero gradient condition is given at the inlet. Temperature field is kept uniform as 300 K within the domain as initial condition and at inlet, while outlet temperature is given zero gradient condition.

The solver is run in parallel on 24 processors using domain decomposition, in which the geometry and associated fields are broken into sub domains and each processor performs computation for the sub domains. Public domain `openmpi` implementation of standard message passing interface (MPI) is used for parallel running. The domain is decomposed using simple method with 2 splits in x and y direction and 6 splits in z-direction.

The solution of pressure is carried out using GAMG (Geometric Agglomerated algebraic Multi Grid) solver while other variables such as velocity, species mass fraction, enthalpy, k and ω are solved using linear `smoothsolver`. Relaxation factors used for pressure, velocity, species mass fraction, enthalpy, k and ω are 0.3, 0.7, 0.7, 0.7, 0.7 and 0.7 respectively.

The various descritization schemes for divergence, gradient and laplacian terms in conservation equations are specified using *fvschems* dictionary. The schems specified for the simulation in Table-5.2:

CFD simulations with parameters and boundary conditions as described above were performed for three different meshes having 84 $\times 10^3$, 307 $\times 10^3$ and 714 $\times 10^3$ tetrahedral cells. Calculations for 10 different cases of inlet air velocities i.e. 6, 8, 10, 12, 15, 18, 20, 22, 25 and 30 m/s were performed for each mesh. The Figure 5.15 shows, velocity contours obtained with inlet air velocity of 30 m/s for the three meshes considered. It can be seen that core structure of vortex flow is captured properly with increasing the mesh resolution.

Table 5.2: Descritization schemes used in OpenFOAM

Modeling term	Keyword for scheme	Description	Scheme
Convection term	*divSchemes*	Descritization of divergence terms with an operator ∇.	*Bounded Gauss upwind*
Gradient term	*gradSchemes*	Descritization of gradient terms with operator ∇	*default Gauss linear*
Diffusive term	*lapacianSchemes*	Descritization of terms with Laplacian operator ∇^2	*Gauss linear corrected*
Time derivative	*ddtSchemes*	Descritization of time derivatives	*steadyState*
Other	*InterpolationSchemes*	Point to point interpolation of value	*Default linear*
	snGradSchemes	Component of gradient normal to cell value	*Default corrected*

Figure 5.16 (a) shows the velocity vectors, which demonstrates the formation of forced vortex flow inside the cyclone separator. It can be seen the flow is highly rotational inside the

cyclone. The injected particles get separated from flow depending on the balance between forces acting on particle, i.e. gravity and drag. Figure 5.16 (b) shows the steady state particle tracks obtained for the case on inlet air velocity of 30 m/s. It can be seen that lighter particles leave the cyclone while heavier particles settle and gets collected at the bottom. The overall separation efficiency is obtained as a ratio of particle mass leaving the cyclone and particle mass introduced at the inlet. The results with various meshes are compared with experimental measurements as shown in Figure 5.17. As the mesh count increases the prediction improved which can be attributed to fact that the velocity profiles are accurately calculated with higher mesh counts. This exercise validates the OpenFOAM solver. It seen that to obtain accurate results we need to accurately capture the velocity field inside the computational domain.

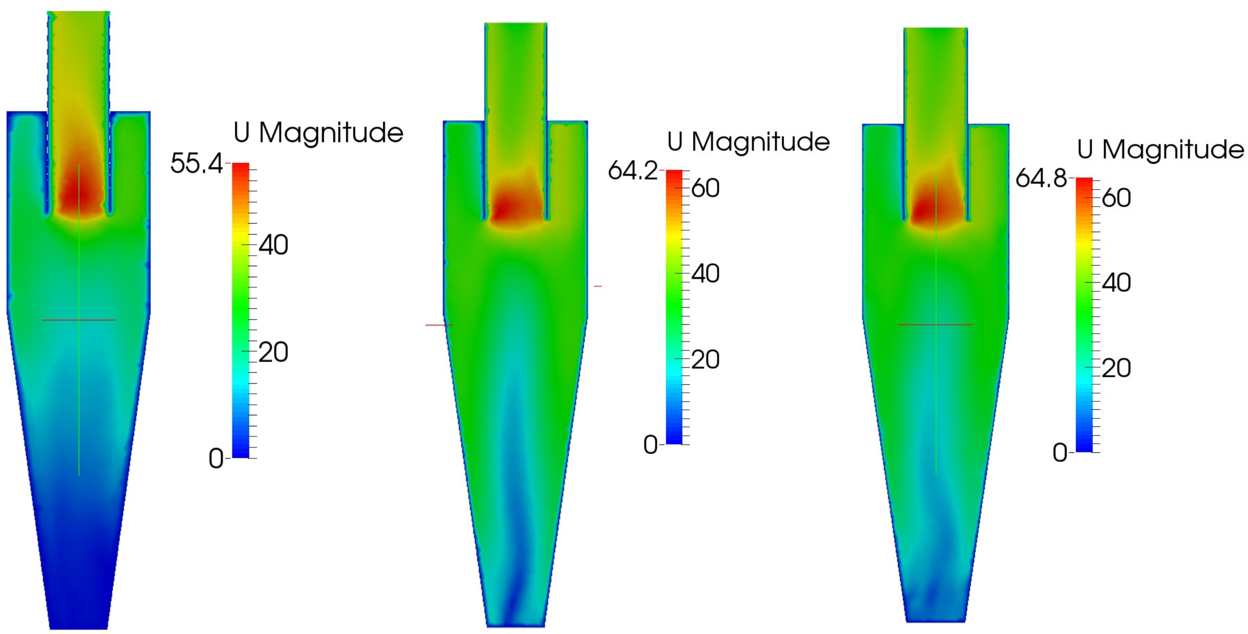

(a) (b) (c)

Figure 5.15: Velocity contours obtained for case with inlet air velocity of 30 m/s (a) Mesh-1(84×10^3 cells) (b) Mesh-2 (307×10^3 cells) (c) Mesh-3 (714×10^3 cells)

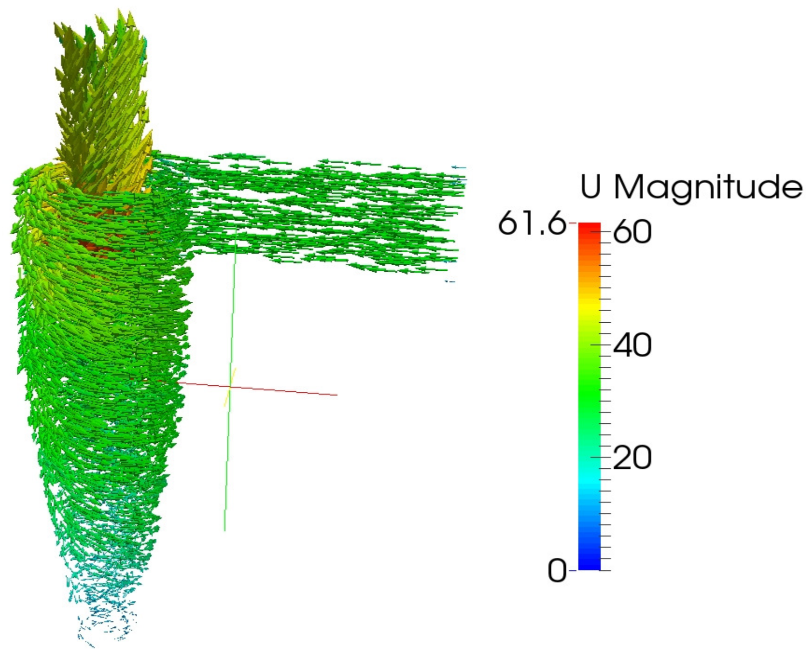

Figure 5.16 (a) : Velocity vectors obtained using Euler-Lagrangian simulation for cyclone separator validation test case at inlet air velocity of 30 m/s, using Mesh-3 (714×10^3 cells)

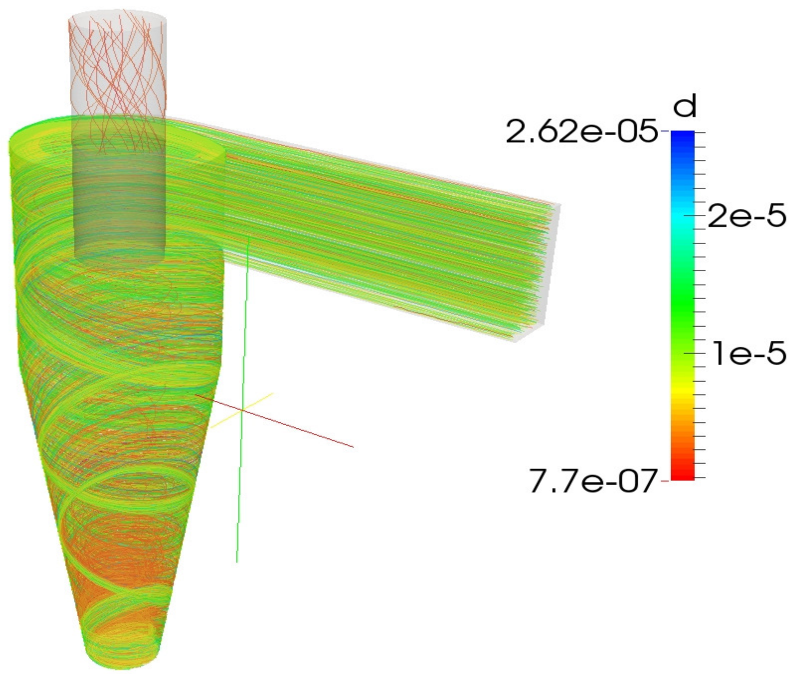

Figure 5.16 (b) : Particle tracks obtained using Euler-Lagrangian simulation for cyclone separator validation test case at inlet air velocity of 30 m/s, using Mesh-3 (714×10^3 cells)

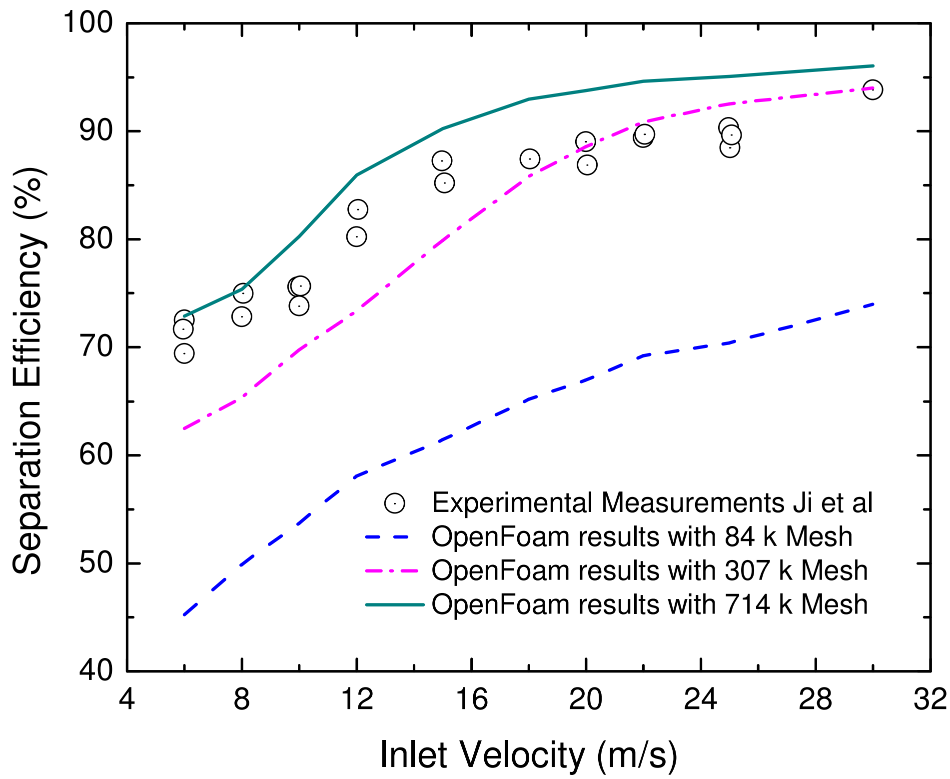

Figure 5.17: Separation efficiency predictions by CFD compared with experimental data.

5.5.3 Euler-Lagrangian Simulation for Air-Water Loop drum

The geometry of the drum is as shown in Figure 5.18. It can be seen that as we move from separation interface to exit, the area available for flow sharply reduces near the exit and the flow accelerates near the exit. For CFD calculations only the space above separation interface was considered. Table-5.3 gives the some of the simulation cases considered in this study. The total air flow rate is taken as 7500 lpm, i.e. 500 lpm per tail pipe channel. The corresponding superficial velocities at the interface are calculated as shown in Table-5.3.

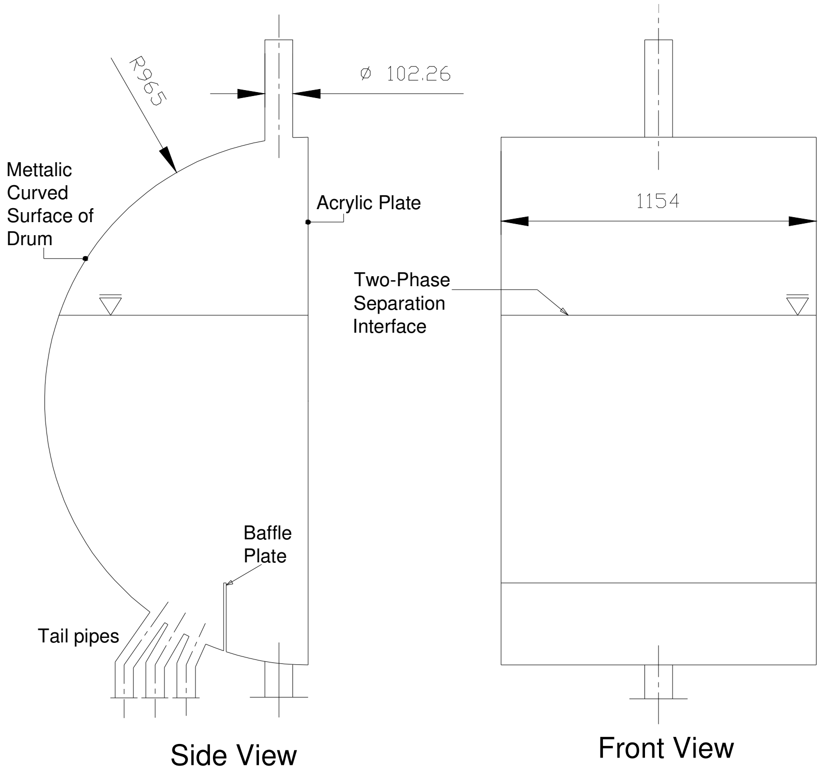

Figure 5.18 : Geometry of AWL drum.

Table 5.3 – Simulation cases for AWL & boundary conditions

Sr. No.	Swell Level (m)	Total air flow rate (lpm)	Velocity of air at interface (m/s)	Turbulent Kinetic Energy – $\boldsymbol{k}$ (m^3/s^3)	Specific Dissipation Rate – $\boldsymbol{\omega}$ (m^2/s^3)
1	0.3	7500	0.155	8.998×10^{-5}	0.284
2	0.5	7500	0.128	6.154×10^{-5}	0.209
3	0.75	7500	0.117	5.110×10^{-5}	0.181
4	0.965	7500	0.112	4.726×10^{-5}	0.170
5	1.1	7500	0.113	4.819×10^{-5}	0.173
6	1.3	7500	0.119	5.372×10^{-5}	0.188
7	1.5	7500	0.135	6.821×10^{-5}	0.227
8	1.7	7500	0.173	1.125×10^{-5}	0.341
9	1.8	7500	0.224	1.880×10^{-5}	0.524
10	1.85	7500	0.281	2.973×10^{-5}	0.779
11	1.9	7500	0.454	7.719×10^{-5}	1.831

Simulations are also carried out for total air flow rate of 6000lpm and 3000 lpm covering the range of air flows for which entrainment was measured. The superficial velocity varies with swell level though the total air flow rate is same, because of curvature of the drum. The air gets separated at interface and is treated as continuous phase with “Euler” formulation. At the interface droplets are formed due to bubble rupture and are treated as discrete phase (Lagrangian) for simulation. Droplets were assumed to be spherical in shape. The flux of droplets and size distribution present at the interface is one of the important input parameter for simulation. The droplet size distribution measured experimentally is used for simulation. The droplet ejection velocity can be conservatively taken as 1 m/s. Figure 5.19 shows mesh generated for the case-4 swell level 0.965 m, (Table-5.3). The domain is descritized with 1164×10^3 tetrahedral elements. The element size near the exit of drum and in the exit pipe is kept smaller than the remaining domain, in order to capture the sharp gradients of velocity and other fields, and to effectively reduce the computational time by using coarser mesh on other areas. In the meshed domain, the bottom surface is taken as inlet, pipe exit is taken as outlet, remaining all surfaces are taken as wall boundary.

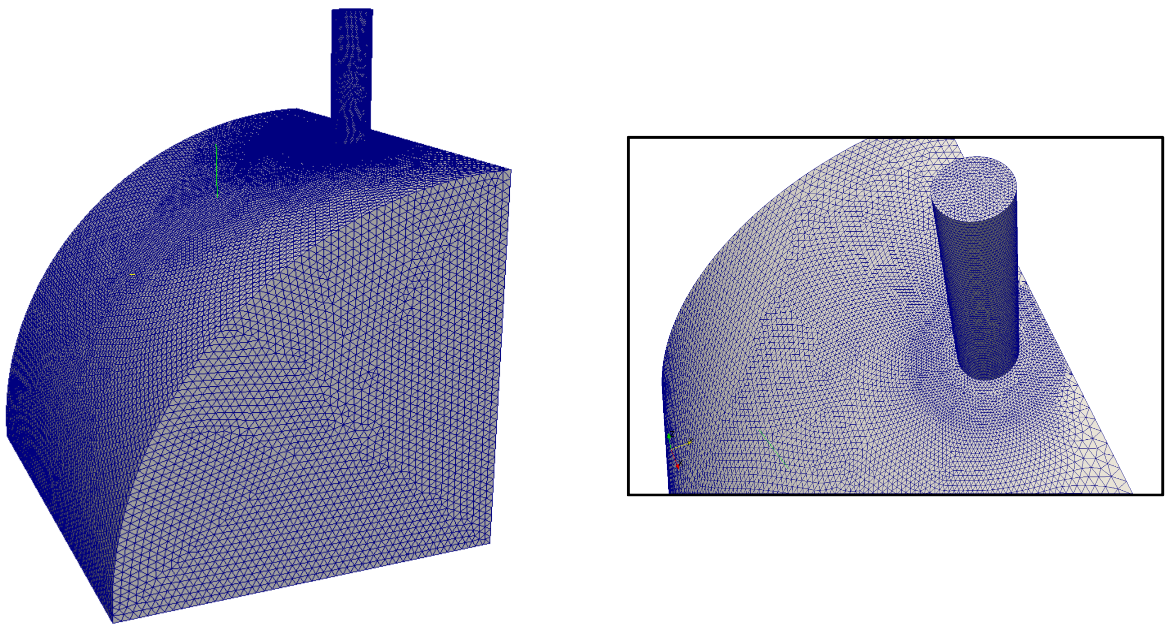

(a) (b)

Figure 5.19: Mesh used for case-4 (swell level 0.965m) 1523 k tetrahedral elements

The calculations were performed in three steps. First the flow was solved using "*potentialFoam*" solver, a solver for velocity potential to calculate the flux-field from which velocity field was obtained. The velocity field obtained was then used as initial condition for "*simpleReactingParcelFoam*" solver, which solves conservation equations for mass, momentum and energy as described in earlier section. In this step, no droplets were injected and a converged solution for flow, pressure and energy field was obtained. In third step, droplets were injected in to the flow (converged solution from earlier step) and iterations were performed untill the steady state results with droplets (Lagrangian phase) were obtained.

The fluid considered for simulation was air at ambient pressure and temperature. The polynomial based thermodynamic model for properties of air were modeled as described by following equations.

$$\rho_{air} = 4.0097 + (-0.016954) \times T + (3.3057 \times 10^{-5}) \times T^2 + (-3.0042 \times 10^{-8}) \times T^3 + (1.0286 \times 10^{-11}) \times T^4 \quad (5.46)$$

$$C_{p-air} = 948.76 + (0.39171) \times T + (-9.5999 \times 10^{-4}) \times T^2 + (1.393 \times 10^{-6}) \times T^3 + (-6.2029 \times 10^{-10}) \times T^4 \quad (5.47)$$

$$\mu_{air} = 1.5061 \times 10^{-6} + (6.16 \times 10^{-8}) \times T + (-1.819 \times 10^{-11}) \times T^2 \quad (5.48)$$

$$\lambda_{air} = 0.0025219 + (8.506 \times 10^{-5}) \times T + (-1.312 \times 10^{-8}) \times T^2 \quad (5.49)$$

The air temperature T was taken as 300 K. The dispersed phase was represented by solid spherical droplets having droplet size distribution as per Equation (5.1) & (5.2). The DSD was entered as an input in tabular form in "*reactingCloudProperties*" file in "*constant*" directory of test case. For simulations, the spherical drag and gravity forces were considered. No heat transfer, combustion, chemical reaction, radiation and evaporation models were applied. The density of droplets was taken as 1000 kg/m^3. Temperature of particles was also taken as 300 K. The turbulent dispersion of particles was considered with Discrete Random Walk (DRW) model. [87]. Interaction of droplets with solid wall was modeled as "capture" condition, which represents the deposition of droplet on wall. The particles interaction with inlet and outlet was modeled as "escape" condition. The droplets were injected at the inlet uniformly with velocity of 1m/s. The initial conditions for velocity in the computational domain were obtained by using "potentialFoam" solver. Velocity at the wall was taken as zero (No slip condition). For turbulence, $k-\omega-SST$ model [88] has been used. Table-5.3 gives the inlet boundary conditions for velocity, k and ω for the cases considered. Standard wall functions were used for k and ω at the solid walls. Pressure was kept fixed at the outlet boundary and zero gradient condition was given at the inlet. Temperature field was kept uniform as 300 K within the domain as initial condition and at inlet boundary, while outlet boundary temperature was given zero gradient condition.

The various descritization schemes for divergence, gradient and laplacian terms in governing equations were specified using "fvschems" dictionary of OpenFOAM case directory. The schemes specified for the simulation are as per Table-5.4.

Table 5.4: Descritization schemes used in OpenFOAM simulation of cyclone separator

Modelling term	Keyword for scheme	Description	Scheme
Convection term	*divSchemes*	Descritization of divergence terms with an operator ∇.	*Gauss upwind*
Gradient term	*gradSchemes*	Descritization of gradient terms with operator ∇	*default Gauss linear*
Diffusive term	*lapacianSchemes*	Descritization of terms with Laplacian operator ∇^2	*Gauss linear corrected*
Time derivative	*ddtSchemes*	Descritization of time derivatives	*steadyState*
Other	*InterpolationSchemes*	Point to point interpolation of value	*Default linear*
	snGradSchemes	Component of gradient normal to cell value	*Default corrected*

Figure 5.20 shows the velocity contours obtained for the case-4 (Table-5.3). The acceleration of flow near the exit is clearly seen in the Figure 5.20. The flow in the exit pipe is not symmetric due to the fact that it is placed off the centerline of geometry. Velocity at the interface is of the order of 0.11 m/s, while maximum velocity of 20.6 m/s was found to be near the exit. As discussed earlier in validation test case that the accurate prediction of velocity flow patterns gives accurate results for Lagrangian simulation also. The mesh shown in Figure 5.19 was refined to get higher resolution mesh and the simulation was carried out to obtain the velocity flow patterns in the drum. Figure 5.21 shows the variation of velocity along the vertical line aligned with axis of exit pipe for the three meshes. Figure 5.22 shows the velocity magnitude along the horizontal line at the cross-section of exit pipe for the various meshes considered in simulation. These figures show that the mesh size with 15.2 lacs is sufficiently fine to capture the velocity gradients. The meshing parameters were thus optimized and the same were used to generate meshes for other simulation cases.

The droplets trajectories obtained after Euler-Lagrangian simulation for case-4 are shown in Figure 5.23 (a) and (b). It can be seen that the heavier droplets travel some distance above the interface and fall back to the interface (inlet boundary). Droplets of size 50 to 60 microns and smaller were found to be entrained in bulk of the flow and travel up to the throat region near exit and till the outlet. Very few of them get deposited on side walls. Velocity of droplets is shown in Figure 5.23 (b).

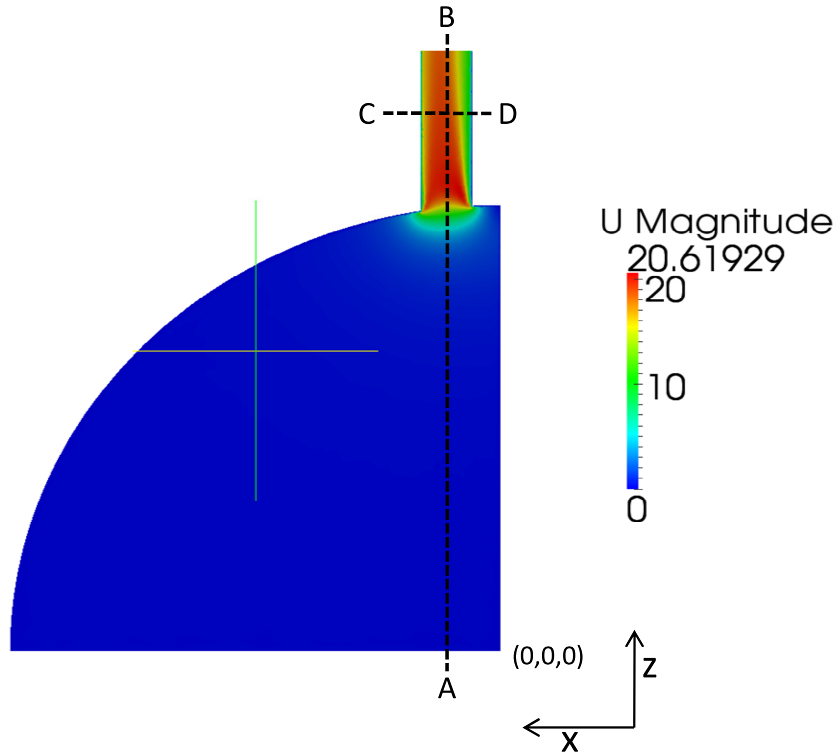

Figure 5.20: Velocity field for Air obtained using Euler Simulation

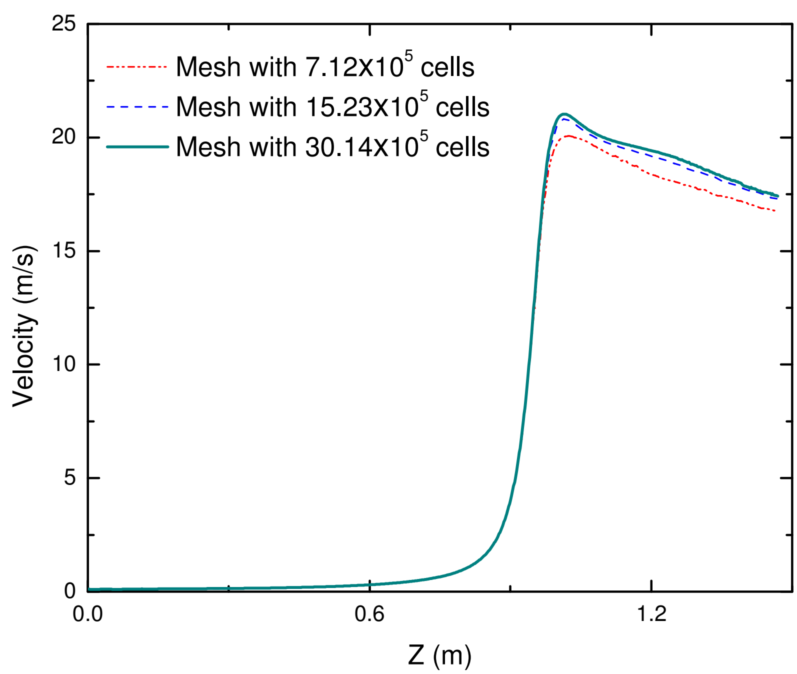

Figure 5.21: Velocity magnitude predicted along line AB (as shown in Figure 5.20) for different meshes considered

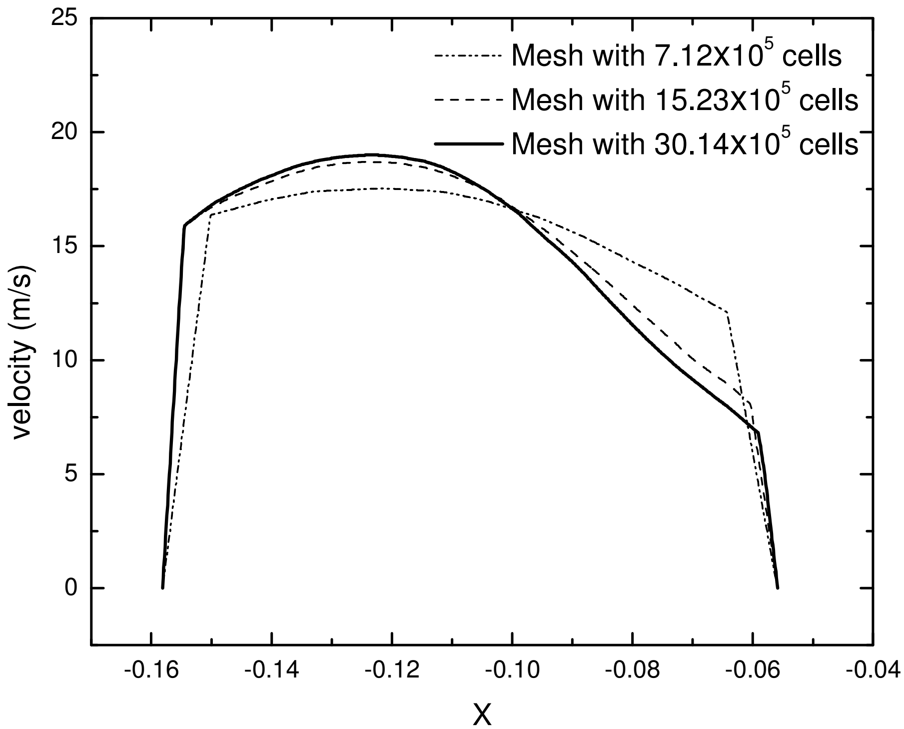

Figure 5.22: Velocity magnitude predicted along line CD (as shown in Figure 5.20) for different meshes considered.

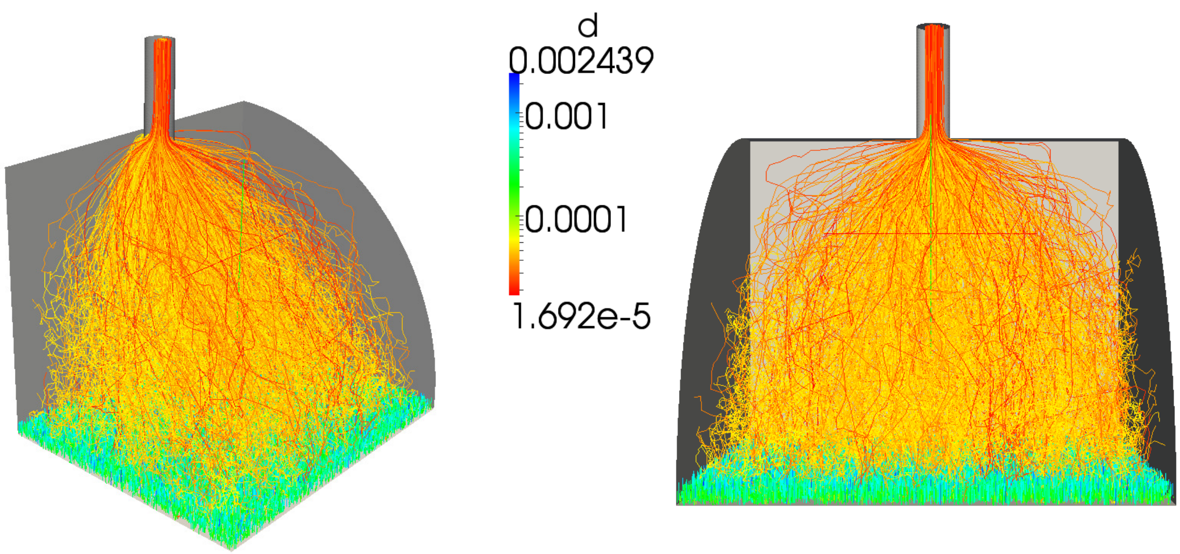

(a)

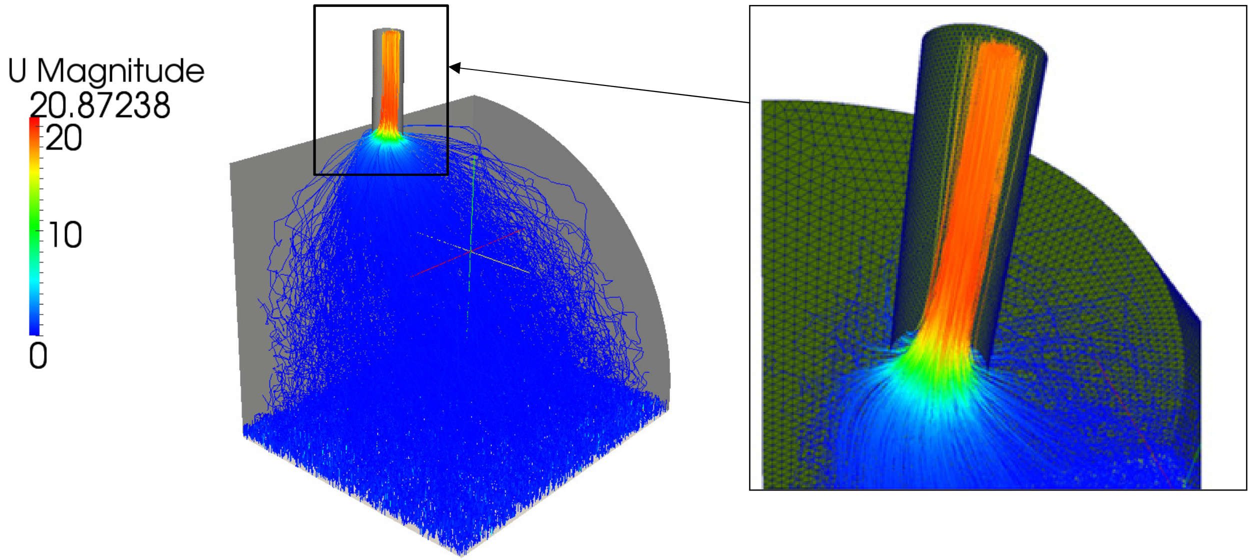

(b)

Figure 5.23: Particle tracks obtained for CFD simulation case-4 (Table-5.3): (a) tracks colored with droplet diameter (b) tracks colored with droplet velocity.

The droplets at exit attain the velocity of air, which is a characteristic of entrained droplets. Similar results are obtained for other cases also. Based on the cumulative mass of droplets at the exit, the entrainment at exit was found.

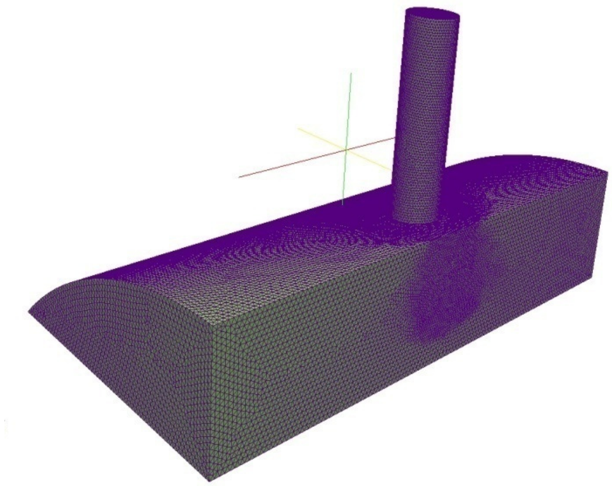

(a)

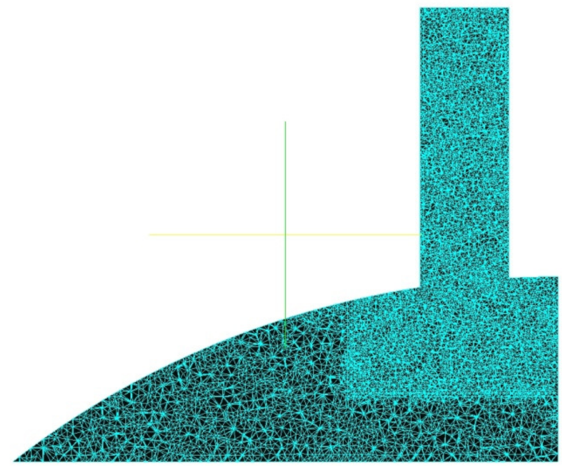

(b)

Figure 5.24: Mesh used for AWL Euler-Lagrangian simulation case no 8. (a) 3-D view, (b) cross-sectional view showing mesh density near exit

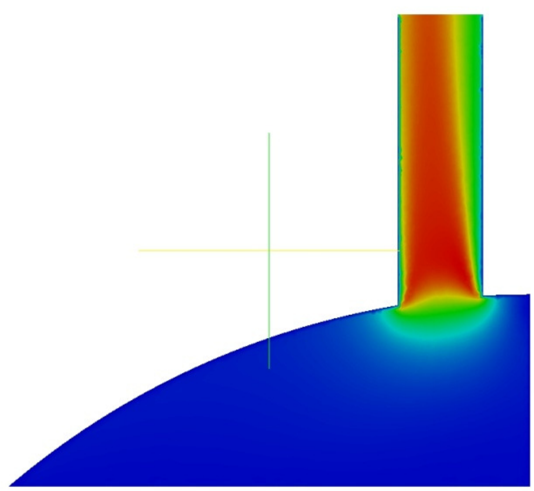

Figure 5.25: Velocity contours obtained for AWL Euler-Lagrangian simulation case no 8.

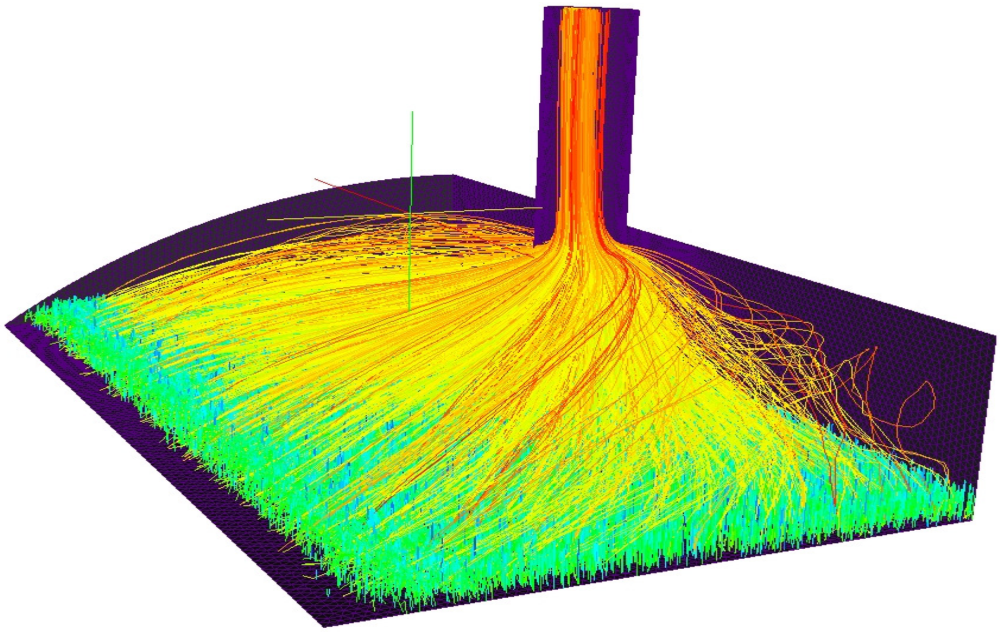

(a)

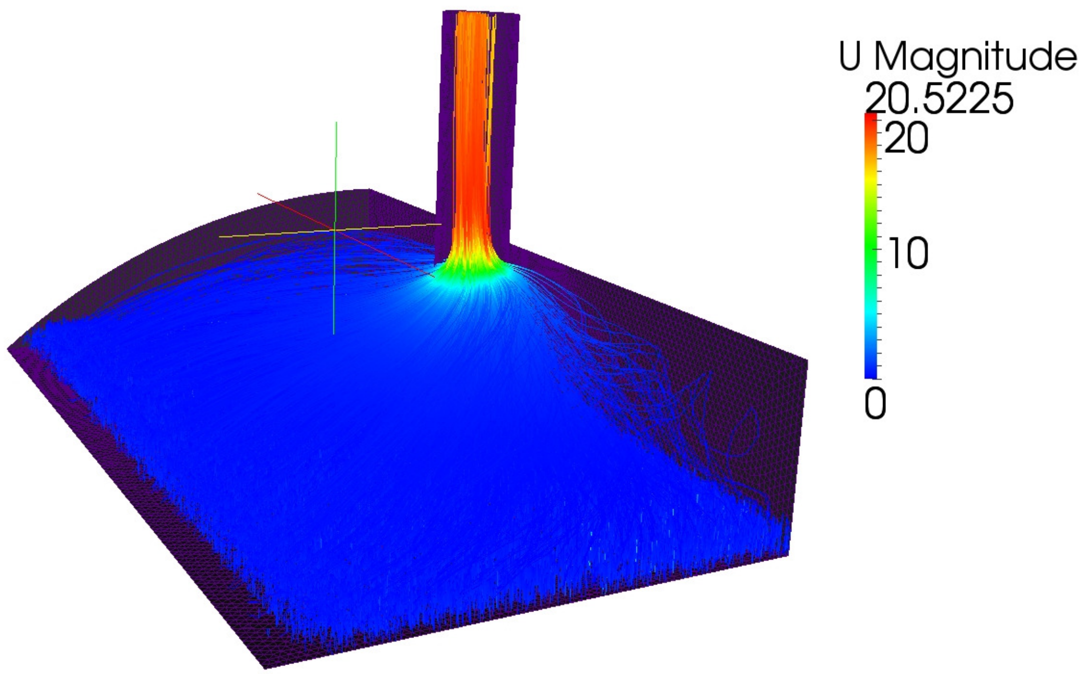

(b)

Figure 5.26: Particle tracks obtained for AWL Euler-Lagrangian simulation case no 8. (a) tracks colored with droplet diameter (b) tracks colored with droplet velocity

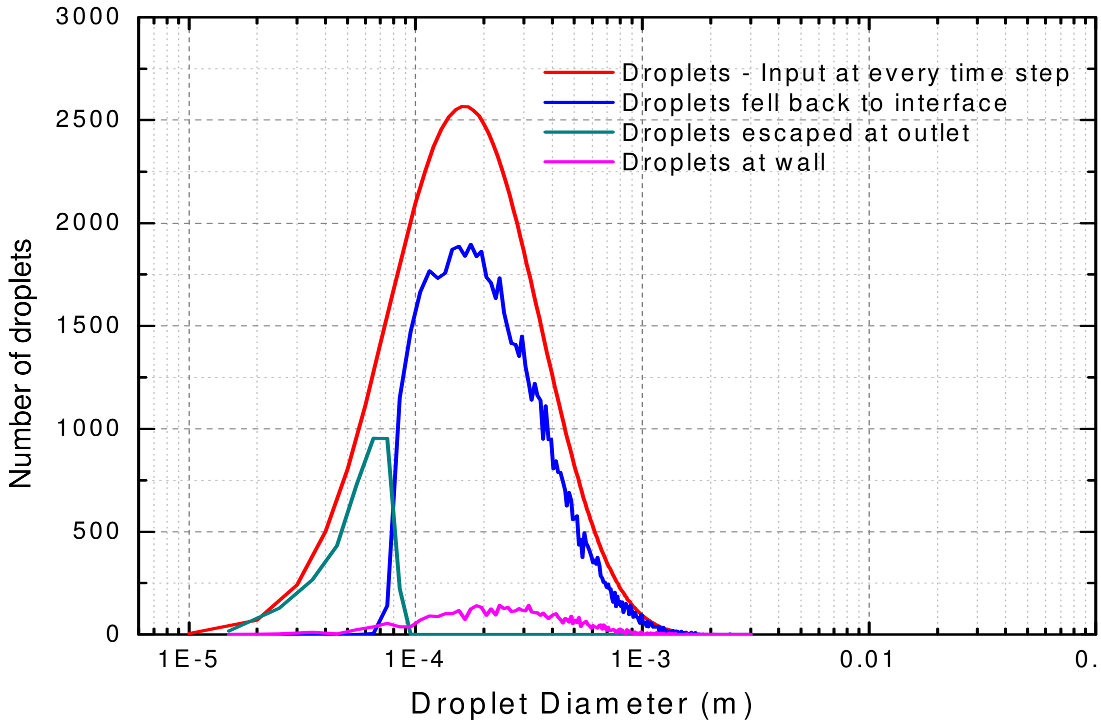

Figure 5.27: Histogram of droplets from CFD simulation

Figure 5.27 shows the histogram (statistics) of droplets injected at inlet, droplets collected outlet and fell back to inlet and droplets deposited on wall. It can be seen that most of the small sized water droplets (diameter < 100 μm) were carried out of drum with air and thus constitute the carryover amount. Most of the heavier droplets fell back to inlet and some got deposited on wall.

Figure 5.28 shows the spatial distribution of droplets at the inlet of the domain considered for simulation. It can be seen that droplets are uniformly distributed at the inlet as per the given boundary condition. Figure 5.29 shows the droplet distribution at the outlet cross-section and the axial velocity contours. It can be seen that maximum droplet size at outlet is of the order of 90 to 100 microns and the droplets are concentrated at the center where the velocities are high.

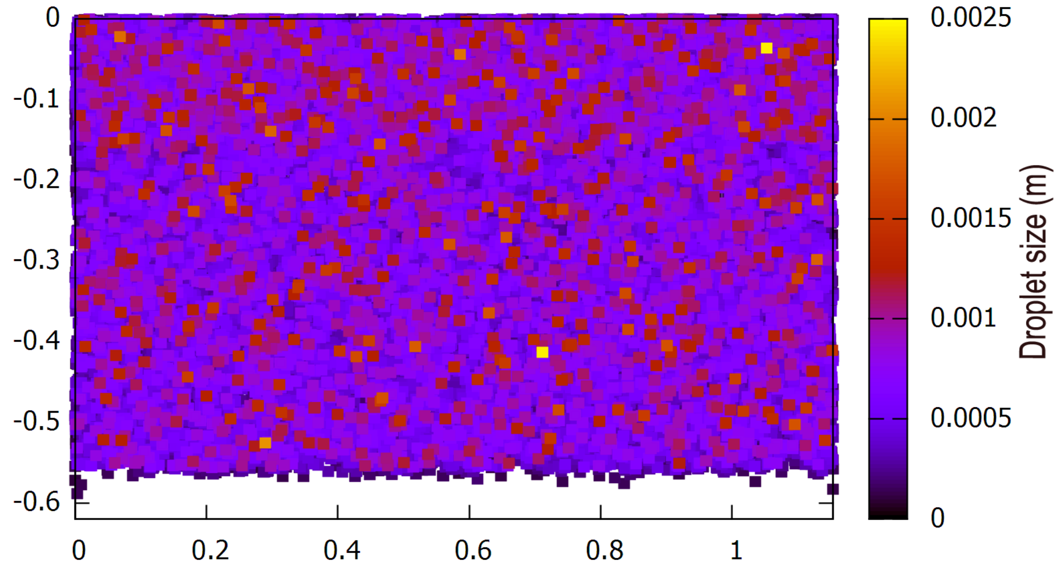

Figure 5.28: Droplet distribution at the inlet

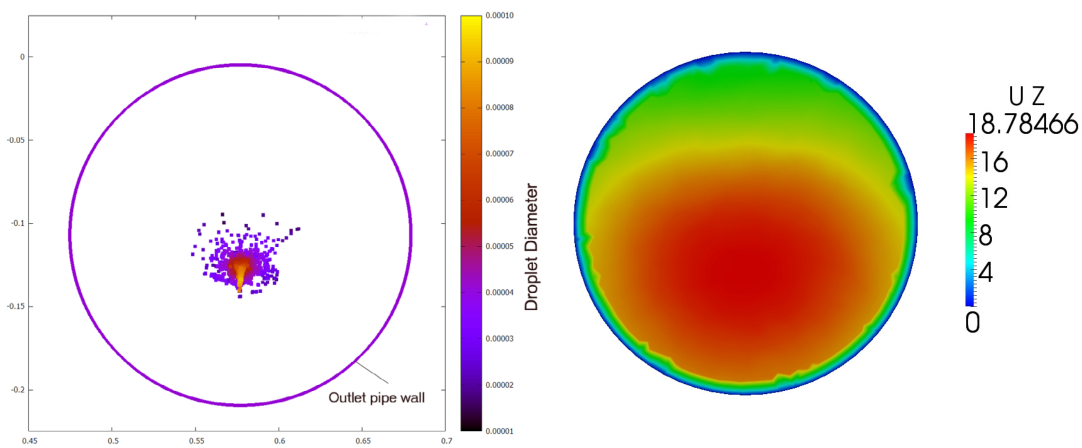

Figure 5.29: Droplet distribution at the outlet

The entrainment obtained for all the cases listed in Table-5.3 is shown in Figure 5.30. Figure 5.30 also shows the result for cases for total air flow rate of 6000 lpm and 3000 lpm. Herein, the results from correlations and 3-D calculations with OpenFoam are compared.

Carryover prediction by Euler-Lagrangian CFD calculations show similar trends at lower operating levels (0.3 to 1.5m) for case of 7500 total air flow rate, when compared with Kataoka & Ishii correlation [30]. For the 3000 lpm case the predictions are significantly smaller. The correlation indicates that entrainment is governed by low & intermediate gas flux region for low levels and shows sharp rise in entrainment in high gas flux region. CFD predictions show smooth transition between these regions. Estimates by CFD are conservative near the transition point between intermediate gas flux regions to high gas flux region. It can be seen that CFD predictions are comparable/close to predictions by correlation for higher flow rate cases (7500 lpm and 6000 lpm)

For 3-D CFD simulations with swell level > 1.8 m, many droplets were seen deposited on the wall of domain ("stick" condition for interaction of droplet to side walls of drum is applied in solver). Therefore entrainment predicted was smaller than the measurements. At these levels the entrainment out of drum is governed by high gas flux momentum controlled regime and near surface regime. At levels closer to exit as seen in Figure 5.1, the swell level was oscillating and intermittently large fragments were thrown out to exit. The CFD simulation considers a fixed domain with fixed inlet boundary i.e. a constant non-oscillating level. Also a fixed DSD is given to CFD calculations with maximum droplet diameter of 2.7 mm. As observed in experiments large liquid fragments are also entrained in the flow, which is difficult to simulate with the current CFD case set-up. Because of these reasons, predictions are not accurate for these cases. Near the exit air velocity increases rapidly as cross-sectional area for flow reduces. CFD simulation results show the air velocity is 10 m/s or higher in the vicinity of exit and in exit pipe it reaches as high as 20 m/s. It was found that equation for high gas flux regime by Kataoka and Ishii [30] is applicable in this region. Kataoka and Ishii [30] have stated that, in high gas flux regime and near surface regime, entrainment consists of all the droplets from pool surface. Measuring data in this region is difficult as surface is highly agitated. The only data available to Kataoka and Ishii was by Rozen et al. [21], who obtained the data by extrapolating entrainment measured in momentum controlled region. Kataoka and Ishii [30] have also shown that in this regime the entrainment increases sharply, $E_{fg} \propto \left(J_g^*/h^*\right)^{7-20}$, and no reliable data were available and thus it was set as upper limit of entrainment i.e. $E_{fg} = 4.0$. Therefore correlation also predicts constant carryover of 400 % at swell level above 1.8 m. The 3-D Euler-Lagrangian simulations near the exit region are not accurate as it does not account for the fluctuating level and the formation of large liquid fragments and their conveyance through exit pipe.

For prototype case, the reactor will have a trip based on high level in the steam drum to avoid the excessive carryover to steam line. CFD Simulations from AWL thus provide important guidelines and understanding for conducting similar CFD exercises for prototype.

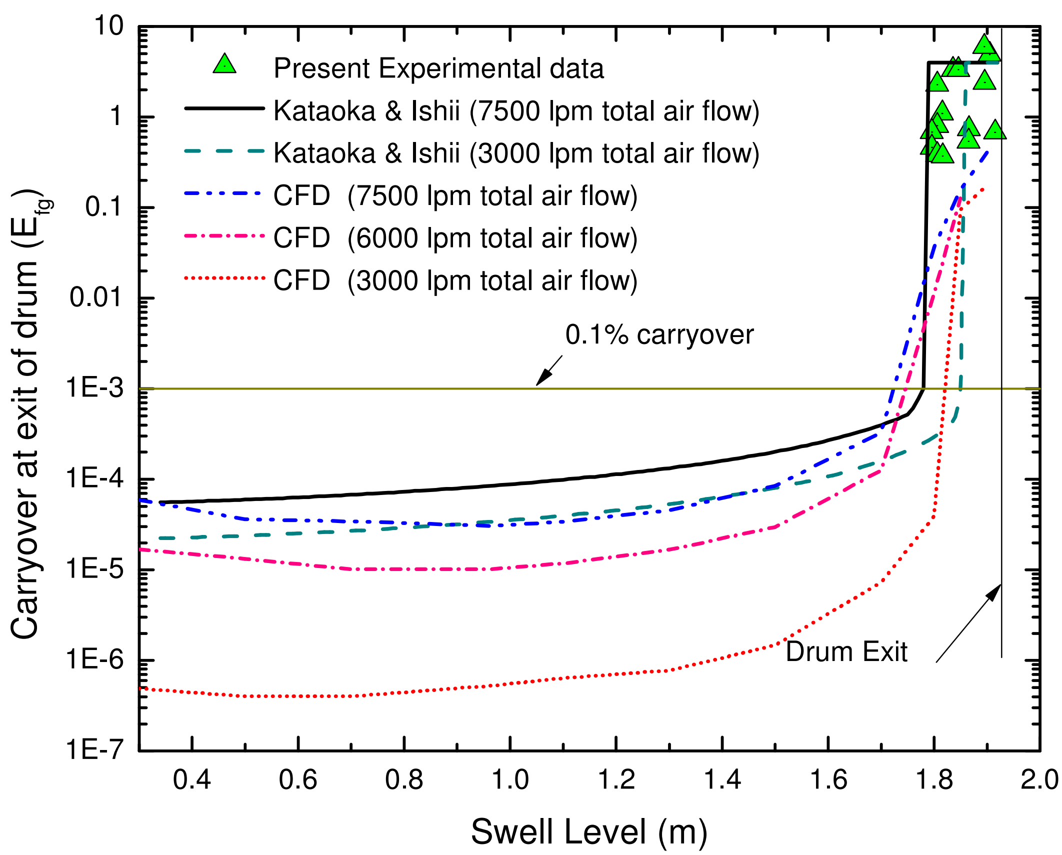

Figure 5.30: Comparison of prediction of carryover by E-L simulations, correlations and experimental data.

5.6 Euler-Lagrangian Simulation for AHWR drum

The geometry considered for simulation is as shown in Figure 1.2. The AHWR steam drum has diameter of 4.0 m and length of 11.0 meter and four steam outlets connected to common steam header. The geometry is modeled and meshes are obtained as shown in Figure 5.31 (a), (b) and (c).

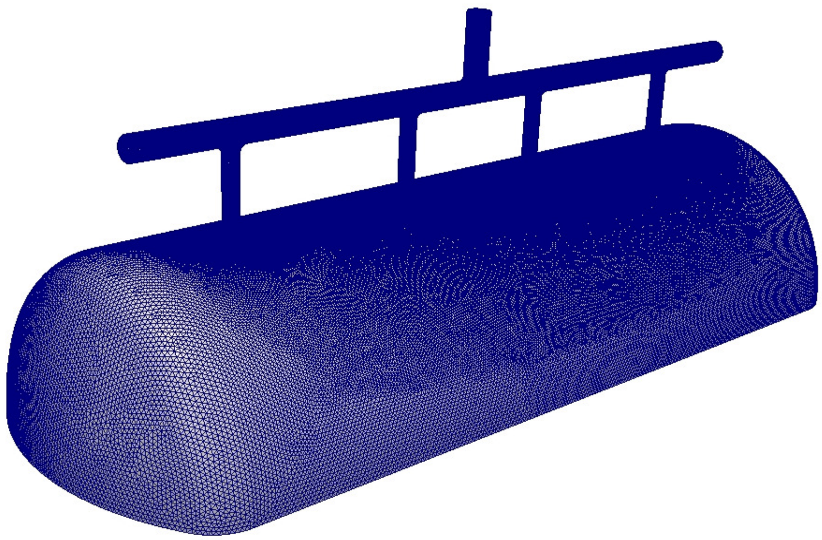

(a)

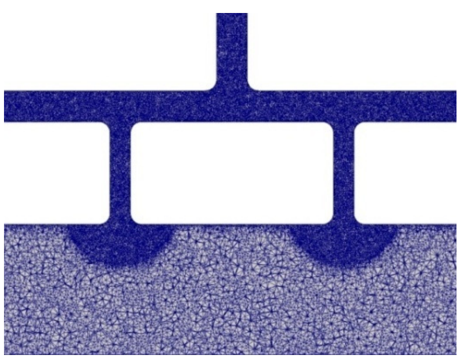

(b)

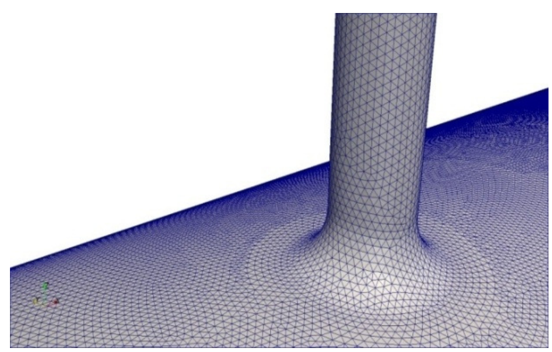

(c)

Figure 5.31: 3-D modeling and Meshing of AHWR steam drum

From previous studies with AWL drum, it was seen that finer meshes are only required near the outlet exit region and in the outlet pipes including common header. Figure 5.31 (b) shows the mesh gradation near the exit region. Table-5.5 gives the simulation cases considered. Only vapor portion of the drum is considered as a computational domain. As domain has fixed inlet boundary representing the separation interface, it can be noted that the level fluctuations are not accounted here for simulation. The physical properties of steam at 70 bar and 285 ^{O}C are assigned to the fluid considered in the domain.

Table 5.5 – Simulation cases for AHWR steam drum & boundary conditions

Sr. No.	Swell Level	Velocity of steam at interface	Turbulent Kinetic Energy ($\boldsymbol{k}$) for air	Specific Dissipation Rate ($\boldsymbol{\omega}$) for air
1	2	6.347×10^{-2}	1.51×10^{-5}	3.634×10^{-3}
2	2.2	6.379×10^{-2}	1.53×10^{-5}	3.659×10^{-3}
3	2.4	6.478×10^{-2}	1.57×10^{-5}	3.737×10^{-3}
4	2.6	6.654×10^{-2}	1.66×10^{-5}	3.876×10^{-3}
5	2.8	6.925×10^{-2}	1.80×10^{-5}	4.097×10^{-3}
6	3	7.329×10^{-2}	2.01×10^{-5}	4.433×10^{-3}
7	3.2	7.934×10^{-2}	2.36×10^{-5}	4.958×10^{-3}
8	3.4	8.888×10^{-2}	2.96×10^{-5}	5.833×10^{-3}
9	3.6	10.57×10^{-2}	4.20×10^{-5}	7.533×10^{-3}

Eulerian calculations are carried out first to obtain converged velocity fields inside the drum. Figure 5.32 shows velocity patterns obtained for Case-1 described in Table-5.5. The case test set-up i.e. turbulence models, solution control parameters, parallel processing algorithm etc are as explained in detail for AWL case.

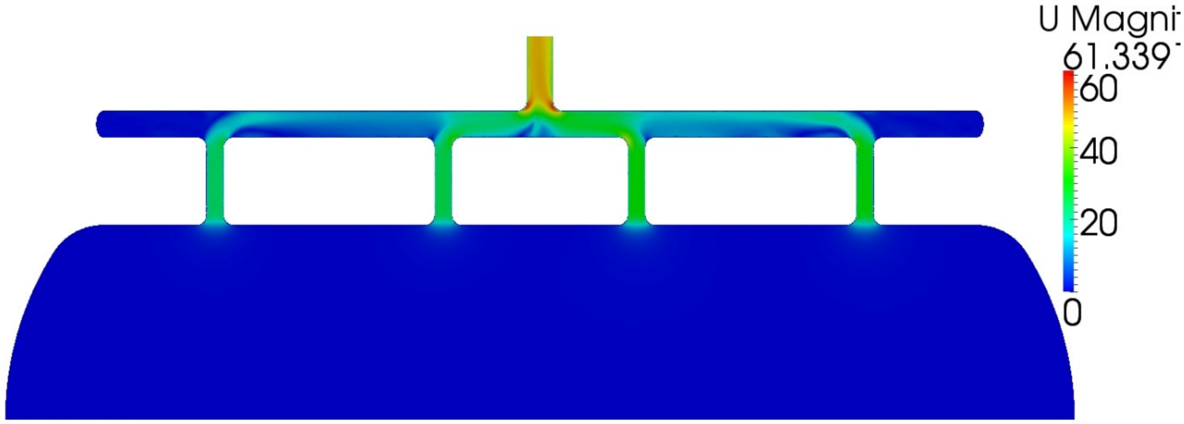

Figure 5.32: Velocity field calculated for AHWR steam drum (case-1, Table-5.5)

Once the converged solutions for velocity pattern for all the cases is obtained, Lagrangian calculations with two-way coupling is carried out using OpenFoam solver described in earlier sections. The droplet size distribution is crucial input parameter for this simulation. Since we do not have experimental measurements on DSD for AHWR case, it can be assumed that the DSD will be similar to that of AWL as described by equation (5.1) and (5.2), with same distribution parameters. However, the maximum droplet diameter in case of high pressure high temperature steam-water mixture will be much smaller, as effect of change in physical properties. The surface tension for steam-water is 0.017633 N/m while for air-water it is 0.0711942 N/m, i.e. 4 times smaller than air-water mixture. The droplet formation mechanisms will be same irrespective of fluids; however the quantification of droplets will be affected by fluid properties. We can use the non-dimensional numbers for arriving at maximum size of droplet for steam-water case. The droplet formation processes are often characterized with Weber number as described below:

$$We = \frac{Kinetic\ Energy}{Surface\ energy} = \frac{\rho U^2 d}{\sigma} \tag{5.50}$$

If the maximum Weber number, $We - max = \rho U^2 d_{max}/\sigma$ is conserved for both cases i.e. model and prototype, since we know maximum droplet diameter measured in model, the maximum droplet diameter for prototype i.e. AHWR steam drum is found out to be 0.9 mm, assuming that droplet velocities at the time of formation are of same magnitude. Based on this information the DSD for AHWR case is obtained (as shown in Figure 5.33).

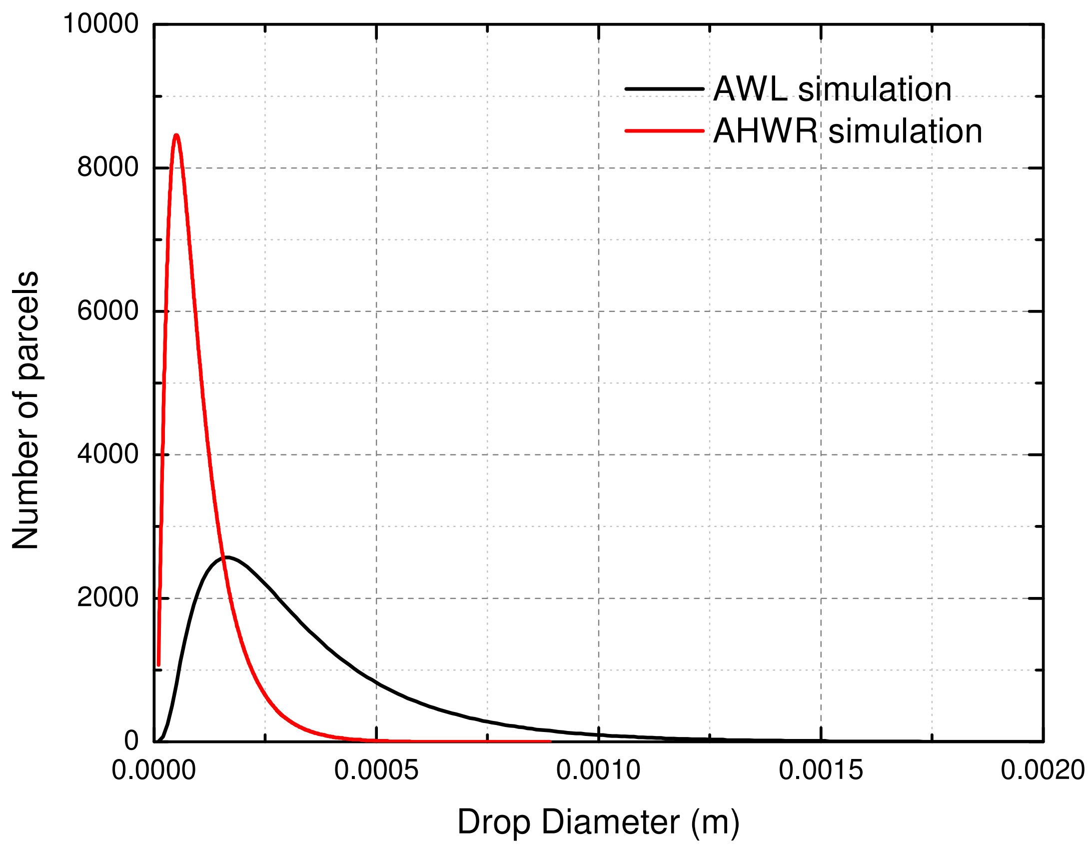

Figure 5.33: Droplet size distributions considered for AWL and AHWR simulation cases

The Lagrangian calculations are being performed for all the cases described in Table-5.5. Figure 5.34 and 5.35 shows the droplet trajectories for case-3, Table-5.5. Based on the mass of droplets carried out to exit of drum and mass of droplets added at the inlet entrainment is found out. Figure 5.36 shows result obtained based on the simulation cases completed. The entrainment sharply increases for operating level > 3.5 m, indicating the high gas flux regime. Below this level, it can be seen that predictions from CFD simulations are matching very well with Kataoka and Ishii [30] correlation. As seen from AWL experiments and CFD simulations for high gas flux regime, the effects of oscillating level and formation of large liquid fragments have not been accounted. Therefore predictions for cases with level > 3.5 m are not so accurate. A Volume of Fluid (VOF) approach would provide better simulations for such cases (high gas flux regime), however it may not be fast and economical compared to the present approach. So even with these known limitations of present approach, we still can produce reliable information on carryover process. From Figure 5.36 it can be concluded that swell level shall be always maintained below 3.5 m in order to maintain carryover less than a 0.1 % as prescribed by IAPWS [83].

Figure 5.34: Particle tracks / droplet trajectories colored with diameter obtained for Case-3, Table-5.5.

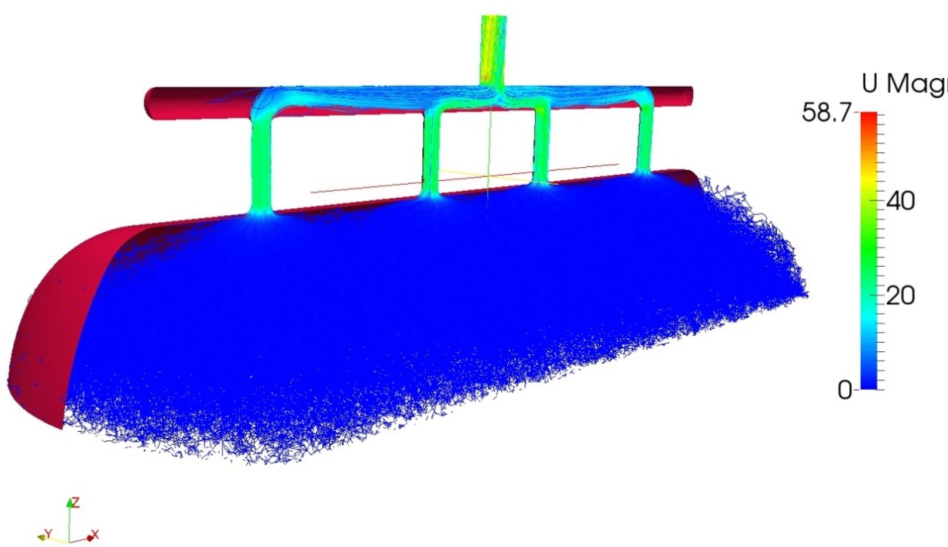

Figure 5.35: Particle tracks / droplet trajectories colored with velocity obtained for Case-3, Table-5.5.

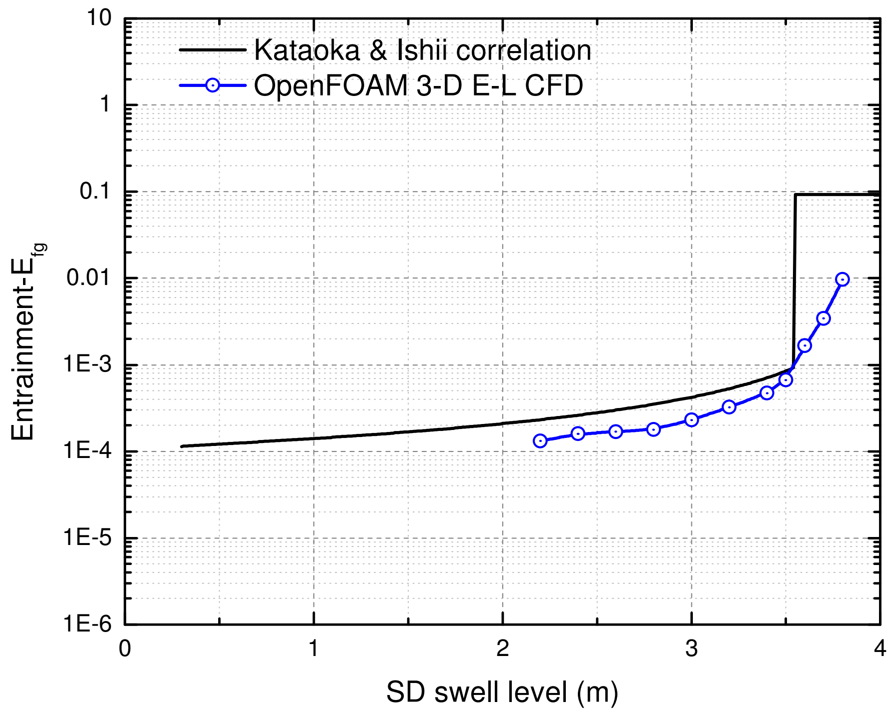

Figure 5.36: Carryover prediction for AHWR steam drum based on CFD calculations

5.7 Summary and conclusion

The AHWR steam drum which has circular cross-section and horizontal layout (4 meter diameter and 11 meter length) provides sufficient area for gravity separation i.e. (due to density difference between steam and water) of steam from mixture. The carryover i.e. conveyance of liquid droplets from separation interface to exit of drum for AHWR steam drum can be conservatively estimated provided the droplet size, velocity distribution and vapor flow velocity/patterns above the interface are known. Analytical models and empirical correlations from literature were studied. It was found that experiments in relevant geometry (similar to AHWR steam drum) are not readily available. Also detailed investigations on droplet generation, size distribution was necessary to develop further understanding of phenomenon. A scaled down model of prototype and experimental facility Air-Water Loop (AWL) was constructed with transparent windows for visual observations. The facility operates with air-water mixture at atmospheric conditions. Experimental measurements on carryover were carried out at high operating swell levels and database of carryover at high gas flux regime or near surface regime was obtained. The observation confirms the claims made by previous studies that near surface entrainment are as high as 400%. At various swell levels, droplet size distributions were obtained by utilizing high speed photography combined with shadowgraph technique and image processing algorithms. The size distribution was fitted with ULLN distribution curves and distribution parameters were obtained. Euler-Lagrangian methodology was used to calculate the droplet trajectories and carryover. 3-D CFD calculations were performed using OpenFOAM solver to obtain velocity flow patterns in vapor space. Lagrangian tracking of droplets within the 3-D computational domain was carried out. The comparison between correlations and E-L simulations showed that CFD calculations are close to correlation at lower operating levels where entrainment out of drum is governed by deposition controlled regime. The E-L simulations may not be particularly accurate for cases with swell level near the exit, as effects of level fluctuations and violent ejection of water fragments is not considered. The E-L methodology was extended for prototype calculations. For Lagrangian simulations in AHWR steam drum, the DSD was obtained by assuming that maximum Weber number is conserved for model and prototype. CFD results have been found to agree well with Kataoka & Ishii [30] correlation for low and intermediate gas flux regime. It is also concluded that for AHWR steam drum the swell level shall be always maintained below 3.5 m in order to maintain carryover less than a 0.1 % as prescribed by IAPWS [83]. For the operating level below 3.5 meters the carryover is well within acceptance criteria.

Chapter 6

Experiments and analysis of pool void fraction and swell level in drum

6.1 Introduction

As discussed in earlier chapter, the entrainment/carryover from a bubbling pool surface is function of superficial velocity of carrier gas phase, and the vapor space height, i.e. distance of separation interface from the exit of equipment. As observed during experiments in AWL, with increase in gas/vapor flow rate the swell level increases as a result of increase in average pool void fraction. The vapor space height is thus function of average pool void fraction. The pool void fraction/gas holdup is function of number of parameters such as (a) gas/vapor flow rate, (b) hydraulic diameter of vessel, (c) liquid flow rate, (d) fluid properties such as density, viscosity, surface tension etc. which are in turn function of operating pressure and temperature. The injected gas occupies part of volume of pool in the form of bubbles. The bubbles rise upwards from inlet to separation interface, due to buoyancy however; their motion is opposed by the decelerating forces such as drag, lift and virtual mass force. The force balance on the bubble determines its velocity and residence time inside the pool. The forces depend on bubble volume and surface and projected area. Thus the bubble diameter is most important parameter for bubble dynamics inside the pool. The bubble frequency/numbers and size distribution within the pool thus finally determines the average pool void fraction. This bubble dynamics and its dependence of several parameters form a complex problem to be solved. Most often the void fraction is estimated using simplified empirical correlations including 1-D drift flux models. These correlations are obtained from experiments in identical geometries at variety of operating conditions as vast as possible. There are several such correlations available in literature and validity of a particular correlation for an application under considerations remains in question.

In our application where a large pool of bubbles is encountered the hydraulic diameter of vessel is too large when compared with the geometries in which the experiments have been performed to obtain standard void fraction models. Very few experiments exist in literature which deals with the large diameter vessels. Also in our case since the steam drum is a horizontal cylindrical vessel with two phase flow from side bottom part, the flow cross-section varies along with height of pool. Therefore accurate prediction of pool void fraction and swell level for steam drum geometry can be only ensured after detailed experimental and analytical studies. We have therefore carefully measured the bubble size distribution, pool void fraction and swell level during experiments in AWL. In this chapter these measurements are described, along with its comparison with empirical correlations from literature and 3-D CFD simulation of pool swell phenomenon. The chapter will also discuss the information extracted from detailed data available from CFD simulation such as local gas and liquid velocities, local void fraction, slip velocity etc. and determination of drift flux parameters from CFD simulations.

6.2 Experimental measurement of average pool void fraction

Steady state experiments were conducted in AWL with some initial water inventory in the drum, and injecting air flow at the bottom of tail pipe section of 15 pipes connected to drum. The air flow was kept same in all the 15 pipes and was increased in steps i.e. 0 lpm, 50 lpm, 100 lpm, 150 lpm, 200lpm, 250lpm and so on up to 400 lpm. Please refer to Chapter 4 for more details. During experiments it was observed that the two-phase flow in the drum causes the level to swell. This swell level, i.e. location of separation interface from bottom of drum was recorded visually through the transparent window of setup. It was also observed that the level in water tank reduces and corresponding water inventory is transported to drum (Figure 4.2), This happens to maintain momentum balance between the drum and water tank via the downcomer line. Also some water inventory from tail pipes is also transported to drum as void occupies space in tail pipes. The total water volume in the drum can be calculated as follows:

$$\begin{aligned} &Volume\ of\ water\ in\ drum \\ &\quad = Intial\ water\ volume\ in\ drum + Volume\ transported\ from\ water\ tank \\ &\quad + Volume\ transported\ from\ tail\ pipes \end{aligned} \tag{6.1}$$

$$\begin{aligned} V_{water-final} = V_{water\ at\ intial\ drum\ level} + A_{water\ tank}(L_{Water\ Tank-initial} \\ - L_{Water\ tank-final}) + \sum_{i=1}^{i=15} (A_{tailpie}\ \alpha_{tailpipe} L_{2-\emptyset})_i \end{aligned} \tag{6.2}$$

The volume transported form water tank is calculated from cross-sectional area of tank and change in the level. The volume from each tail pipe is calculated as a product of void fraction in tail pipe, cross-sectional area and length of two-phase portion i.e. distance from air injection point to the drum inlet. Since the void fraction in tail pipe is not measured directly, it is estimated from void fraction correlation by Thom [69] which was found to be the most accurate correlation which satisfies the steady state flow data (see previous chapter 4 for more details).

Now we can therefore calculate the average pool void fraction based on volume corresponding to swell level and water volume as follows:

$$\alpha_{pool} = \frac{V_{swell-level} - V_{water-final}}{V_{swell-level}} \tag{6.3}$$

The volume corresponding to a given operating level is calculated geometrically as shown in Figure 6.1. Figure 6.1 (a) shows the scenario when operating level is below the centerline of drum, and Figure 6.1 (b) shows scenario when operating level is above the centerline of the drum.

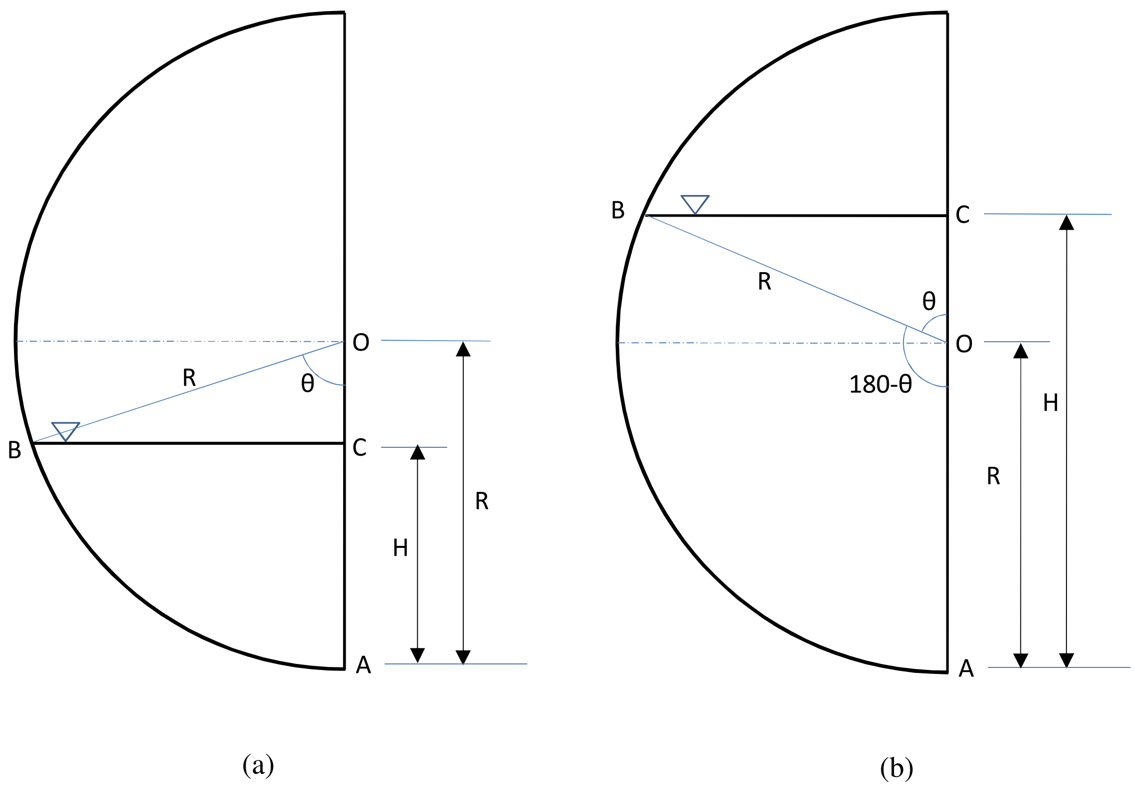

Figure 6.1: Calculation of volume of horizontal drum for given operating level (a) when level is below centerline (b) when level is above the centerline of cross-section

Figure 6.1 shows the cross-section of AWL drum without baffle plates. The area occupied by baffle plate is negligible and can be omitted from volume calculation.

When the level is below the centerline of drum the corresponding volume can be given as:

$$V_H = [Area\ occupied\ by\ sector\ OAB - Area\ of\ traingle\ OBC] \times length\ of\ drum \tag{6.4}$$

$$V_H = \left[\pi R^2 \left(\frac{\theta}{360}\right) - \frac{1}{2} BC \times OC\right] \times L_{drum} \tag{6.5}$$

$$V_H = \left[\pi R^2 \left(\frac{sin^{-1}\left(\frac{BC}{OB}\right)}{360}\right) - \frac{1}{2} BC \times OC\right] \times L_{drum} \tag{6.6}$$

Where

$$BC = \sqrt{(OB^2 - OC^2)} = \sqrt{(R^2 - (R - H)^2)} \tag{6.7}$$

$$OC = (R - H)$$

$$OB = R$$

When the level is above the centerline of drum the corresponding volume can be given as:

$$V_H = [Area\ occupied\ by\ sector\ OAB + Area\ of\ traingle\ OBC] \times length\ of\ drum \tag{6.8}$$

$$V_H = \left[\pi R^2 \left(\frac{180 - \theta}{360}\right) + \frac{1}{2} BC \times OC\right] \times L_{drum} \tag{6.9}$$

$$V_H = \left[\pi R^2 \left(\frac{180 - sin^{-1}\left(\frac{BC}{OB}\right)}{360}\right) + \frac{1}{2} BC \times OC\right] \times L_{drum} \tag{6.10}$$

Where

$$BC = \sqrt{(OB^2 - OC^2)} = \sqrt{(R^2 - (H - R)^2)} \tag{6.11}$$

$$OC = (H - R)$$

$$OB = R$$

Numbers of steady state experiments were performed and the experimental database for pool void fraction at measured air and water flows rate was created. Figure 6.2 shows the pool void fraction data.

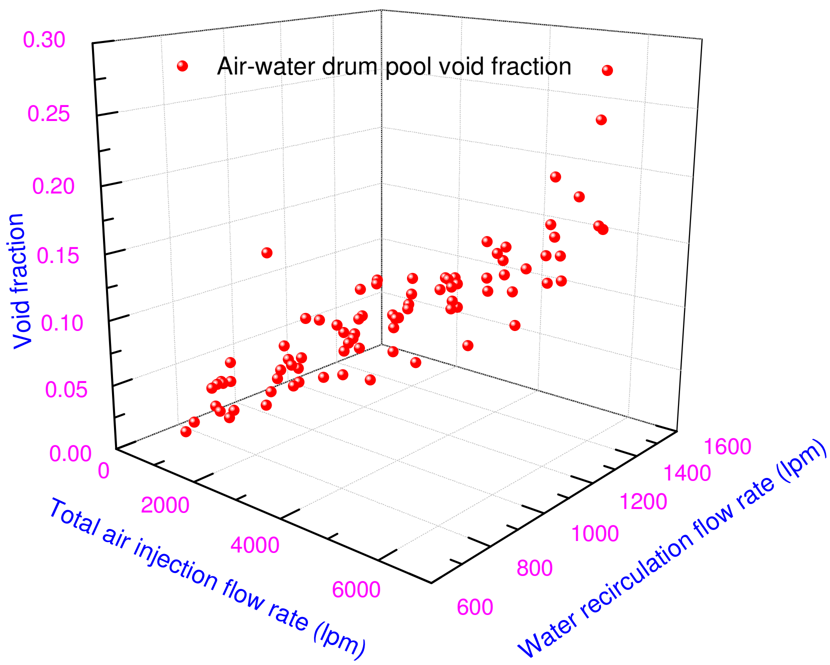

Figure 6.2: Average pool void fraction data from AWL experiments.

6.3 Prediction of pool void fraction using drift flux models

The two-phase flows ideally needs modeling of two velocities of two phases and associated interphase mass, momentum and energy transfer. Though ideal it is not practical to have such rigorous modeling, therefore simplified approaches such as drift flux model has been extensively used in engineering calculations. The approach has been found to be quite accurate for analyzing two-phase co-current flows in small diameter pipes. Such models have been incorporated in state of the art thermal-hydraulic codes as well [89].

However, for the large diameter pipe case the suitability of such correlations is not ensured [89]. The distinction between large diameter and small diameter pipes is done based on the observation of flow pattern and bubble dynamics. For small diameter pipes the size of bubble is restricted by the walls, and hence slugs are formed, these slug bubbles are stable. In large diameter pipes, as the bubble tries to grow larger, its shape at the upper surface is not restrained and distortions cause Taylor instabilities and bubble breaks up in to smaller cap bubbles. These bubbles affect the flow around them and induce turbulence which is significantly different than the small diameter case. Also flow regimes observed in larger diameter pipes are different than small diameter pipes. The distinction between small and large diameter pipe is based on following criteria:

For large diameter pipes $D_H^* = \frac{D_H}{\sqrt{\frac{\sigma}{g(\rho_l - \rho_g)}}} \geq 40$ and for smaller diameter pipes $D_H^* < 40$ (6.12)

In large diameter pipes, it also observed that the bubbles try to concentrate in the central high velocity region with relatively bubble deficient zone near the walls. The liquid velocity near the wall becomes negative and recirculation patterns are formed. The distribution parameter in drift flux model thus can become significantly different owing to such strong recirculation flows.

For air-water case the transition of small to large diameter pipe occurs at hydraulic diameter of 0.108 m, i.e. 108 mm. Hydraulic diameter for steam drum for the current geometry is much higher than this threshold and thus standard drift flux correlations may not be able to predict the pool void fraction accurately.

The drift flux correlation is generally expressed as:

$$\frac{\langle J_g \rangle}{\langle \varepsilon_g \rangle} = \langle\langle v_g \rangle\rangle = C_0 \langle J \rangle + U_{gl} \tag{6.13}$$

Where J_g, ε_g, v_g and J are the superficial gas velocity, the void fraction, the gas velocity and the mixture volumetric flux respectively. $\langle \quad \rangle$ and $\langle\langle \quad \rangle\rangle$ means the area averaged quantity over a cross-sectional flow area and the void-fraction-weighted mean quantity, respectively. The distribution parameter, C_0 and the drift velocity, U_{gl} are given as follows:

$$C_0 \equiv \frac{\langle \varepsilon_g J \rangle}{\langle \varepsilon_g \rangle \langle J \rangle} \tag{6.14}$$

$$U_{gl} \equiv \frac{\langle v_{gl} \varepsilon_g \rangle}{\langle \varepsilon_g \rangle} = \frac{\langle (v_g - J) \varepsilon_g \rangle}{\langle \varepsilon_g \rangle} \tag{6.15}$$

Where v_{gl} is local drift velocity of a gas phase which is defined as $v_{gl} = v_g - J$

The distribution parameter C_0 has been given by Ishii [90] based on experimental data on fully developed flows, for vertical flow in round tubes as:

$$C_0 = 1.2 - 0.2 \sqrt{\frac{\rho_g}{\rho_l}} \tag{6.16}$$

And the drift velocity for bubbly flow regime is given as:

$$U_{gl} = \sqrt{2} \left(\frac{\sigma g (\rho_l - \rho_g)}{{\rho_l}^2} \right)^{1/4} \left(1 - \langle \varepsilon_g \rangle \right)^{1.75} \tag{6.17}$$

However above equations (equation (6.16) & (6.17)) give excellent predictions for vertical upward two-phase flows in relatively smaller diameters (0.025-0.050 m) pipes. However, in large diameter pipes applicability of above equations is not ensured. A recirculation flow pattern may develop in large diameter pipe at lower flow rates. The distribution parameters can be significantly different owing to change in flow patterns as a result of large diameter of cross-section.

Kataoka and Ishii [91] found that drift velocity in pool system depends on vessel diameter, system pressure, gas flux and fluid properties. They proposed following correlations valid for drift velocity while using eq (6.16) for distribution parameter.

For low viscous fluid case: i.e. $N_{\mu f} \leq 2.25 \times 10^{-3}$

$$U_{gl}^{+} = 0.0019(D_H^*)^{0.809}\left(\frac{\rho_g}{\rho_l}\right)^{-0.157}\left(N_{\mu f}\right)^{-0.562} for\ D_H^* \leq 30,$$

$$U_{gl}^{+} = 0.030\left(\frac{\rho_g}{\rho_l}\right)^{-0.157}\left(N_{\mu f}\right)^{-0.562} for\ D_H^* > 30 \tag{6.18}$$

Where $N_{\mu f} = \frac{\mu_l}{\sqrt{\rho_l \sigma \sqrt{\frac{\sigma}{g(\rho_l - \rho_g)}}}}$

For higher viscous fluid case: i.e. $N_{\mu f} > 2.25 \times 10^{-3}$

$$U_{gl}^{+} = 0.0019(D_H^*)^{0.809}\left(\frac{\rho_g}{\rho_l}\right)^{-0.157}\left(N_{\mu f}\right)^{-0.562} for\ D_H^* \leq 30,$$

$$U_{gl}^{+} = 0.92\left(\frac{\rho_g}{\rho_l}\right)^{-0.157} for\ D_H^* > 30, \tag{6.19}$$

Where $N_{\mu f} = \frac{\mu_l}{\sqrt{\rho_l \sigma \sqrt{\frac{\sigma}{g(\rho_l - \rho_g)}}}}$

Hibiki and Ishii [89] has further developed void fraction correlation for the large pipe diameter cases with upward two phase flow at wider range of volumetric gas flux. The correlation showed satisfactory agreement with experimental data considered. The experimental data under various operating conditions such as hydraulic diameter (0.102 – 0.480 m), pipe to length ratios (1.2-108), pressures (0.1-1.5 MPa), mixture volumetric fluxes (0.03-6.1 m/s) and fluid systems (air-water, steam-water) was considered by Hibiki and Ishii [89].

Hibiki and Ishii [89] proposed use of non-dimensional drift flux equation in the following form:

$$\frac{\langle J_g^+\rangle}{\langle \varepsilon_g\rangle} = \langle\langle v_g^+\rangle\rangle = C_0\langle J^+\rangle + U_{gl}^+ \tag{6.20}$$

Where $\langle J_g^+\rangle = \dfrac{\langle J_g\rangle}{\left(\frac{\sigma g(\rho_l-\rho_g)}{\rho_l{}^2}\right)^{1/4}}$, $\langle J^+\rangle = \dfrac{\langle J\rangle}{\left(\frac{\sigma g(\rho_l-\rho_g)}{\rho_l{}^2}\right)^{1/4}}$, $\langle\langle v_g^+\rangle\rangle = \dfrac{\langle\langle v_g\rangle\rangle}{\left(\frac{\sigma g(\rho_l-\rho_g)}{\rho_l{}^2}\right)^{1/4}}$ (6.21)

After detailed comparison with experimental data, Hibiki and Ishii [89] proposed a set of applicable correlations for large diameter pipes at high gas flux which are applicable based on the flow regimes. For bubbly flow ($\langle\alpha\rangle \le 0.3$) the drift flux parameters can be described by:

$$C_0 = exp\left\{0.475\left(\frac{\langle J_g^+\rangle}{\langle J^+\rangle}\right)^{1.69}\right\}\left(1-\sqrt{\frac{\rho_g}{\rho_l}}\right) + \sqrt{\frac{\rho_g}{\rho_l}} \quad for\ 0 \le \frac{\langle J_g^+\rangle}{\langle J^+\rangle} \le 0.9 \tag{6.22}$$

$$C_0 = \left\{-2.88\,\frac{\langle J_g^+\rangle}{\langle J^+\rangle} + 4.08\right\}\left(1-\sqrt{\frac{\rho_g}{\rho_l}}\right) + \sqrt{\frac{\rho_g}{\rho_l}} \quad for\ 0.9 \le \frac{\langle J_g^+\rangle}{\langle J^+\rangle} \le 1.0 \tag{6.23}$$

$$U_{gl}^+ = U_{gl,B}^+ exp(-1.39\langle J^+\rangle) + U_{gl,P}^+\big(1.0 - exp(-1.39\langle J^+\rangle)\big) \tag{6.24}$$

Where the value of $U_{gl,B}^+$ is calculated from equation (6.17) while values for $U_{gl,P}^+$ are calculated from eq (6.18) and (6.19).

The above correlation by Hibiki and Ishii [89] is easier to apply for a pipe with constant flow cross-section, where the superficial gas velocity and volumetric flow flux values remain constant. But for our case as seen from Figure 6.1 (a) and (b) as the operating level increases form bottom of drum the flow area changes and corresponding hydraulic diameter also varied accordingly. Due to this, the values of superficial velocity of phases also change as we traverse form inlet to exit of drum. In order to consider this, we can determine void fraction in a small volume bounded by a strip of height Δh as shown in Figure 6.3. As we traverse from bottom to top, void fraction in each strip, corresponding volume of water and air in each strip can be estimated. When the cumulative water volume matches with the experimental value, that level is considered as predicted swell level with the correlation. This will also enable to predict the average pool void fraction using drift flux models from literature. Basically the drift flux correlation is applied in the small strip of volume with assumption of fully developed flow and the strip volume representing the pipe with corresponding hydraulic diameter. From experiment it is seen that very few bubbles reach to the down comer region of the drum, hence the void fraction in the down comer region can be considered to be zero.

Figure 6.4 & 6.5 shows the swell level and average pool void fraction predicted by Hibiki and Ishii [89] correlation for the AWL experiment with initial level of 0.65 m. The comparison shows that though predictions match at lower values of gas flux, they deviate significantly at higher flow rates (total air flow rate > 1500 lpm). The predictions were made for other experiments and the comparison of predicted pool average void fraction versus measured void fraction is made in Figure 6.6. The predictions are higher than the measurements and are not accurate.

It can be noted that most of the data used in development of Ishii correlation is still from pipe diameters smaller than 0.3 m, therefore the flow pattern effects in larger pool like AWL drum is not accounted. Therefore a dedicated correlation for large pools is required.

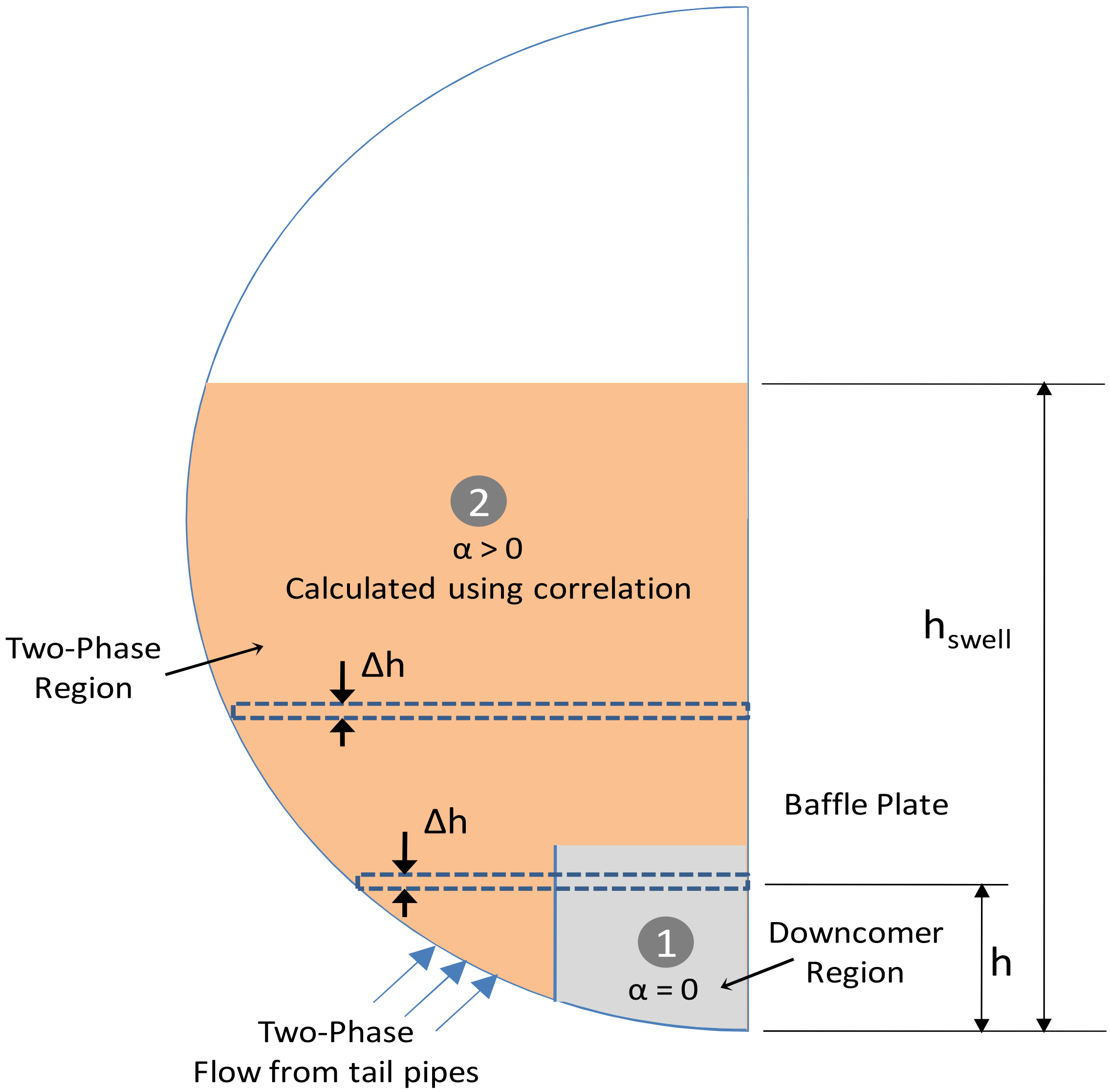

Figure 6.3: Calculation of void fraction for AWL drum with varying cross-sectional area

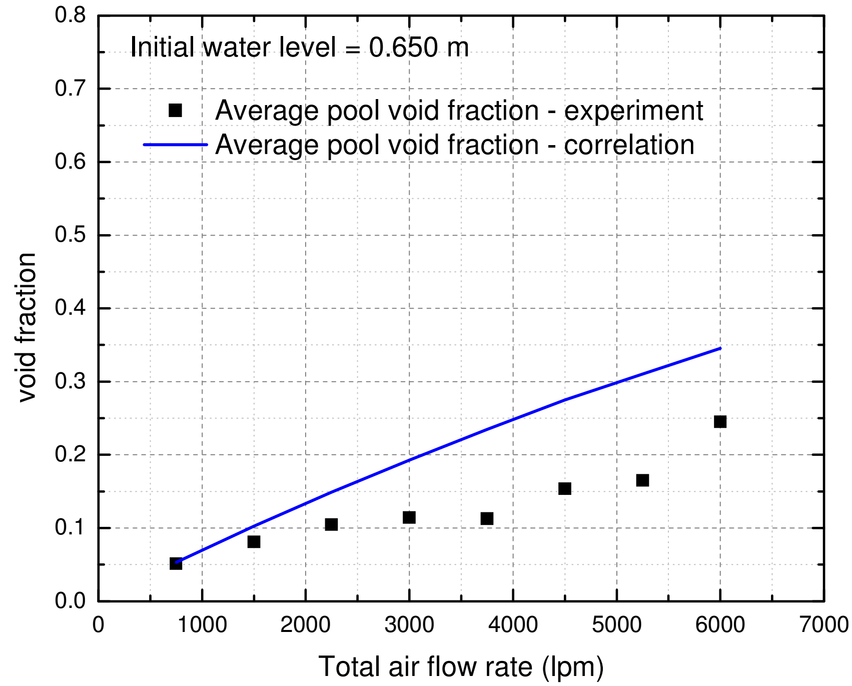

Figure 6.4: Comparison between predicted void fraction (by Hibiki and Ishii [89] correlation) with experiment (initial level = 0.650 m)

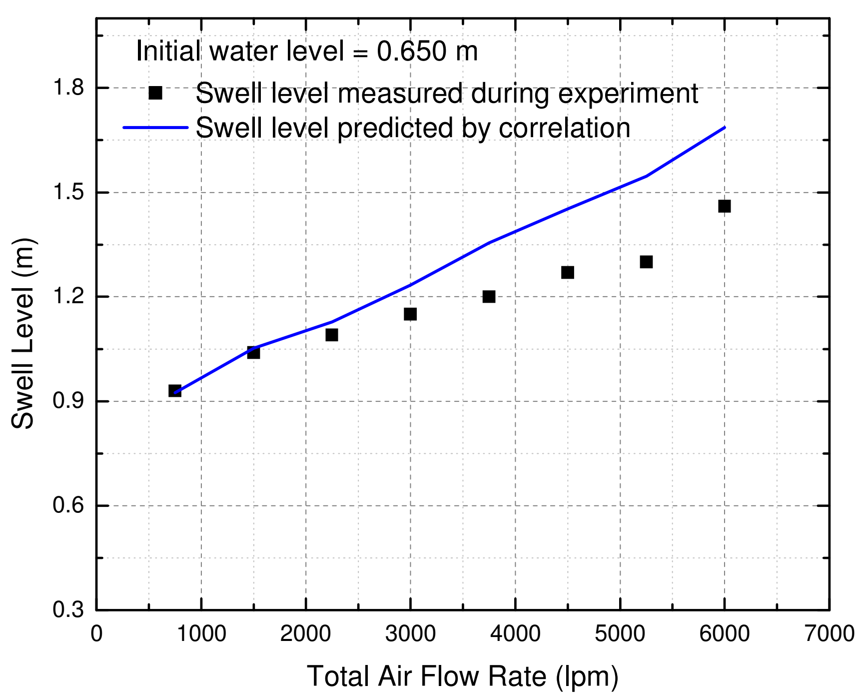

Figure 6.5: Comparison between predicted swell level (by Hibiki and Ishii [89] correlation) with experiment (initial level = 0.650 m)

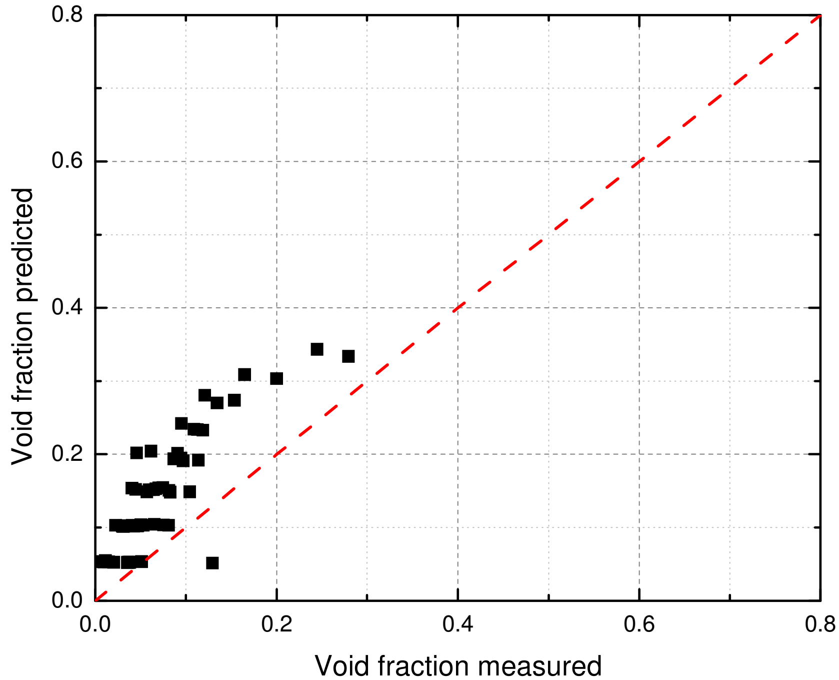

Figure 6.6: Void fraction predicted by Hibiki and Ishii [89] correlation for several set of experiments in AWL

Boesmans et al. [92] proposed a drift flux based correlation specifically developed for large bubbling pool situation. They considered the effect of recirculation patterns on distribution parameter, C_0. The drift flux equation (6.13) can be re written using equation (6.17) in generalized form and introducing constants C_1 and n as follows:

$$\frac{\langle J_g \rangle}{\langle \varepsilon_g \rangle} = C_0 \langle J_g + J_l \rangle + C_1 \left(\frac{\sigma g (\rho_l - \rho_g)}{{\rho_l}^2} \right)^{1/4} \left(1 - \langle \varepsilon_g \rangle \right)^n \tag{6.25}$$

$$\frac{1}{\langle \varepsilon_g \rangle} = C_0 \frac{\langle J_g + J_l \rangle}{\langle J_g \rangle} + \frac{C_1}{\langle J_g \rangle \left(\frac{\rho_l{}^2}{\sigma g (\rho_l - \rho_g)} \right)^{1/4}} \left(1 - \langle \varepsilon_g \rangle\right)^n \tag{6.26}$$

From continuity equation it can be written than

$$\rho_l \langle J_l \rangle + \rho_l \langle J_l \rangle = 0 \tag{6.27}$$

Therefore equation can be written as

$$\frac{1}{\langle \varepsilon_g \rangle} = C_0 \left(1 - \frac{\rho_g}{\rho_l}\right) + \frac{C_1}{Fr} \left(1 - \langle \varepsilon_g \rangle\right)^n \tag{6.28}$$

Where $Fr = Froude\ number = \ \langle J_g \rangle \left(\frac{\rho_l{}^2}{\sigma g (\rho_l - \rho_g)} \right)^{1/4}$

Assuming $\rho_g \ll \rho_l$

Finally it can written as:

$$\frac{1}{\langle \varepsilon_g \rangle} = C_0 + \frac{C_1}{Fr} \left(1 - \langle \varepsilon_g \rangle\right)^n \tag{6.29}$$

Boesmans et al. [92] derived expression for C_0, theoretically with understanding the fact that in large bubbling pool the bubbles tend to gather in central region and recirculation patterns are formed near the walls (see Figure 6.7). The pool conditions can be represented by an idealized flow pattern as shown in Figure 6.8.

The distribution parameter was expressed as

$$C_0 = \frac{1}{2k'} + \frac{1}{2\langle \varepsilon_g \rangle} \tag{6.30}$$

With assumption of $\langle \varepsilon_2 \rangle = 0\ and\ \langle \varepsilon_1 \rangle = \langle \varepsilon_g \rangle / k^{'}$

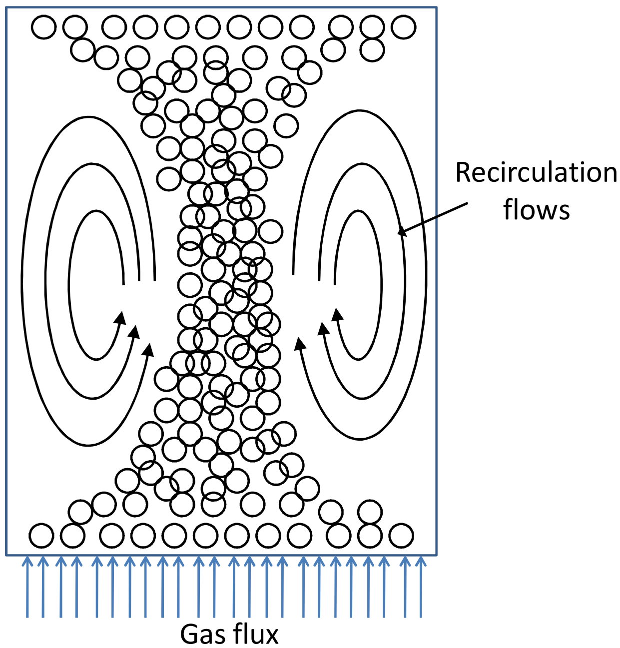

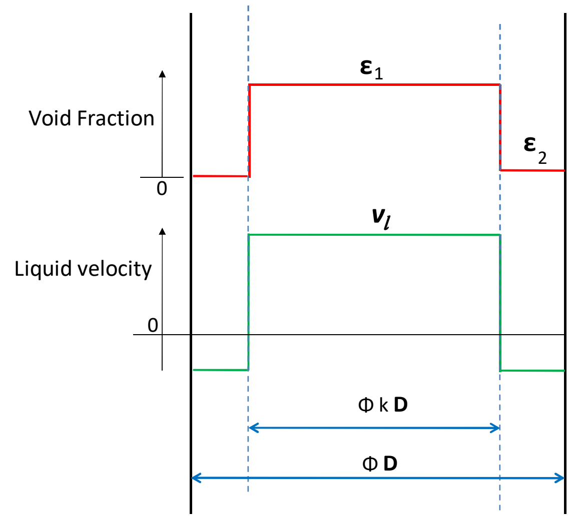

Figure 6.7: Distribution of bubbles inside large pool and flow recirculation patterns

Figure 6.8: Idealized flow pattern for large pool with core occupied by bubbles and liquid recirculation close to walls

The final form of equation as proposed by Boesmans et al. [92] is as follows:

$$\frac{1}{\langle \varepsilon_g \rangle} = C_0 + 2\frac{C_1}{Fr} \tag{6.31}$$

Where

$$C_0 = 1.2, C_1 = 1.373 \; for \; bubbly \; flow \; i.e. Fr < 0.5 \tag{6.32}$$

And (6.33)

$$C_0 = 1.2, C_1 = 1.373 + 0.177\left(\frac{\rho_g}{\rho_l}\right)^{-0.25} \; for \; Churn - turbulent \; flow \; i.e. Fr \geq 0.5$$

Equation (6.32) & (6.36) was used for calculating the pool void fraction following the methodology described earlier (Figure 6.3).

Figure 6.9 and 6.10 shows the comparison of swell level and void fraction predicted with correlation by Boesmans et al. [92] and experiment with initial level 0.650 m. Figure 6.11 and 6.12 shows predicted void fraction and swell level for all experiments compared with measurements on a parity plot. It can be seen that the swell level is accurately predicted within ± 5 % of measurement. The correlation by Boesmans et al. [92] gives much better accuracy than the Hibiki and Ishii [89] correlation. Therefore this correlation is recommended for calculating average pool void fraction.

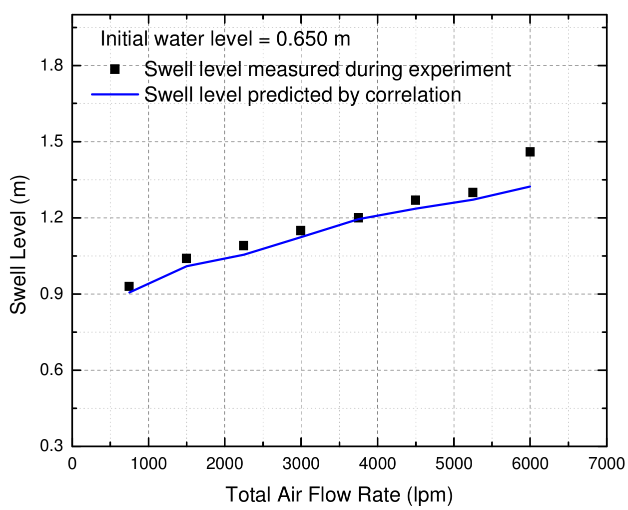

Figure 6.9: Comparison of swell level predicted with correlation by Boesmans et al. [92] with experimental measurements (initial level =0.650 m)

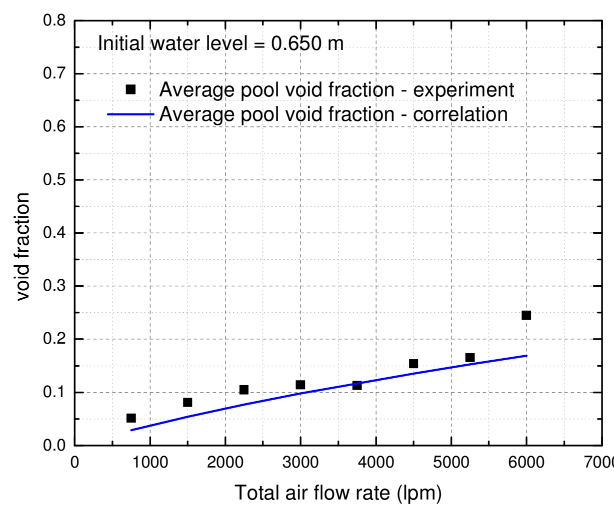

Figure 6.10: Comparison of pool void fraction predicted with correlation by Boesmans et al. [92] with experimental measurements (initial level =0.650 m)

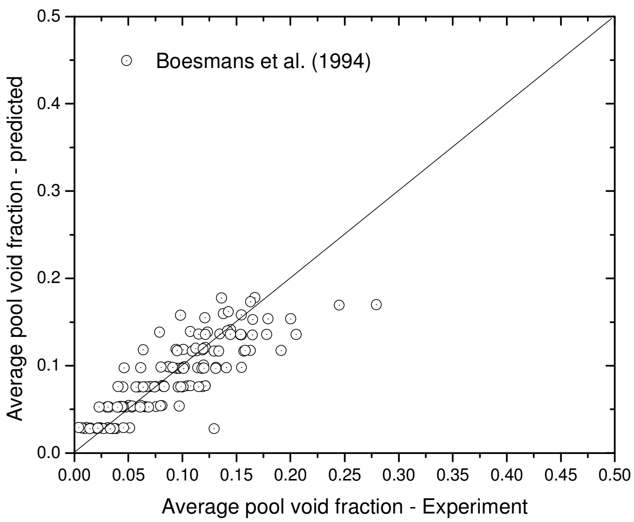

Figure 6.11: Comparison of predicted void fraction using correlation by Boesmans et al. [92] with experiments

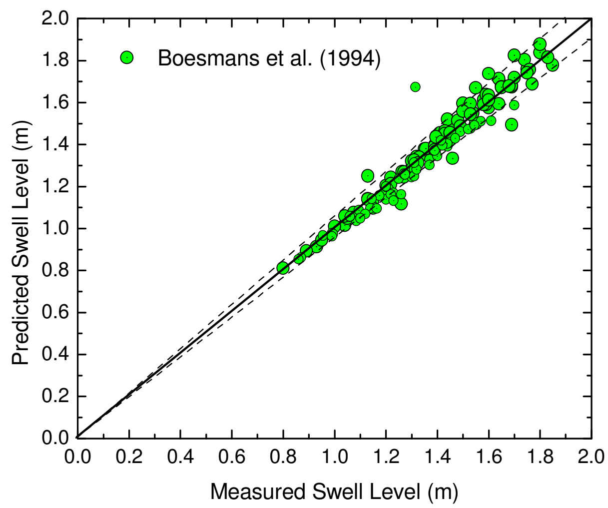

Figure 6.12: Comparison of predicted swell level using correlation by Boesmans et al. [92] with experiments

6.4 Photographic investigations on bubble size distributions

The transparent acrylic windows of AWL drum have enabled us to conduct some photographic investigations on the bubble size distribution inside the pool. Figure 6.13 shows the photograph of AWL drum taken during an experiment showing the bubbles inside the pool.

The bubbles injected from tail pipe move upwards in the pool and tend to gather in the central region of flow and further they are distributed evenly near the separation interface. Recirculation flows were observed near the curved metallic wall of drum (to the left of photograph) as well the flat wall of drum (to the right side of photograph). Very few bubbles could reach the baffle region.

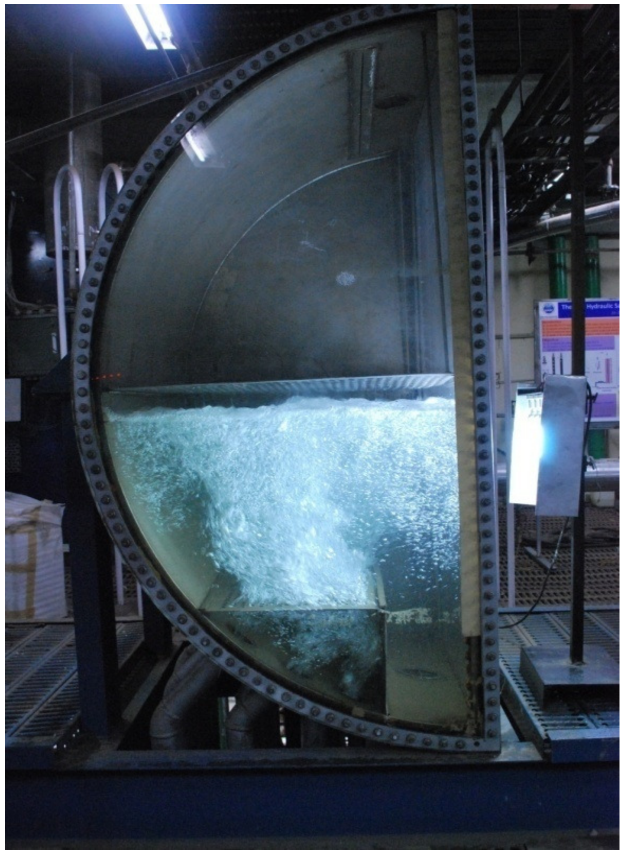

Figure 6.13: Photograph of bubbling pool of AWL drum

In order to obtain bubble size distribution, we took number of still photographs in various regions of pool. Digital camera Nikon D60 with resolution of 3872 x 2592 pixels (10 MP) was used to take photographs from different regions (near baffle plate, near top surface). Nikon 18.0-55.0 mm f/3.5-5.6 lens was used to take photographs. Aperture was kept at f8 and shutter speed was maintained at 1/640 seconds which was sufficient to freeze the motion of bubbles in photograph. CFL bulbs were used to assist the light available for photography. A scale was put on the surface of acrylic sheet while taking the image to get calibration constant.

The images obtained (some images are illustrated in Figure 6.14 (a), 6.15 (a)) were then processed manually to pick up the clearly visible bubbles. Overlapping bubbles were neglected.

The image processing gives the binary image consisting bubbles in white on a black background as shown in Figure 6.14 (b) and 6.15 (b).

These binary images were then analyzed using image processing algorithm which gives the area occupied by each white blob (which represents bubble), its centroid, equivalent diameter, major & minor axis and orientation. Figure 6.16 & 6.17 shows the bubble size distribution (histogram/frequency count) and cumulative relative frequency obtained using image analysis.

Figure 6.14 (a): Sample image-1 of bubbles in AWL drum pool

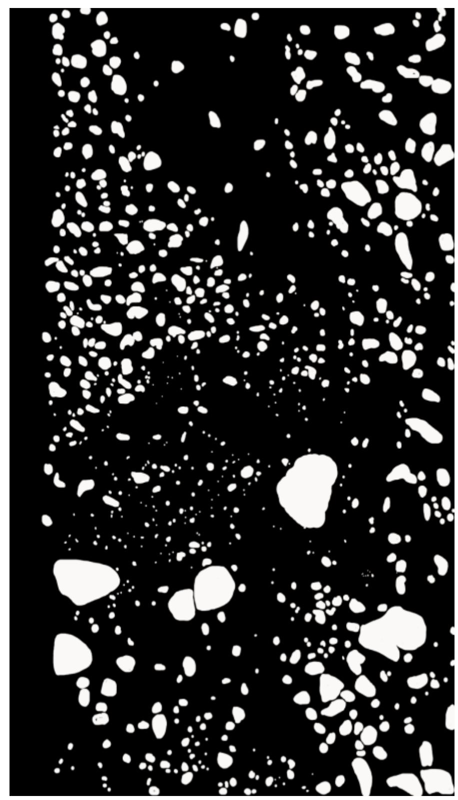

Figure 6.14 (b): Binary image obtained after processing sample image-1 as shown in Figure 6.14 (a)

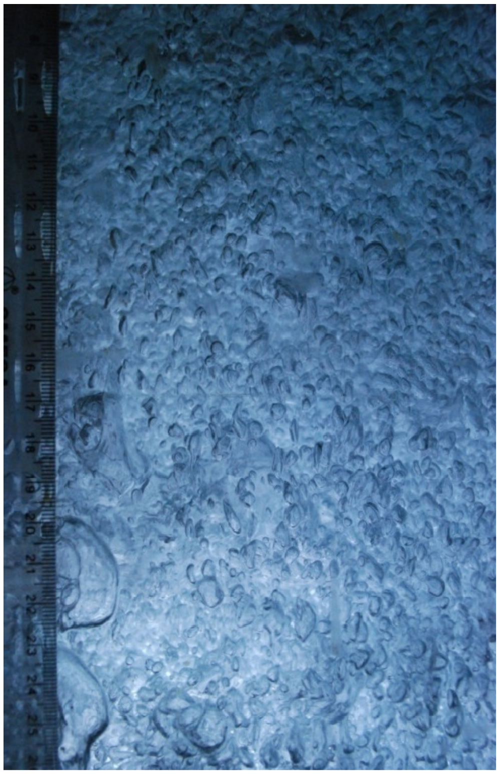

Figure 6.15 (a) Sample image-2 of bubbles in AWL drum pool

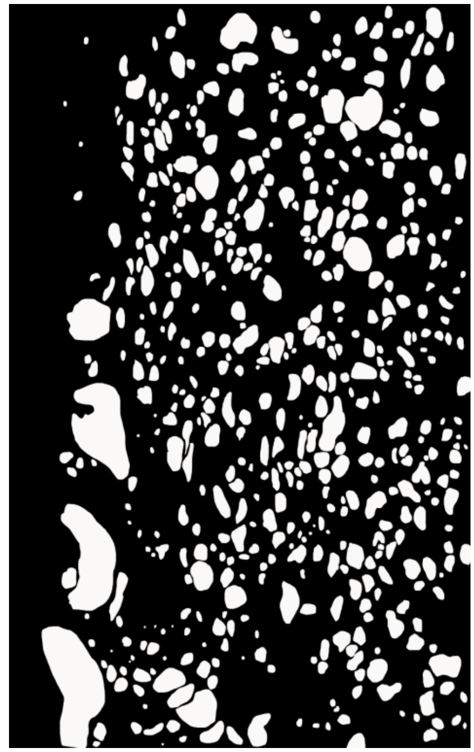

Figure 6.15 (b): Binary image obtained after processing sample image-2 as shown in Figure 6.15 (a)

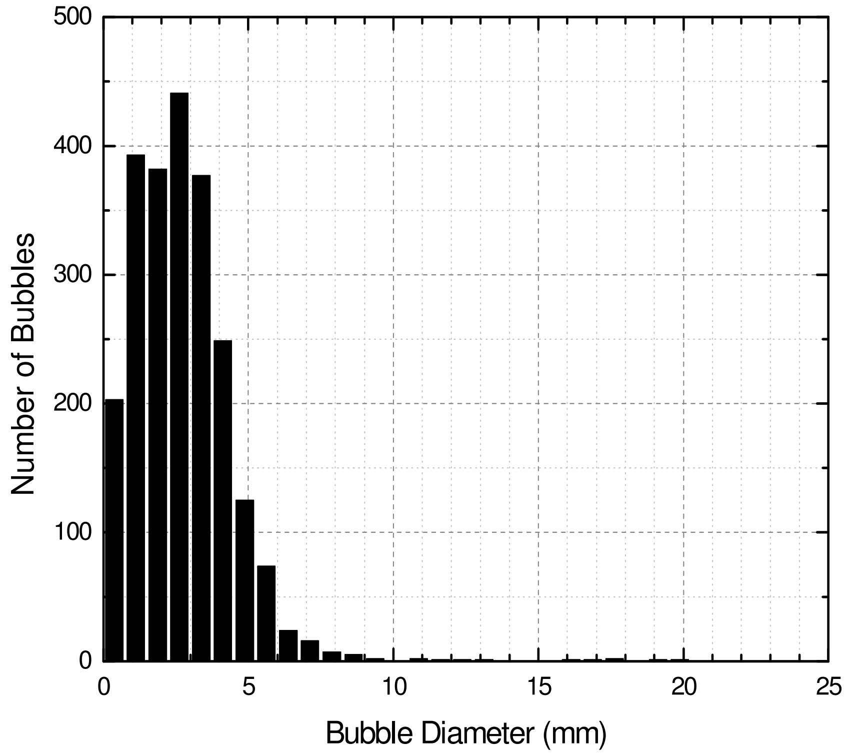

Figure 6.16: Histogram / Frequency count of bubbles

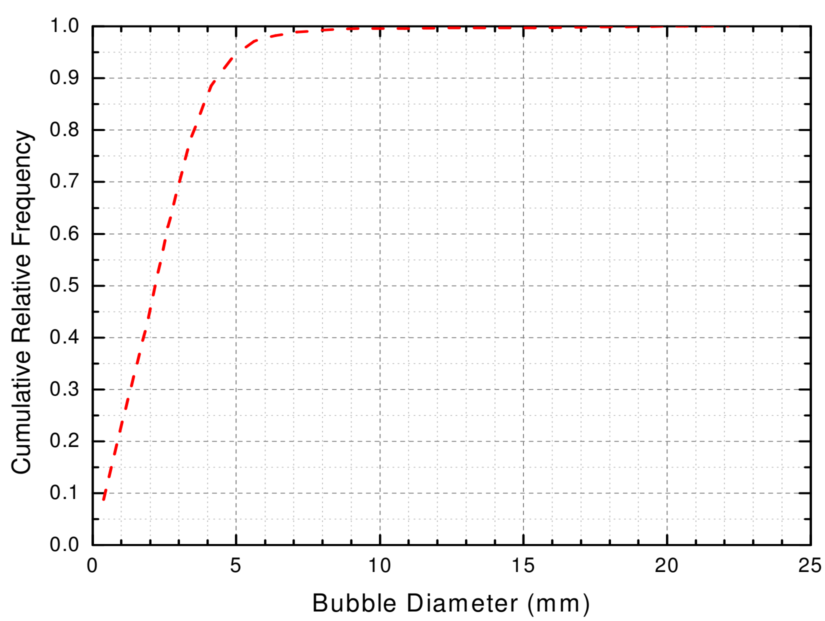

Figure 6.17: Relative Cumulative Frequency

The histogram (Figure 6.16) shows most of the bubbles are smaller than 5 mm. (66 % of bubbles are smaller than 3 mm, 85% of bubbles are smaller than 4 mm and 95 % of bubbles are 0 to 5 mm size).

Based on the distributions the volumetric mean diameter (VMD) and Sauter Mean Diameter (SMD) are obtained using following equation:

$$VMD = d_{30} = \left\{\frac{1}{n}\sum_{i=1}^{n} d_i^3\right\}^{\frac{1}{3}} \tag{6.34}$$

$$SMD = d_{32} = \frac{\sum_{i=1}^{n} d_i^3}{\sum_{i=1}^{n} d_i^2} \tag{6.35}$$

The VMD is calculated to be 3.9 mm. The SMD is calculated to be 5.5 mm. The SMD represents the average size of bubble. SMD is diameter of bubble that has same volume to surface area ratio. Since the bubbles are poly dispersed distribution, it can be suitably represented by SMD in numerical calculations.

The information from the photographic studies is utilized in CFD simulation of flow discussed in subsequent sections.

6.5 CFD simulation of void distribution in the AWL drum

Drift flux model method is relatively simple and easy to use; however it gives only information about average void fraction. Two-phase computation fluid dynamics has been employed in this study in order to obtain detailed information on void distribution, liquid and gas velocities in the two-phase flow pool of drum. The "*twoPhaseEulerFoam*" solver from OpenFOAM 2.3.1, which solves the two incompressible fluid phases with one phase dispersed in other is used for simulations. The solver, its validation and application to the problem is described in subsequent sections.

6.5.1 Solver "*twoPhaseEulerFoam*": Governing equations

In this solver, both phases are described using Eulerian conservation equations and thus it is referred as Euler-Euler model. Each phase is treated as continuum, each inter-penetrating each other, and is represented by averaged conservation equations. The averaging process introduces the phase fraction α in to the equation sets, which is defined as the probability that a certain phase is present at a certain point in space and time.

The governing equations are written as follows:

Continuity equation: (6.36)

$$\frac{\partial}{\partial t}(\alpha_k \rho_k) + \frac{\partial}{\partial x_i}(\alpha_k \rho_k \boldsymbol{u}_{k,i}) = 0$$

Momentum equation: (6.37)

$$\frac{\partial}{\partial t}(\alpha_k \rho_k u_{k,i}) + \boldsymbol{u}_j \frac{\partial}{\partial x_j}(\alpha_k \rho_k \boldsymbol{u}_{k,i}) = -\alpha_k \frac{\partial P}{\partial x_i} + \alpha_k \rho_k g + \frac{\partial}{\partial x_j}\left(\alpha_k (\mu + \mu_t) \frac{\partial \boldsymbol{u}_{k,i}}{\partial x_j}\right) + F_I$$

Where subscript k denotes the phase (gas and liquid, i.e. $k = l, g$). The void fraction of phase is denoted by α_k.

The LHS of equation (6.37) represents terms for rate of change of momentum and convective flux of momentum respectively. The RHS of equation (6.37) represents the pressure gradient, body force due to gravity, total stress (includes laminar and turbulent stress) and interfacial momentum transfer. The term F_I represents the averaged interfacial momentum transfer which accounts for average effect of the forces acting at the interface between continuous and dispersed phase, e.g. force acting on bubbles in case of gas phase dispersed in fluid.

The above methodology applicable to all flow regimes, including separated, dispersed or intermediate regimes, since the flow topology is not prescribed. However, the formulation of the inter-phase momentum transfer term and two-phase turbulence model has to be accurate and shall describe the nature of flow. The main components of interfacial momentum term are forces due to drag, lift, virtual mass force and turbulent dispersion at the interface.

The drag force is directly proportional to the projected area, density of continuous phase and square of the relative velocity. In case of gas bubbles in liquid/water it can be written as:

$$F_D = \frac{1}{2} C_D \rho_l \left(\frac{\pi}{4} d_b^2\right) \left(v_g - v_l\right)^2 \tag{6.38}$$

The drag coefficient is dependent on Reynolds number of particle/bubble. The standard Schiller-Naumen drag laws are used in the current simulation studies.

The bubble moving in a liquid experiences lift force due to vorticity at its upstream. The lift force is proportional to the cross product of slip velocity and curl of liquid velocity, with direction perpendicular to both of them. It is also referred as transverse lift force. The lift force is most significant in radial direction of the cross-section. Lift force is given as:

$$F_L = -C_L \rho_l \left(\frac{\pi}{6} d_b^3\right) \left(v_g - v_l\right) \frac{\partial v_l}{\partial r} \tag{6.39}$$

In case of large pipe size and pool situations the strong recirculation flows are observed (upflow of liquid in central region while downward flow of liquid near the walls) which suggests that radial gradient $\frac{\partial v_l}{\partial r}$ to be negative and thus F_L a positive force. Which also means the bubbles will be forced to move towards wall away from central region, however in practice it is not the case, and bubbles tend to gather in central region. This suggests that value of lift coefficient must be negative. The value of C_L can be taken in the range of -0.08 to 0.23 (Joshi [93]).

The virtual mass force occurs when the bubbles accelerate relative to fluid flow. The inertia of liquid phase encountered by the accelerating bubbles exerts a "virtual mass force" which is given as:

$$F_{VM} = C_{VM}\alpha_g\rho_l\left(\frac{Dv_l}{Dt} - \frac{\partial v_g}{\partial t}\right), where\ \frac{D\boldsymbol{v}_l}{Dt} = \frac{\partial \boldsymbol{v}_l}{\partial t} + (\boldsymbol{v}_l.\nabla)\boldsymbol{v}_l \tag{6.40}$$

The value of C_{VM} can be chosen between 0 to 0.5.

When the bubbles move along the path which is fluctuating, the fluctuations may cause the bubbles to disperse. The associated force is called as turbulent dispersion force. It is given as:

$$F_{TD} = -C_{TD}C_D\left(\frac{\pi}{4}d_b^2\right)\frac{1}{2}\rho_l(\boldsymbol{v}_g - \boldsymbol{v}_l)\frac{\vartheta_{TB}\nabla\alpha_g}{\alpha_g} \tag{6.41}$$

The turbulent dispersion force tries to distribute the bubbles and flatten the holdup (void fraction) profile at the given plane. The value of turbulent dispersion coefficient is generally taken in the range of 0.008 to 0.007. (Joshi [93]).

The two-phase flow turbulence is simulated using mixture $k-\varepsilon$ equation as proposed by Behzadi et al. [94]. This model offers reasonable accuracy at low computational cost. It is assumed that both phases fluctuate as one entity and one set of equations for mixture can be solved. The mixture $k-\varepsilon$ equation is based on summation of the two corresponding phase-averaged transport equations for k and ε of two phases. The equation can be written as:

k_m equation: (6.42)

$$\frac{\partial}{\partial t}(\rho_m k_m) + \nabla.(\rho_m \boldsymbol{u}_m k_m) = \nabla.\frac{\mu_m^t}{\sigma_m}\nabla k_m + \mathrm{P}_k^m - \rho_m \varepsilon_m + S_k^m$$

ε_m equation: (6.43)

$$\frac{\partial}{\partial t}(\rho_m \epsilon_m) + \nabla.(\rho_m \boldsymbol{u}_m \epsilon_m) = \nabla.\frac{\mu_m^t}{\sigma_m}\nabla \epsilon_m + \frac{\epsilon_m}{k_m}(C_{\epsilon 1}\mathrm{P}_k^m - C_{\epsilon 2}\rho_m \epsilon_m) + \mathrm{C}_{\epsilon 3}\frac{\epsilon_m}{k_m}S_k^m$$

The mixture properties in above equations are as follows:

$$\rho_m = \alpha_l \rho_l + \alpha_g \rho_g \tag{6.44}$$

$$k_m = \left(\alpha_l \frac{\rho_l}{\rho_m} + \alpha_g \frac{\rho_g}{\rho_m} C_t^2\right)\epsilon_l \tag{6.45}$$

$$\boldsymbol{u}_m = \frac{\alpha_l \rho_l \boldsymbol{u}_l + \alpha_g \rho_g \boldsymbol{u}_g C_t^2}{\alpha_l \rho_l + \alpha_g \rho_g C_t^2} \tag{6.46}$$

$$\mu_m^t = \frac{\left(\alpha_l \mu_l^t + \alpha_g \mu_g^t C_t^2\right)\rho_m}{\alpha_l \rho_l + \alpha_g \rho_g C_t^2} \tag{6.47}$$

$$\mathrm{P}_k^m = \alpha_l \mathrm{P}_k^l + \alpha_g \mathrm{P}_k^g \tag{6.48}$$

$$S_k^m = S_k^l + S_k^g = \overline{F_I u_l'} = -A_g\left(\left(2\alpha_g (C_t - 1)^2 k_l\right) + \left(\eta_l \nabla \alpha_g . \boldsymbol{u_r}\right)\right) \tag{6.49}$$

TwoPhaseEulerFoam is a transient solver for solving two-phase gas-liquid flow, which uses PIMPLE algorithm. PIMPLE algorithm is a combination of PISO and SIMPLE algorithms.

PISO and SIMPLE both are iterative solvers, but PISO is for transient solutions while SIMPLE is used for steady state solution. In SIMPLE algorithm solves conservation equations iteratively using relaxation factors to obtain the convergence of solution. PISO solves the transient equations in time space by marching with suitable time step (to maintain Courant number < 1.0) so that solution convergence is ensured. If we simply use PISO to solve complex problems in time domain, we may end up with a extremely small time step and non-practical solution time. In PIMPLE algorithm adds the SIMPLE algorithm for each time step, i.e. equations are solved for more than one time within the same time step using relaxation factors. Figure shows the structure of PIMPLE. Solution procedure starts with initialization of fields and time. In a given time step, the PIMPLE loop is run for more than one time i.e. as specified by keyword "*nOutercorrectors*". In PIMPLE the mass conservation is solved with known velocity fields to obtain phase fractions for both the phases. The solution for phase volume fraction is carried out using MULES (Multidimensional Universal Limiter with Explicit Solution) method. MULES is an iterative technique with the implementation of Flux Corrected Transport (FCT, Zalesak [95]) and is considered reliable for the boundedness of scalar field. Then the momentum equation is solved for predicting, the velocities by using the pressure field from previous iteration. Prior to that, all the inter-phase forces are calculated and updated continuously, which is required for solving momentum equation. Energy equation is also solved, which is kind of intermediate solution to update the temperature / enthalpy fields and fluid properties. The pressure field is then solved using pressure correction equation in PISO loop. The pressure correction equation can be solved for more than one time and is specified by keyword "*ncorrectors*". Turbulence related equations are then solved at the end of PISO. The PIMPLE loop is solved for multiple times before proceeding to next time step. Relaxation factors are not used in last loop of PIMPLE i.e. prior advancing in next time step.

For many cases that are very unstable PIMPLE has proved to get a smooth convergence. In the OpenFOAM code, pressure equation is solved for number of times specified by "*nCorrectors*" and pressure-momentum coupling is solved number of times specified by "*nOuterCorrectors*".

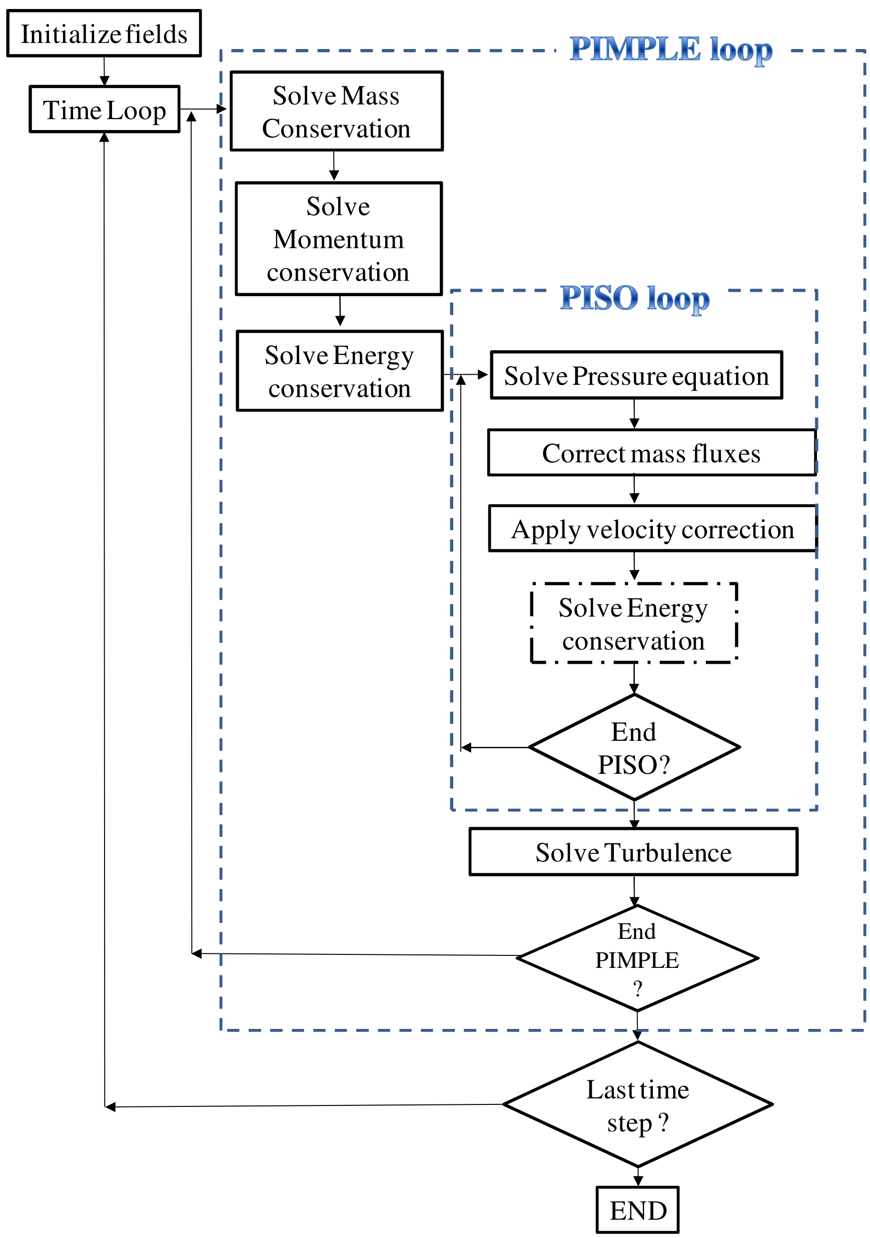

Figure 6.18: PIMPLE algorithm of two-phase flow solver.

6.5.2 Validation test cases for "*twoPhaseEulerFoam*" solver

Validation of "*twoPhaseEulerFoam*" solver is carried out by simulating the experiments performed by Hills [96] in a bubble column of 0.138 m diameter and 1.37 m height, where in air-water was used at working fluid. The column is filled with water and air is injected at the bottom of column using sparger. Axial water velocity and gas hold up profile at elevation of 4.34 time diameter i.e. 0.598 m from bottom were measured. Air injection rate was varied during experiments. A case of superficial gas velocity of 64 mm/s has been taken up for simulation.

6.5.2.1 Geometry and Meshing

A vertical pipe of diameter 0.138m and height 1.37 m was used as test section during the experiments. Air is injected at bottom and top of the pipe is open to atmosphere. The schematic of case is as shown in Figure 6.19. Figure 6.20 shows the various meshes generated using Gambit (commercial package) and Gmsh (open source code) software. Various meshes are used for CFD simulation to study the effect of grid on the final solution. Details of these meshes considered are given in Table-6.1:

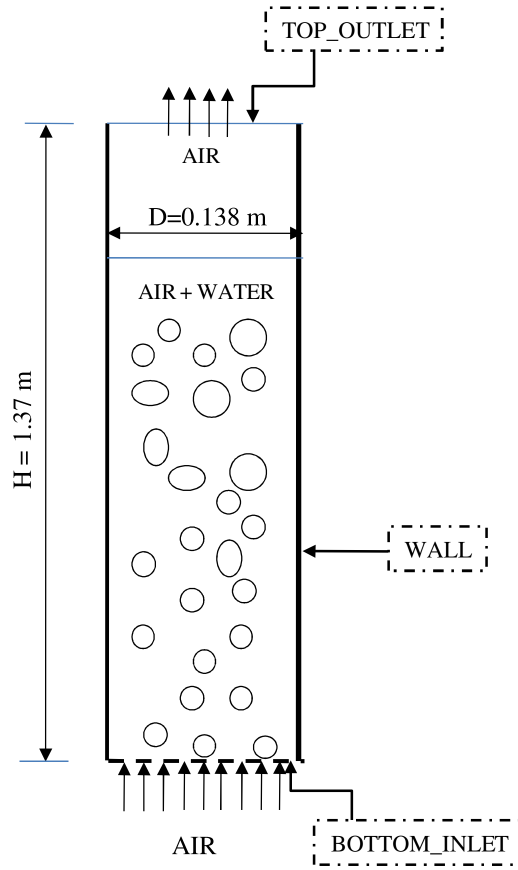

Figure 6.19: Geometry of Bubble Column for validation test case

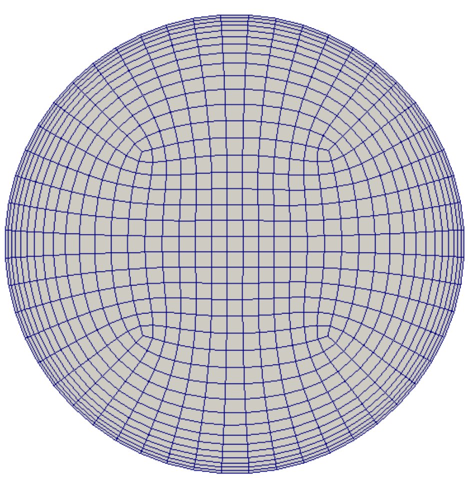

Figure 6.20 (a) : Cross-sectional view of Mesh-1

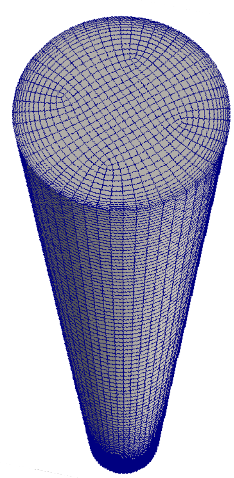

Figure: 6.20 (b): 3-D view of Mesh-1

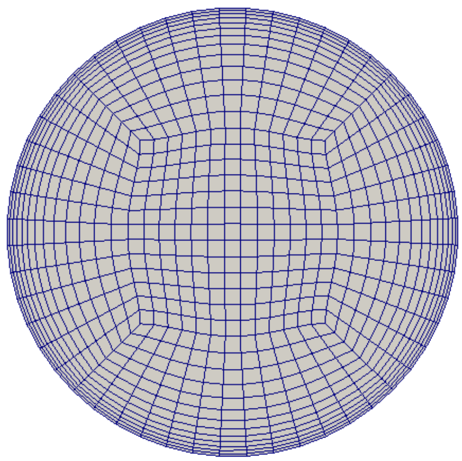

Figure 6.20 (c): Cross-sectional view of Mesh-2

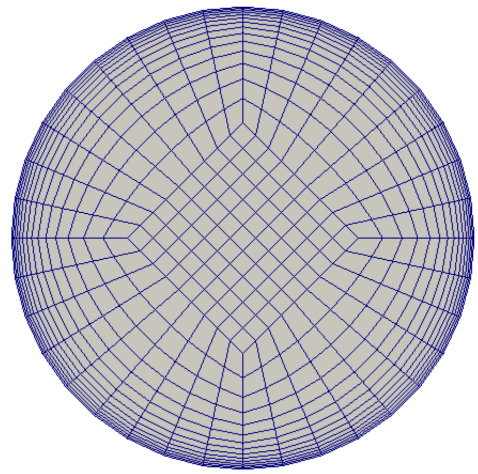

Figure 6.20 (d): Cross-sectional view of Mesh-3

Table 6.1: Mesh Properties (validation test case for Hills [96] experiment)

Parameter	Mesh-1	Mesh-2	Mesh-3
Number of cells	104780	134355	174915
Aspect Ratio (max)	28.65	35.56	11.29
Non-orthogonality (max)	29.83	27.70	25.71
Non-orthogonality (average)	4.52	4.92	4.45
Maximum Skewness	0.44	0.64	0.69

6.5.2.2 Boundary Conditions

The initial boundary conditions are given in the “0” directory of the OpenFoam test case directory. The initial conditions involve initialization of “*Internal Field*” such as pressure, void fraction, air and water fluid velocities and Turbulence quantities within the computational domain. The boundary conditions for each patch (Bottom_ilet, Top_outlet and Wall) are specified for all the variables as described below and Table 6.2:

6.5.2.2.1 Inlet boundary condition

a. **Gas hold up / void fraction** (α_{air}) **:**

The inlet void fraction is given as non-uniform distribution simulating the actual conditions of profile which corresponds to sparger inlet conditions where the inlet air injection is not uniform. It is modelled using a "*groovyBC*" utility of OpenFOAM. The void fraction variation is modelled as $\alpha_{air} = 0.26 - 0.1699\left(\frac{r}{R}\right)^3$ Where $\frac{r}{R}$ is dimensionless radial distance from centre of bubble column.

b. **Gas velocity** (U_{air})**:**

The inlet gas velocity is described by constant "*fixedValue*" type and value is set to the superficial velocity of gas at inlet.

c. **Liquid velocity** (U_{water})**:**

Since only gas is injected at bottom and liquid gets recirculated inside the column, the inlet liquid velocity is described by constant "*fixedValue*" type and value is set to the zero.

d. **Pressure** $(P\ )$**:**

The pressure at inlet is described by "*fixedFluxPressure*" type and value is set to hydrostatic head of liquid column acting at bottom inlet. The "*fixedFluxPressure*" condition adjusts the pressure gradient such that the flux on the boundary is that specified by the velocity boundary condition.

e. **Turbulent kinetic energy** $(k\ )$**:**

The turbulent kinetic energy is described by constant "*fixedValue*" type and value is calculated as per equation (5.51). i.e. $k = \frac{3}{2}\left(U_{ref} I\right)^2$. This value is calculated from velocity of air at inlet.

f. Turbulent energy dissipation rate (ϵ)

The turbulent energy dissipation rate is described by constant "*fixedValue*" type and value is calculated as per equation (5.52) i.e. $\epsilon = C_\mu^{3/4} \frac{k^{3/2}}{0.07L}$, where C_μ (=0.09) is the turbulent parameter that relates turbulent viscosity with k and ε,L is the turbulent length scale, which is equal to the column diameter for cylindrical columns.

6.5.2.2.2 Outlet boundary condition

a. Gas hold up / void fraction (α_{air}) :

At the outlet, *inletOutlet* boundary condition is used for gas holdup. The *inletOutlet* boundary condition is normally the same as *zeroGradient*, but it switches to *fixedValue* if the velocity vector next to the boundary aims inside the domain (backward flow). The value of that fixed value is inlet value, which is 1 in this case.

b. Gas velocity (U_{air}):

For outlet gas velocity, *pressureInletOutletVelocity* boundary condition is used. The *pressureInletOutletVelocity* boundary condition is a blend of *pressureInletVelocity* and *inletOutlet* boundary conditions. The *pressureInletVelocity*, velocity is computed from difference between total and static pressure where the direction is normal to the patch faces. This boundary condition can be described as at velocity *inletOutlet* boundary condition patches for where the pressure is specified and zero-gradient is applied for outflow (as defined by the flux) and for inflow the velocity is obtained from the patch-face normal component of the internal-cell value.

c. Liquid velocity (U_{water}):

The liquid velocity at outlet is set as *pressureInletOutletVelocity* boundary condition as described above.

d. Pressure (P):

The pressure at outlet is described by constant "*fixedValue*" type and value is set to atmospheric pressure since the bubble column is open to atmosphere.

e. Turbulent kinetic energy (k):

The turbulent kinetic energy is described by constant "*zeroGradient*" condition.

f. **Turbulent energy dissipation rate (ϵ):**

The turbulent energy dissipation rate is described by is described by constant "*zeroGradient*" condition.

6.5.2.2.3 wall boundary condition

a. Gas hold up / void fraction (α_{air}) :

At wall the void fraction is set to zero by "*fixedValue*" type condition.

b. Gas velocity (U_{air}):

At wall the gas velocity is set to zero by "*fixedValue*" type condition.

c. Liquid velocity (U_{water}):

At wall the liquid velocity is set to zero by "*fixedValue*" type condition.

d. Pressure (P):

The pressure at wall is described by "*fixedFluxPressure*" type .

e. Turbulent kinetic energy (k):

At wall the turbulent kinetic energy is set to zero by "*fixedValue*" type condition.

f. Turbulent energy dissipation rate (ϵ)

At wall, the turbulent energy dissipation rate is described with wall function using the boundary condition type "*kqRWallFunction"*. This works similar to the zero gradient conditions. Near the wall, the *epsilonWallFunction* is used, where the value of ϵ is given as $\epsilon = C_{\mu}^{3/4} \frac{k^{3/2}}{0.41x}$ where x is the distance of first node to wall.

6.5.2.2.4 Internal fields / Initial conditions:

The initial fields into the internal domain, corresponding to initial liquid height, are set by using *funkySetFields* utility in OpenFOAM.

a. Gas hold up / void fraction (α_{air}) **:**

The bubble column is filled water up to certain height and during experiments the dispersion height (swell level) after air injection is mentioned to be 0.9 m. Therefore the air void fraction above 0.9 m is set to 1.0 and below it is set to average void fraction during experiment.

b. Gas velocity (U_{air})**:**

Gas velocity is set to be uniform value corresponding to inlet air velocity.

c. Liquid velocity (U_{water})**:**

The initial liquid velocity is set to zero.

d. **Pressure** (P)**:**

The pressure is set to hydrostatic pressure according to the height within the bubble column.

e. Turbulent kinetic energy (k):

Initial value of Turbulent Kinetic Energy is set to value corresponding to inlet value.

f. **Turbulent energy dissipation rate (ϵ):**

Initial value of Turbulent energy dissipation rate is set to value corresponding to inlet value.

6.5.2.2.5 Discretization schemes

Temporal, divergence, gradient and laplacian terms in Eqs. (6.36) and (6.37) are discretized separately in OpenFOAM by using proper discretization schemes. The details of the schemes used are summarized in Table 6.3.

Temporal discretization schemes: The term *ddtShemes* represents the choice of time scheme. For transient simulation various options are available in OpenFOAM, such as, Euler, Crank-Nicolson or backward discretization. Euler scheme is a first order bounded implicit scheme, which remains sufficiently accurate due to the small time step limitation created by the Courant number. The other schemes CrankNicolson and backward are second order accurate but are unbounded. The unbounded behavior of these schemes may end up in unfeasible solution of the problem.

Table 6.2: Boundary conditions used for OpenFOAM CFD simulation of bubble column

Boundary field	Bottom_inlet	Top_outlet	Wall
Void fraction	*GroovyBC*	*inletOutlet*	*fixedValue*
Gas velocity	*fixedValue*	*pressureInletOutletVelocity*	*fixedValue*
Liquid velocity	*fixedValue*	*pressureInletOutletVelocity*	*fixedValue*
Pressure	*fixedFluxPressure*	*fixedValue*	*fixedFluxPressure*

Table 6.3: Discretization schemes used in OpenFOAM CFD simulation of bubble column

Modeling term	Keyword of scheme	Description	Scheme
Convection term	*divSchemes*	Discretization of divergence terms with operator ∇	*Upwind*
Gradient term	*gradSchemes*	Discretization of gradient terms with operator ∇	*Default Gauss Linear*
Diffusive term	*laplacianSchemes*	Discretization of terms with Laplacian operator ∇^2	*Default Gauss linearcorrected*
Time derivative	*ddtSchemes*	Discretization of time derivatives	*Euler*
Others	*InterpolationSchemes*	Point to point interpolation of the value	*Default linear*
	snGradSchemes	Component of gradient normal to cell face	*Default corrected*

Gradient discretization schemes: The *gradSchemes* defines the discretization schemes for the gradient terms. In these simulations, *default Gauss linear* scheme is used as a *gradSchemes*. *Default* means that the *Gauss linear* scheme will be applied to all the gradient terms. The *Gauss* keyword specifies the standard finite volume discretization of Gaussian integration. When a Gauss discretization is used the values are interpolated from cell centers to face centers. Thatis,by usin gauss divergence theorem volume integral is converted to surface integral as shown below. These face values are then calculated by using cell center values with linear interpolation.

$$\int_V \nabla \emptyset dV = \oint_{\partial V} ds \emptyset = \sum_{fc} s_{fc} \emptyset_{fc} \tag{6.50}$$

Where fc denotes the cell face.

Divergence discretization schemes: The *divSchemes* defines the scheme used to solve convective term in the momentum equation. The convection term is descritized as below:

$$\int_V \nabla(\rho u \emptyset) dV = \oint_{\partial V} ds.(\rho u \emptyset) = \sum_{fc} s_{fc} (\rho u)_{fc} \emptyset_{fc} \tag{6.51}$$

The values of mass flux ρu and $\emptyset$ at cell faces is interpolated using convection differencing scheme. In this case, first order upwind is used as a divergence scheme. Though the upwind scheme used here is only first order accurate, it is considered to be more appropriate due to its boundedness characteristics. While other schemes, such as, central differencing are unbounded even though they are second order accurate.

Laplacian discretization schemes: The *laplacianSchemes* defines the laplacian scheme, and it is applied to the terms with the laplacian operator for diffusional terms. In the present work, the operator is set to default Gauss linear corrected. Here the word corrected expresses the surface normal gradient scheme and indicates an unbounded, conservative and second order numerical behavior.

Interpolation Schemes:A centered interpolation scheme is used under *interpolationSchemes*, which is set to default linear. This indicates that the linear interpolation scheme is used for calculating all (indicated by default as discussed in *gradSchemes*) the gradient values at the face. A *snGradSchemes* indicates the surface normal gradient schemes, and evaluates the gradient normal to the face center shared by two cells. A surface normal gradient is evaluated at a cell face; it is the component, normal to the face, of the gradient of values at the centers of the two cells that the face connects. In this case it is default corrected.

6.5.2.2.6 Post processing:

The main post-processing tool provided with OpenFOAM is Paraview, an open-source visualization application. Paraview uses the Visualization Toolkit (VTK) as its data processing and rendering engine and can therefore read any data in VTK format. OpenFOAM includes the foamToVTK utility to convert data from its native format to VTK format.

6.5.2.3 Results and discussion

Figure 6.21 to 6.24 shows the salient results for the mean values calculated for gas hold up and liquid velocity in axial direction throughout the domain and also at cross-section where z=0.598 (for Mesh-1). The results obtained are in excellent agreement with experimentally measure values as shown in Figure 6.25 & 6.26.

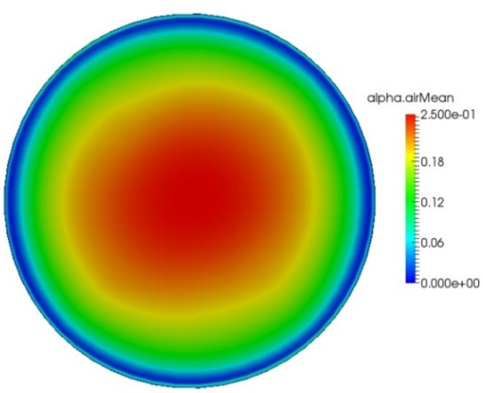

Figure 6.21: Void fraction (hold-up) for air at z = 0.598 m (validation test case for Hills experiment [96])

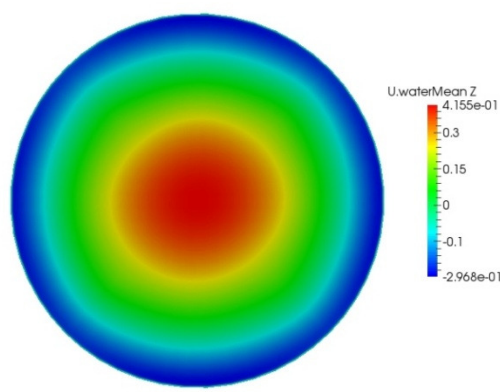

Figure 6.22: Axial velocity of water at z = 0.598 m (validation test case for Hills experiment [96])

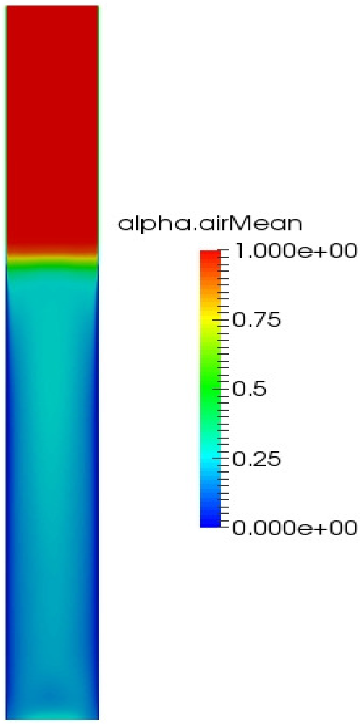

Figure 6.23: Axial variation of void for air (validation test case for Hills experiment [96])

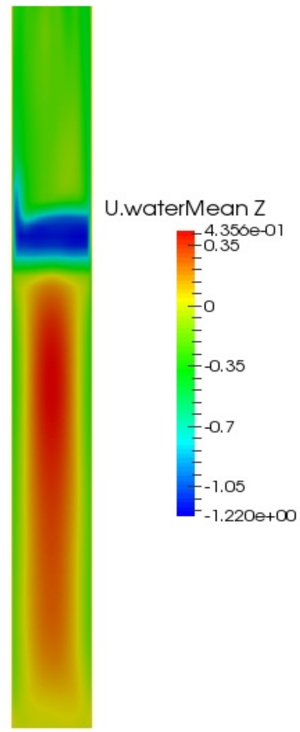

Figure 6.24: Axial variation of water velocity (validation test case for Hills experiment [96])

Menzel [97] has experimentally measured void fraction / hold-up and liquid velocity profiles in a bubble column with constant diameter of 0.6 m and height of 3.45 m. Air-water is used as working medium and air is injected at the bottom of column at superficial velocities of 0.012, 0.024, 0.048 and 0.096 m/s. CFD simulations were carried out for the geometry by Menzel [97] and the comparison of prediction for air superficial velocity of 0.096 m/s is shown in Figure 6.27 and 6.28. The CFD predictions agree very well with the measurements.

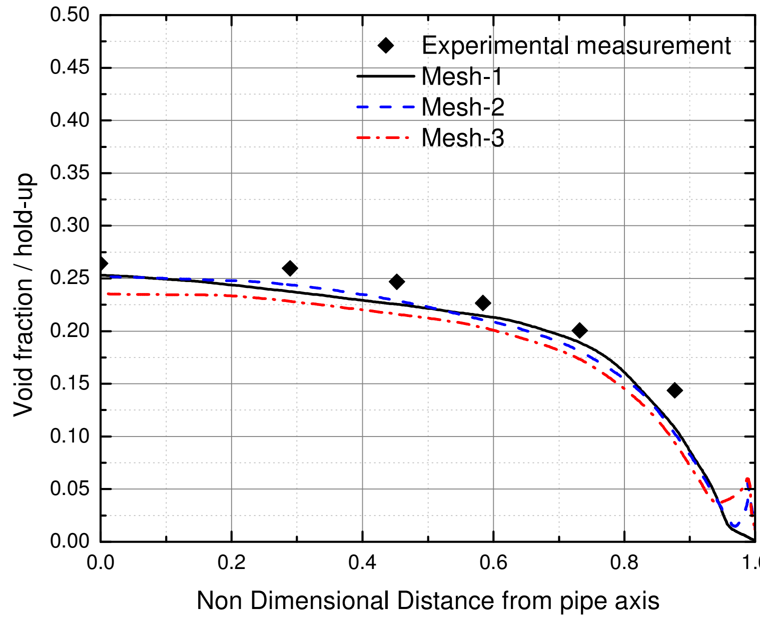

Figure 6.25: Comparison of void fraction of air predicted by CFD with experimental data by Hills [96].

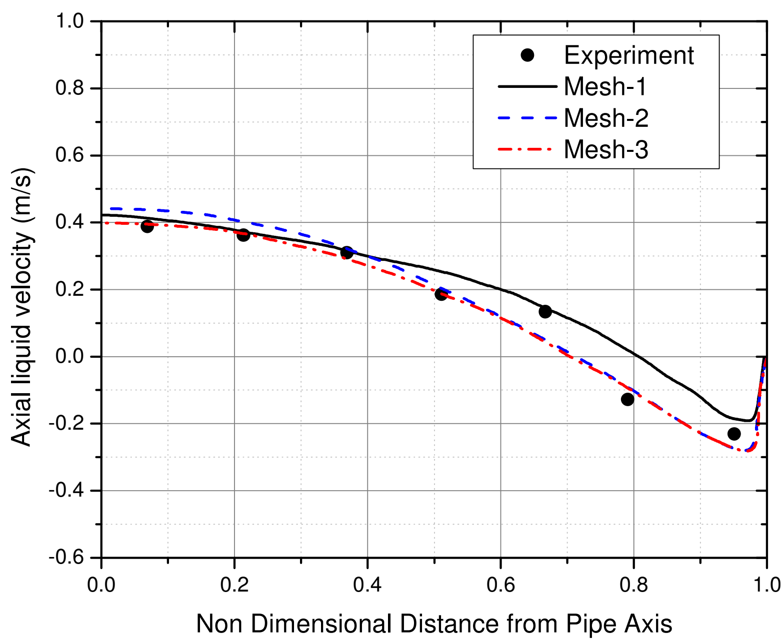

Figure 6.26: Comparison of axial velocity of water predicted by CFD with experimental data by Hills [96]

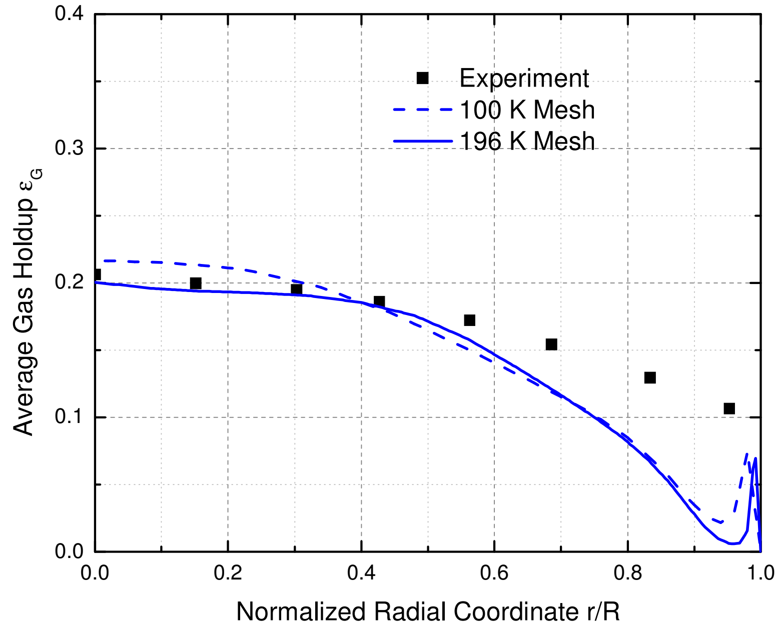

Figure 6.27: Comparison of void fraction profile predicted by CFD with experimental data (Menzel et al. [97])

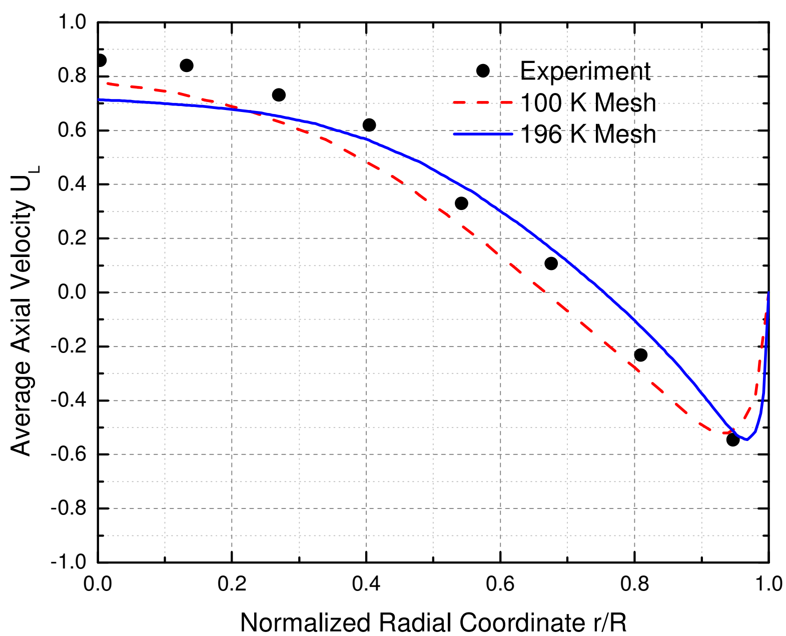

Figure 6.28: Comparison of axial velocity of water predicted by CFD with experimental data (Menzel et al. [97])

6.6 CFD simulations of pool swell in AWL drum

On the similar lines of previous validation test cases, the E-E solver of OpenFOAM was used to simulate the pool swelling phenomenon in AWL drum. Figure 6.29 shows the computational domain considered. Here instead of 15 individual inlet pipes, an averaged flow inlet is considered in the form of a plane covering the AWL drum length. This represents the distributed flow inlet instead of 15 inlets. Similarly the down comer and outlet is also simulated as distributed area. The geometry of AWL drum is complicated as the circular pipes intersect with circular drum at various angles, this lead to very high number of meshes (more than 100 lacs). The solver was observed to take huge CPU time to converge due to high mesh numbers and having transient simulation for sufficient time (generally we run it for 150 seconds or more) was becoming practically impossible. The simplification of boundaries as shown in Figure 6.29 allowed us to simulate sufficient run time with available computational resources. Figure 6.30 shows the mesh used to descritize the computational domain. The mesh was generated using free meshing tool Gmsh. The mesh was constructed by first generating a surface mesh representing the cross-section of AWL drum and then extruding it in horizontal direction to get the final geometry.

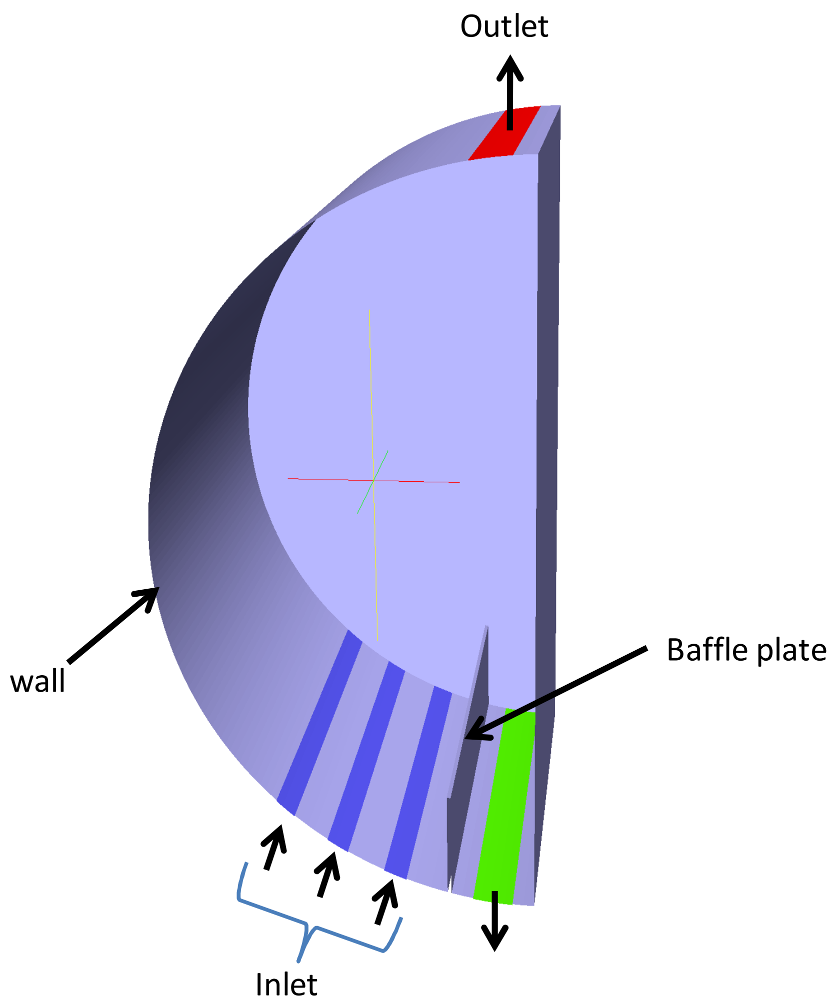

Figure 6.29: Geometry and boundaries considered for AWL drum two phase simulation

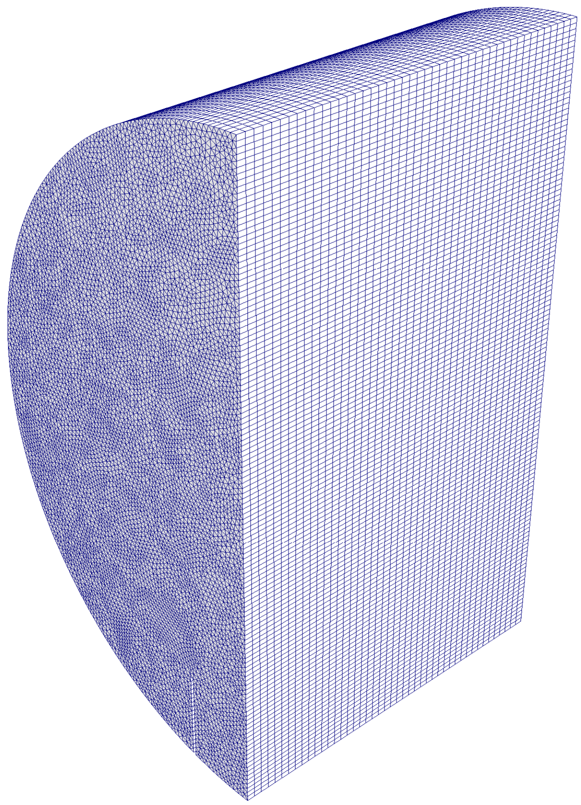

Figure 6.30: Mesh used for AWL drum two-phase simulation (total cells-3.67 lacs)

6.6.1 Simulation cases considered

During experiments in AWL, the drum is filled with water up to a certain level and air is injected in tail pipe bottom at rate of 50 to 400 lpm in steps of 50 lpm each in all 15 tail pipes. As discussed in earlier section 5.1, some inventory from water tank is naturally transferred to drum as a result of momentum balance between drum and water tank. The average pool void fraction is calculated as described in section 5.1. The void fraction in each tail pipes (Type-I, II and III rows) is predicted using void fraction correlation (see validation of AWL steady state data, Chapter 4.). Table-6.4 summarizes test data considered for the CFD simulation of drum. The corresponding boundary conditions provided for simulation are described in Table-6.5. The void fraction value used for simulation at the inlet of drum corresponds to area averaged void fraction of all the tail pipes. The inlet water and air velocities are calculated based on the area of inlet boundary, void fraction at inlet and required volumetric flow rate.

Table 6.4: Test conditions considered for two-phase simulation in AWL drum

Sr. No.	Air flow rate (lpm)	Water flow rate to drum inlet (lpm)	Initial drum level (m)	Swell level (m)	Type-I tail pipe void fraction	Type-II tail pipe void fraction	Type-III tail pipe void fraction	Swell volume	Total Water volume in drum
1	750	890	0.650	0.93	0.17	0.27	0.32	0.80	0.76
2	1500	1055	0.650	1.04	0.25	0.27	0.33	0.93	0.85
3	2250	1147	0.650	1.09	0.3	0.32	0.38	0.98	0.88
4	3000	1226	0.650	1.15	0.34	0.37	0.43	1.05	0.93
5	3750	1274	0.650	1.2	0.39	0.41	0.48	1.10	0.98
6	4500	1250	0.650	1.27	0.42	0.44	0.52	1.18	0.99
7	5250	1365	0.650	1.3	0.45	0.47	0.54	1.21	1.01
8	6000	1401	0.650	1.46	0.48	0.51	0.58	1.37	1.03

Table 6.5: Boundary condition for inlet boundary for two-phase flow simulation

Sr. No.	Air flow rate (lpm)	Water flow rate to drum inlet (lpm)	Total Water volume in drum	Void fraction	Air velocity (m/s)	Water velocity (m/s)
1	750	890	0.76	0.25	0.23	0.07
2	1500	1055	0.85	0.28	0.41	0.08
3	2250	1147	0.88	0.33	0.52	0.09
4	3000	1226	0.93	0.38	0.61	0.09
5	3750	1274	0.98	0.43	0.67	0.10
6	4500	1250	0.99	0.46	0.75	0.10
7	5250	1365	1.01	0.49	0.83	0.10
8	6000	1401	1.03	0.52	0.88	0.11

The initial conditions for level in the drum are maintained such that it corresponds to the total water volume in the drum calculated during experiments. The boundary conditions for $k - \varepsilon$ are calculated as described by equation (5.52 and 5.52). The other solution parameters are maintained similar to the validation test cases (as described in section 6.5.2.2).

6.6.2 Salient results and discussions:

The CFD simulation gives detailed information on local velocity of air and water, local void fraction inside the computational domain. Figure 6.31 (a) to (d) shows the instantaneous void fraction distribution in AWL drum two-phase pool at different transient time of simulation. The separation interface fluctuation is captured in simulations which is similar to experimental observations. Figure 6.32 shows the time averaged void fraction at time t = 100 seconds. The swell level is measured from this time averaged void fraction and interface height is the height at which void fraction > 0.75. The velocity pattern for water is shown in Figure 6.33. It is clearly seen that strong recirculation flows are generated inside the drum forcing most of the void towards the central core of flow.

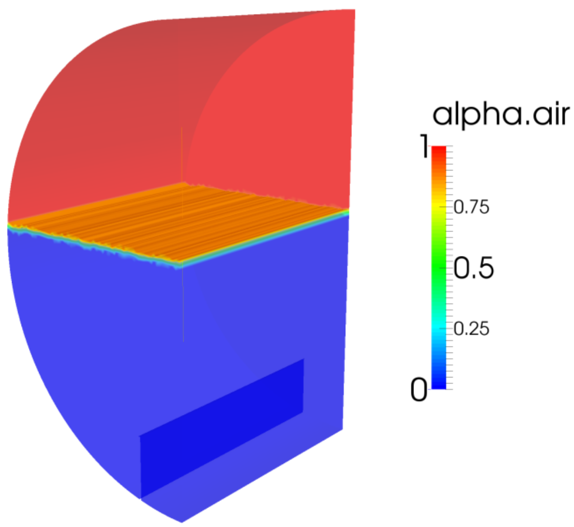

(a) t =0 s.

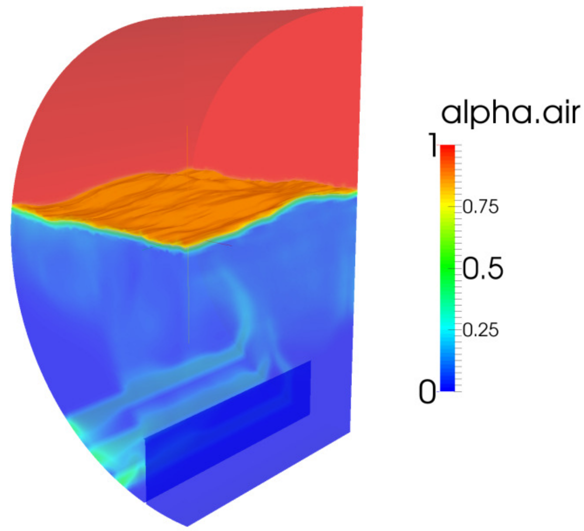

(b) t = 95 s.

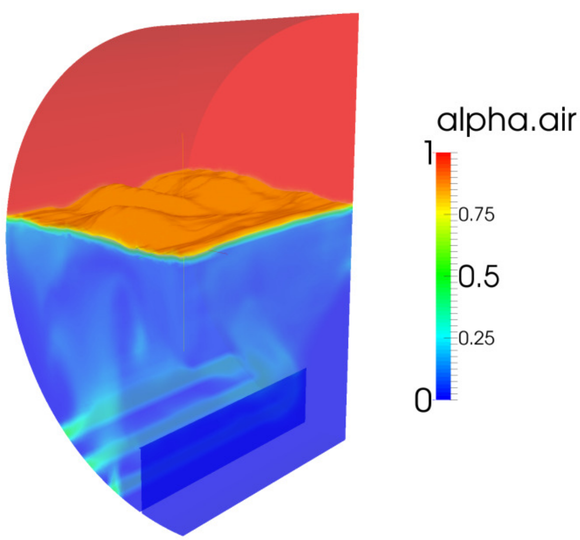

(c) t =96 s.

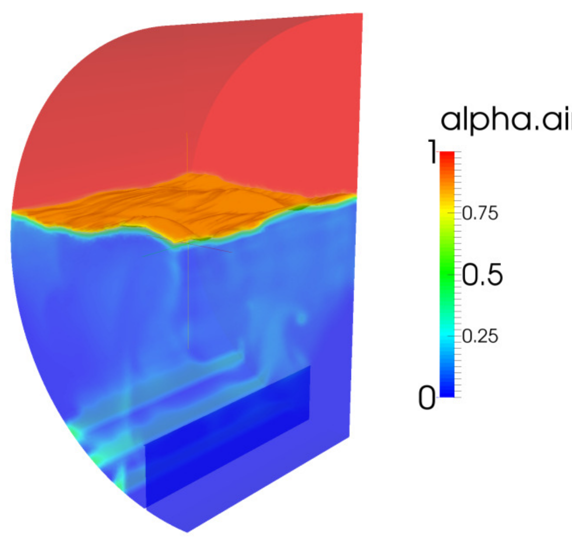

(d) t = 97 s.

Figure 6.31 : Instantaneous void fraction distribution obtained using CFD for case-4, Table 6.5 at time (a) t=0, (b) t= 95 s. (c) t= 96 s., (d) t= 97 s.

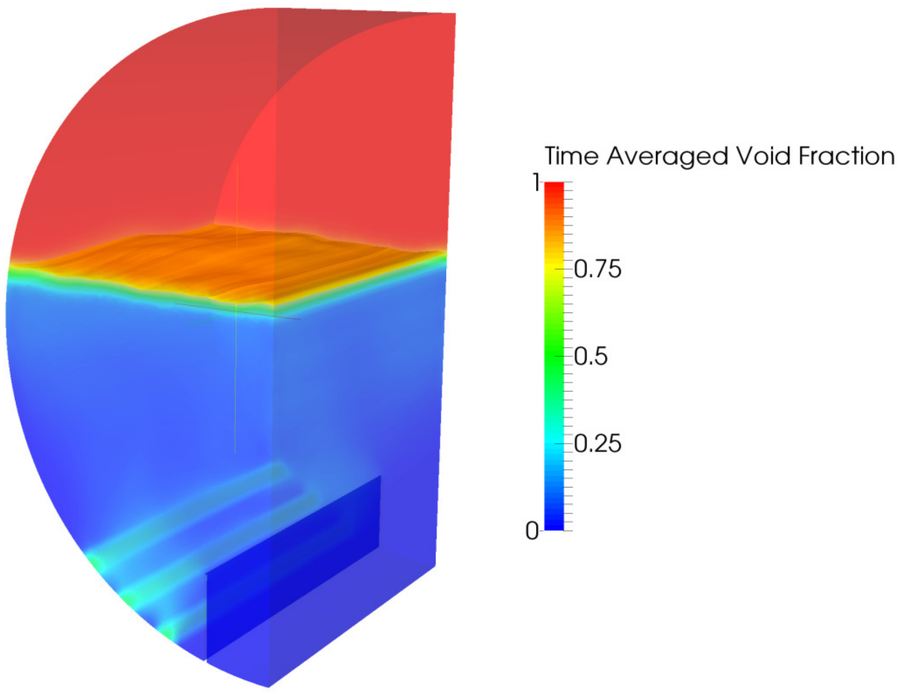

Figure 6.32: Time averaged void fraction distribution in drum (t = 100 seconds)

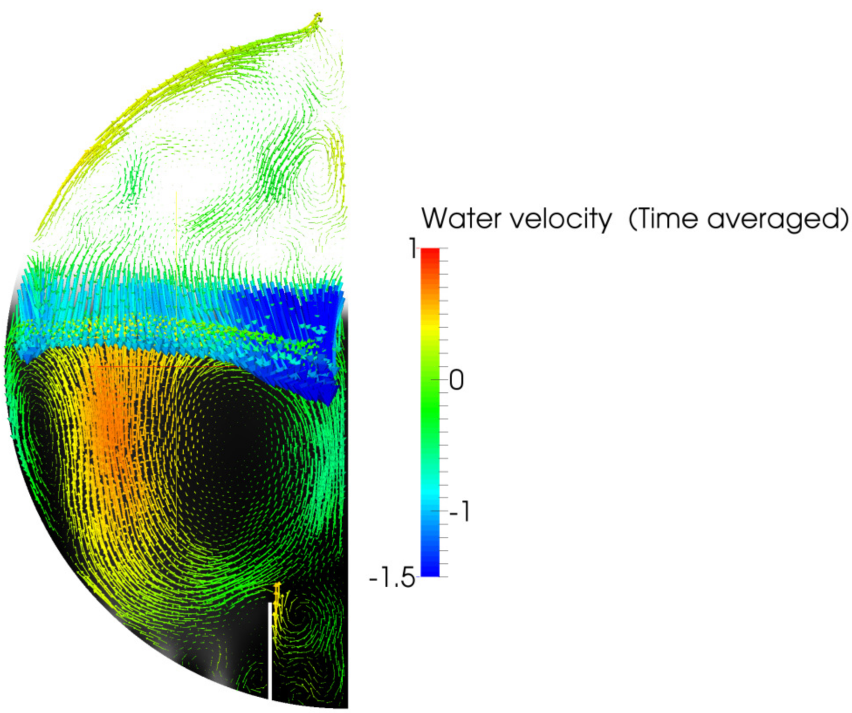

Figure 6.33 : Time averaged water velocity vector plot for case-4, Table-6.5, t = 100 sec.

Figure 6.34 shows the void fraction profiles at various elevations inside the drum. Figure 6.35 shows the time averaged local velocities of air and water and slip velocity at different elevations inside the drum. It can be seen that slip velocity varries between 0.3 to 0.4, and it is contant at the given cross-section.

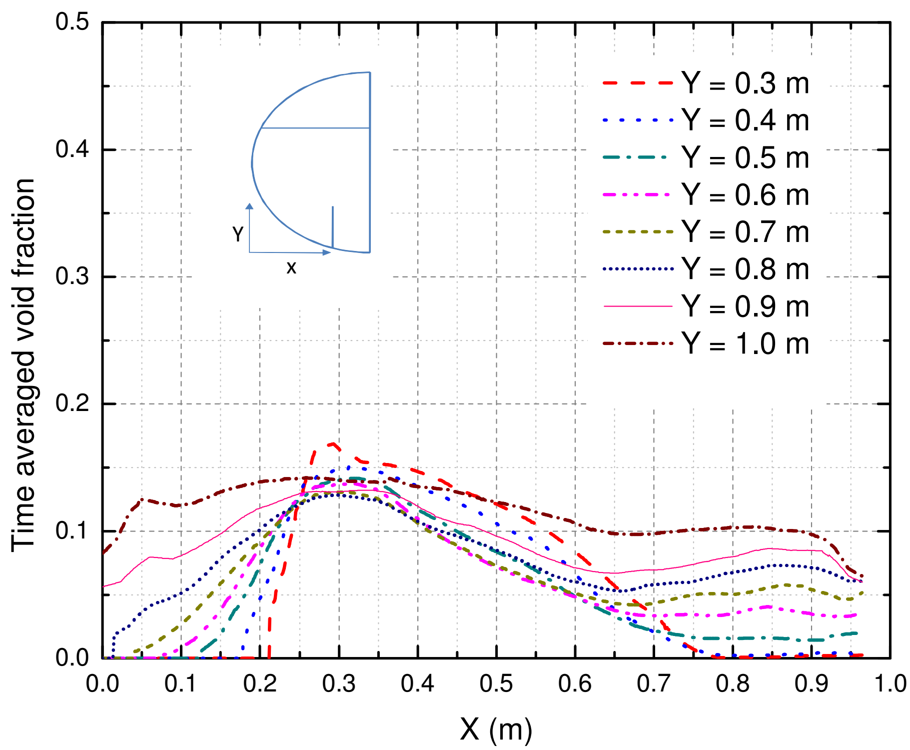

Figure 6.34: Void fraction (time averaged) profiles inside the drum at various elevations (Y=0.3 to 1.0 m) for case-4 described in Table 6.5.

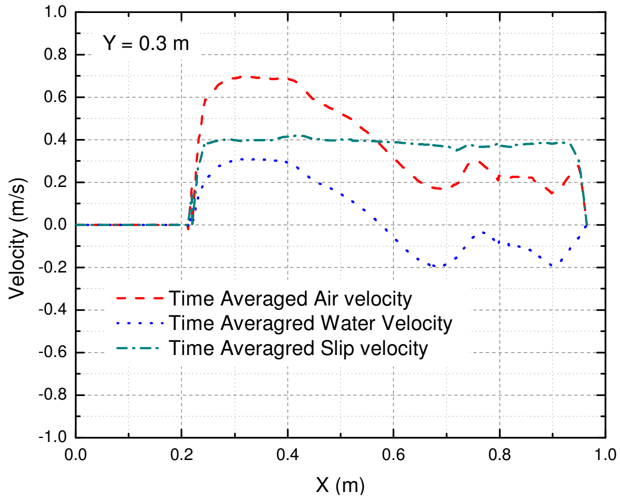
Y = 0.3 m
Velocity (m/s)
X (m)
Time Averaged Air velocity
Time Averagred Water Velocity
Time Averagred Slip velocity
1.0
0.8
0.6
0.4
0.2
0.0
-0.2
-0.4
-0.6
-0.8
-1.0
0.0
0.2
0.4
0.6
0.8
1.0

(a)

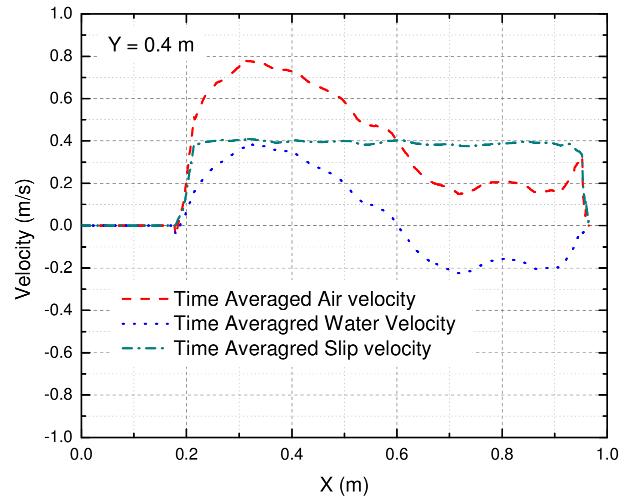
Y = 0.4 m
Velocity (m/s)
X (m)
Time Averaged Air velocity
Time Averagred Water Velocity
Time Averagred Slip velocity
1.0
0.8
0.6
0.4
0.2
0.0
-0.2
-0.4
-0.6
-0.8
-1.0
0.0
0.2
0.4
0.6
0.8
1.0

(b)

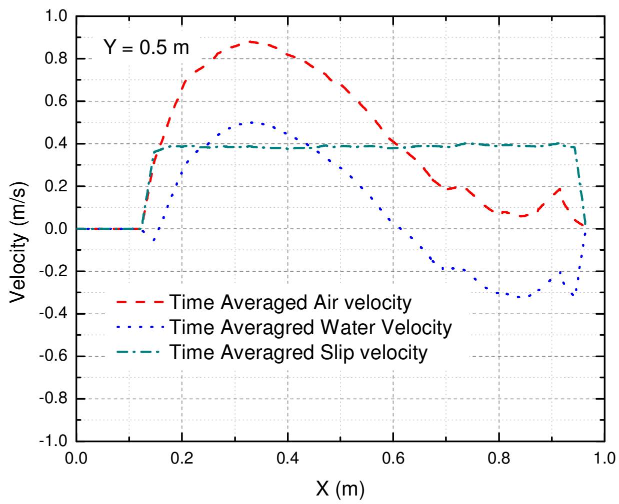
Y = 0.5 m
Velocity (m/s)
X (m)
Time Averaged Air velocity
Time Averagred Water Velocity
Time Averagred Slip velocity
1.0
0.8
0.6
0.4
0.2
0.0
-0.2
-0.4
-0.6
-0.8
-1.0
0.0
0.2
0.4
0.6
0.8
1.0

(c)

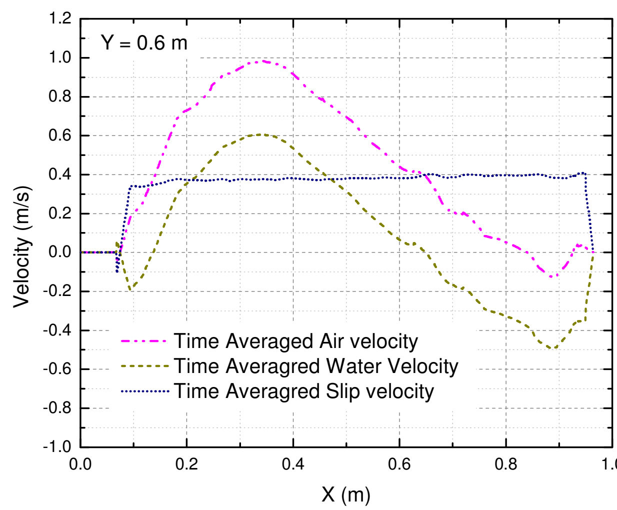
Y = 0.6 m
Velocity (m/s)
X (m)
Time Averaged Air velocity
Time Averagred Water Velocity
Time Averagred Slip velocity
1.2
1.0
0.8
0.6
0.4
0.2
0.0
-0.2
-0.4
-0.6
-0.8
-1.0
0.0
0.2
0.4
0.6
0.8
1.0

(d)

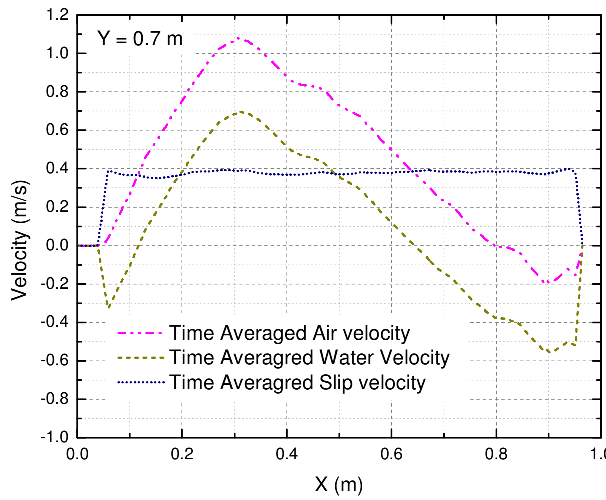

(e)

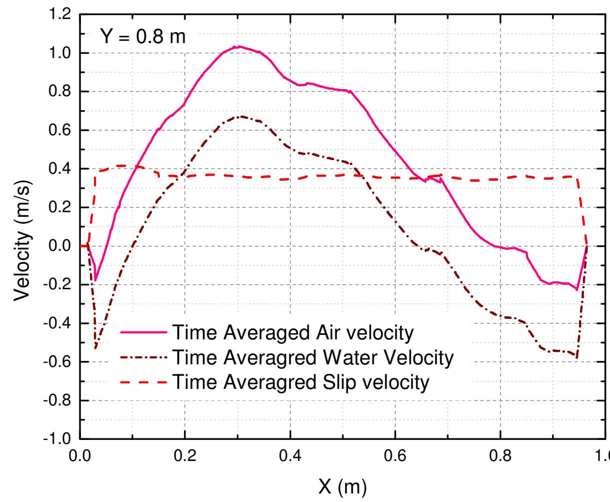

(f)

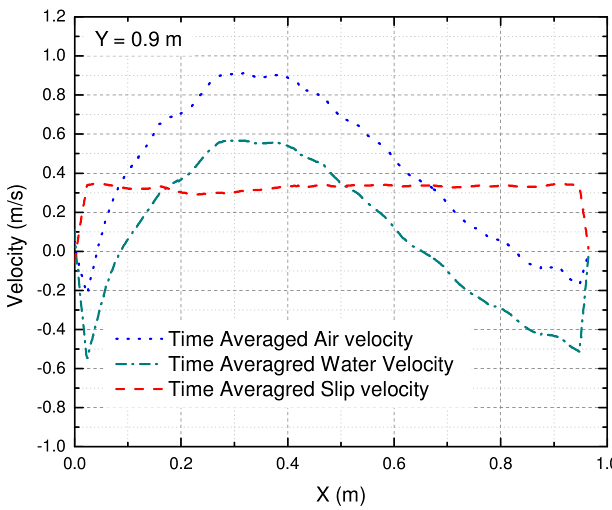

(g)

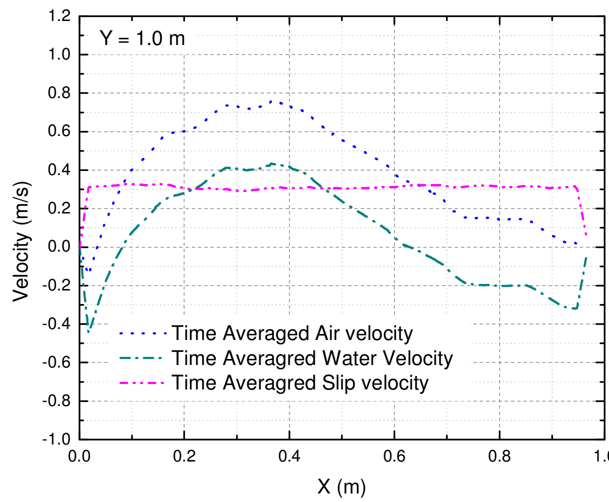

(h)

Figure 6.35: Profiles of time averaged local air and water velocity and slip velocity at different elevations inside the AWL drum pool (case-4, Table 6.5).

The swell level was predicted using CFD simulation for the cases described in Table-6.5. The comparison of predictions for swell level and average pool void fraction is shown in Figure 6.36 & 6.37 respectively.

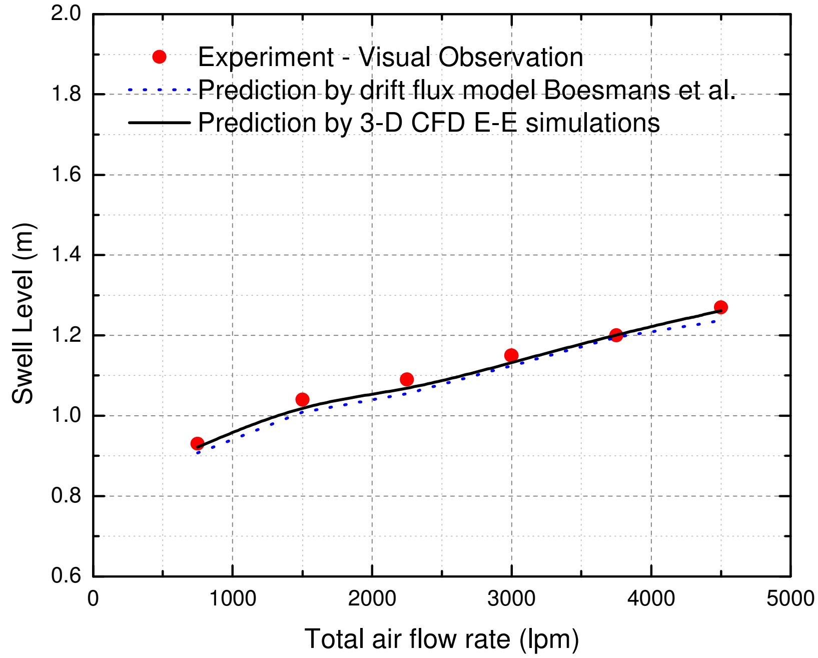

Figure 6.36: Comparison of swell level predicted by CFD simulations with experimental measurements (initial level =0.650 m)

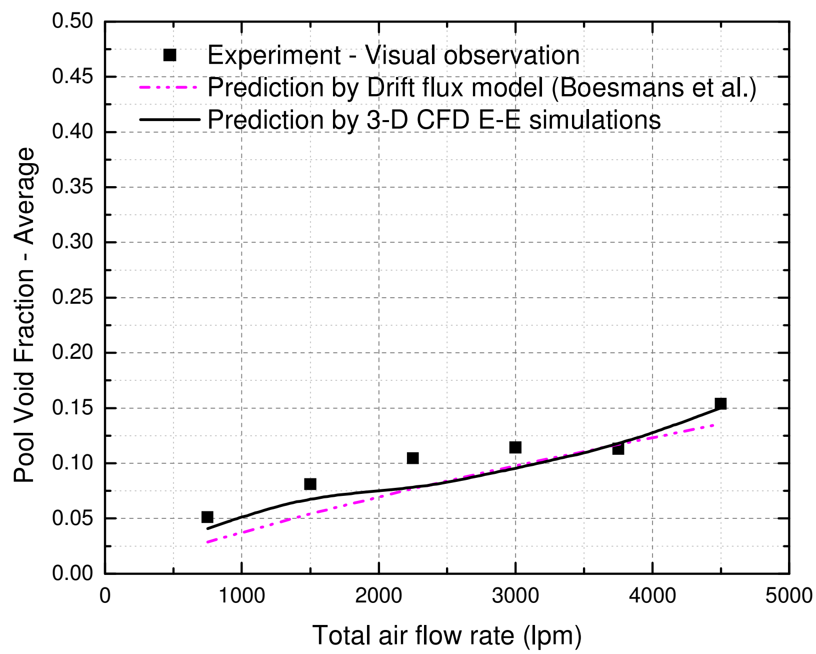

Figure 6.37: Comparison of void fraction predicted by CFD simulations with experimental measurements (initial level =0.650 m)

6.7 Development of drift flux model using CFD simulations:

6.7.1 Drift flux model equations

The drift flux model gives the relationship between the flow rate of gas and liquid phases to the quantitative description of their distribution. The drift flux model can be written as:

$$\frac{\langle \overline{j_g} \rangle}{\langle \overline{\varepsilon_g} \rangle} = C_0 \langle \overline{j_g + j_l} \rangle + C_1 \tag{6.52}$$

Where overbar denotes the time averaged quantity and $\langle \quad \rangle$ denotes the Area averaging. The ε_g, j_g and j_l are local void fraction, local gas superficial velocity and local liquid superficial velocity respectively. The local superficial velocity can be defined from the local velocity of individual phases as follows:

Consider a small cross-sectional area a as shown in Figure 6.38. Let q_g and q_l be the volumetric flow rates of gas and liquid through this small area. Within this small area, gas occupies some portion and we can then define the local gas fraction ε_g based on area ratio. Now, thus the local superficial velocity can be defined as follows:

$$j_g = \lim_{a \to 0} \left(\frac{q_g}{a} \right) = \varepsilon_g v_g \tag{6.53}$$

And

$$j_l = \lim_{a \to 0} \left(\frac{q_l}{a} \right) = \varepsilon_l v_l = \left(1 - \varepsilon_g\right) v_l \tag{6.54}$$

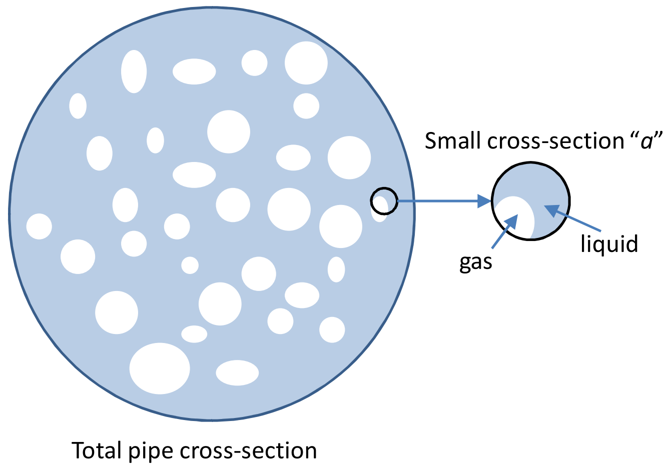

Figure 6.38: Cross-sectional view of two-phase flow in a pipe.

And local instantaneous volumetric flow rate can be given as $j = j_l + j_g$ based on above. The instantaneous local real velocity of gas and liquid can be defined as:

$$v_l = \left(\frac{j_l}{\varepsilon_l}\right) = \left(\frac{j_l}{1-\varepsilon_g}\right) \text{ and } v_g = \left(\frac{j_g}{\varepsilon_g}\right) \tag{6.55}$$

The local drift velocity can be written as

$$v_{gl} = \left(v_g - j\right) \tag{6.56}$$

Multiplying above equation with ε_g we get

$$\varepsilon_g v_{gl} = \varepsilon_g v_g - \varepsilon_g j \tag{6.57}$$

$$\varepsilon_g v_{gl} = j_g - \varepsilon_g j \tag{6.58}$$

i.e.

$$j_g = \varepsilon_g j + \varepsilon_g v_{gl} \tag{6.59}$$

Applying time and space averaging we can write above equation as:

$$\langle \overline{j_g} \rangle = \langle \overline{\varepsilon_g j} \rangle + \langle \overline{\varepsilon_g v_{gl}} \rangle \tag{6.60}$$

diving above equation with $\langle \overline{\varepsilon_g} \rangle$ we get

$$\frac{\langle \overline{j_g} \rangle}{\langle \overline{\varepsilon_g} \rangle} = \frac{\langle \overline{\varepsilon_g j} \rangle}{\langle \overline{\varepsilon_g} \rangle} + \frac{\langle \overline{\varepsilon_g v_{gl}} \rangle}{\langle \overline{\varepsilon_g} \rangle} \tag{6.61}$$

which is equal to

$$\frac{\langle \overline{j_g} \rangle}{\langle \overline{\varepsilon_g} \rangle} = \frac{\langle \overline{\varepsilon_g j} \rangle \langle \overline{j} \rangle}{\langle \overline{\varepsilon_g} \rangle \langle \overline{j} \rangle} + \frac{\langle \overline{\varepsilon_g v_{gl}} \rangle}{\langle \overline{\varepsilon_g} \rangle} \tag{6.62}$$

The local drift velocity v_{gl} can be expressed in terms of local slip velocity and local gas fraction as follows:

$$v_{gl} = v_g - \left(j_g + j_l\right) = v_g - \left(\varepsilon_g v_g + \left(1 - \varepsilon_g\right) v_l\right) \tag{6.63}$$

$$v_{gl} = v_g - \varepsilon_g v_g - v_l + \varepsilon_g v_l = \left(1 - \varepsilon_g\right)\left(v_g - v_l\right) = \left(1 - \varepsilon_g\right) v_{slip}$$

Equation (6.62) can be rewritten as:

$$\frac{\langle \overline{j_g} \rangle}{\langle \overline{\varepsilon_g} \rangle} = \frac{\langle \overline{\varepsilon_g j} \rangle \langle \overline{j} \rangle}{\langle \overline{\varepsilon_g} \rangle \langle \overline{j} \rangle} + \frac{\langle \overline{\varepsilon_g \left(1 - \varepsilon_g\right) v_{slip}} \rangle}{\langle \overline{\varepsilon_g} \rangle} \tag{6.64}$$

Finally we can define the drift flux parameters and void fraction as follows:

$$\frac{\langle \overline{j_g} \rangle}{\langle \overline{\varepsilon_g} \rangle} = C_0 \langle \overline{j} \rangle + C_1 \tag{6.65}$$

Where

$$C_0 = \frac{\langle \overline{\varepsilon_g j} \rangle}{\langle \overline{\varepsilon_g} \rangle \langle \overline{j} \rangle} \tag{6.66}$$

$$C_1 = \frac{\langle \overline{\varepsilon_g (1 - \varepsilon_g) v_{slip}} \rangle}{\langle \overline{\varepsilon_g} \rangle}$$

6.7.2 Calculation of distribution parameters from CFD simulations

As seen in Figure 6.34 and 6.35, the CFD simulations enable us to estimate the local velocity and air, water, local hold up/void fraction and also slip velocity. This information can be used in deriving the above distribution parameters. An experiment which measures these local quantities throughout the pool is extremely rare and very difficult. The CFD simulation which is equivalent to numerical experiment thus provides us opportunity to look into individual parameters in details and develop the drift flux model parameters.

The time and space averaged distribution parameters (as per Equation (6.64)) are determined for AWL drum CFD simulations, at different cross-sections. The cross-sections considered are at y=0.3 to 1.4 m at interval of 0.1 m. Thus total 12 cross-sectional planes are considered. The local values are read on these planes using the "*swak4Foam*" expressions. "*swak4Foam version 0.4.0*" is a open source library developed for OpenFOAM, where user can specify expressions involving the fields being calculated and evaluate them.

The computed values of $\langle \overline{J_g} \rangle$, $\langle \overline{J_g} \rangle$, C_0, C_1 and $\langle \overline{\varepsilon_g} \rangle$ at various air flow rates and at different elevations of drum are shown in Table 6.6 to 6.9. It can be observed that the values of distribution parameters $C_0$and C_1 depend on the local hold up. With increasing local hold-up, the C_0 reduces and approaches value of 1.0. The parameter C_1 also approaches to become 0 as the local hold up increases. This is expected behaviour because as hold up increases the void / gas distribution tends to become uniform (C_0=1.0). At 100% void fraction, i.e. in gas space above separation interface, since the $\langle \overline{j_g} \rangle = \langle \bar{J} \rangle$, C_1 becomes 0. Figure 6.39 and 6.40 shows the variation of distribution parameters with respect to local hold up.

Table-6.6: Values of superficial velocities, void fraction and drift flux parameters calculated by CFD for case-2

Plane	**Distance from bottom (m)**	**Flow rate per channel**	$\langle \overline{j_g} \rangle$	$\langle \overline{j_l} \rangle$	C_0	C_1	$\langle \overline{\varepsilon_g} \rangle$
1	0.3	100	0.029	0.0008	3.119	0.335	0.042
2	0.4	100	0.028	0.0002	3.716	0.339	0.035
3	0.5	100	0.026	0.0002	4.087	0.343	0.029
4	0.6	100	0.025	0.0001	4.150	0.344	0.027
5	0.7	100	0.024	0.0013	3.613	0.344	0.029
6	0.8	100	0.024	0.0003	2.810	0.319	0.038
7	0.9	100	0.024	0.0007	1.985	0.309	0.051
8	1	100	0.077	0.0402	1.351	0.123	0.485
9	1.1	100	0.026	0.0002	0.996	0.000	1.000

Table-6.7: Values of superficial velocities, void fraction and drift flux parameters calculated by CFD for case-3

Plane	Distance from bottom (m)	Flow rate per channel	$\langle \overline{j_g} \rangle$	$\langle \overline{j_l} \rangle$	C_0	C_1	$\langle \overline{\varepsilon_g} \rangle$
1	0.3	150	0.044	0.0016	2.947	0.309	0.064
2	0.4	150	0.042	0.0003	3.477	0.319	0.052
3	0.5	150	0.039	0.0005	4.091	0.336	0.041
4	0.6	150	0.038	0.0006	3.859	0.338	0.042
5	0.7	150	0.370	0.0000	3.161	0.337	0.048
6	0.8	150	0.037	0.0006	2.523	0.323	0.059
7	0.9	150	0.037	0.0012	1.858	0.298	0.079
8	1	150	0.048	0.0105	1.931	0.306	0.130
9	1.1	150	0.055	0.0107	1.015	0.016	0.917
10	1.2	150	0.038	0.0000	1.000	0.000	1.000

Table-6.8: Values of superficial velocities, void fraction and drift flux parameters calculated by CFD for case-4

Plane	Distance from bottom (m)	Flow rate per channel	$\langle \overline{j_g} \rangle$	$\langle \overline{j_l} \rangle$	C_0	C_1	$\langle \overline{\varepsilon_g} \rangle$
1	0.3	200	0.058	0.0020	3.269	0.307	0.069
2	0.4	200	0.056	0.0002	3.775	0.315	0.057
3	0.5	200	0.053	0.0012	3.665	0.315	0.055
4	0.6	200	0.052	0.0016	3.044	0.316	0.063
5	0.7	200	0.051	0.0017	2.540	0.317	0.073

6	0.8	200	0.050	0.0019	2.104	0.313	0.084
7	0.9	200	0.049	0.0021	1.788	0.307	0.096
8	1	200	0.049	0.0024	1.422	0.288	0.120
9	1.1	200	0.130	0.0483	2.121	0.293	0.313
10	1.2	200	0.055	0.0037	1.008	0.085	0.965
11	1.3	200	0.052	0.0000	1.000	0.000	1.000

Table-6.9: Values of superficial velocities, void fraction and drift flux parameters calculated by CFD for case-5.

Plane	Distance from bottom (m)	Flow rate per channel	$\langle \overline{J_g} \rangle$	$\langle \overline{J_l} \rangle$	C_0	C_1	$\langle \overline{\varepsilon_g} \rangle$
1	0.3	250	0.072	0.0021	3.141	0.298	0.087
2	0.4	250	0.070	0.0001	3.569	0.301	0.074
3	0.5	250	0.066	0.0008	3.694	0.309	0.067
4	0.6	250	0.063	0.0008	3.074	0.311	0.075
5	0.7	250	0.061	0.0003	2.440	0.306	0.090
6	0.8	250	0.060	0.0006	2.010	0.295	0.106
7	0.9	250	0.060	0.0008	1.676	0.288	0.124
8	1	250	0.060	0.0018	1.417	0.271	0.149
9	1.1	250	0.062	0.0011	1.226	0.253	0.178
10	1.2	250	0.125	0.0376	1.116	0.091	0.694
11	1.3	250	0.067	0.0014	0.998	0.002	0.993
12	1.4	250	0.068	0.0000	1.000	0.000	1.000

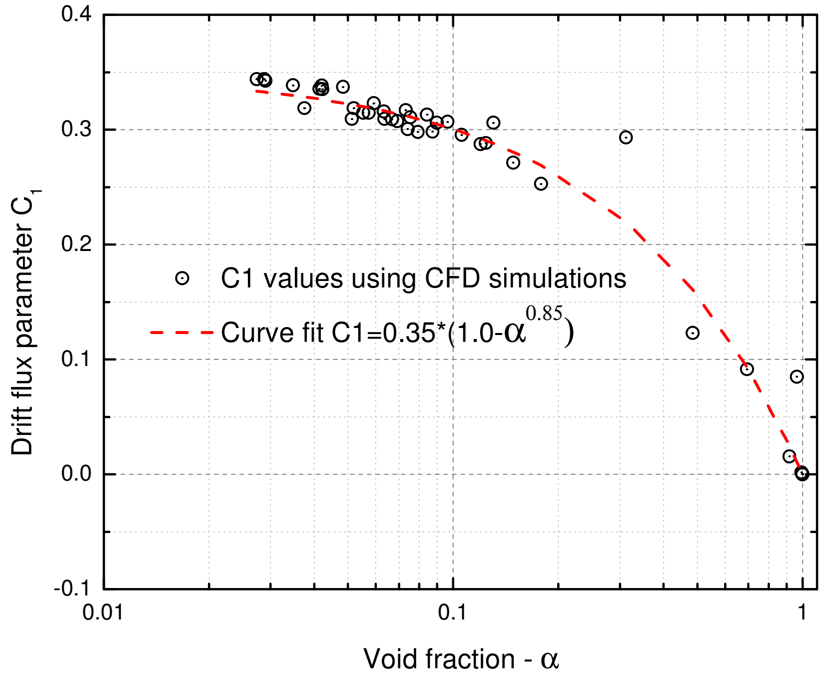

Figure 6.39: Drift flux parameter C_1 estimated from CFD simulations

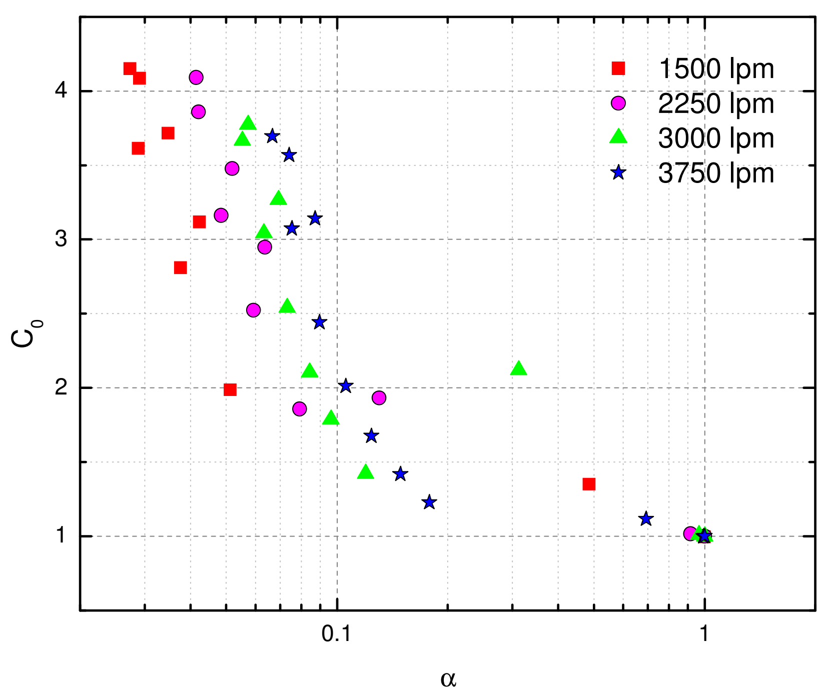

Figure 6.40: Drift flux parameter C_0 estimated from CFD simulations.

As shown in Figure 6.39, the C_1can be represented by the equation$0.35\left(1.0-\left(\langle\overline{\varepsilon_g}\rangle\right)^{0.85}\right)$. The Figure 6.40 indicates that C_0 has dependence on local hold up as well as superficial gas velocity. Form Figure 6.41 it can be seen that $\frac{C_0}{\langle \overline{J_g}\rangle}$ falls on a single curve which can be represented by an exponential decay curve $20 + 400e^{-35\langle\overline{\varepsilon_g}\rangle}$.

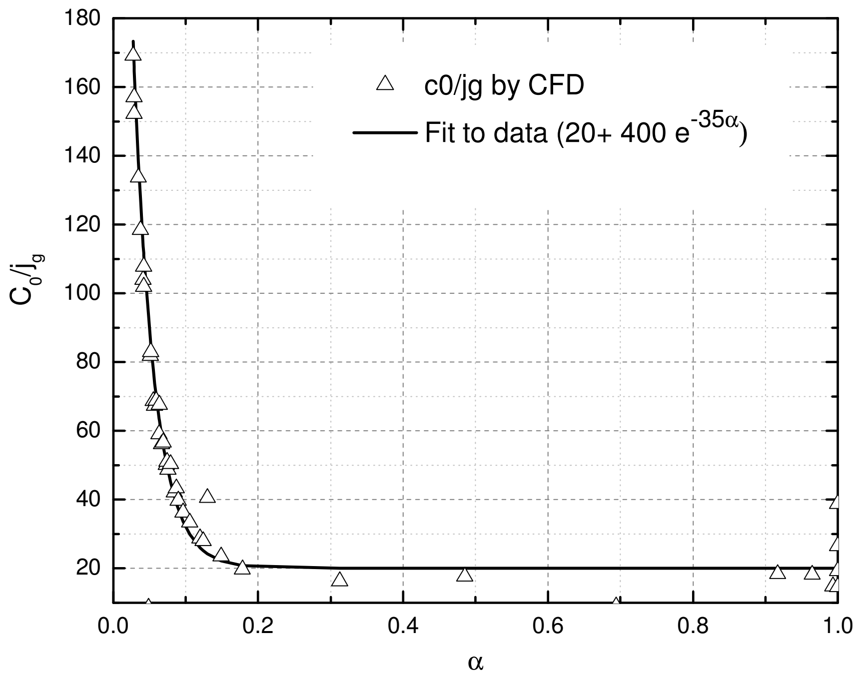

Figure 6.41: Variation of $\frac{C_0}{\langle \overline{J_g}\rangle}$ with respect to local hold up.

This information is used to recommend a drift flux model.

6.7.3 Recommendations for drift flux model based on CFD simulations

The analysis / curve fitting to the distribution parameters estimated form CFD simulations indicates that we can use:

$$C_1 = 0.35\left(1.0 - \left(\langle\overline{\varepsilon_g}\rangle\right)^{0.85}\right) = \frac{2.15}{\left(\dfrac{{\rho_l}^2}{\sigma g(\rho_l - \rho_g)}\right)^{1/4}}\left(1.0 - \left(\langle\overline{\varepsilon_g}\rangle\right)^{0.85}\right) \tag{6.67}$$

$$\& \; C_0 = \langle\overline{J_g}\rangle\left(20 + 400e^{-35\langle\overline{\varepsilon_g}\rangle}\right) \tag{6.68}$$

The above equation can produce value of C_0 smaller than 1.0, in case of very small values of $\langle\overline{J_g}\rangle$, therefore it is suggested that C_0 shall be calculated as

$$C_0 = \max\left(\langle\overline{J_g}\rangle\left(20 + 400e^{-35\langle\overline{\varepsilon_g}\rangle}\right), 1.0\right) \tag{6.69}$$

The equation (6.65) combined with Equation (6.67) and (6.69) are utilized to predict the pool void fraction and swell level for AWL drum case. Figure 6.42 shows the predicted swell level with proposed correlation.

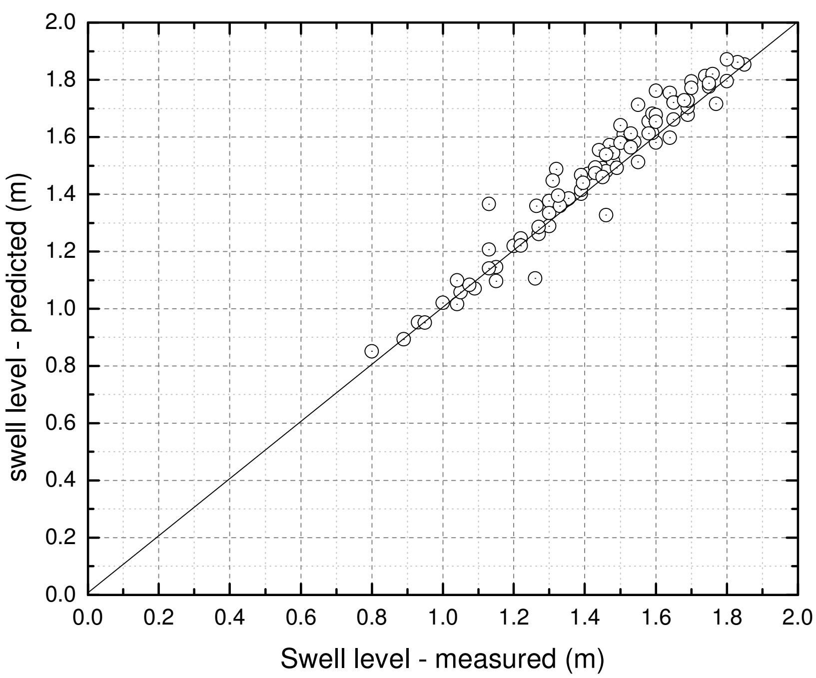

Figure 6.42: Comparison of predicted swell level using proposed drift flux correlation with experimental measurements.

It is seen that the predictions with proposed correlation are slightly higher (conservative) than the measurements but are in good agreement compared to conventional drift flux correlations.

6.8 Experimental measurement of local void fraction and comparison with CFD

As discussed in earlier section 6.2, the swell level measurement indicates the average void fraction of the pool, however there is 3-D distribution of void fraction / hold up inside the drum depending on the local flow pattern. The local hold up is experimentally measured in AWL using multi point conductance probe. Figure 6.43 shows schematic conductance probe to explain the working principle.

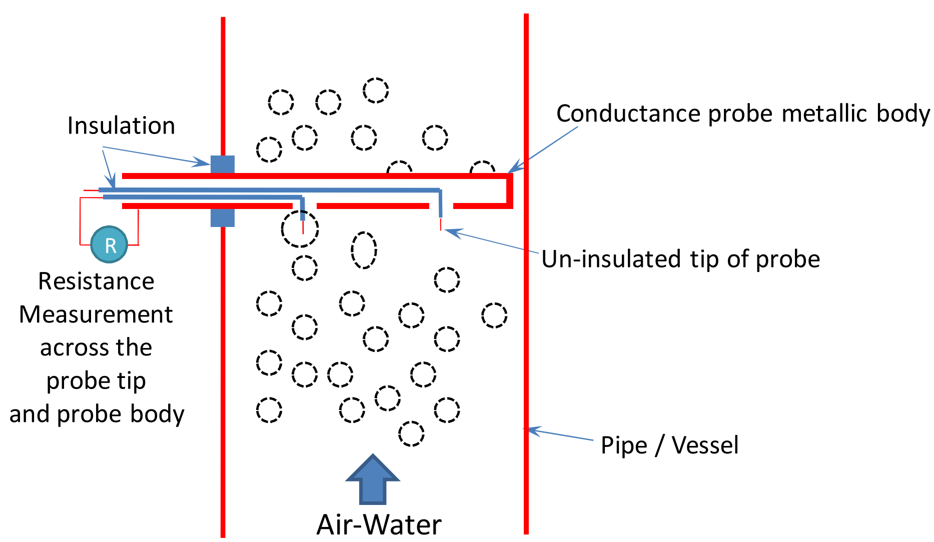

Figure 6.43: Multi-point conductance probe (working principle).

As shown in figure the conductance probe has a metallic body which is directly inserted in pipe/vessel. The metallic body is insulated from the pipe / vessel walls. The probe tips are placed across the flow cross-section facing towards the flow of bubbles. The probe tip is constructed with insulated copper wire and the insulation is removed at the tip. The resistance between the probe body and tip is measured by an electronic circuit. When there is no bubble, the water surrounding the tip gives high conductivity / low resistance value. In presence of air bubble, the resistance between tip and body is high. The measurement of resistance in time domain gives pulses of high resistance values corresponding to presence of bubble. The ratio of duration of high resistance pulse to the total time of measurement gives the local void fraction/ hold up.

8 number of multi-point conductance probes are installed in AWL drum as shown in Figure 6.44. Each probe has 10 measurement points / probe tips. The details of the probe locations in the AWL drum and probe tip distances are shown in Figure 6.44 and 6.45 respectively. The conductance probe body is made up from 6 mm diameter SS tube with 1 mm wall thickness. The probe number CP-6, CP-7, Cp-8, CP-9, CP-10 and CP-11 are installed in the cross-section of drum in axial direction along the drum length (see the front view of drum in Figure 6.44). The probes CP-12 and CP-13 are installed in transverse direction as seen in side view of AWL drum (Figure 6.44). Thus total 80 points / probe tips are placed in AWL drum to give experimental measurement of local hold up. The electronic circuit scans / measures the resistance at probe tips in each 50 mili-seconds interval. The hold-up value is recorded after integration of the signal for each 10 second interval.

Figure 6.46 (a) shows the transient signal obtained from a probe tip (probe no 10, point 1). During experiment the air injection flow rate is kept constant for all the channels. Sufficient time is allowed to collect the steady state data from all the probe points. The data is then time averaged to obtain the local hold up value for a given air injection flow rate (see Figure 6.46 (b)). The time averaged local hold up for each probe point gives the profile of void fraction for the probe.

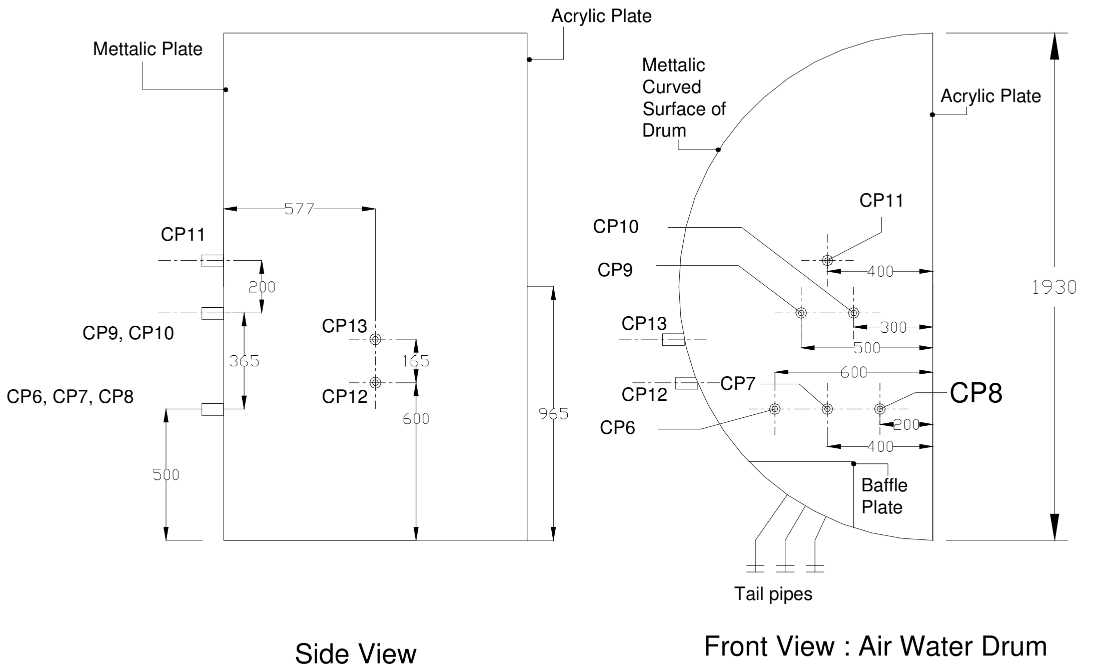

Figure 6.44: Locations of Conductance probes installed in AWL drum.

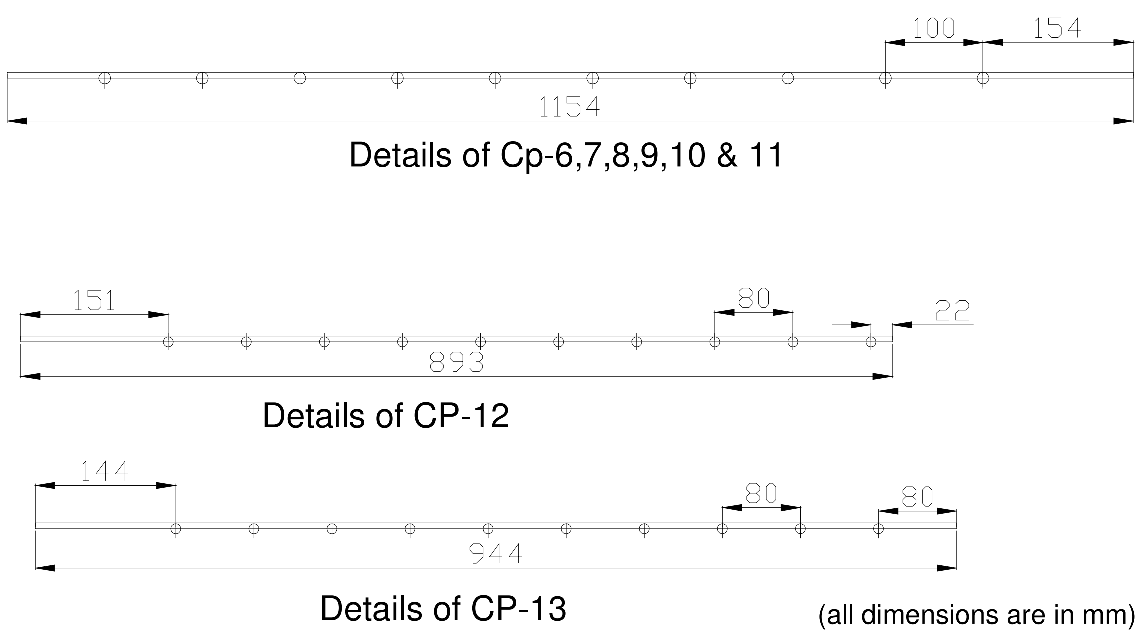

Figure 6.45: Geometrical details of multi-point conductance probes.

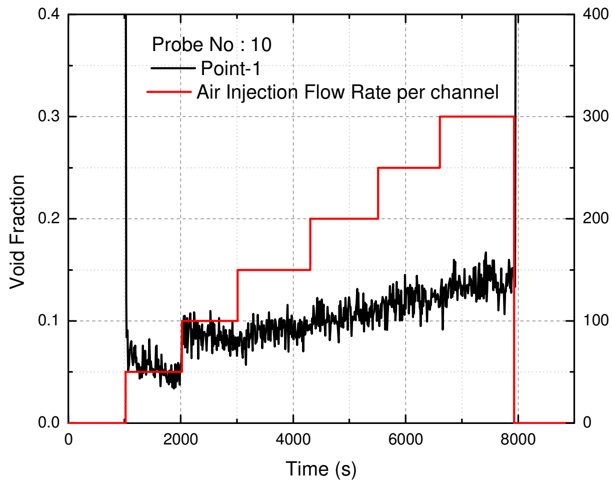

(a)

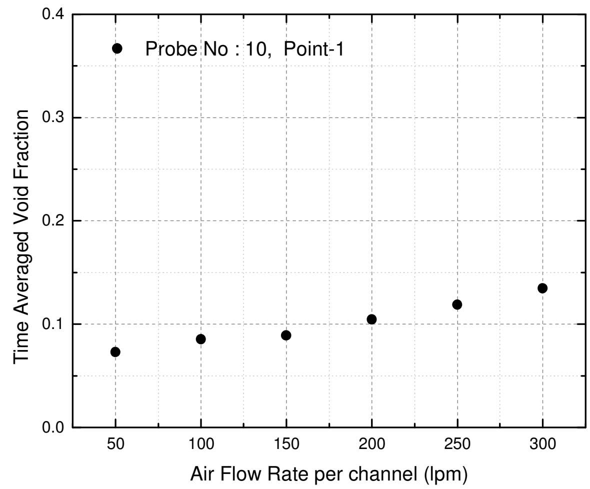

(b)

Figure 6.46 : (a) Transient signal from conductance probe and (b) time averaged void fraction estimated from transient signal

After collecting the data, it was found that some probe tip measurements were either indicating zero or one (i.e. zero or full range). These points either have damaged tips during installation of have problems in transmitting signal. The data from probe no 7 and 12 was not fit for analysis due to this reason. Also some of the tips from probe 6, 10 and 13 were also either indicating full range or zero values. However, the healthy data is plotted and compared with the CFD simulation results.

Figure 6.47 (a) to (f) shows the comparison for air flow rate of 300 lpm per channel. Point 3,6 and 7 for probe no. 6, Point no 9 for Probe no. 8, Point no 6 and 7 for probe no .10, point no. 1, 2, 3, 4 and 10 for probe no 13 were not reading properly, which can be seen in those plots. However the comparison with available data shows excellent match with CFD simulation results.

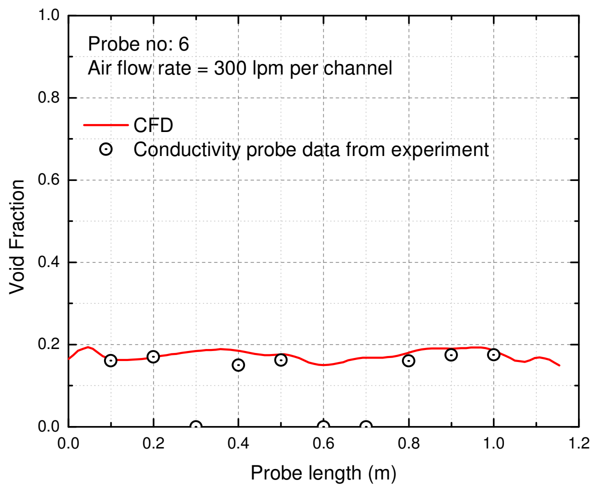

Figure 6.47 (a)

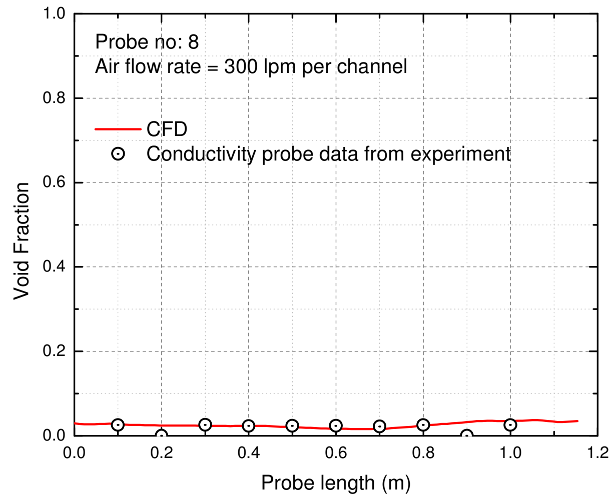

Figure 6.47 (b)

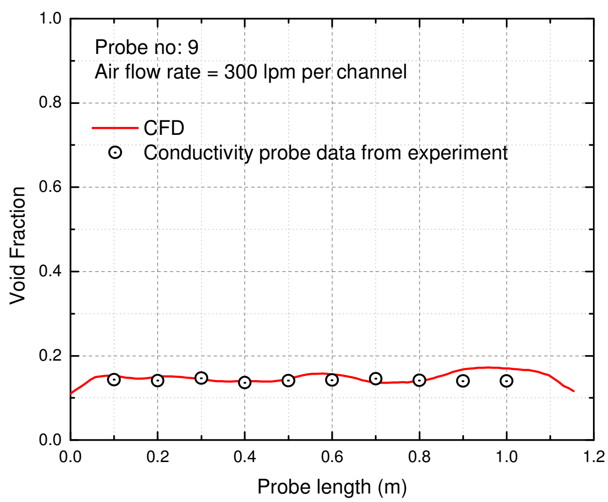

Figure 6.47 (c)

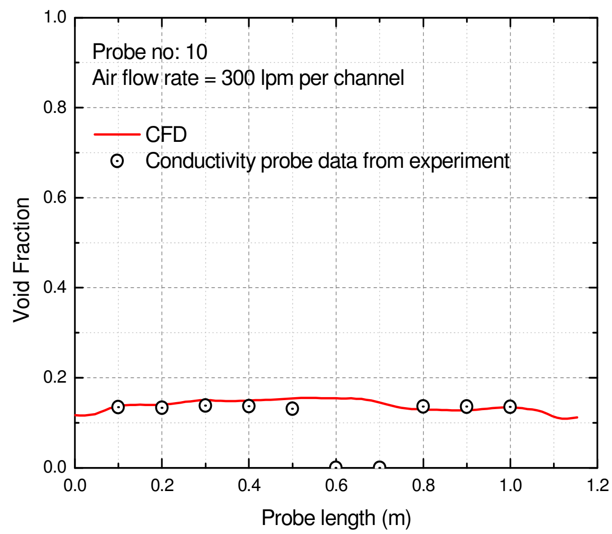

Figure 6.47 (d)

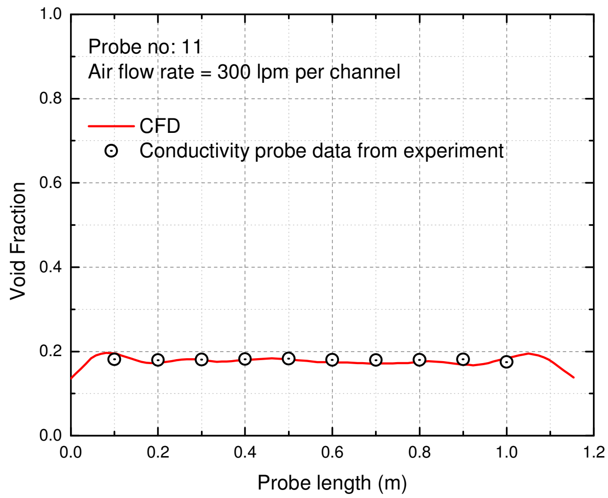

Figure 6.47 (e)

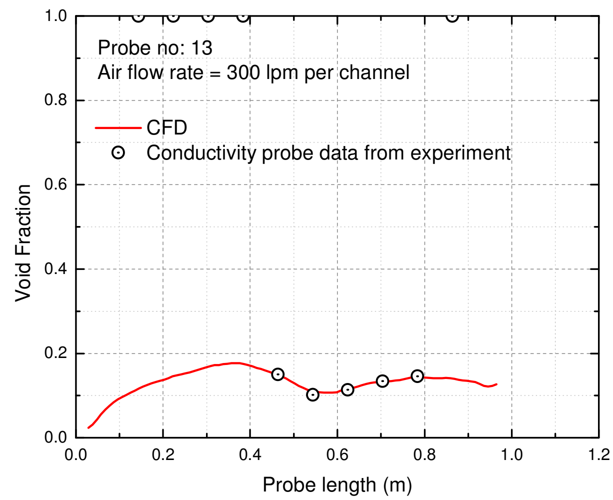

Figure 6.47(f)

Figure 6.47 : Comparison of probe data with CFD simulations for air flow rate of 300 lpm per channel (initial drum level 650 mm)

Similarly the comparison for different air flow rates is shown in Figure 6.48 to 6.52. Most of the data compares very well with CFD predictions. For figure 6.50 (e) and 6.53 (e), i.e. for probe no 11 at air flow rates 150 and 100 lpm there is large difference between the measurement and CFD predictions. It can be noted from Table 6.4, row no 2 & 3 i.e. for air injection flow rates of 100 and 150 lpm per channel the swell level is around 1.04 and 1.09 m, and the probe no11 is installed at the elevation of 1.065 m in the drum. The swell level predicted by CFD is 1.02 and 1.07 m. Therefore CFD shows higher local void fraction than recorded by the probe. There can be larger discrepancy in measured and predicted value when the probe location is close to swell level, hence the variation is acceptable. It can be noted that for other probe locations which remain submerged, the predictions are in well agreement with measurements.

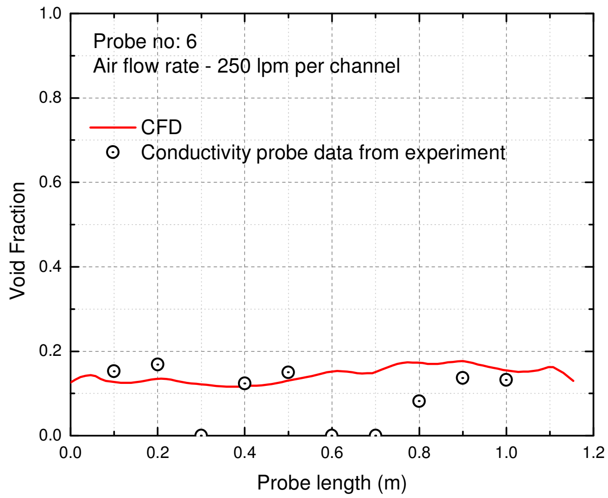

Figure 6.48 (a)

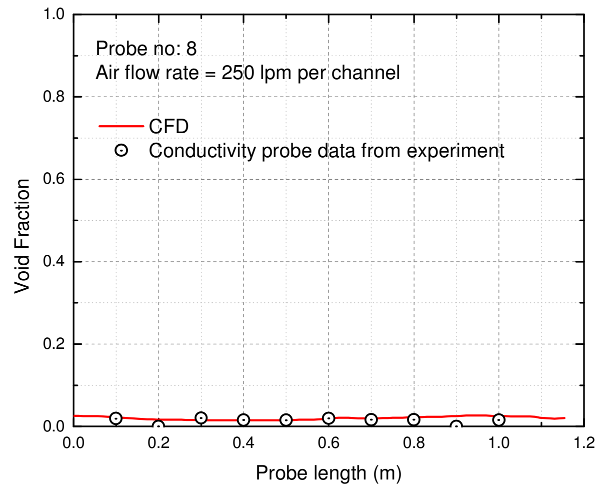

Figure 6.48 (b)

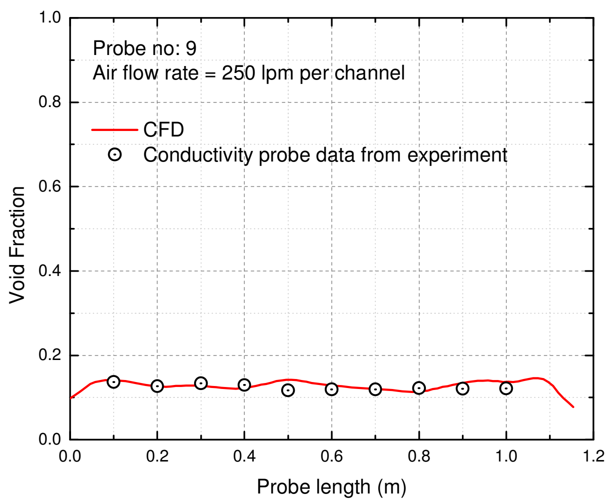

Figure 6.48 (c)

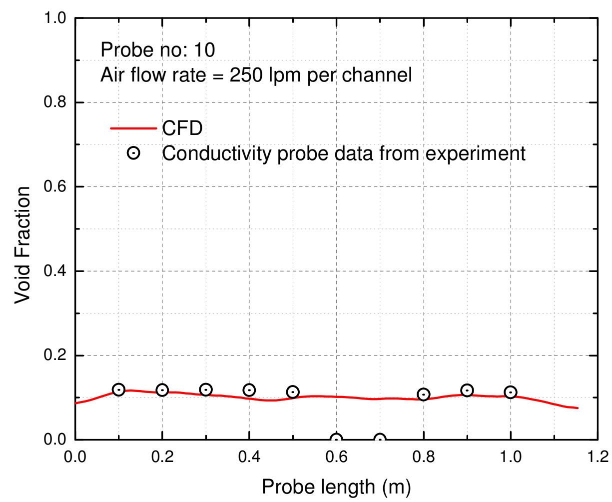

Figure 6.48 (d)

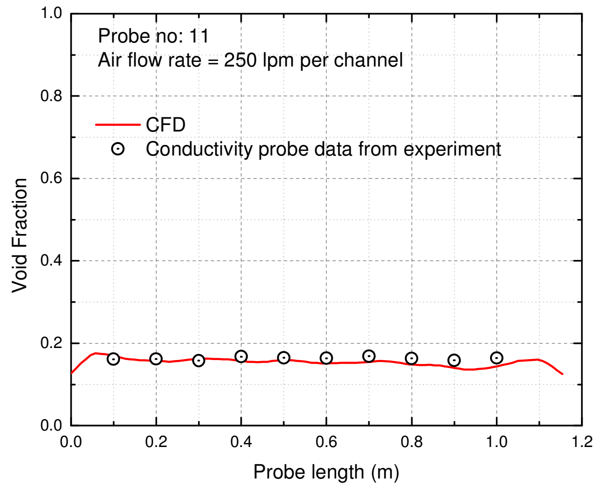

Figure 6.48 (e)

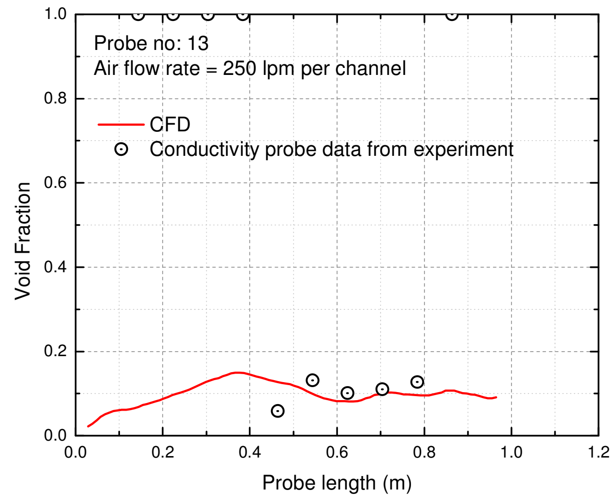

Figure 6.48 (f)

Figure 6.48 : Comparison of probe data with CFD simulations for air flow rate of 250 lpm per channel (initial drum level 650 mm)

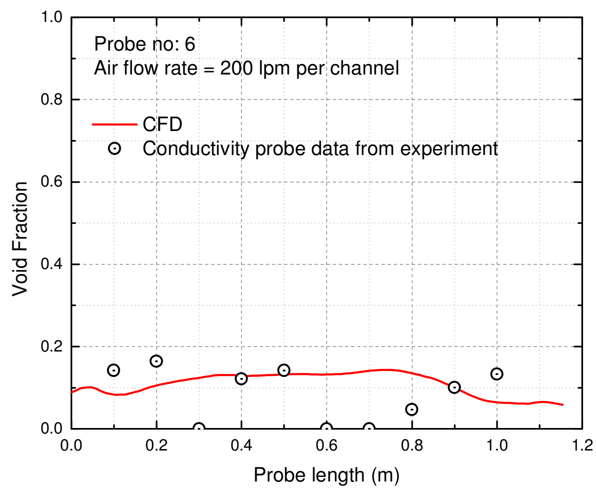

Figure 6.49 (a)

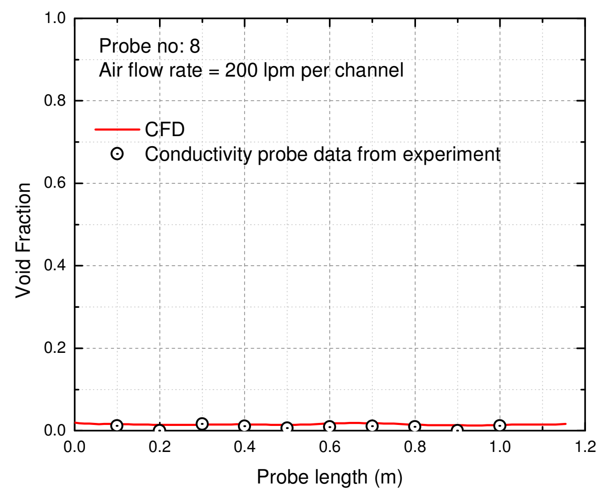

Figure 6.49 (b)

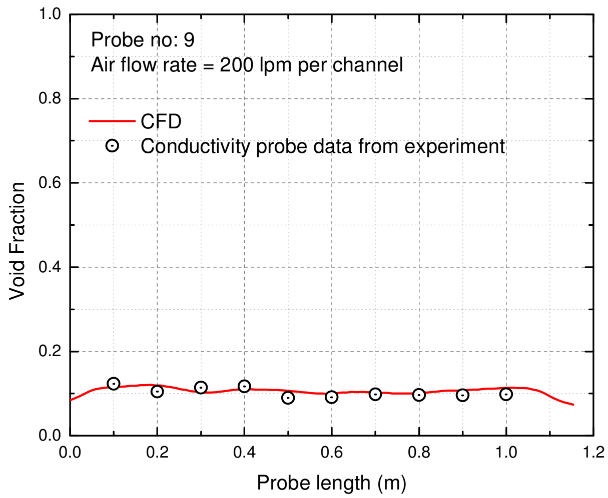

Figure 6.49 (c)

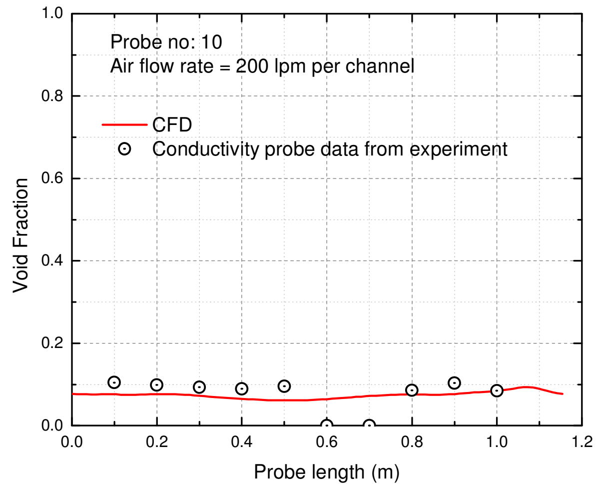

Figure 6.49 (d)

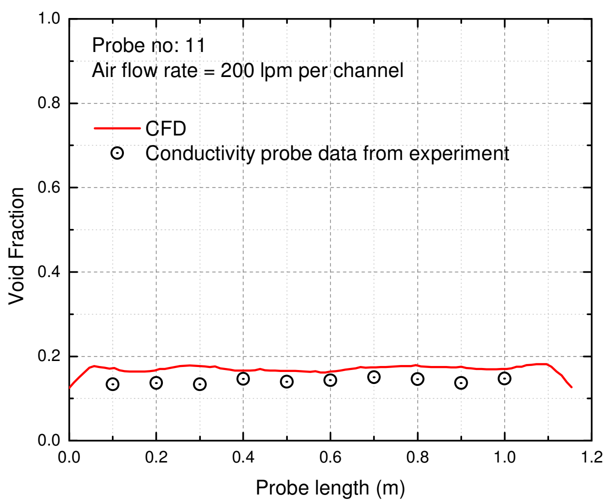

Figure 6.49 (e)

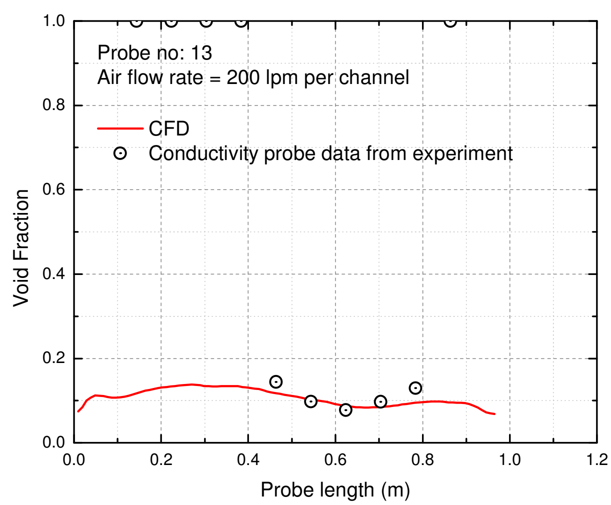

Figure 6.49 (f)

Figure 6.49 : Comparison of probe data with CFD simulations for air flow rate of 200 lpm per channel (initial drum level 650 mm)

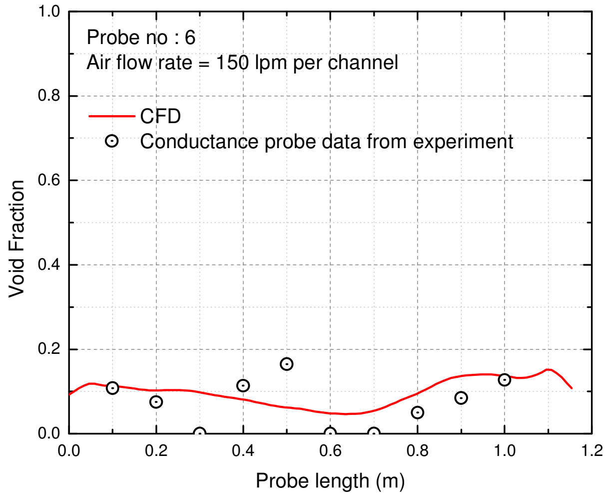

Figure 6.50 (a)

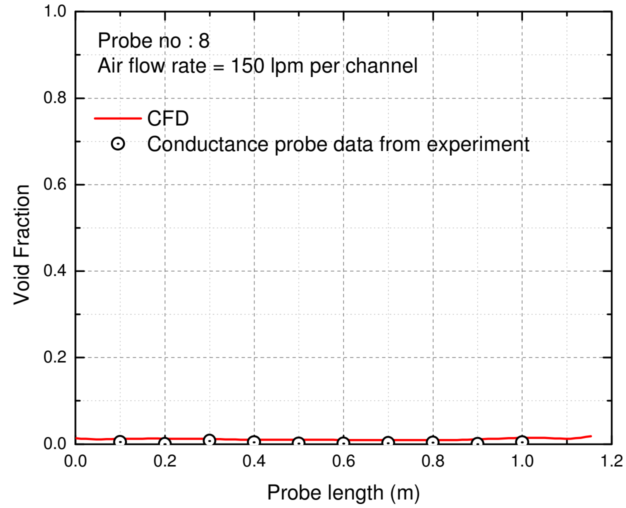

Figure 6.50 (b)

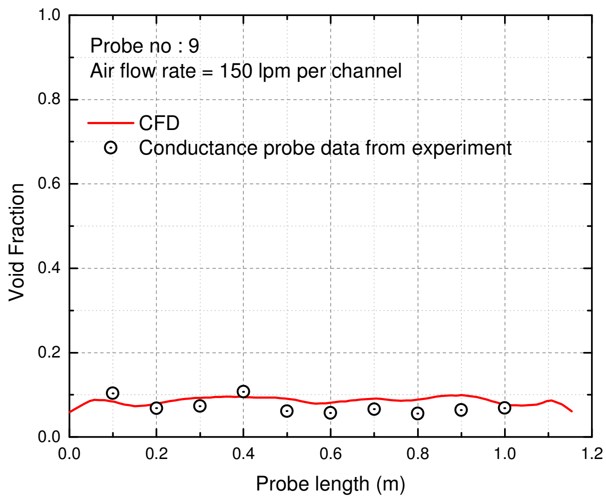

Figure 6.50 (c)

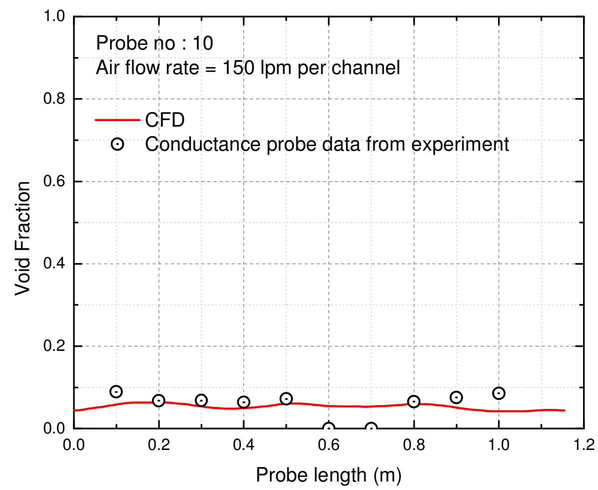

Figure 6.50 (d)

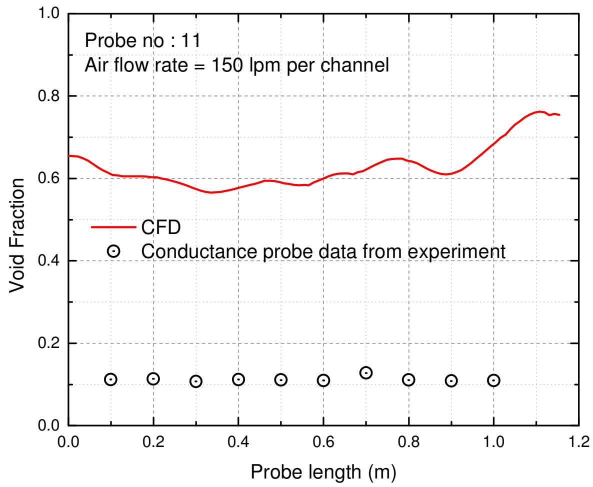

Figure 6.50 (e)

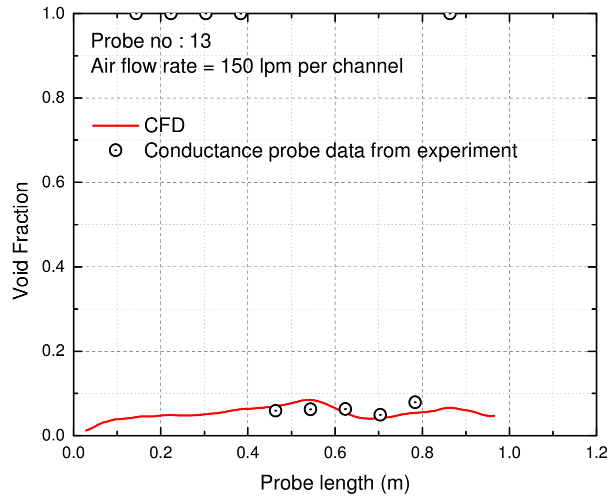

Figure 6.50 (f)

Figure 6.50 : Comparison of probe data with CFD simulations for air flow rate of 250 lpm per channel (initial drum level 650 mm)

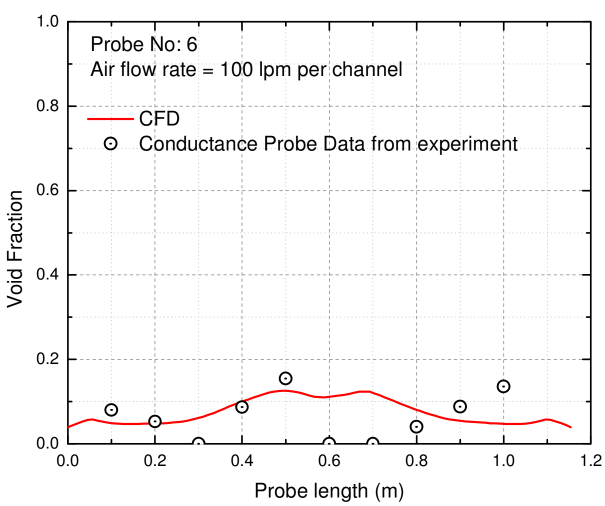

Figure 6.51 (a)

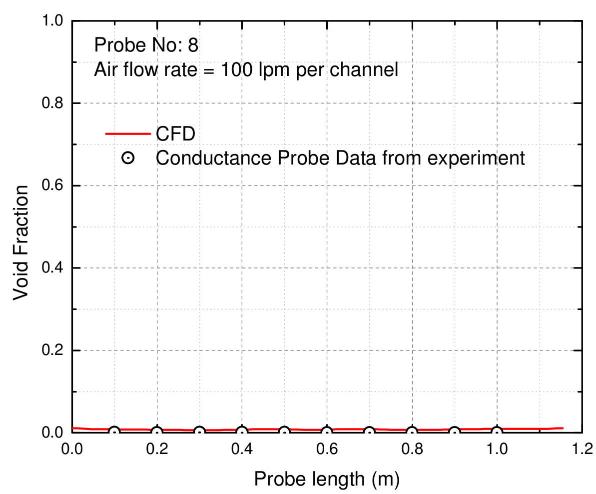

Figure 6.51 (b)

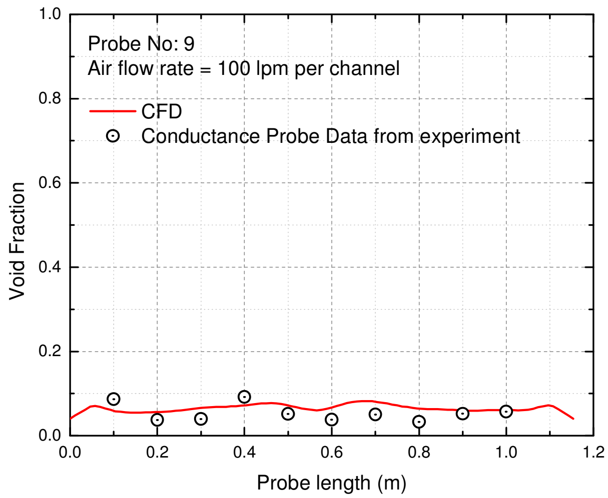

Figure 6.51 (c)

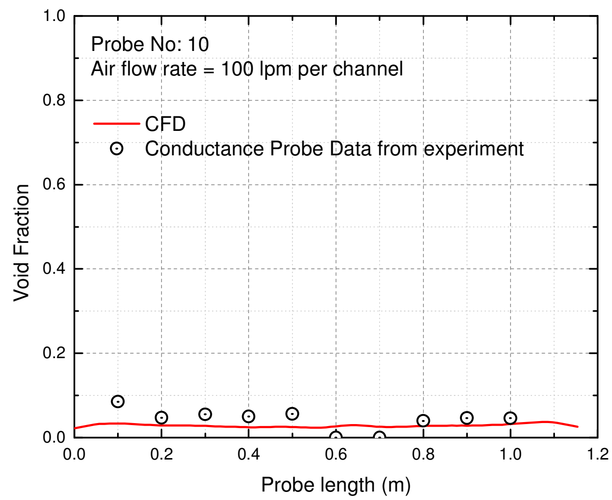

Figure 6.51 (d)

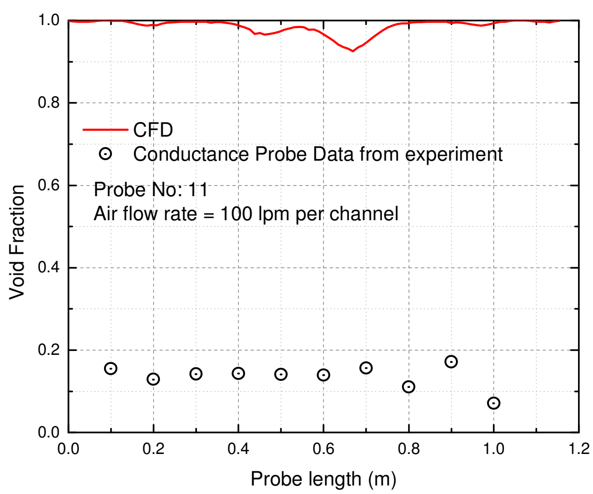

Figure 6.51 (e)

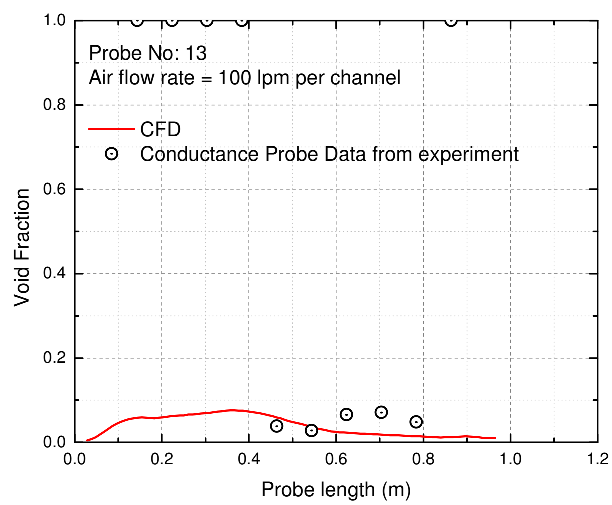

Figure 6.51 (f)

Figure 6.51 : Comparison of probe data with CFD simulations for air flow rate of 250 lpm per channel

(initial drum level 650 mm)

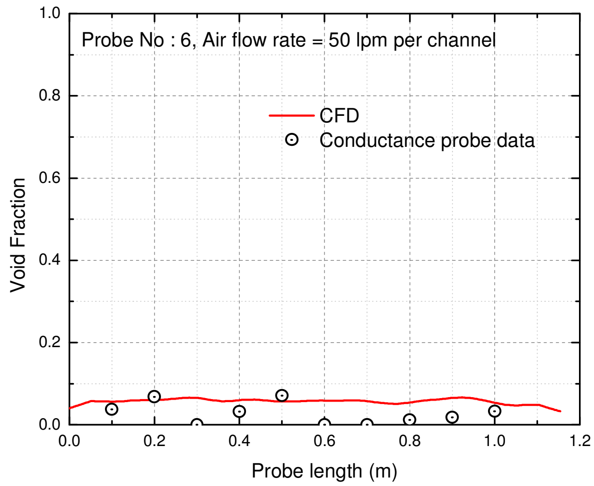

Figure 6.52 (a)

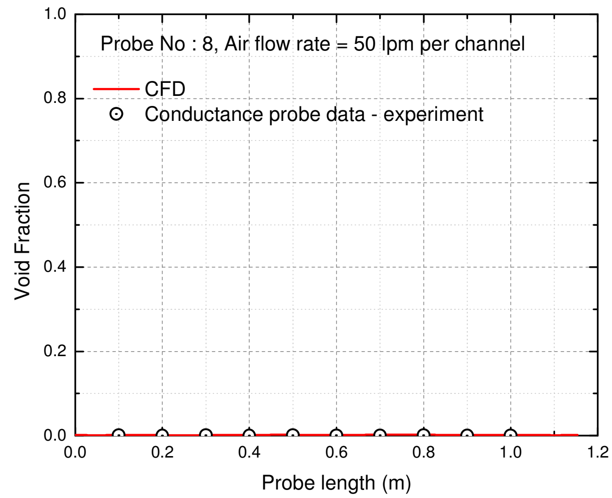

Figure 6.52 (b)

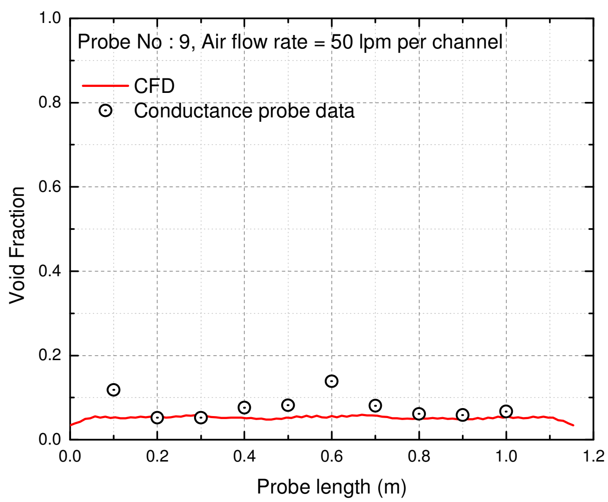

Figure 6.52 (c)

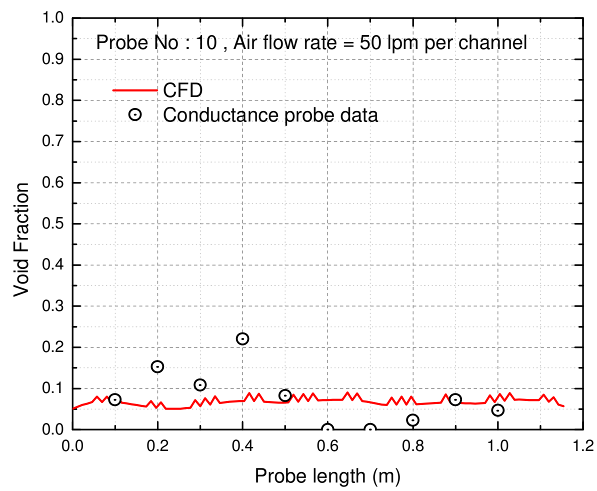

Figure 6.52 (d)

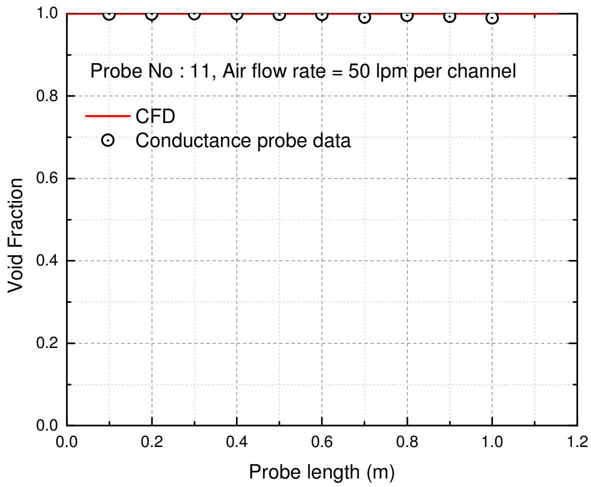

Figure 6.52 (e)

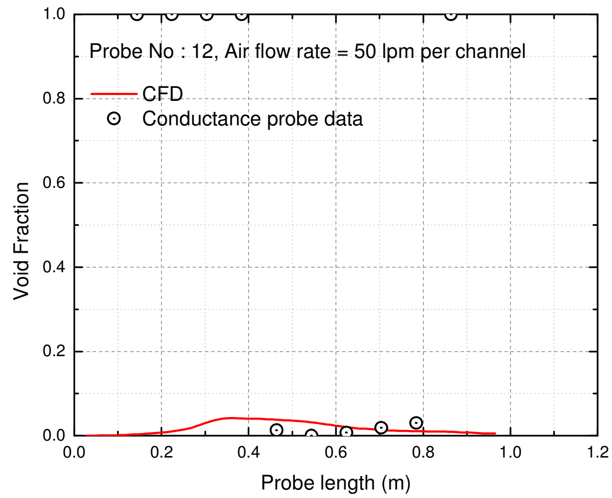

Figure 6.52 (f)

Figure 6.52 : Comparison of probe data with CFD simulations for air flow rate of 250 lpm per channel (initial drum level 650 mm)

The comparison with local measurements of hold up and CFD as well as comparison of swell level predicted by CFD with experimental measurements establish that CFD results are very accurate.

6.9 Prediction of variation of swell level for AHWR steam drums.

Figure 6.53 shows the schematic of MHTS of AHWR. The boiling occurs within the core and the two-phase flow is transported to drum via tail pipes. Steam drum is approximately situated 30 meters above the core exit. During the start up of reactor the MHTS is initially filled to maintain steam drum level above the baffle plates. The space above the water level is pressurized up to 70 bar using steam from external boiler connected to steam drum at the top. The loop is heated up by making the reactor critical (neurotic point of view) and the reactor power is adjusted to be 2% of nominal full power (i.e. 18.4 MW in total 452 fuel channels, i.e. 40.0 kW per channel). The natural circulation flow is automatically established due to the buoyancy difference between the tail pipe and down comer. As the loop heats up the volume of water expands and water level in steam drum will rise. The inventory corresponding to the swelling is removed from steam drum and level is maintained at 0.8 m. This level management continues till the MHT temperatures reach the saturation point corresponding to 70 bar, i.e. 285 ^{O}C. The boiling is initiated in core at this point and steam drum pressure is only controlled. The steam bubbles occupy part of volume of tail pipes and the corresponding water volume is transported to steam drum. At this stage boiling two-phase flow is established in tail pipes, and the steam is separated in steam drum. In order to maintain the steam drum pressure, this steam is removed from top and equal mass of water is added to steam drum from feed water line so that total mass of water in MHTS is conserved. The reactor power is then increased from 2% FP to 100% FP, in steps as required for power production. Please note that water inventory is not removed from steam drum as the boiling initiates. The steam drum level will swell with rise of power as flow quality and void fraction at the exit of core will increase. Figure 6.44 shows the variation of void fraction at core exit (in tail pipe) with reactor power. The corresponding water recirculation flow rate and steam flow rate at inlet of steam drum is shown in Figure 6.45.

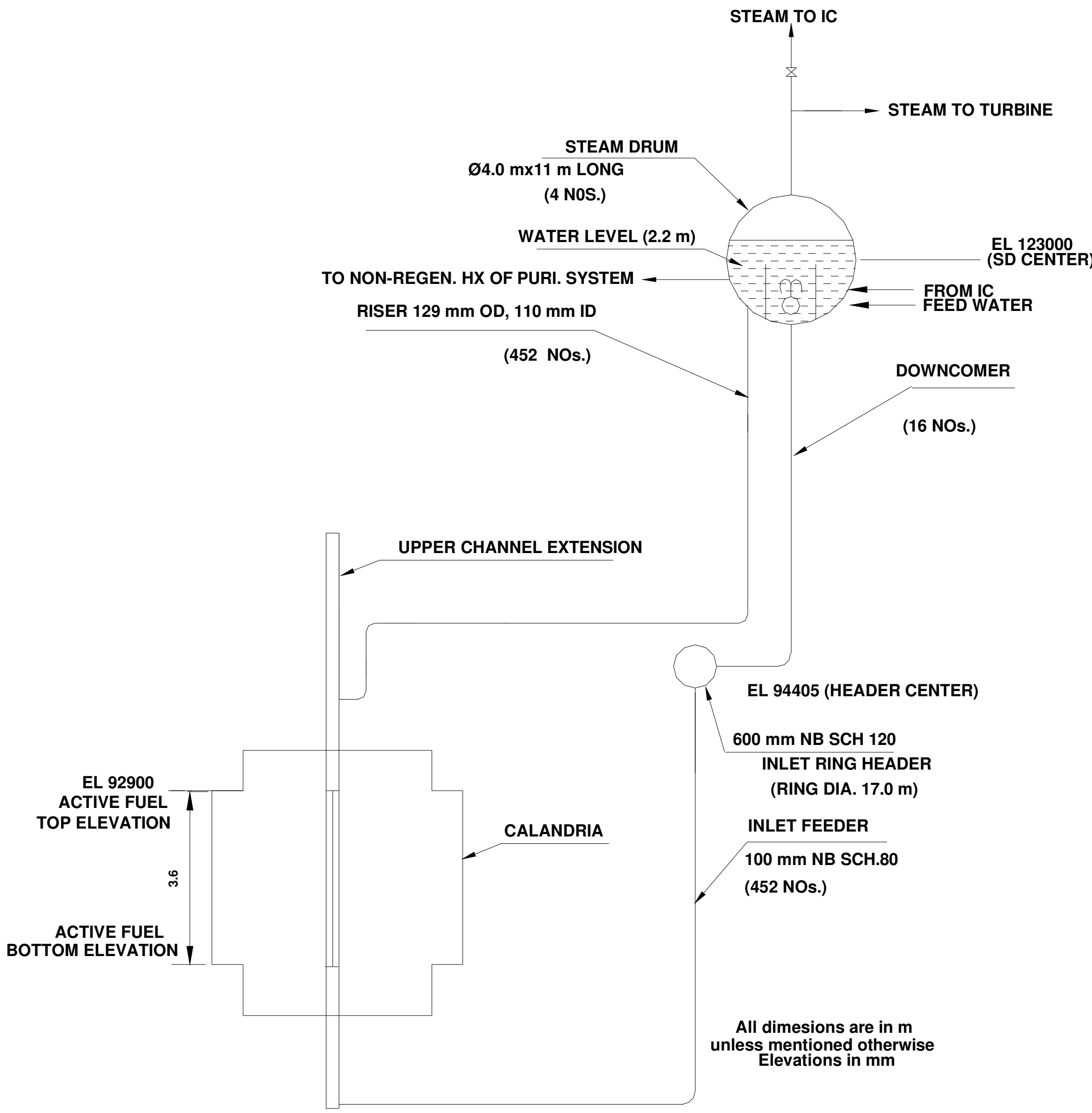

Figure 6.53: Schematic of Main Heat Transport System (MHTS) of AHWR

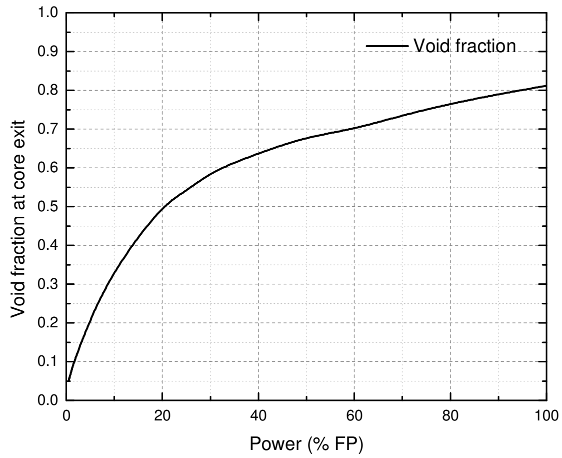

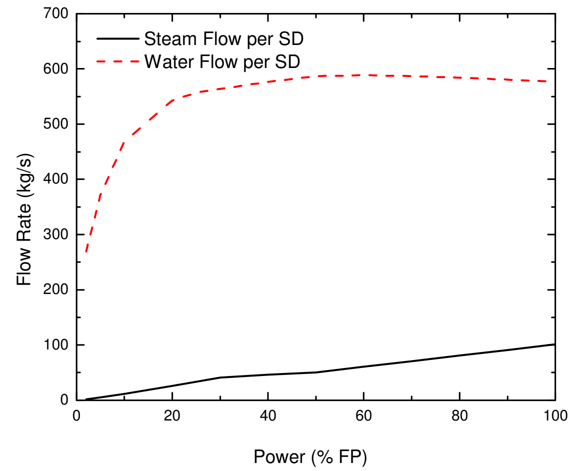

Figure 6.54: Variation of void fraction in tail pipe of AHWR with power.

Figure 6.55: Variation of steam and water flow rate with power for AHWR.

The variation of void fraction and flow rates with power is considered as an input to calculate the swell level in steam drum. Also the tail pipe void fraction enables us to calculate additional water volume transported in steam drum. Methodology explained in Figure 6.3 is followed here for AHWR steam drum, and full circular cross-section is considered for calculation. The drift flux model by Boesmans et al. [92] is used to predict the swell level variation and average pool void fraction in steam drum, which is shown in Figure 6.46. The calculation results predict swell level of 2.23 m at 100% FP. It has been estimated from CFD simulations (as described in chapter 5, section 5.6) that the carryover is below acceptable level when swell level is maintained below 3.5 m. Thus we can conclude that swell level in AHWR steam drum at 100% FP is sufficiently low so that carryover does not pose major concern for its operation and gravity separation will be efficient.

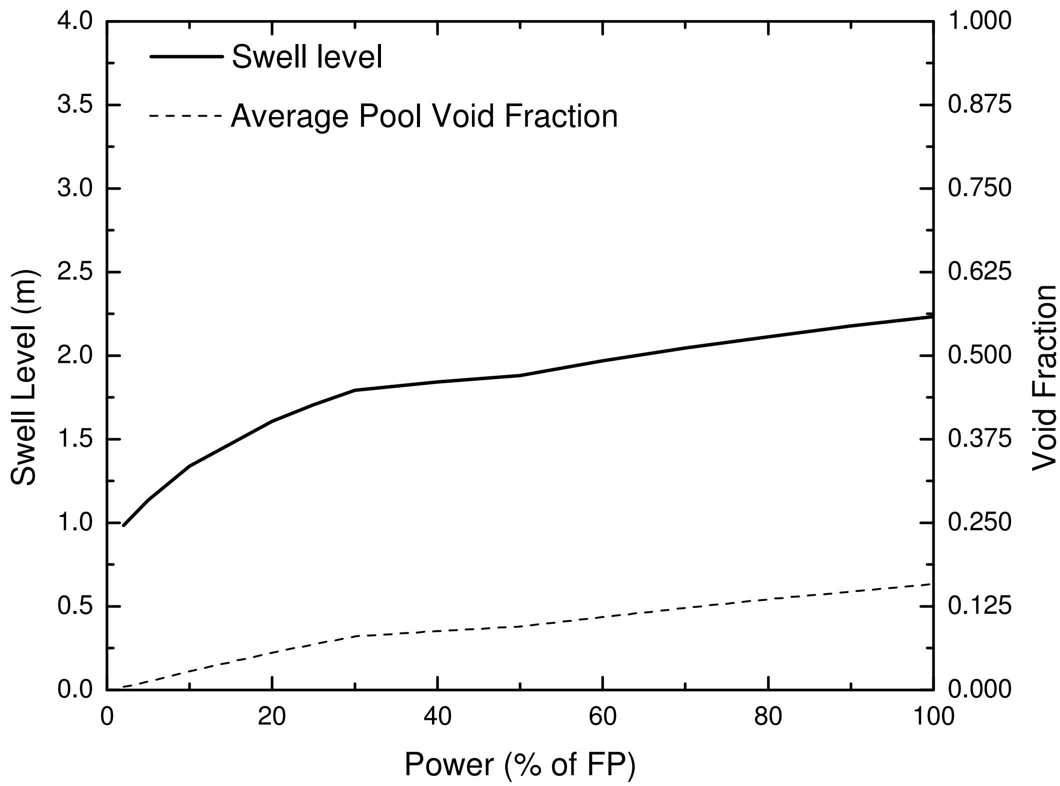

Figure 6.56: Predicted variation of swell level and average pool void fraction for AHWR.

6.10 Conclusion

Accurate prediction of swell level of two-phase mixture inside the steam drum is one of the major concerns during the design calculations. The steam drum geometry, which is a horizontal large diameter cylinder with multiple inlets at bottom and central region separated from bulk of flow for down comer connection, adds complexity to the problem. The flow cross-section varies inside the drum as two-phase mixture flows upward. The large values of hydraulic diameter rules out the use of conventional drift flux models which are valid for small diameter pipe flows. Large recirculation zones are observed in experiments. The void distribution inside large pool of drum plays a significant role determining the average pool void fraction and corresponding swell level.

Several experiments were carried in AWL to collect data on pool void fraction as a function of boundary flows and initial inventory. Validation of these data with various drift flux models available from literature was carried out. Conventional models were found to predict higher pool void fraction and higher swell levels compared to experiment. Drift flux model given by Boesmans et al. [92] which considers the phenomenon of strong internal recirculation flows was found to predict the swell level very accurately.

Photographic investigations were carried out during AWL experiments and bubble size distributions were obtained using image processing. The SMD which represents the poly dispersed bubble sizes was obtained from distributions. OpenFOAM solver "*twoPhaseEulerFoam*" which solves dispersed flows of two incompressible fluids was utilized to simulate the flow inside the AWL drum. The solver was first validated against the experimental data from literature. The comparison with bubble column experiments with CFD simulations showed that accurate predictions can be obtained. The CFD simulations for AWL drum produced excellent results on swell level predictions when compared with AWL experiments. The advantage of validated CFD simulation is that it can be treated as numerical experiment and detailed information of many parameters can be obtained that are difficult to measure in actual experiments. For example, the CFD simulations produced void fraction profiles, local liquid and gas velocities and local slip velocity. This information was used to obtain the drift flux distribution parameters. The CFD simulations on AWL drum were used to develop a new drift flux model which accurately predicted the swell level.

The local void fraction / hold up profiles were measured experimentally using multi-point conductance probes. The CFD predictions of hold up profiles were found to be in good agreement with the measurements with conductance probes.

This detailed analysis of flow and void distributions in AWL drum pool, and comparison with experiments has given a strong confidence for calculation methods employed. The drift flux models were then extended to predict the swell and average pool void fraction for AHWR steam drum case. It was found that the swell level for AHWR steam drum at 100 % full power operation will be around 2.2 m, which is well below of threshold for unacceptable carryover.

Chapter 7

Summary

Efficiency of two-phase flow separation in steam drums is affected by the amount of droplets carried out of equipment. This carryover can be detrimental to health of steam piping and turbine blades. Estimation of carryover is thus of major concern for new designs of steam drum which intend not to use mechanical separator. For case of AHWR, the steam separation is based on purely due to gravity to avoid excessive system pressure drop associated with mechanical separators. Literature review showed that carryover depends on the superficial gas velocity and distance of separation interface from the exit of equipment i.e. vapor/gas phase height. Lower superficial velocity of gas at interface gives lower value of carryover, and more the height of vapor space lesser is carryover. To reduce the steam velocity at interface, the cylindrical steam drum of AHWR is kept horizontal. Increasing the steam drum diameter will also ensure that enough space is available above the two-phase flow separation interface in the drum. These precautions taken in design are based on lessons from literature. However, exact estimation of carryover and distribution of two-phase flow inside the drum is required for design acceptance.

Literature review also indicated that empirical approach available for solution of above problem may not be universally applicable and any such correlation need to be rigorously tested for the geometry under consideration. Applicability of experimental information from previous experiments was also under question since most of them are performed in vertical cylindrical vessels and have small hydraulic diameters. Analytical approaches are applicable in any geometry since they are based on basic equations of conservation of mass, momentum and well tested closure laws for drag, lift forces considered. However, these approaches need more information such as droplet size and velocity distributions, bubble size distributions if we predict the complete process using conservation laws. Literature was found to be devoid of relevant information on such inputs required for horizontal steam drum geometry. This has prompted us to take up detailed experimental, analytical studies along with use of CFD techniques to understand and predict the flow dynamics in horizontal steam drum where steam separation is based purely on gravity.

With aim to collect detailed data on droplet size distributions, bubble size distributions, void distribution in pool, swell level/ location of interface in the drum, a scaled down test facility was designed. The scaled down experiments have been carried using air-water mixture which has allowed visual observation. The flows were scaled in order to maintain similar superficial flow velocities and void fractions at the drum inlet. Facility was also designed to operate without any pump and flows are generated due to natural circulation. Steady state experiments were performed and the measured flows and pressure drops were validated using numerical techniques. The post-test comparison of model and prototype has indicated that model will adequately simulate prototype conditions.

The measurements on droplet size distribution were carried out using high speed photography. The photography revealed the mechanism of formation of droplets, which is due to fragmentation of bubble dome film at the separation interface. The size distribution was found to follow Upper Limit Log Normal (ULLN) distribution. The distribution parameters were obtained. A simple one-dimensional Lagrangian particle tracking code was developed and utilized to perform parametric studies. The studies have shown that droplet ejection velocity can be considered to be order of 1 m/s in order to accurately predict the critical droplet diameter and associated carryover. 1-D particle tracking code predicted the carryover reasonably well when compared with experiments and best available correlations. 3-D Euler-Lagrangian simulations for AWL were taken up. OpenFOAM solver "*simpleReactingParcelFoam*" was used. The solver solves bulk flow with Euler formulation and droplets are tracked in the bulk flow with given set of boundary conditions. The solver was validated for cyclone separator geometry and experiments from literature. The droplet size distributions obtained in experiments were used for CFD simulations for AWL to predict the carryover. Since the flow cross-section rapidly reduces close to drum top, the superficial velocity of gas increases rapidly and also the carryover. The threshold of such sudden rise of carryover is accurately predicted with CFD simulations. The solver was extended for AHWR steam drum simulation. The droplet size from air-water mixture data was extended for steam-water conditions for AHWR using similitude of Weber number. The CFD simulations showed that for the rated steam flow rate at 100% reactor power, if the operating level is less than 3.5 m, the carryover is very small (< 0.1%) and acceptable as per internationally accepted guidelines.

Since the carryover depends on the swell level (operating level) inside the drum, its accurate prediction is important and accurate methods for such predictions need to be established. Conventional drift flux models over predict the pool void fraction and swell level, since they are developed from experiments in small diameter pipes. Whereas the hydraulic diameter for concerned geometry is larger and strong internal flow recirculation occurs. Experimental database on average pool void fraction and swell level was generated in AWL. A special drift flux model given by Boesmans et al [92] for pool type situations was found to predict the swell level accurately. Photographic studies were conducted to obtain bubble size distributions and corresponding Suater Mean Diameter (SMD) which was used as input for CFD simulations. CFD simulations with "*twoPhaseEulerFoam*" solver from OpenFOAM were carried out. Solver was first validated against experimental data from literature on bubble columns of diameter varying from 0.3 m to 1.0 m. The validated solver was then used to predict the void distribution in AWL drum which was compared with the local void fraction measured using multi-point conductivity probes. The predictions agree very well with measurements. The swell level predicted is also in close agreement with experiments. Based on the detailed data on local fluid velocities and local void fractions obtained in CFD simulations, a new drift flux model was proposed. The proposed model also predicts the swell level in close agreement with measurements. The validated drift flux model was then used to predict the swell level in AHWR steam drum. It was found that the swell level for AHWR steam drum at 100 % full power operation will be around 2.2 m, which is well below of threshold for unacceptable carryover.

The complete analysis of carryover phenomenon including dynamics of flow above and below separation interface with experiments and CFD techniques was thus established and it is proven that AHWR steam drum is adequate and acceptable.

References:

1. R. K. Sinha, A. Kakodkar, 2006, Design and development of the AHWR – The Indian Thorium fuelled innovative nuclear reactor, Nucl. Eng. Des. 236, 683–700.

2. Wang W-Z et al 2007 Failure analysis of the final stage blade in steam turbine Eng. Fail. Anal. 14 632–41

3. Mazur Z, Hernández-Rossette A and García-Illescas R 2006 Investigation of the failure of the L-0 blades Eng. Fail. Anal. 13 1338–50

4. Chynoweth J M, Gerzen G S and Tomala R W 1996 Root cause analysis of low pressure turbine blade failure Proc. of the American PowerConf., 58th Annual Meeting (Chicago: Illinois Institute of Technology) vol 58 pp 1230–6

5. Haag M 2009 Untersuchungen zur schädigungsentwicklung an ampfturbinenwerkstoffen infolge von wassertropfenerosion MastersThesis, Technische Universität Kaiserslautern

6. Förster S 2010 Untersuchungen des strömungsmechanischen Einflusses verschiedener Erosionsstufen an Dampfturbinen-Niederdruck- Beschaufelungen Masterarbeit, Hochschule für Technik und Wirtschaft Berlin

7. Kirlos H. S., Kevorkov D., Uihlein A.and Medraj M., Water droplet erosion of stainless steel turbine blades, Mater. Res. Express 4 (2017) 086510, https://doi.org/10.1088/ 2053-1591/aa7c70

8. Davis R. F., 1940, The Physical Aspect of Steam Generation at High Pressures and Problem of Steam Contamination, Proc. Inst. Mech. Engrs.

9. Zenz F. A. and Weil N. A., 1958, A theoretical empirical approach to the mechanism of particle entrainment from fluidized beds, A.I.Ch.E.Jl, 4(4), 473.

10. Cheng S. I. and Teller A. J., 1961, Free entrainment behavior in sieve trays, A.I.Ch.E.Jl, 7(2), 283.

11. Newitt D. M., Dombrowski N. and Knelman F. H., 1954, Liquid entrainment - 1. The mechanism of drop formation from gas or vapour bubbles, Trans. Instn Chem. Engrs 32, 244.

12. Garner F. H., Ellis S. R. M. and Lacey J. A., 1954, The size distribution and entrainment of droplets, Trans. Instn. Chem. Engrs 32, 222.

13. Spiel D. E., 1994, The sizes of the jet drops produced by air bubbles bursting on sea and fresh water surfaces, Tellus 46B, 325.

14. Aiba S. and Yamada T., 1959, Studies on Entrainment, A.I.Ch.E. Journal, 5(4), 506.

15. Rozen A. M., Golub S. I., Davydov I. F., 1970, Some laws governing drop carryover, Sovt. Phys. Doklady 14(7), 648.

16. Afeti G. M., Resch F. J., Distribution of the liquid aerosol produced from bursting bubbles in sea and distilled water, Tellus B: Chemical and Physical Meteorology, 42:4, 378-384, 1990.

17. Wu J., Production functions of film drops by bursting bubbles, Journal of physical oceanography, 31, 3249-3257, 2001.

18. Gunther A., Walchli S. and Rohr P. R. von, 2003, Droplet production from disintegrating bubbles at water surfaces. Single vs. multiple bubbles, Int. J. Multiphase Flow 29, 795.

19. Kientzler C. F.,Arons A. B., Blanchard D. C. and Woodcock A. H., 1954, Photographic investigation of the projection of droplets by bubbles bursting at a water surface, Tellus 6, 1-7.

20. Blanchard D. C., Syzdek, L. D., Film drop production as a function of bubble size, J. Geophys. Res., 94 (C4), 10999-11002, 1988.

21. Sterman L. S., 1958, On the theory of steam separation, Sovt. Phys. – Tech. Phys. 28(7), 1562.

22. Kolkolostev V. A., 1952, Investigation of the operation of the steam space of the ISV evaporator, Trudy, MEI.

23. Mochizuki H. and Hirao Y., 1993, Development of steam separator performance analysis code and its validation-carryover experiments, J. Nucl. Sci. Tech. 30(10), 1059-1070.

24. Cosandy J. O., Gunther A., Rohr P. R. von, 2001, Entrainment of soluble and non soluble tracers from a boiling water surface, Nucl. Engg. Desgn 208, 87.

25. Cosandy J. O., Gunther A. and Rohr P. R. von, 2003, Transport of salts and micron-sized particles entrained from a boiling water pool, Expt. Thermal and Fluid Science. 27, 877.

26. Sun D. C., Xiang Y., Tian W. X., Liu L. C., Zhang p., Qiu S. Z., Su G. H., 2015, Experimental investigation of upper plenum entrainment in AP1000, Progress in Nuclear Energy, 80, 80-85.

27. Sun D. C., Tian W. X., Qui S. Z., Su G. H., Zhang P., Liu J. C., Ma Y. Y., 2014, Scaling analysis of AP1000 ADS-4 entrainment and depressurization, Progress in Nuclear Energy, 74, 71-78.

28. Zhang P., Li W., Di Z., Xiao H., Chen L., Chang H., Chen P., 2017, An experimental study of pool entrainment with side exit, Annals of Nuclear Energy, 110, 406-411.

29. Kruzhilin G. N., 1951, The dependence of the permissible vapor load upon the pressure, Izv.Akad.Nauk.Otd.Tekh.Nauk. 7, 1106.

30. Kataoka I. and Ishii M., 1984, Mechanistic modeling of pool entrainment phenomenon, Int. J. Heat and Mass Transfer 27(11), 1999.

31. Nayak A. K., Jain V., Vijayan P. K., Saha D. and Sinha R. K., 2000, Study on the carryover behavior in the steam drum of the advanced heavy water reactor, Sixteenth National Convention of Mechanical Engineers and All India Seminar on Future Trends in Mechanical Engineering, Sept 29-30, 2000.

32. Koch M. K., Voβnacke A., Starflinger J., Schutz W. and Unger H., 2000, Radionuclide re-entrainment at bubbling water pool surfaces, J. Aerosol Sci. 31, 1015.

33. Iyer K., Prabhudharwadkar M. and More R. Z., 2010, Experimental study of liquid carryover in a separator drum, Nucl. Engg. Desgn 240, 76.

34. Basu D. N., Patil N. D., Bhattacharyya S., Das P. K., 2012, Experimental investigations of droplet carryover from the separator drum of an air-lift loop simulating a scaled-down AHWR, Experimental Thermal and Fluid Science 42, 163–173.

35. Kocamustafagullari G., Smits S. R., Razi J. and Huang W. D., 1993, Droplet size modeling in annular flow, Proceedings Sixth International Tropical Meeting on Nuclear Reactor Thermal Hydraulics, NURETH-6, Vol.2, 1021-1030.

36. Kim H. and No H. C., 2005, Liquid entrainment and off-take through the break at the top of a vessel, Nucl. Engg. Desgn. 235, 1675.

37. Voβnacke A., Koch M. K., and Unger H., 1997, RECOM: A code for the simulation of radionuclide resuspension at bubbling water pool surfaces, Proc. Annual Meeting on Nuclear Technology 97, Aachen, Germany, 206-209.

38. Minges J., Schutz W. and Koch M. K., 1998, KAREX-Experimentec zum radiologischen Quellterm infolge Resuspension, Projekt Sicherheitsforschung, Jahresbericht 1997, FZKA 6126, Forschungszentrum Karlsruhe, pp. 517-523.

39. Panasenko M.D., 1959, Correlation of Mechanical Carryover by steam, Teploenergetika, 1959.

40. Crowe, C.T., Sommerfeld, M. and Tsuji, Y. (1998) Multiphase Flows with Droplets and Particles, CRC Press, Boca Raton, FL

41. Harlow F., Welch J. E., 1965, Numerical Calculation of time dependent viscous incompressible flow of fluid with free surface, The Physics of Fluids, 8-12, 2182:2189.

42. Harlow F., Welch J. E., 1966, Numerical study of large amplitude free surface motions, Phys. Fluid, 9, 842-851.

43. Pai MG , Desjardins O , Pitsch H . Detailed simulations of primary breakup of turbulent liquid jets in crossflow. In: Ann Res Briefs; 2008. p. 451–66 .

44. Herrmann M . A balanced force refined level set grid method for two-phase flows on unstructured flow solver grids. J Comp Phys 2008;227:2674–706 .

45. Lebas R , Ménard T , Beau PA , Berlemont A , Demoulin FX . Numerical simulation of primary break-up and atomization: dns and modelling study. Int J Multi- phase Flow 2009;35:247–60.

46. Noh, W. F., Woodward p., 1976, SLIC (Simple Line Interface Calculation), In:A. I. van der Vooren and P. J. Xandbergen, Eds., Lecture Notes in Physics, Springer, New York, P. 330.

47. Youngs D. L. , 1982, Time dependent mnultimaterial flow with large fluid distortion, Numerical methods for fluid dynamics, Academic Press New York, 1982, pp27-39.

48. Wacławczyk T., Koronowicz T., 2005, Modeling of the flow in systems of immiscible fluids using Volume of Fluid method with CICSAM scheme, *Turbulence*, **8**, 267-276.

49. Ubbink O., Issa R.I., 1999, Method for capturing sharp fluid interfaces on arbitrary meshes, *J. Comput. Phys.*, **153**, 26-50.

50. Sussman M , Puckett EG . A coupled level set and volume-of-fluid method for computing 3d and axisymmetric incompressible two-phase flows. J Comp Phys 2000 ;162:301–37.

51. Fedwik, R., Aslam, T., Mrriman, B., and osher, S., 1999, A non-oscillatory eulerian approach to interfaces in multimaterial flows (the ghost fluid method), J. Comput. Phys. 152, 457-492.

52. Welter K.B., Wu Q., You Y., Abel K., McCreary D., Bajorek S.M., Reyes J.N., 2004, Experimental investigation and theoretical modeling of liquid entrainment in a horizontal tee with a vertical-up branch, International Journal of Multiphase Flow 30, 1451–1484.

53. Zhaoming Meng, Lifang Liu, Lei Ding, Xiaoliang Fu, Wenxi Tian, Yanhua Yang, G.h. Su, 2015, Comparative study on effect of air–water and steam–water mediumson liquid entrainment through ADS-4 in AP1000, Experimental Thermal and Fluid Science 69, 149–157

54. Chexal B. and Lellouche G., 1986, A full range drift flux correlation for vertical flows (revision 1), EPRI-NP-3989-SR, Electric Power Research Institute.

55. Kataoka I. and Ishii M., 1987, "Drift flux model for large diameter pipe and new correlation for pool void fraction", Heat and Mass Transfer, 30 (9), 1927-1939.

56. Vijayan P. K., Patil, A. P., Pilkhwal, D. S., Saha and D., Venkat Raj, V., 2000, An assessment of pressure drop and void fraction correlation with data from two-phase natural circulation loops, Heat and Mass Transfer, 36, 541-548.

57. Vijayan P. K., Pilkhwal, D. S., Saha, D., Venkat Raj, V., Patil, A. P., Sane, N. K., 2000, An assessment of void fraction correlations for various orientations of flow geometry, proceedings of the fourth ISHMT-ASME Heat and Mass Transfer Conference and fifteenth National Heat and Mass Transfer Conference, 777-782.

58. Coddington P. and Macian, R., 2002, A study of the performance of void fraction correlations used in the context of drift-flux two-phase flow models, Nuclear Engineering and Design, 215, 199–216.

59. Woldesemayat M. A., Ghajar A. J., 2007, Comparison of void fraction correlations for different flow patterns in horizontal and upward inclined pipes, International Journal of Multiphase Flow, 33, 347-370.

60. Ghajar, A. J., Bhagwat, S. M., 2013, Effect of void fraction and two-phase dynamic viscosity models on prediction of hydrostatic and frictional pressure drop in vertical upward gas–liquid two-phase flow, Heat Transfer Engineering, 34(13), 1044-1059.

61. Chexal, B., 1996, Understanding void fraction in steady and dynamic environments, TR-106326 / RP-8034-14, Electric Power Research Institute.

62. Bestion, D., 1990. The physical closure laws in the CATHARE code. Nucl. Eng. Des. 124, 229–245.

63. Dix, G. E., 1971, Vapor Void Fractions for Forced Convection with Subcooled Boiling at Low Flow Rates, Ph.D. thesis,University of California, Berkeley.

64. Bhagwat S. M., and Ghajar A. J., 2012, Flow Pattern and Pipe Orientation Independent Semi-Empirical Void Fraction Correlation for a Gas–liquid Two-Phase Flow Based on the Concept of Drift Flux Model, Proc. of ASME 2012 Summer Heat Transfer Conference, Puerto Rico.

65. Lockhart R. W., and Martinelli R. C., 1949, Proposed Correlation of Data for Isothermal Two Phase, Two Component Flow in Pipes, Chemical Engineering Progress, 45, 39–48.

66. Chisholm D., 1973, Pressure Gradients Due to Friction During Flow of Evaporating Two Phase Mixtures in Smooth Tubes and Channels, International Journal of Heat and Mass Transfer, 16, 347–358.

67. Spedding P. L., and Chen, J. J., 1984, Holdup in Two Phase Flow, International Journal of Multiphase Flow, 10, 307–339.

68. Smith S. L., 1969, Void Fraction in Two Phase Flow: A Correlation Based Upon an Equal Velocity Head Model, Institute of Mechanical Engineers, 184(36), 647–664.

69. Thom J. R. S., 1964, Prediction of Pressure Drop During Forced Circulation Boiling of water, International Journal of Heat and Mass Transfer, 7, 709–724.

70. Zivi S. M., 1964, Estimation of Steady State Steam Void Fraction by Means of the Principle of Minimum Entropy Production, Trans. ASME, Journal of Heat Transfer, 86, 247–252.

71. Barcozy C. J., 1966, A Systematic Correlation for Two Phase Pressure Drop, Chemical Engineering Progress, 62(44), 232–249.

72. Awad M.M., and Muzychka Y.S., 2005b, “Bounds on TwoPhase Flow: Part II Void Fraction in Circular Tubes,” Proceedings of International Mechanical Engineering Congress and Exposition, Orlando, FL (DVD).

73. Zuber N., Findlay J.A., 1965. Average volumetric concentration in two-phase flow systems, J. Heat Transfer, 87, 435–468.

74. Rouhani S. Z., and Axelsson E., 1970, Calculation of Void Volume Fraction in the Subcooled and Quality Boiling Regions, International Journal of Heat and Mass Transfer, 13, 383–393.

75. Gomez L. E., Shoham O., Schmidt Z., Choshki R. N., and Northug T., 2000, Unified Mechanistic Model for Steady State Two Phase Flow: Horizontal to Upward Vertical Flow, Society of Petrolium Enginners Journal, 5, 339–350.

76. Hibiki T., and Ishii M., 2003, One-Dimensional Drift Flux Model and Constituive Equations for Relative Motion Between Phases in Various Two-Phase Flow Regimes, International Journal of Heat and Mass Transfer, 46, 4935–4948.

77. Blasius, H., 1913, Das Anhlichkeitsgesetz bei Reibungsvorgangen in Flussikeiten, Gebiete Ingenieurw, 131, 1–41.

78. Colebrook, C. F., 1939, Turbulent Flow in Pipes, With Particular Reference to the Transition between the Smooth and Rough Pipe Laws, Journal of Institute of Civil Engineering, 11, 1938–1939.

79. Churchill S.W., 1977, Friction Factor Equation Spans All Fluid- Flow Regimes, Chemical Engineering, 7, 91–92.

80. Yu Xu, Xiande Fang, Xianghui Su, Zhanru Zhou, Weiwei Chen, 2012, Evaluation of frictional pressure drop correlations for two-phase flow in pipes, Nuclear Engineering and Design, 253, 86– 97.

81. Muller-Steinhagen H., Heck K., 1986. A simple friction pressure drop correlation for two-phase flow in pipes. Chem. Eng. Prog. 20, 297–308.

82. McAdams W.H., Wood W.K., Bryan, R.L., 1942. Vaporization inside horizontal tubes-II-benzene–oil mixtures. Trans. ASME 66, 671–684.

83. The International Association for the Properties of Water and Steam, Technical Guidance Document: Steam Purity for Turbine Operation, IAPWS TSD5-13 (2013).

84. Schiller I., & Naumann. Z., Ver. Deutsch Ing., 1935.

85. Z. Ji., Z. Xiaong., X. Wu., H. Chen., H. Wu., Experimental investigations on a cyclone separator performance at an extremely low particle concentration, Power Technology, 191 (2009) 254-259.

86. P. Rosin., and E. Rammler., 1933, The laws governing the fineness of powdered coal, J. Inst. Fuel., 7:29-36.

87. A. D. Gosman and E. loannides., 1983, “Aspects of computer simulation of liquid-fuelled combustors”, J. Energy, 7(6), 482-490.

88. Menter, F. R., 1994, “Two-equation eddy-viscosity turbulence models for engineering applications”, AIAA-journal, 32(8), 1598-1605.

89. T. H. Hibiki, M. Ishii, “One-dimensional drift flux model for two-phase flow in large diameter pipe” International Journal of Heat and Mass Transfer 46 (2003) 1773–1790.

90. M. Ishii, One-dimensional drift–flux model and constitutive equations for relative motion between phases in various two-phase flow regimes, ANL-77-47, USA, 1977.

91. I. Kataoka, M. Ishii, Drift–flux model for large diameter pipe and new correlation for pool void fraction, Int. J. Heat Mass Transfer 30 (1987) 1927–1939.

92. B. Boesmans., J. Berghmans., “Level swell in pool boilinh with liquid circulation”, Int. J. Heat Mass Transfer, 38(6), (1995), 989-998.

93. J.B. Joshi, Computational flow modelling and design of bubble column reactors,Chem. Eng. Sci. 56 (2001) 5893–5933.

94. A. Behzadi, R.I. Issa, H. Rusche, Modelling of dispersed bubble and droplet flow at high phase fractions, Chem. Eng. Sci. 59 (2004) 759–770.

95. S.T. Zalesak, Fully multidimensional flux-corrected transport algorithm for fluids, J. Comput. Phys. 31 (1979) 335–362.

96. J.H. Hills, Radial non-uniformity of velocity and voidage in a bubble column, Trans. Inst. Chem. Eng. 52 (1974) 1–9.

97. T. Menzel, T. Weide, O. Staudacher, U. Onken, Reynolds stress model for bubble column reactor, Ind. Eng. Chem. Res. 29 (1990) 988–994.

APPENDIX-A: AWL scaling to the AHWR steam drum

According to the specifications of the latest design of AHWR:

Total core flow rate (452 channels) = 2141 kg/s.

Total mass flow rate per steam drum (113 channels) = 535.25 kg/s.

Total mass flow rate for 28 channels = m_T = 132.63 kg/s.

Steam flow rate for 452 channels = 408.0 kg/s.

Steam flow rate for 28 channels = m_s = 408.0×28÷452= 25.274 kg/s.

Volumetric steam flow rate for 28 channels of prototype = $(Q_s)_P$ = 25.274÷36.32

= 0.69587 m^3/s = 41752.20 lpm.

Average core exit quality = 19.1%.

Water flow rate for 28 channels of prototype = $m_w = m_T - m_s$ = 132.63-25.274 = 107.356 kg/s

Volumetric water flow rate for 28 channels of prototype = $(Q_L)_P$ = 107.356÷740.16= 0.14504 m^3/s.

Steam drum diameter of prototype = $(D_{SD})_P$ = 4.0 m

Prototype steam drum length = $(L_{SD})_P$ =11.0 m.

Tail pipe ID in prototype = $(D_{TP})_P$ = 0.110 m.

A simplified cross-section of the steam drum is as shown in Figure B-1.

From Figure A-1,

$$OC = \sqrt{OA^2 - AC^2} = \sqrt{2.0^2 - 0.5^2} = 1.936 \text{ m}$$

$$BC = OB - OC = 2.0\text{-}1.936 = 0.064 \text{ m}$$

$BD = BC + CD = 0.064+0.534= 0.6$ m

$OD = OB - BD = 2.0\text{-}0.6 = 1.4$ m

$EF = \left(\sqrt{OF^2 - OD^2}\right) - DE = \left(\sqrt{2^2 - 1.4^2}\right) - 0.5 = 0.9283$ m

$GH = \sqrt{OH^2 - OG^2} = \sqrt{2^2 - 0.2^2} = 1.99$ m.

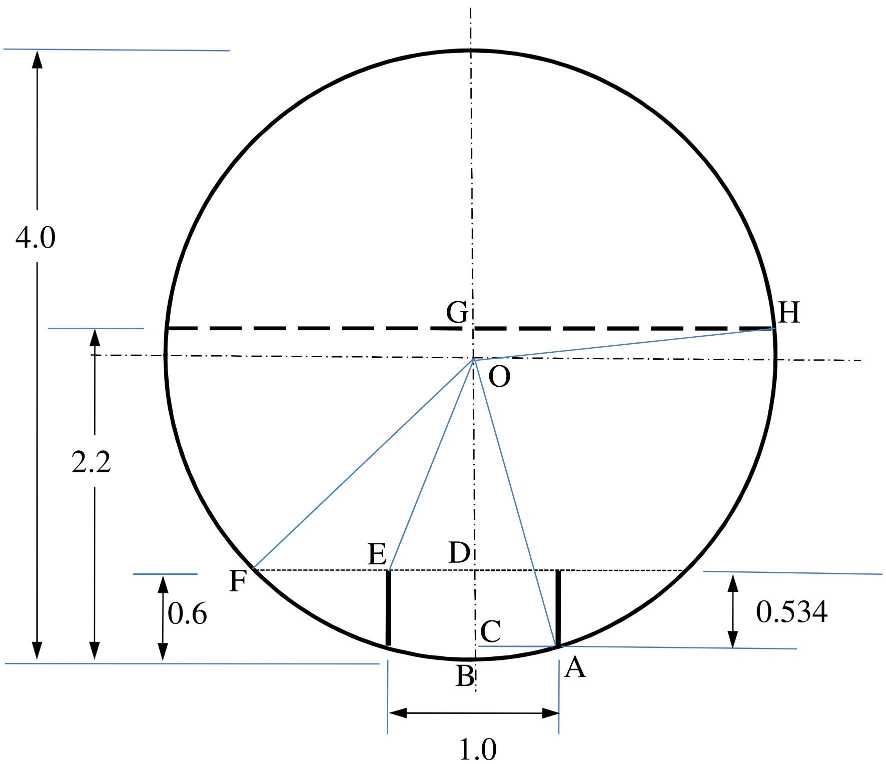

Figure A-1: Simplified schematic of prototype steam drum.

Superficial velocities of phases in tail pipe

Tail pipe inside diameter in prototype, $(d_{TP})_P = 0.110$ m

Flow area of 28 tail pipes, $(A_{TP})_P = 28.0 \times \frac{\pi}{4} \times 0.110^2 = 0.26609$ m^2

Mass flux in prototype, $G = m_T / (A_{TP})_P$ =132.63 ÷ 0.26609 = 498.435 kg/m^{2}s

Superficial velocity of gas in prototype, $\left(J_{G-TP}\right)_P = \frac{Gx}{\rho_g}$ = (498.435×0.19) ÷ 36.32 = 2.607 m/s

Superficial velocity of liquid in prototype, $\left(J_{L-TP}\right)_P = \frac{G(1-x)}{\rho_l}$ = (498.435×0.81) ÷ 740.19

= 0.5454 m/s.

The superficial velocity of gas in model= $\left(J_{G-TP}\right)_M$ = 2.102 m/s (Refer to Appendix-A)

The superficial velocity of liquid in model= $\left(J_{L-TP}\right)_M$ = 0.484 m/s (Refer to Appendix-A)

Thus comparing the superficial velocities in model and prototype tail pipes it is found that the simulated gas and liquid superficial velocities deviate from prototype by -19% and -11% respectively.

Ratios of Tail pipe pitch and tail pipe diameter in the model and prototype

$\left(\frac{Pitch}{Tail\ pipe\ dia}\right)_P$ = 0.390÷0.110 = 3.5454

$\left(\frac{Pitch}{Tail\ pipe\ dia}\right)_M$ = 0.203÷0.0627 = 3.2376

Thus the above ration in model deviates from prototype by -8.68 %.

Entry losses from Tail pipe to steam drum riser portion

For steam drum riser in prototype at baffle's top, $(2\times EF)_P = 2\times 0.9283 = 1.8566\,\text{m}$.

Flow area in riser portion (at the top of baffle plates) of prototype, $(A_R)_P$ = 1.8566×2.25 = 3.62037 m^2.

$(K_I)_P = \left[1 - \frac{(A_{TP})_P}{(A_R)_P}\right]^2$ = 0.85840

For model,

$\left(A_R\right)_M = 0.917238903 \text{m}^2$ (refer Appendix-A)

$\left(A_{TP}\right)_M = 0.08645 \, \text{m}^2$

$$\left(K_I\right)_M = \left[1 - \frac{\left(A_{TP}\right)_M}{\left(A_R\right)_M}\right]^2 = 0.8203$$

The local loss coefficient from tail pipe to steam drum riser portion in model deviates from prototype by -4.43% only.

Superficial velocities of phases at steam drum riser portion.

Superficial velocity of gas in prototype, $\left(J_{G-R}\right)_P = \frac{Q_s}{\left(A_R\right)_P} = \frac{0.69587}{3.62037} = 0.19220$ m/s

Superficial velocity of gas in model, $\left(J_{G-R}\right)_M = \frac{Q_a}{\left(A_R\right)_M} = \frac{0.18172543}{0.917238903} = 0.1981 \, \text{m/s}$

Superficial velocity of liquid in prototype, $\left(J_{L-R}\right)_P = \frac{Q_L}{\left(A_R\right)_P} = \frac{0.14504}{3.62037} = 0.04006 \text{/s}$

Superficial velocity of liquid in the model $\left(J_{L-R}\right)_M = \frac{Q_w}{\left(A_R\right)_M} = \frac{0.1591}{0.917238903} = 0.0456 \, \text{m/s}$

Thus the superficial velocity of gas and liquid at steam drum riser portion for the model deviates from prototype by +3.06% and +13.82 % respectively.

Superficial velocity of gas at interface of phase separation.

For steam drum at interface in prototype, $\left(2 \times GH\right)_P = 2 \times 1.99 = 3.98 \, \text{m}$

Interface area in SD of prototype, $\left(A_{IF}\right)_P = 3.98 \times 1.950 = 7.761 \text{ m}^2$

Superficial velocity of gas at interface of steam and water separation,

$$(J_{G-IF})_P = \frac{(Q_s)_P}{(A_{IF})_P} = \frac{0.69587}{7.761} = 0.089662 \text{ m/s}$$

Superficial velocity of gas in model at interface = $(J_{G-IF})_M = 0.0823$ m/s (refer to Appendix-A)

The superficial velocity of gas at interface in model deviates from prototype by -8.21 %.

Superficial velocity of liquid at cross flow area above the baffle plate

Cross flow area in steam drum above baffle plates of prototype (i.e. between the riser top to the steam water separation interface), $(A_{BI})_P = 1.950 \times (2.2 - 0.534) = 3.2487$ m^2

Superficial velocity of liquid, $(J_{L-BI})_P = \frac{(Q_l)_P}{(A_{BI})_P} = \frac{0.14504}{3.2487} = 0.04464$ m/s

Superficial velocity of liquid at cross flow area above baffle plate for the model = $(J_{L-BI})_M = 0.0456$ m/s (refer to Appendix-A)

Thus the superficial velocity of liquid at cross flow area above baffle plate for the model deviates from the prototype by +2.13 %.

Superficial velocity of liquid in down comer region of steam drum

Baffle spacing in prototype, $(B_S)_P = 1.0\,\text{m}$

Baffle length, $(L_S)_P = 1.95\,\text{m}$

Flow area between baffle spacing, $(A_{BS})_P = 1.95 \times 1.0 = 1.95\,\text{m}^2$

Total down comer flow rate, $(Q_{TDC})_P = \frac{132.63}{740.19} = 0.17918\,\text{m}^3\text{/s}$

Superficial velocity of liquid, $\left(J_{L-BS}\right)_P = \frac{\left(Q_{DC}\right)_P}{\left(A_{BS}\right)_P} = \frac{0.17918}{1.95} = 0.09187$ m/s

Superficial velocity of liquid in down comer region for model $= \left(J_{L-BS}\right)_M = 0.0858$ m/s (refer Appendix-A)

Thus superficial velocity of liquid in down comer region for model deviates from prototype by -6.62 %.

Local losses in down comer region

Loop down comer pipe ID in prototype, $\left(d_{DC}\right)_P = 0.2731\,\text{m}$

Flow area of down comer pipe in prototype, $\left(A_{DC}\right)_P = \frac{\pi}{4} \times 0.2731^2 = 0.05857783\ \text{m}^2$

$$\left(K_E\right)_P = 0.5\left[1 - \frac{\left(A_{DC}\right)_P}{\left(A_{BS}\right)_P}\right]^{0.75} = 0.5\left[1 - \frac{0.05857783}{1.95}\right]^{0.75} = 0.48869$$

Loop down comer pipe ID in model, $\left(d_{DC}\right)_M = 0.1345\text{m}$

Flow area of down comer pipe in model, $\left(A_{DC}\right)_M = \frac{\pi}{4} \times 0.1345^2 = 0.0142080\,\text{m}^2$

$$\left(K_E\right)_M = 0.5\left[1 - \frac{\left(A_{DC}\right)_M}{\left(A_{BS}\right)_M}\right]^{0.75} = 0.5\left[1 - \frac{0.0142080}{0.4876848}\right]^{0.75} = 0.4890$$

Thus the local loss from down comer region to down comer pipe in model deviates from prototype by +0.07 %.

Local loss at exit of steam drum

Steam exit pipe ID in prototype, $\left(d_{SE}\right)_P = 0.18258\,\text{m}$

Flow area of down comer pipe in prototype,

$$(A_{SE})_P = 4.0 * \left(28/452\right)\left(\frac{\pi}{4}\right)(0.18258)^2 = 0.006487477\ \mathrm{m}^2$$

Exit losses from steam drum in prototype

$$(K_E)_P = 0.5\left[1 - \frac{(A_{SE})_P}{(A_{IF})_P}\right]^{0.75} = 0.5\left[1 - \frac{0.006487477}{7.761}\right]^{0.75} = 0.49968$$

Exit losses from stem drum in model

$$(K_E)_M = 0.5\left[1 - \frac{(A_{SE})_M}{(A_{IF})_M}\right]^{0.75} = 0.5\left[1 - \frac{0.00131382}{0.971723}\right]^{0.75} = 0.49949$$

Thus the local losses at steam drum exit for model deviates from prototype by -0.039%.

Ratio of steam drum length to diameter

$$\left(\frac{Steam\ \ Drum\ \ length}{Steam\ \ drum\ \ dia}\right)_P = \frac{1.95}{4.0} = 0.4875$$
$$\left(\frac{Steam\ \ Drum\ \ length}{Steam\ \ drum\ \ dia}\right)_M = \frac{1.154}{1.93} = 0.5979$$

Thus the ratio of steam drum length to steam drum diameter in model deviates from prototype by

+22.6 %.

Ratio of baffle height to drum diameter.

$$\left(\frac{Baffle\ \ Height}{Steam\ drum\ dia}\right)_P = \frac{0.534}{4} = 0.1335$$
$$\left(\frac{Baffle\ \ Height}{Steam\ drum\ dia}\right)_M = \frac{0.23088}{1.93} = 0.119626$$

Thus the ratio of baffle height to drum diameter in model deviates from prototype by -10.39 %.

Annexure-B

Implementation of OpenFOAM solver “simpleReactingParcelFoam”

The Figure B-1 shows the code implemented in main file “simpleReactingParcelFoam.c” of the solver. It employs the SIMPLE corrector loop to solve the governing equations of flow. The solver algorithm is shown in Figure B-2.

```
while (simple.loop())
{
    Info<< "Time = " << runTime.timeName() << nl << endl;

    parcels.evolve();

    // --- Pressure-velocity SIMPLE corrector loop
    {
        #include "UEqn.H"
        #include "YEqn.H"
        #include "EEqn.H"
        #include "pEqn.H"
    }

    turbulence->correct();

    runTime.write();

    Info<< "ExecutionTime = " << runTime.elapsedCpuTime() << " s"
        << "  ClockTime = " << runTime.elapsedClockTime() << " s"
        << nl << endl;
}

Info<< "End\n" << endl;
```

Figure B-1: Main code of solver “*simpleReactingParcelFoam*”

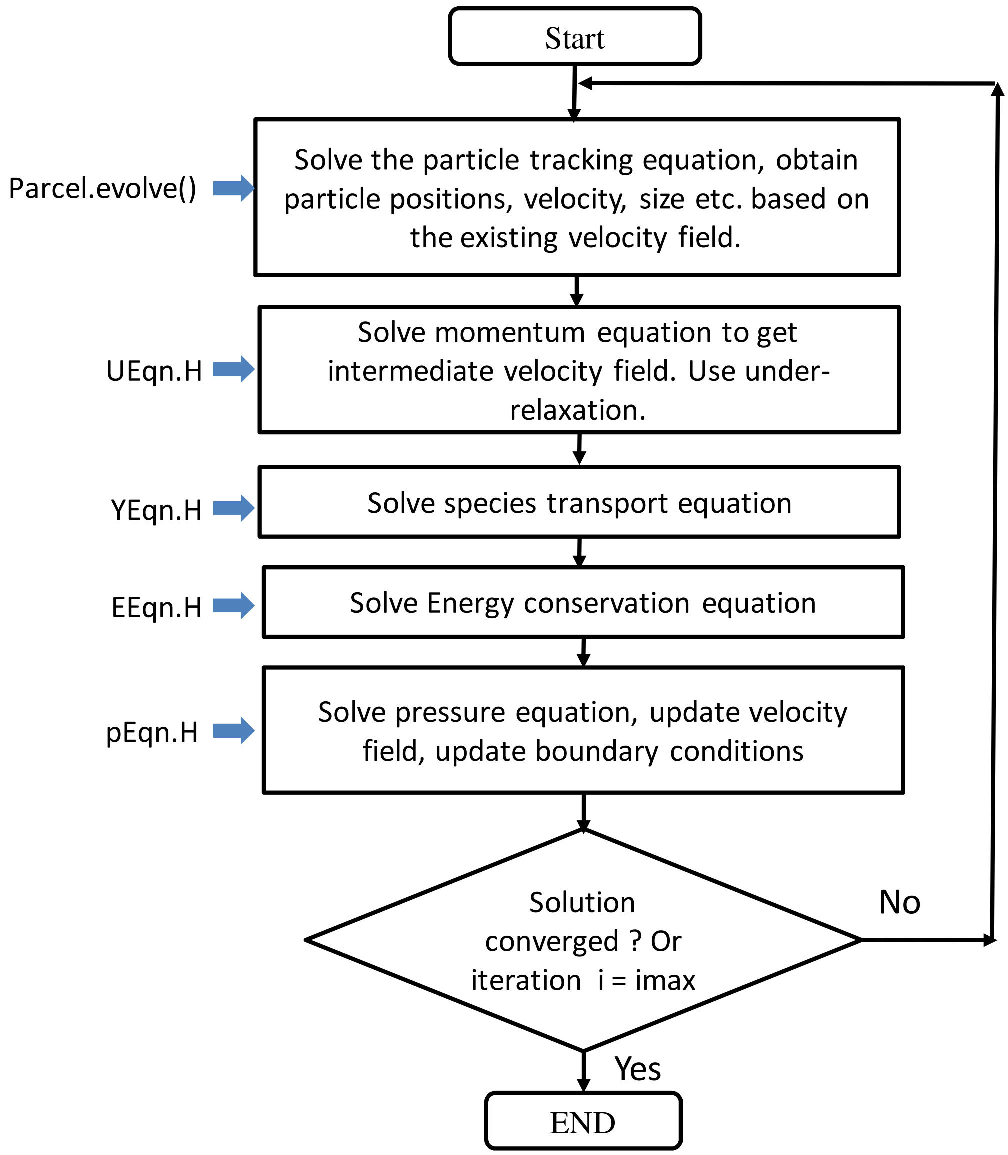

Figure B-2: Algorithm of "*simpleReactingParcelFoam*"

The Lagrangian equations for parcels of particles/droplets are first solved based on the velocity field calculated from previous time step. Following which the momentum equation is solved. The equation 5.22 is modeled in "UEqn.H" which is shown in Figure B-3. The various terms in UeEqn.H correspond to momentum equation. "`fvm::div(phi, U)`" represents the convective part of meomentum i.e. $\nabla.(\rho\boldsymbol{u}\boldsymbol{u})$. the term "`turbulence->divDevRhoReff(U)`" is the divergence of the stress tensor i.e. $\nabla.\boldsymbol{\tau}$ and is evaluated as $\mu_{eff}(\nabla\boldsymbol{u} + (\nabla\boldsymbol{u}^T))$, where μ_{eff}

represents the effective viscosity i.e. dynamic viscosity μ and turbulent viscosity μ_t . "`rho.dimensionedInternalField()*g`" represents the body force due to gravity i.e. $\rho \boldsymbol{g}$. "`parcels.SU(U)`" represents the source term due to particles in momentum equation i.e. $S_{i,mo}$. The OpenFOAM makes a provision of specifying user defined source terms to equations of mathematical model using "`fvOptions`" framework. In present case we have not added any user-defined source terms to any of the equations. Therefore all code lines with "`fvOptions`" are not relevant to final equations and algorithm. "`UEq().relax()`" applies relaxation parameter to equation terms related to velocities and "`solve(UEqn.() == -fvc::grad(p))`" solves the equation with now adding the pressure gradient term $-\nabla P$.

```
tmp<fvVectorMatrix> UEqn
(
    fvm::div(phi, U)
  + turbulence->divDevRhoReff(U)
 ==
    rho.dimensionedInternalField()*g
  + parcels.SU(U)
  + fvOptions(rho, U)
);

UEqn().relax();

fvOptions.constrain(UEqn());

solve(UEqn() == -fvc::grad(p));

fvOptions.correct(U);
```

Figure B-3: "UEqn.H" employed in "*simpleReactingParcelFoam*" solver

Figure B-4 shows the important part of code "`YEqn.H`". The scalar transport equation of species formed due to reactions, processes of mass transfer between the two phases is constructed in solver as per equation (5.27). The term "`mvConvection->fvmDiv(phi, Yi)`" represents the term for convection of species i.e. $\nabla.(\rho \boldsymbol{u} Y_i)$. "`fvm::laplacian(turbulence->muEff(), Yi)`" represents the diffusion term of species $\nabla.\dot{\boldsymbol{J}}$. The diffusion due to turbulence is dominant and the diffusion is expressed as $\nabla.\dot{\boldsymbol{J}} = -\rho D_t \nabla Y_i = -\rho \frac{\mu_t}{\rho Sc_t} \nabla Y_i = \frac{\mu_t}{Sc_t} \nabla Y_i = \mu_t \nabla Y_i$. "`parcels.SYi(i, Yi)`" represents the source term from discrete phase S_i. "`combustion->R(Yi)`" adds the source term due to combustion/reaction representing term R_i of the equation (5.27). "`fvOptions(rho, Yi)`" represents the user defined source terms if any.

```
fvScalarMatrix YEqn
(
    mvConvection->fvmDiv(phi, Yi)
  - fvm::laplacian(turbulence->muEff(), Yi)
 ==
    parcels.SYi(i, Yi)
  + combustion->R(Yi)
  + fvOptions(rho, Yi)
);

YEqn.relax();

fvOptions.constrain(YEqn);

YEqn.solve(mesh.solver("Yi"));

fvOptions.correct(Yi);
```

Figure B-4: "YEqn.H" employed in "*simpleReactingParcelFoam*" solver

Figure B-5 shows the code "EEqn.H" for solving the energy conservation equation used in the solver. The term "`mvConvection->fvmDiv(phi,he)`" represents the convective part of energy equation i.e. $\nabla.(\rho h \boldsymbol{u})$ The variable "`he`" could be enthalpy or internal energy. The term "`fvc::div(phi, volScalarField("K", 0.5*magSqr(U)))`" represents the term $\nabla.(\rho K \boldsymbol{u})$ in equation (5.25). "`fvm::laplacian(turbulence->alphaEff(), he)`" accounts for the term $\nabla.q$ which is expressed as $\nabla.q = \nabla.(\lambda \nabla T) = \nabla.\left(\lambda \nabla (h/\rho C_p)\right) =$

$\left(\frac{\lambda}{\rho C_p}\right)\nabla^2 h = \Gamma\nabla^2 h$ where Γ is thermal diffusivity. Effect of turbulence on thermal diffusion is considered by defining $\Gamma_{eff} = \frac{C_p}{C_v}(\Gamma + \Gamma_t)$. "`parcels.Sh(he)`" represent the energy source term due to discrete phase. "`radiation->Sh(thermo)+combustion->Sh()`" are the terms corresponding to the source term due to radiation and combustion. "`fvOptions(rho, he)`" allows to consider the user defined source terms, which is not relevant here as no such sources are specified. "`thermo.correct();`" updates the fluid properties based on the available enthalpy/temperature field.

```
fvScalarMatrix EEqn
(
    mvConvection->fvmDiv(phi, he)
  + (
        he.name() == "e"
      ? fvc::div(phi, volScalarField("Ekp", 0.5*magSqr(U) + p/rho))
      : fvc::div(phi, volScalarField("K", 0.5*magSqr(U)))
    )
  - fvm::laplacian(turbulence->alphaEff(), he)
 ==
    parcels.Sh(he)
  + radiation->Sh(thermo)
  + combustion->Sh()
  + fvOptions(rho, he)
);

EEqn.relax();

fvOptions.constrain(EEqn);

EEqn.solve();

fvOptions.correct(he);
thermo.correct();
radiation->correct();
```

Figure B-5: "EEqn.H" employed in "*simpleReactingParcelFoam*" solver

Pressure correction equation:

The pressure field has to be solved with a equation constructed from momentum and continuity. Consider the form of continuity and momentum as follows:

$$\nabla.(\boldsymbol{u}) = 0 \tag{B.1}$$

&

$$\frac{\partial \boldsymbol{u}}{\partial t} + \nabla.(\boldsymbol{uu}) - \nabla.(\vartheta \nabla \boldsymbol{u}) = -\nabla \frac{P}{\rho} \tag{B.2}$$

The density is assumed to be constant in above equations. The momentum equation in descritized form can be written as:

$$\mathrm{a_p} \boldsymbol{u}_p = H(\boldsymbol{u}) - \nabla \frac{P}{\rho} \tag{B.3}$$

Where

$$H(\boldsymbol{u}) = -\sum_n a_n \boldsymbol{u}_n + \frac{u^0}{\Delta t} \tag{B.4}$$

The first term of $H(\boldsymbol{u})$ represents the matrix coefficients of the neighbouring cells multiplied by their velocity, while the second part contains the unsteady term and all the sources except the pressure gradient.

Equation (B.3) can be written as:

$$\boldsymbol{u}_p = \frac{H(\boldsymbol{u})}{\mathrm{a_p}} - \frac{\nabla(P/\rho)}{\mathrm{a_p}} \tag{B.5}$$

The continuity equation is descritized as:

$$\nabla.(\boldsymbol{u}) = \sum_f \boldsymbol{S}.\boldsymbol{u_f} = 0 \tag{B.6}$$

Where $\boldsymbol{S}$ is outward-pointing face area vector and the $\boldsymbol{u_f}$ velocity on the face. The velocity on the face is obtained by interpolating the semi discretised form of the momentum equation as follows:

$$\boldsymbol{u_f} = \left(\frac{H(\boldsymbol{u})}{\mathrm{a_p}}\right)_f - \left(\frac{\nabla(P/\rho)}{\mathrm{a_p}}\right)_f \tag{B.7}$$

By substituting this equation into the descritized continuity equation obtained above, we obtain the pressure equation:

$$\nabla.\left(\frac{1}{\mathrm{a_p}}\nabla(P/\rho)\right) = \nabla.\left(\frac{H(\boldsymbol{u})}{\mathrm{a_p}}\right) = \sum_f \boldsymbol{S}\left(\frac{H(\boldsymbol{u})}{\mathrm{a_p}}\right)_f \tag{B.8}$$

The pressure equation is implemented in the solver as shown in Figure B-6. A scalar field "`rAU`" is constructed using code "`volScalarField rAU(1.0/UEqn.A());`" which basically represents $\frac{1}{\mathrm{a_p}}$. A vector field "`rhorAUf`" is constructed by code "`surfaceScalarField rhorAUf("rhorAUf", fvc::interpolate(rho*rAU));`" which is $\frac{1}{\rho \mathrm{a_p}}$. A volume vector field "`HbyA`" i.e. $\frac{H(\boldsymbol{u})}{\mathrm{a_p}}$ is constructed using code "`volVectorField HbyA("HbyA", U); HbyA = rAU*UEqn.H();`". Similarly the surface scalar field "`phiHbyA`" i.e. $\left(\frac{H(\boldsymbol{u})}{\mathrm{a_p}}\right)_f$ is also constructed. The pressure equation term "`fvc::div(phiHbyA)`" which represents the $\nabla.\left(\frac{H(\boldsymbol{u})}{\mathrm{a_p}}\right)_f$. The term "`- fvm::laplacian(rhorAUf, p)`" represents $\nabla.\left(\frac{1}{\mathrm{a_p}}\nabla(P/\rho)\right)$. "`parcels.Srho()`" is the term for mass from the particle phase. The pressure equation is solved in a loop for number of times specified by number of correctors, which can be specified as a solution parameter in input. The density is corrected before and after solving the pressure equation by first removing and then adding the compressibility effect term "`psi*p`". After this correction the velocity field is updated, boundary conditions are updated and source terms are updated if any.

```
thermo.rho() -= psi*p;

volScalarField rAU(1.0/UEqn().A());
volVectorField HbyA("HbyA", U);
HbyA = rAU*UEqn().H();

UEqn.clear();

surfaceScalarField phiHbyA
(
    "phiHbyA",
    fvc::interpolate(rho)*(fvc::interpolate(HbyA) & mesh.Sf())
);

fvOptions.makeRelative(fvc::interpolate(rho), phiHbyA);

while (simple.correctNonOrthogonal())
{
    fvScalarMatrix pEqn
    (
        fvc::div(phiHbyA)
      - fvm::laplacian(rho*rAU, p)
     ==
        parcels.Srho()
      + fvOptions(psi, p, rho.name())
    );

    fvOptions.constrain(pEqn);

    pEqn.solve();

    if (simple.finalNonOrthogonalIter())
    {
        phi = phiHbyA + pEqn.flux();
    }
}

p.relax();

// Second part of thermodynamic density update
thermo.rho() += psi*p;

#include "compressibleContinuityErrs.H"

U = HbyA - rAU*fvc::grad(p);
U.correctBoundaryConditions();
fvOptions.correct(U);

rho = thermo.rho();
rho = max(rho, rhoMin);
rho = min(rho, rhoMax);
rho.relax();
```

Figure B-6: Implementation of pressure correction equations in “*simpleReactingParcelFoam*”